Genetic full waveform inversion to characterise fractures

Antonio Fuggi

School of Earth and Environment
University of Leeds

Submitted in accordance with the requirements for the degree of
Doctor of Philosophy

December 2021

Intellectual Property and Publication Statements

I confirm that the work submitted is my own and that appropriate credit has been given where reference has been made to the work of others.

Acknowledgements

This research project is funded by a studentship from the Engineering and Physical Sciences Research Council (EPSRC) and partially funded by ION Geophysical. Without their financial support this work would not have been possible. I also acknowledge the High Performance Computing facility at the University of Leeds, ARC4, where this work was undertaken.

First and foremost, I would like to express my most sincere gratitude to my supervisor Mark Hildyard for his support and guidance throughout this PhD journey, for having always encouraged to trust my own initiatives and given me the freedom to explore my own ideas.

I would like to thank Roger Clark for his constant source of advice ("Look at the big picture!") and laughs; for his precious help to finding new opportunities beyond the academic world.

My sincere thanks goes to Andy Hooper for all his invaluable advise and help on the geophysical inverse theory and the Neighbourhood Algorithm.

I would like to thank John Brittan, who acted as my external supervisor, for his support and incentive during, and after, the 3-month internship at ION Geophysical. I extend my gratitude to all ION team: Ian Jones, Claudia Hagen, Ross O'Driscoll, for providing training and technical support, and Chris Tyson for hosting me throughout the internship period.

I would like to thank Ahmadreza Hedayat, who provided the ultrasonic laboratory measurements and guided me in their analysis. His contribution has been essential to this work.

Thanks also to Harry Holmes who gave me useful feedback on different parts of this work.

During my project I had the opportunity to work as an intern to the dGB Earth Sciences. I gratefully thank EPSRC who funded the internship and all the dGB team: Paul de Groot, Arnold Huck, Hardeep Jaglan, Nanne Hemstra for their technical support and promoting new research ideas. Thanks to Victoria and Airat for their friendship

and to have had memorable time in the Netherlands.

Particular thanks to all people who contributed to making my time in Leeds unforgettable: the "*latin lunchers*": Marco, Luca, Lucia, Lisa, Ezechiel, with whom we shared lunches, coffees, and laughs. To Giuseppe and Charlotte for the fun and their moral support during my lows. To Sofia for the long walks during the pandemic to reduce stress and enjoy the few English sunny days. I thanks Manolis, with whom I shared the first part of my PhD journey, for welcoming me in the research group as a longtime friend, and for having had great time during the conferences.

A very special thanks goes to my dad, mum, sisters, and brother who were always close to me despite the geographical distance. I can only say: *grazie per il vostro incoraggiamento e amore senza fine. Grazie per avermi insegnato chi sono!.*
The deepest thank must go to my better half, Lucia, who shared with me almost half of my entire life. Thanks for your continue support and your encouragement to look at the positive side of things and believe more in myself. Regardless anything else, I feel profoundly lucky to have you in my life.

Abstract

Active seismic methodologies provide a non-invasive tool to remotely characterise the physical properties of fractures at a wide range of scales, and have a positive impact in helping to solve rock engineering problems in a variety of geo-industrial applications. With current advances in seismic processing tools, such as full waveform inversion (FWI), and accurate models of seismic wave interaction with fractures, seismic characterisation of fractures can be tackled by utilising the entire seismic wavefield recorded at the receiver locations. A two-step strategy, using the genetic algorithm (GA) for global optimisation and the Neighbourhood Algorithm (NA) for evaluating uncertainties, was developed to simultaneously estimate the fracture properties (both fracture specific stiffness and equivalent fracture stiffness) and the background material properties directly from seismic waveforms. The optimisation involves minimising the difference between the observed (measured) and forward-modelled full waveforms through the finite difference code WAVE3D.

The development, named Genetic Algorithm Full-Waveform Fracture Inversion (GA-FWFI), looks beyond conventional seismic methods which focus on characterising fracture-induced anisotropy, by reducing the need to manually condition the data (e.g. manual picking of seismic phases), and by providing a robust means to explore multiple solutions. The development also allows the gap between different representations of fracturing to be bridged within a comprehensive method which can employ both discrete fracture and effective fracture models.

GA-FWFI is tested initially on synthetic ultrasonic experiments with parallel fractures. Results confirm that the method can effectively invert for physical properties such as fracture stiffness, location, background material properties, while the posterior probability density (PPD) show that inversions are very well constrained. GA-FWFI is then applied to waveforms from a laboratory experiment investigating fracture slip and again results show high degree of accuracy.

GA-FWFI is then utilised to unveil the coupling between discrete fracture networks (DFNs) and their equivalent fracture zone properties. The results reveal that the transition from a medium with open cracks to one with welded interfaces leads to the equivalent media having the equivalent medium stiffness non-linearly related to the crack specific stiffness. An attribute χ is proposed which helps guide the interpretation of a cracked medium by giving a range of likely values for crack size and crack stiffness. This work paves the way for novel strategies to seismically characterise fractures.

Contents

Abbreviations

DFN	Discrete Fracture Network
PPD	Posterior Probability Distribution
PDF	Probability Density Function
GA	Genetic Algorithm
NA (NAB)	Neighbourhood Algorithm
FWI	Full Waveform-Inversion
GA-FWFI	Genetic Algorithm Full Waveform Fracture Inversion
EM	Equivalent (or Effective) Medium
HTI	Horizontal Transverse Isotropy

Symbols

Symbol	**Meaning**	**Units**
ϵ	crack density	
L	Average fracture spacing	m
D_f	$1/L$	m^{-1}
Z_n	Normal fracture compliance	$\mathrm{m\ Pa}^{-1}$
Z_s	Shear fracture compliance	$\mathrm{m\ Pa}^{-1}$
B_n	Normal equivalent fractured medium compliance	Pa^{-1}
B_s	Shear equivalent fractured medium compliance	Pa^{-1}
N_f	Number of fractures	
S_f	Area of fractures	m^{-2}
N_c	Number of cracks	
S_c	Area of cracks	m^{-2}
κ_n	Normal fracture specific stiffness	$\mathrm{Pa\ m}^{-1}$
$\kappa_n^{(c)}$	Normal crack specific stiffness	$\mathrm{Pa\ m}^{-1}$
κ_n^{vf}	Normal volumetric fracture stiffness	Pa
$\kappa_n^{vf,GA}$	GA inverted volumetric normal fracture stiffness	Pa
κ_s	Shear fracture specific stiffness	$\mathrm{Pa\ m}^{-1}$
$\kappa_s^{(c)}$	Shear crack specific stiffness	$\mathrm{Pa\ m}^{-1}$
κ_s^{vf}	Volumetric shear fracture stiffness	Pa
χ	$\kappa_n^{vf,GA}/\kappa_n^{vf}$	
ϕ	Fracture strike	
δ	Fracture dip	
Δu_z	Shear displacement	m
η	$(N_cS_c)/(N_fS_f)$	
R	(GA population size)/(space dimension)	

List of Figures

List of Tables

Chapter 1

Introduction

1.1 Preamble

The extensive presence of fractures throughout the Earth's upper crust and their key role in a multitude of physical processes in the subsurface make them a prominent target in a variety of geo-industrial applications, such as hydrocarbon and geothermal exploration (Sayers, 2007; Liu and Martinez, 2012), rock damage and stability investigation (Hildyard et al., 2005; Hildyard, 2007), carbon capture and storage (Iding and Ringrose, 2009; March et al., 2018) and nuclear waste repositories monitoring (MacQuarrie and Mayer, 2005; Tsang et al., 2015).

Therefore, the ability to identify fractures in different geological settings (Figure 1.1), and at different scales, can have a significant impact on characterising fluid flow in the subsurface, paramount in reservoir management and in the final disposal of spent nuclear fuel (Figure 1.1(a)), on determining the stability of engineered structures and excavations, and even on understanding the evolution of the englacial water flow system which controls the water storage, pressure, glacier sliding, and release of glacial outburst floods (Fountain et al., 2005) (Figure 1.1(c)).

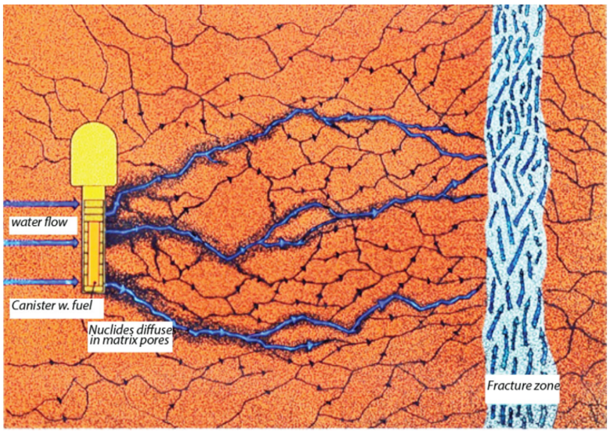

(a) A model example of leaking in crystalline fractured rock in KBS-3V repository type (Tsang et al., 2005)

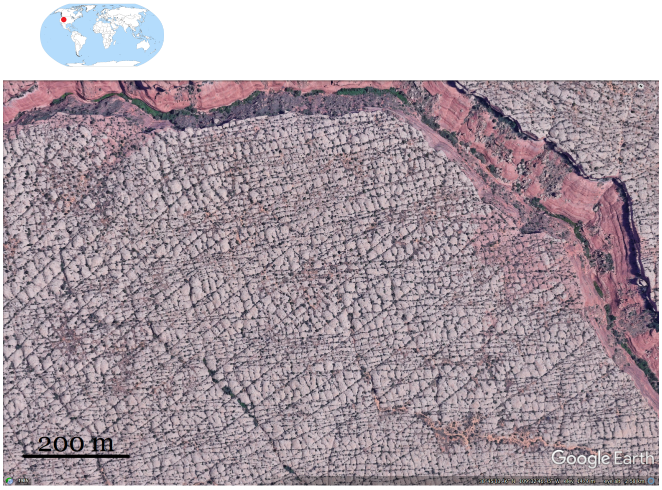

(b) Fracture outcrop in Arches National Park, Utah (USA). Monoclinic symmetries in fractured sandstone. Image taken from Google Earth (coordinate 38°44'55.6"N 109°32'25.0"W)

(c) Aerial image of cracks in Pine Island Glacier's ice shelf (Antarctica), January 2010 (Washington, 2010).

Figure 1.1: Fractures and cracks in different geological settings.

The characterisation of fractures or fractured rocks can be derived from a range of geophysical measurements. For instance, core and image logs such as borehole televiewers have been designed to image the subsurface fractures cutting through a borehole; whereas sonic logging tools, which can use Stoneley waves as well as P-waves, are utilised to produce a detailed understanding of small-scale cracks by estimating their locations and permeability (Hornby et al., 1989). Although their usage is essential in the fracture network model building, these methods are limited by the small sampling area and the high cost (Liu and Martinez, 2012). Furthermore, the characterisation of the fracture network properties might be inaccurate if there are only a few sparse wells containing fractures information. On the contrary, a seismic survey provides a non-invasive tool to characterise remotely physical properties of a wide range of fracture scales, and it has the advantage of wider coverage, lower cost, and deeper penetration.

1.2 Motivation

Popular seismic methodologies, used as tool for fracture detection, exploit the directional dependence of seismic attributes (velocity, frequency, amplitude, attenuation), referred to as seismic anisotropy, as well as the physical phenomenon of shear wave birefringence. The first makes use of methods such as Azimuthal Amplitude Variation (AVOA) (Rüger and Tsvankin, 1997; Rüger, 1998) or Normal Move-Out (NMO) variation with azimuth (Bakulin et al., 2000) to provide anisotropy maps over the survey area. These can be converted to crack density and orientation according to the penny-shaped crack model (Hudson, 1980; Hudson, 1981). Whereas the second defines the physical splitting of shear waves into two separate polarised wavefields, S_1 and S_2 (Alford, 1986). The interpretation of these two wavefields, quantified in the the time-lag between S_1 and S_2 and their polarisations, leads to an estimation of the fracture density and fracture orientation, respectively. Nevertheless, the focus of these methodologies lies in the characterisation of fracture-induced anisotropy of the equivalent fractured medium by analysing only the change in wave amplitude or the change in time arrival.

However, with advances in seismic processing tools, such as reverse-time migration (RTM) and full-waveform inversion (FWI) (Virieux and Operto, 2009; Warner et al., 2013; Jones, 2018), and fully developed accurate models of seismic wave interactions with fractures (Hildyard et al., 1995; Hildyard, 2007), seismic characterisation of fractures and fracture zones can be exploited by utilising the entire seismic wavefield recorded at the receiver locations.

Moreover, although fracture location, density, and orientation are commonly extracted from seismic data, fracture specific stiffness is less often determined (Worthington, 2007; Worthington, 2008). However, several authors have shown the importance of estimating mechanical properties of fractures, quantified by fracture stiffness, in order to evaluate the fluid flow through the fractures (Pyrak-Nolte and Nolte, 2016) as well as the visibility of macrofractures in seismic data (Worthington, 2007). Although Hildyard and Young (2002), Hildyard et al. (2005), and Parastatidis et al. (2021) have provided a data driven methodology to diagnose the state of fracturing by estimating the fracture specific stiffnesses, this approach is based on a trial and error strategy to match modelled and observed data.

Therefore, the main aim of this work consists in providing a semi-automated method, with limited data processing, to characterise fractured media with respect to both the discrete fracture attributes and the effective fracture parameters directly from seismic waveforms. To achieve this goal, a waveform inversion technique GA-FWFI (Genetic Algorithm-Full Waveform Fracture Inversion) has been developed and applied to

1. small scale experiments (both synthetic and active ultrasonic laboratory measurements) for estimating discrete fracture properties, such as fracture location, and specific fracture stiffness,

2. bigger scale experiments in a simulated cross hole seismic survey. In this case equivalent fracture set orientation (fracture dip, and fracture strike), bulk stiffness, and fracture intensity have been appraised in different discrete fracture network scenarios.

In both cases the seismic wave propagation and its interaction with fractures and fractured media has been modelled using the fully-elastic finite difference modelling code WAVE3D (Hildyard et al., 1995).

The proposed alternative scheme tries to look beyond the conventional local-optimisation FWI for velocity models building (Virieux and Operto, 2009; Warner et al., 2013) introduced in Section 1.6, and investigates a two-step method involving a global optimization technique, the genetic algorithm (GA), and uncertainties evaluation using the neighbourhood algorithm (NA) (Sambridge, 1999a). A schematic overview of this project can be seen in Figure 1.2.

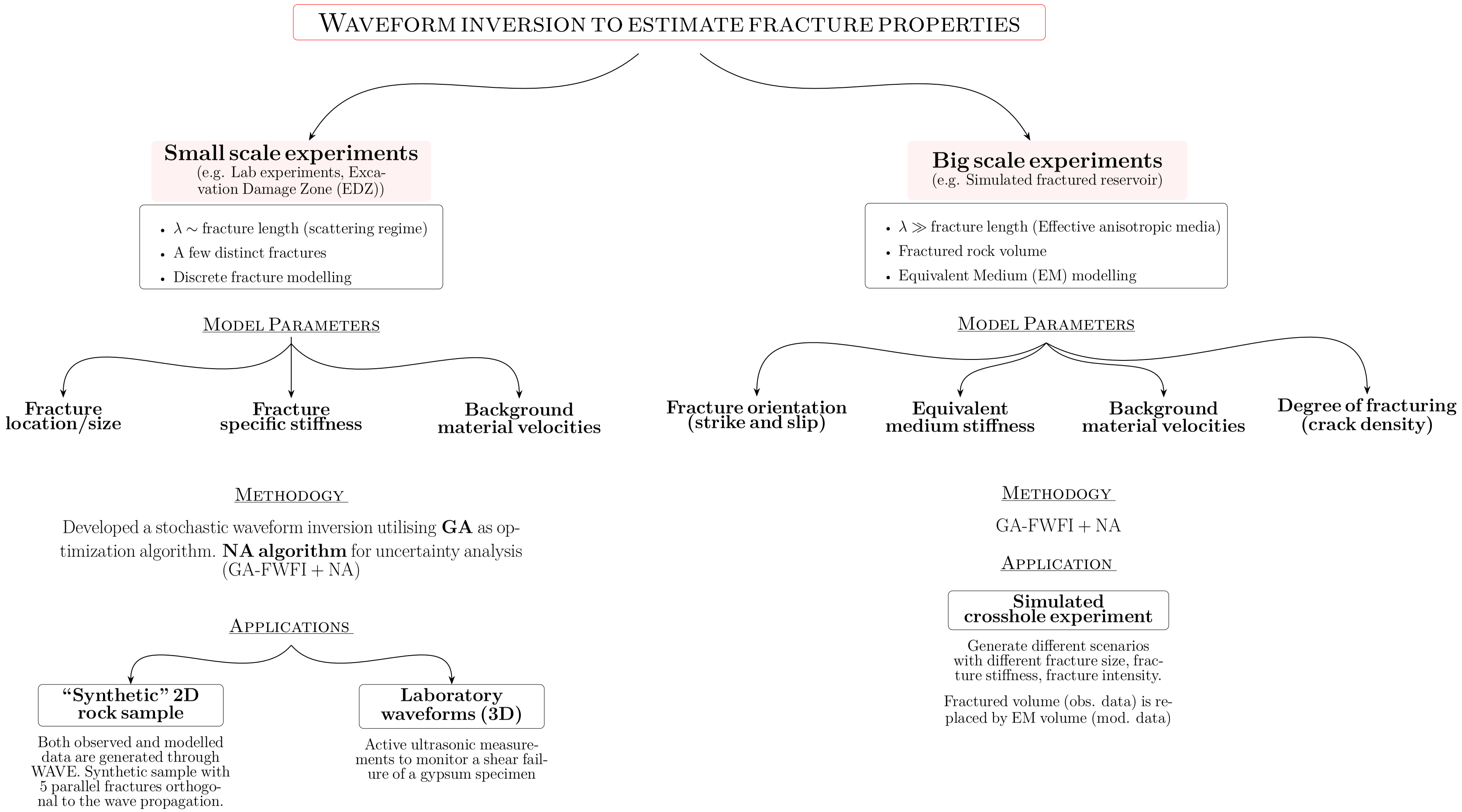

- $\lambda \sim$ fracture length (scattering regime)
- A few distinct fractures
- Discrete fracture modelling

- $\lambda \gg$ fracture length (Effective anisotropic media)
- Fractured rock volume
- Equivalent Medium (EM) modelling

Developed a stochastic waveform inversion utilising **GA** as optimization algorithm. **NA algorithm** for uncertainty analysis (GA-FWFI + NA)

Both observed and modelled data are generated through WAVE. Synthetic sample with 5 parallel fractures orthogonal to the wave propagation.

Active ultrasonic measurements to monitor a shear failure of a gypsum specimen

Generate different scenarios with different fracture size, fracture stiffness, fracture intensity.

Fractured volume (obs. data) is replaced by EM volume (mod. data)

Figure 1.2: Schematic overview of this work.

1.3 Chapter overview

This thesis is organised in 6 chapters. The first of these gives the reader an overview of the key objectives and motivation for this thesis, as well as an essential introduction to the relevant concepts used throughout the thesis, such as the numerical solution of the wave equation (the forward problem), which is the core of waveform inversion techniques, the general inverse theory, and an introduction of the least-square FWI.

Chapter 2 addresses theories for modelling the seismic response in cracked media by using both the explicit fracture representation, and the equivalent medium modelling in the two flavours of the displacement-discontinuity theory. Additionally, it presents WAVE3D the program used in this project to simulate the wave propagation and interaction with fractures and fracture zones. Finally, it introduces the concept of seismic anisotropy with a focus on the fracture-induced anisotropic parameters and how the latter are characterised through seismic surveys.

Chapter 3 presents the implementation of the GA-FWFI approach, that is a stochastic waveform inversion approach developed by the author, discussing the suitability of a global optimisation method for the inversion of the fracture parameters. Some diagnostic analytical experiments are shown in order to examine the degree of accuracy and convergence of the algorithm, and the ability of the NA method to appraise the model ensemble. Findings of synthetic ultrasonic data inversion in a fractured medium containing 5 parallel fractures are also presented.

Chapter 4 builds on findings of Chapter 3 to explore the suitability of the global inversion scheme for a series of laboratory active ultrasonic measurements. These were analysed in order to investigate the mechanical and geophysical processes occurring during shear failure of rock joints. Both shear and compressional waveforms were inverted to estimate the variation of the specific fracture stiffnesses with the shear stress applied to the rock sample, the discontinuity location, and the velocities of the background medium.

Chapter 5 focuses on assessing the effectiveness of the equivalent medium theory (displacement discontinuity theory) for discrete fracture network (DFN) models by means of GA-FWFI. It is analysed how the discrete fracture parameters such as crack density, crack size, and crack specific stiffness influence the equivalent fracture parameters, such as the equivalent fracture orientation, and the bulk stiffness, in a set of 54 different DFN scenarios.

The final chapter assesses the findings presented in the previous chapters, and discusses the results obtained in relation to the objective of this thesis. Finally, at the end of the chapter a proposal of some further work for the future is given.

1.4 The forward problem: solving the seismic wave equation

An indispensable tool for seismic motion studies and a key requirement for solving the waveform inversion problem is founded on the solution of the *forward problem*, which consists in the ability to solve the seismic wave equation. The solution of the wave equation allows the description of the propagation of the seismic waves though the Earth.

The forward problem, in a general form, can be written as

$$\mathbf{G}(\mathbf{m}) = \mathbf{d} \tag{1.1}$$

where $\mathbf{m}$ is a vector that contains the set of physical properties which describe the subsurface model, $\mathbf{G}$ is a non-linear operator that calculates the seismic wavefield everywhere in the medium given the model $\mathbf{m}$ and some initial boundary conditions, and $\mathbf{d}$ is the data vector which collects the synthetics seismic data at the receiver locations. Therefore, the forward model operator maps elements from the model space $\mathcal{M}$ to the data space $\mathcal{D}$:

$$G : \mathcal{M} \to \mathcal{D}. \tag{1.2}$$

For relatively simple earth models the wave equation has analytical solutions. However, in more realistic representations of the earth's subsurface as a complex heterogeneous medium, is not possible to solve it analytically (Fichtner, 2010). Therefore, numerical strategies need to be implemented.

1.4.1 The finite-difference method to numerically solve the wave equation

The finite-difference (FD) method is a popular technique for solving partial derivative equations and it is the first numerical method that was widely used in seismological research (Igel, 2017). For problems involving space-time dependency, both space and time are discretised on regular grids, and the partial derivatives (continuous) are replaced by the finite differences (discrete).

As an illustration consider the acoustic wave equation, defined as

$$\frac{1}{\boldsymbol{v}_p^2(\boldsymbol{x})}\frac{\partial^2 \boldsymbol{p}(\boldsymbol{x},t)}{\partial t^2} - \rho(\boldsymbol{x})\nabla\cdot\left(\frac{1}{\rho(\boldsymbol{x})}\nabla \boldsymbol{p}(\boldsymbol{x},t)\right) = \boldsymbol{s}(\boldsymbol{x},t), \tag{1.3}$$

where $\boldsymbol{v}_p$ is the acoustic velocity, ρ is density, $\boldsymbol{p}$ is the pressure wavefield, and $\boldsymbol{s}$ an external force which represents the source of seismic wave motion, contains two second derivatives: one in time and one in space.

The second-order central difference method for a generic function f dependent on position x can be approximated as

$$f''(x) \approx \frac{f(x-\Delta x) - 2f(x) + f(x+\delta x)}{\Delta x^2} + \mathcal{O}(\Delta x)^2 \tag{1.4}$$

where Δx represents the discretisation used and $\mathcal{O}(\Delta x)^2$ the error associated to the Taylor series truncation.

Applying the same procedure to the time derivative, and substituting these approximations to Equation (1.3), its second-order FD representation (both in space and time) is thus expressed by

$$p_{i,j}^{n+1} = 2p_{i,j}^{n} + v_p^2\frac{\delta n^2}{\delta h^2}\left(p_{i+1,j}^{n} + p_{i-1,j}^{n} + p_{i,j+1}^{n} + p_{i,j-1}^{n} - 4p_{i,j}^{n}\right) - p_{i,j}^{n-1} + \delta n^2 s_j^n \tag{1.5}$$

where i and j are the spatial grid points along x and y directions, δn and δh ($\delta h = \delta x = \delta y$) represent the temporal and spatial discretisations, respectively.

The stability conditions, as well as the grid dispersion issues are treated more in depth in Section 2.3.2.

1.5 The inverse problem: estimating the model parameters from the seismic data

The seismic *inverse problem* is the opposite of the forward problem discussed in Section 1.4, and represents a quantitative approach to the interpretation of the seismic data in order to infer the elastic properties utilised to parametrise the subsurface. In other words, the subsurface model $\mathbf{m}$ is the unknown of the seismic inverse problem and needs to be estimated from the recorded seismograms $\mathbf{d}^{obs}$.

The non-linear inverse problem corresponding to the forward problem of Equation (1.1) can be generally formulated as

$$\mathbf{G}^{-1}(\mathbf{d}) = \mathbf{m}, \tag{1.6}$$

therefore, elements of the data space are mapped in the model space through a non-linear inverse operator $\mathbf{G}^{-1}$ (Warner et al., 2013):

$$G^{-1} : \mathcal{D} \rightarrow \mathcal{M}. \tag{1.7}$$

Since the inverse problem is not-linear, an explicit solution cannot be found, however the problem can be solved via a series of linearised steps. The problem is also non-unique, i.e. multiple, or perhaps infinite combinations of model parameters can describe equally well the observed seismograms. Such problems are termed *ill-posed* (Tarantola, 2005).

To estimate the subsurface model $\hat{m}$ the inverse problem is often recast as an optimisation problem where the goal is to minimise a so-called *objective* or *misfit* function $\mathcal{S}$ which represents the measure of the distance between the computed seismic dataset ($G_i(\hat{m})$) and the observations (d_i^{obs}) (Tarantola, 2005; Menke, 2012), usually in a least-squares sense:

$$\mathcal{S}(\hat{m}) = \sum_i \left(d_i^{obs} - G_i(\hat{m})\right)^2 . \tag{1.8}$$

$\mathcal{L}_2$-norm is usually employed as measure of the misfit because generates a smoother gradient.

1.5.1 Deterministic and stochastic approaches

The most common way to deal with non-linear inverse problems is to cast them in a framework of deterministic approaches (Snieder, 1998). This involves the linearisation of the problem using a Taylor expansion about a starting background model $\mathbf{m}_0$ (Menke, 2012) which is then iteratively updated based on the local gradient and curvature of the objective function (Tarantola, 1984b; Tarantola, 1984a; Virieux and Operto, 2009; Menke, 2012). Although iterative algorithms, such as gradient-based methods, are more efficient at convergence, they are strongly dependent on the initial model guess $\mathbf{m}_0$. Thus they might converge to the global minimum of the misfit function only if $\mathbf{m}_0$ lies in its basin of attraction or, conversely, be prone to local minima entrapment. The conventional FWI method falls into this deterministic category of inversion, and in Section 1.6.3 it is discussed in more detail how FWI calculates the objective function derivatives with respect to the model parameters, as well as the approaches used to mitigate the non-linearity and non-uniqueness issues of the problem.

An alternative strategy for tackling non-linear inverse problems in the Bayesian framework, where all information of an inverse problem is formulated in probabilistic terms. It follows that the solutions of such inverse problem is not a single *elite* model, but instead a probability density function (PDF) on the model parameters that incorporates uncertainties in the seismic data and prior information (Mosegaard and Tarantola, 1995; Sambridge and Mosegaard, 2002; Tarantola, 2005). This is treated in Section 3.4.1.

The ensemble inference can be seen as a sum of two distinct processes: the *search stage* where the n-dimensional model space is sampled by the models generated through the solution of the forward problem, and an *appraisal stage* where inferences are drawn from the model ensemble generated (Snieder, 1998; Sambridge and Mosegaard, 2002; Sambridge, n.d.). Sampling the model space can also be carried out in different ways: from the systematic exploration of the entire space, which is often computationally unaffordable, to the exploitation of the current state of information about the model (Sambridge and Mosegaard, 2002) making use of stochastic optimisers such as, for example, Simulated Annealing (Kirkpatrick et al., 1983), Particle Swarm Optimisation (Kennedy and Eberhart, 1995), or Genetic Algorithm (Goldberg, 1989). Although these approaches are still computationally demanding, they are more affordable than the pure Markov Chain Monte Carlo (MCMC) algorithms and more robust than deterministic algorithms that are inclined to be entrapped in a local minimum (Sen and Stoffa, 2013; Sambridge and Mosegaard, 2002).

A qualitative comparison between these two categories applied to the Rastrigin function (see Section 3.5.1 for its definition) for a two-parameter space is given in Figure 1.3.

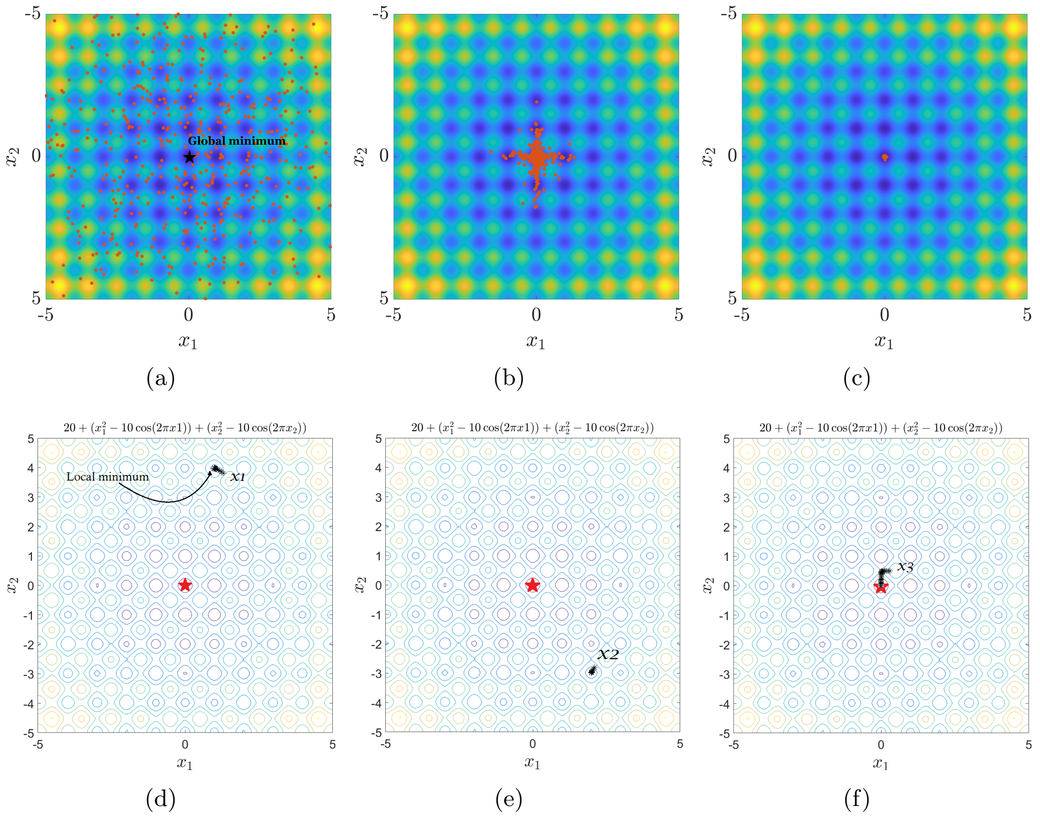

(a) (b) (c)

(d) (e) (f)

Figure 1.3: Qualitative comparison between a global optimization method (Genetic Algorithm (*a*)-(*c*) developed in this study) and a local optimization method (Gradient descent (*d*)-(*f*)) (code modified from Allison, 2012). Both methods are applied to the Rastrigin function ($f(x_1, \ldots, x_n) = An + \sum_{i=1}^{n} \left[x_i^2 - A\cos(2\pi x_i)\right]$) in the same domain (see Section 3.5.1 for more details). The GA method, starting with a random population of individuals (red dots) in (*a*), is able to find the global minimum (black star) after 31 generations (*c*), while the descent method converges towards the nearest minimum as function of the different starting models (X_1, X_2, X_3). Only the case (*f*) shows a correct convergence because the starting model lies in the basin of attraction of the global minimum.

1.6 Full-waveform inversion as a local optimization approach

FWI is a state-of-the-art seismic method that can yield much more accurate quantitative models of any subsurface parameter by adopting whichever approximation of the wave equation (Lailly, 1983; Tarantola, 1984a; Virieux and Operto, 2009; Warner et al., 2013; Jones, 2018). P-wave velocity models are usually retrieved, although recent developments include S-wave velocity (Sears et al., 2008; Guasch et al., 2010), anisotropic parameters (Debens, 2015), and attenuation (Brossier, 2011). An attempt to estimate the spatial distribution and physical properties of fracture zones using a gradient based local FWI was proposed by Zhang et al. (2017).

FWI is based on a data-fitting technique seeking a wiggle-to-wiggle and trace-to-trace match of real and modelled data. This is achieved in a deterministic local fashion that minimises the difference between these two datasets, also referred as the *data residual* $\mathbf{\Delta d}$

$$\mathbf{\Delta d} = \mathbf{d} - \mathbf{d^{obs}} \tag{1.9}$$

via a series of iterative linearised model updates, following

$$\mathbf{m}_{k+1} = \mathbf{m}_k + \mathbf{\Delta m}_k \tag{1.10}$$

where k is the iteration number, and $\mathbf{\Delta m}$ a small model update.

The starting model, that is iteratively updated, contains only long wavelength features. The shorter wavelengths are progressively introduced by inverting higher frequency of the seismic data (the so-called multi-scale approach). The final result is a high-resolution model which honours the physics of the wave propagation limited only by the numerical assumptions used. In fact, compared to the tomographic images derived from ray theory which have a lateral resolution about 5 times the seismic propagating wavelength (Jones, 2018), FWI increases the lateral resolution to a theoretically possible value of half the wavelength (Virieux and Operto, 2009; Jones, 2018). This leads to a potential order of magnitude improvement in parameter model resolution with this wave based method (Jones, 2018).

1.6.1 Brief historical overview

The original study of FWI is attributed to the work of different authors such as Lailly (1983), Tarantola (1984a), Tarantola (1984b), and Mora (1987) in the time domain, and Pratt et al. (1998), Pratt (1999), and Pratt and Shipp (1999) in the frequency domain. They presented a method for inverting seismic data without computing explicitly the partial derivatives with respect to the model parameters (Fréchet derivatives). In fact, they showed that after linearisation the gradient of the objective function, with respect to a given model parameter, can be evaluated by cross-correlating the forward propagated wavefields from a seismic source, with the backward propagated wavefield of the data residual from the receivers. In the geophysical community this approach is often referred to as the *adjoint-state method* (Plessix, 2006; Virieux and Operto, 2009).

Additionally, due to the high non-linearity of the objective function, they also showed that the FWI starting model needed to be accurate enough in order to match the kinematics of the wavefield with an error less than the dominant period in order to avoid *cycle skipping* (Virieux and Operto, 2009; Fichtner, 2010). To mitigate these effects different solutions have been proposed, e.g the multi-scale approach (Bunks et al., 1995) which involves the gradual introduction of shorter wavelengths in the inversion, or more recently the proposal of a optimum predictive filter applied at each iteration in order to reduce the time shift between the modelled and the observed waveforms (Warner and Guasch, 2016).

Due to the computational costs associated with its implementation, this formulation has had to wait almost two decades to be fully tested in two-dimensional geophysical problems. Only recently, have computers had the capabilities to handle 3D problems (Warner et al., 2013).

1.6.2 Model update

The Born approximation is used to solve the inverse problem. Its first-order approximation provides a linear relationship between a small change in the model ($\Delta\mathbf{m}$) and its corresponding small change in the wavefield (scattered wavefield), therefore in the data ($\Delta\mathbf{d}$). Since this relationship is linear, it is also invertible (Virieux and Operto, 2009).

The application of Born approximation implies the knowledge of the residual wavefield at the receiver locations. As stated in the beginning of Section 1.6, the residual wavefield $\Delta\mathbf{d}$ is calculated by subtracting the forward modelled data from the recorded data (equation (1.9)). The objective of the inversion is to minimise the $\mathcal{L}_2$-norm of $\Delta\mathbf{d}$ – also called misfit function $S(\mathbf{m})$.

After some algebra (refer to Virieux and Operto (2009) for a complete mathematical treatment) the expression of $\mathbf{\Delta m}$ as function of the data residual $\Delta\mathbf{d}$ is

$$\Delta\mathbf{m} = -\left[\frac{\partial^2 S(\mathbf{m})}{\partial\mathbf{m}^2}\right]^{-1}\frac{\partial S(\mathbf{m})}{\partial\mathbf{m}} = -\mathbf{H^{-1}}\nabla_{\mathbf{m}}S \tag{1.11}$$

with

$$\nabla_{\mathbf{m}}S = \frac{\partial S(\mathbf{m})}{\partial\mathbf{m}} = \left(\frac{\partial\mathbf{d}^{\mathbf{mod}}(\mathbf{m})}{\partial\mathbf{m}}\right)^T \Delta\mathbf{d} = \mathbf{J}^T\Delta\mathbf{d} \tag{1.12}$$

representing the gradient of the objective function with respect to the model parameters, $\mathbf{H}^{-1} = [\frac{\partial^2 S(\mathbf{m})}{\partial\mathbf{m}^2}]^{-1}$ denote the inverse of the Hessian matrix, and $\mathbf{J}$ being the Jacobian matrix. The perturbation model is searched in the opposite direction of the gradient, that corresponds to the steepest ascent of the objective function at point $\mathbf{m}$, multiplied by the Hessian matrix which defines the curvature of the objective function at the same point.

Since FWI involves the update of a large number of model parameters, computing explicitly the Hessian matrix (and its inverse) is infeasible from a computational time and memory requirement viewpoint (Fichtner, 2010). Therefore, numerical approximations need to be made to circumvent this issue.

1.6.3 Adjoint-state method for the gradient calculation

The *steepest-descent* method is the simplest technique that entails the replacement of the Hessian $\mathbf{H}$ of equation (1.11) with a scalar value (Virieux and Operto, 2009). This is expressed as

$$\Delta\mathbf{m} \approx -\alpha\nabla_{\mathbf{m}}S \tag{1.13}$$

where the global scaling factor α is commonly called *step-length.* In order to calculate the updates of the model $\mathbf{\Delta m}$ through equation (1.13), the gradient vector has to be estimated. Due to its dimension, building explicitly the gradient vector is prohibitive because it would require as many forward models as the vector dimension (from thousands to millions) at each iteration.

To avoid this expensive process, the *adjoint-state method* is implemented which requires only two forward models at each iteration (Tarantola, 1984a; Plessix, 2006). This approach was introduced in the theory of inverse problems in the 1970s by Chavent (1974) in optimization theory and then introduced in the geophysical context by Lailly (1983) and Tarantola (1984a) where the computation of the gradient has connections to the Claerbout's imaging principle (Claerbout, 1985). The *adjoint-state method* involves the following steps:

(*i*) forward-propagation of the source wavefield for each source across the medium to produce a modelled data set

(*ii*) calculation of the data residuals by subtracting the modelled and observed data at each receiver

(*iii*) back-propagation (time-reversal propagation or adjoint) of this residual wavefield from the receivers into the actual medium

(*iv*) crosscorrelation of these forward and backward wavefields in time at each point within the model to form the gradient for each source

(*v*) stack all the gradients obtained over the number of sources to get the Eq. (1.12) at a given iteration

To generate the back-propagation wavefield a second partial differential equation (PDE) needs to be solved (Plessix, 2006). Generally, the forward operator and the adjoint operator are different, and two numerical solvers must be implemented.

However, if the wave equation is *self-adjoint*, then both PDEs can be computed with the same numerical code. This is the case for both the acoustic and the elastic wave equations (Plessix, 2006), on the contrary the viscoelastic wave equation based on velocity-stress formulation is not self-adjoint. A study by Yang et al. (2016) showed that the forward and adjoint equations for the viscoelastic equations, are asymmetric therefore they are not self-adjoint. This was overcome by (Fabien-Ouellet et al., 2017).

A graphical example of building the sensitivity kernel (partial derivative with respect to a given model parameter, in this case v_p) in a 2D gradient velocity model is shown in Figure 1.4. Here the interaction of the forward wavefield and the adjoint wavefield is displayed at four time steps, until the gradient-kernel is completely formed, often referred to as sensitivity kernel or banana-doughnut kernel (Tromp et al., 2005).

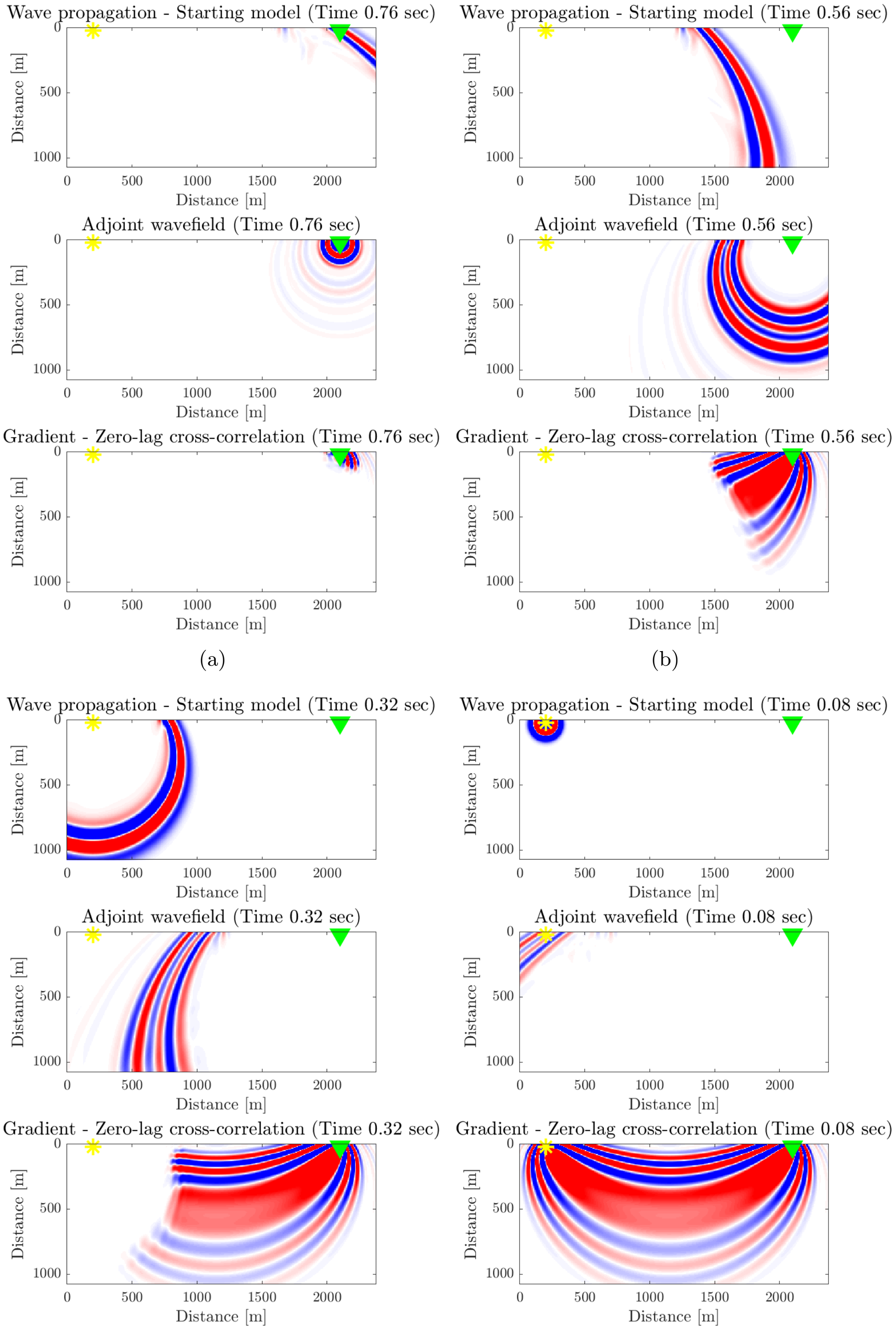

(a) (b)

(c) (d)

Figure 1.4: Example of the computation of sensitivity kernels for v_p by the interaction of the forward wavefield (top figure of each panel) and the adjoint wavefield (middle figure of each panel) at four different time steps in a 2D gradient velocity model. The forward wavefield is constructed backward in time while the adjoint wavefield forward in time. The finite-difference forward modelling code (2D acoustic) has been developed by the author.

1.7 FWI as a global optimization approach

In the last 30 years, different strategies of stochastic FWI have been proposed to overcome the inherent limitations of the gradient-based inversions, and to explore more robust ways for estimating subsurface models. The most popular stochastic methods applied to geophysical problems are genetic algorithms (Stoffa and Sen, 1991; Sambridge and Drijkoningen, 1992; Sajeva et al., 2016), neighbourhood algorithm (Sambridge, 1999a; Sambridge, 1999b), simulated annealing (Sen and Stoffa, 1991), and particle swarm optimisation (Zhe and Hanming, 2013; Chen and Wang, 2017).

First implementations of global FWI were performed in the 1990s to invert single-shot gathers, assuming 1D geological models in an acoustic approximation (Gallagher et al., 1991; Stoffa and Sen, 1991; Sen and Stoffa, 1992; Sambridge and Drijkoningen, 1992; Sambridge, 1999a). This simplified problem parametrisation allowed the discretisation of the model space using only a few model parameters, and a relatively quick solution of the 1D acoustic wave equation. Therefore, the application of FWI was suitable for solving such problems. It is known, in fact, that the search stage suffers the so-called *curse of dimensionality*, indicating that the computational cost grows exponentially with the number of model parameters involved (Fichtner, 2010; Aleardi and Mazzotti, 2017).

Due to the recent growth of high-performance computing, stochastic FWI (using genetic algorithm optimisation) has begun to be applied in deriving 2D and 3D velocity macromodels as starting points for a subsequent optimisation through local FWI (Gao et al., 2014; Tognarelli et al., 2015; Datta and Sen, 2016; Sajeva et al., 2016; Mazzotti et al., 2016), for inverting anisotropic acoustic velocity models in a two-step strategy global-local inversion (using quantum particle swarm optimisation) (Debens, 2015), and to estimate the effective hydraulic aperture and the mechanical compliance of isolated fractures intersecting a borehole through a Bayesian MCMC inversion of full-waveform tube-wave data (Hunziker et al., 2020). A global FWI strategy to search for the optima fracture models through the GA optimisation, and appraise the solution from a Bayesian point of view is discussed in Chapter 3.

Chapter 2

Seismic characterization of fractures: theory and applications

2.1 Preamble

Seismic methods provide a non-invasive tool to characterise remotely physical properties of fractures and fractured zones. The seismic visibility of fractures strongly depends on their mechanical parameters, e.g. fracture stiffnesses, friction angle, cohesion, and their geometric properties, such as fracture size, fracture spacing, and connectivity (Worthington, 2008).

For a complete description of wave-fracture interaction, it is necessary to account for the physics of scattering at each individual discrete fracture by making use of the discrete fracture network (DFN) model representation, e.g. the displacement-discontinuity model (Schoenberg, 1980; Pyrak-Nolte et al., 1990b). However, when the size of the fractures is considerably less than the dominant seismic wavelength, the propagating wave is weakly affected by individual fractures; conversely, it is influenced by the cracked medium as whole. For this reason, equivalent medium (EM) theories, for instance the self-consistent model (Budiansky and O'Connell, 1976), linear-slip model (Schoenberg and Sayers, 1995), penny-shaped cracks method (Hudson, 1980; Hudson, 1981), fractures as collection of cracks (Myer, 2000), well describe the interaction between the seismic wavefield and fractures by combining their effects and the host rock into an equivalent anisotropic solid.

These different theoretical approaches reflect the need to characterise fractures at different ranges of scale. In fact, it has been observed that fractures can span from millimetre-scale microcracks (in core samples) to macroscopic kilometre-long faults throughout the Earth's upper crust (Liu and Martinez, 2012). As well as the numerous mechanical-mathematical models proposed, a large variety of numerical techniques have been employed for modelling elastodynamic behaviour in the presence of fractures or fractured media. They include boundary element methods (BEMs) (e.g. Aliabadi (1997)), finite-element methods (FEMs) (e.g. Mikhailenko (2000)), pseudo-spectral methods (PSMs) (e.g. Lou and Rial (1995)), and finite difference methods (FDMs) (e.g. Vlastos et al. (2003) and Hildyard (2007)).

Throughout this work the program WAVE3D was used to model three-dimensional seismic wave propagation and its interaction with fractures and fractured media.
WAVE3D is a fully-elastic finite difference modelling code that implements discrete fractures into the numerical mesh using the displacement discontinuity theory. It was firstly implemented by Cundall (1992), and then extended to the current version by Hildyard et al. (1995), Hildyard (2001), and Hildyard (2007). A more thorough review of this program is given in Section 2.3.

2.2 Rock fractures - a theoretical overview

An idealized fracture can be conceived as two rough surfaces in partial contact (Figure 2.1). When the asperities of the fracture surfaces are not fully in contact, they give rise to voids, where the distance of separation is called fracture aperture. The mechanical and hydraulic response of fractures is strongly related to the number and topology of these voids' (Hopkins et al., 1987; Myer, 2000; Zimmerman and Main, 2004; Pyrak-

Nolte and Nolte, 2016). Engineering activities as well as natural events can change the state of stress of rock masses, which induces a change in voids geometry and in turn the mechanical behaviour of fractures.

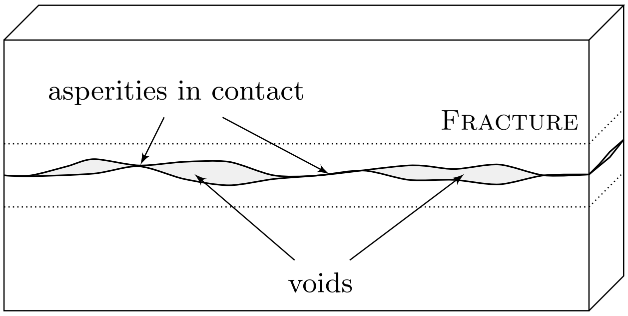

Figure 2.1: Schematic model of a fracture as two rough surfaces in contact. When not fully in contact the surfaces create voids.

Therefore, to predict the mechanical response of a fracture, the relationship between the void geometry and stress needs to be understood. However, it is a difficult task, even in a controlled environment, to measure the topography of the rough surfaces of a fracture (Petrovitch et al., 2013). Instead, as stated in Bandis et al. (1983), Goodman et al. (1968) introduced the concept of fracture specific stiffness as an approach to characterise a single fracture without explicitly measuring the fracture aperture, and it was shown that fracture specific stiffness captures the effect of the excess deformation due to the fracture and its geometry (Petrovitch et al., 2013; Pyrak-Nolte and Nolte, 2016).

Since a fracture might cause a seismic energy partition, generating a reflected and transmitted wavefield due to void areas and contacts, respectively, fracture specific stiffness can be remotely characterised using elastic seismic waves.

2.2.1 The displacement-discontinuity model: the explicit fracture representation

Among many theories proposed to explain the interaction of seismic waves and explicit fractures, the displacement-discontinuity fracture (or linear-slip) model introduced by Schoenberg (1980) and generalised by Pyrak-Nolte et al. (1990b) and Pyrak-Nolte et al.

(1990a), is one of the most widely used within the geophysical community (Liu et al., 2000).

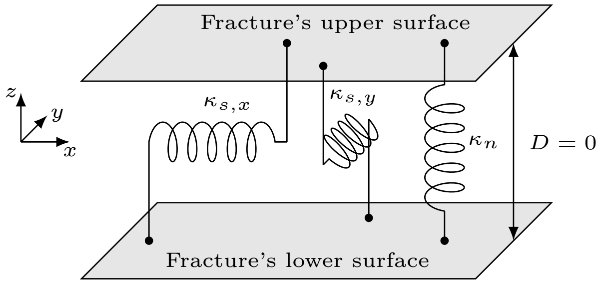

Figure 2.2: Schematic representation of the displacement discontinuity model. Open and closed fractures of zero-width thickness D are represented as distributed normal and tangential springs expressed by normal stiffness κ_n and shear stiffnesses $\kappa_{s,y}$ and $\kappa_{s,x}$, respectively.

In this model, fractures are represented as non-welded interfaces (or discontinuities) and their complex geometry is represented as the boundary between two elastic half spaces: across the fracture plane the tractions are continuous but the displacements are not. The link between the displacement fields and the tractions is given by the specific fracture stiffnesses κ (Schoenberg, 1980; Pyrak-Nolte et al., 1990b). This is analogous to two elastic half spaces coupled by a set of distributed normal and tangential springs expressed by stiffnesses κ_n and κ_s, respectively (Figure 2.2).

Considering a 2-dimensional problem, the boundary conditions on the displacement discontinuity (Δu) for S_v waves (polarised in the $x-z$ plane) and compressional waves, are (Pyrak-Nolte et al., 1990b)

$$\begin{aligned} \Delta u_s &= u_s^{(u)} - u_s^{(l)} = \tau_s/\kappa_s \qquad & \tau_s^{(u)} &= \tau_s^{(l)} \\ \Delta u_n &= u_n^{(u)} - u_n^{(l)} = \sigma_n/\kappa_n \qquad & \sigma_n^{(u)} &= \sigma_n^{(l)} \end{aligned} \tag{2.1}$$

where κ_n and κ_s are the specific normal and shear (or tangential) fracture stiffness, respectively, $\sigma_n = \sigma_{zz}$ is the normal traction to the fracture plane, and $\tau_s = \tau_{zx}$ is the tangential traction in the $x-z$ plane. The superscripts (u) and (l) are referred to the upper and lower surface of the fracture plane, respectively.

Using the boundary conditions in equations (2.1), Pyrak-Nolte et al. (1990b) analytically predicted and experimentally confirmed that for a purely elastic medium, the reflection coefficient R and the transmission coefficient T are frequency dependent and they are functions of the specific stiffness of the fracture. At normal incidence and with equal materiel properties on either side of the fracture they are of the form

$$R_{p,s}(\omega) = \frac{-i\omega}{-i\omega + 2\kappa_{n,s}/Z_{p,s}} \tag{2.2}$$

$$T_{p,s}(\omega) = \frac{2\kappa_{n,s}/Z_{p,s}}{-i\omega + 2\kappa_{n,s}/Z_{p,s}} \tag{2.3}$$

where ω is the angular frequency and $Z_{p,s} = \rho v_{p,s}$ is the seismic impedance. The subscripts $_p$ and $_s$ indicate the P-wave and S-wave, respectively.

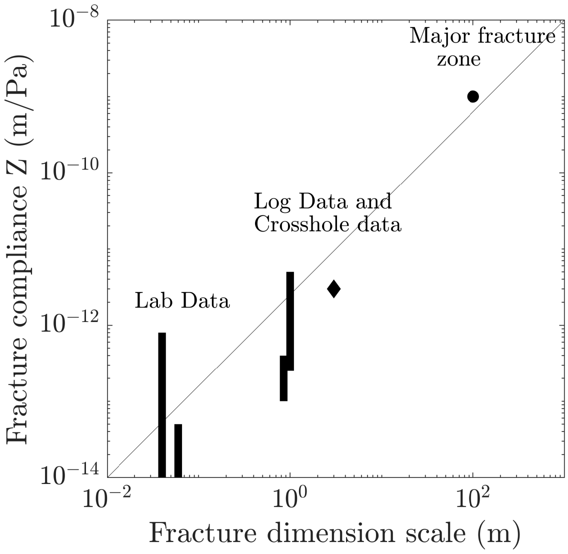

Figure 2.3: Compilation of laboratory and field estimates of dynamic fracture compliance. Modified from (Worthington, 2008).

The specific fracture stiffnesses assume non negative values and they can span the interval $[0, \infty[$. From equations (2.2) and (2.3), as κ approaches 0, $R \to 1$ and $T \to 0$. Therefore, the discontinuity behaves as an open fracture, i.e., all the energy is reflected (Figure 2.5(a)). Conversely, the discontinuity becomes equivalent to a welded interface, i.e., all the energy is transmitted ($T \to 1$, $R \to 0$), when $\kappa \to \infty$ (Figure 2.5(d)). In case of real fractures variation of the fracture specific stiffness along the discontinuity must be taken into account in order to average the transmission coefficient over the different sections of the fracture. This is due to that they depend on the local geometry of the asperities. To do that the following approximations are made (Pyrak-Nolte and Nolte, 1992):

- the local transmission coefficient depends on the local static stiffness;

- regions of different stiffness transmit independently.

The first assumption is valid if the asperity separation is smaller than the wavelength and if the local stiffness varies slowly with respect to a wavelength. Otherwise, the transmitted signal will experience attenuation by scattering that is not accounted for the displacement discontinuity formulation. The second approximation assumes that the total transmission of seismic wave amplitude is the sum of the transmitted amplitudes of individual regions (Pyrak-Nolte and Nolte, 1992).

Figure 2.4(a) shows the modelled waveforms recorded at the receiver location (black triangle) for κ values spanning from $\kappa_n = \kappa_s = \kappa = 1 \cdot 10^{11}$ Pa/m to $\kappa = 1 \cdot 10^{14}$ Pa/m (Figures 2.5(a)-2.5(d)). These simulations show how fractures of differing stiffnesses behave seismically when an elastic wave impinges on their surfaces. Differences in the responses are solely controlled by the fracture stiffness. The end members are $\kappa = 1 \cdot 10^{11}$ Pa/m that simulates an open fracture where the energy is completely reflected off the discontinuity (see the related amplitude spectrum in Figure 2.4(b)), and $\kappa = 1 \cdot 10^{14}$ Pa/m simulates a close fracture where the transmitted wave has almost identical amplitude and frequency content of the control case (no fracture case, Figure 2.5(e)). Two more values are utilised ($\kappa = 1 \cdot 10^{12}$ Pa/m, $\kappa = 1 \cdot 10^{13}$ Pa/m) to show the transition between these two states. The fracture stiffness values were chosen in agreement with the laboratory and field estimates of published dynamic fracture compliances reviewed by Worthington (2008) (Figure 2.3).

The transmission coefficient, expressed in equation (2.3), is both frequency-dependent and complex. Therefore, the shift in phase (Θ_t) of the transmitted wave caused by the fracture can be related to the ratio of its imaginary and real part (Pyrak-Nolte et al., 1990a). The derivative of the phase shift with respect to the angular frequency gives

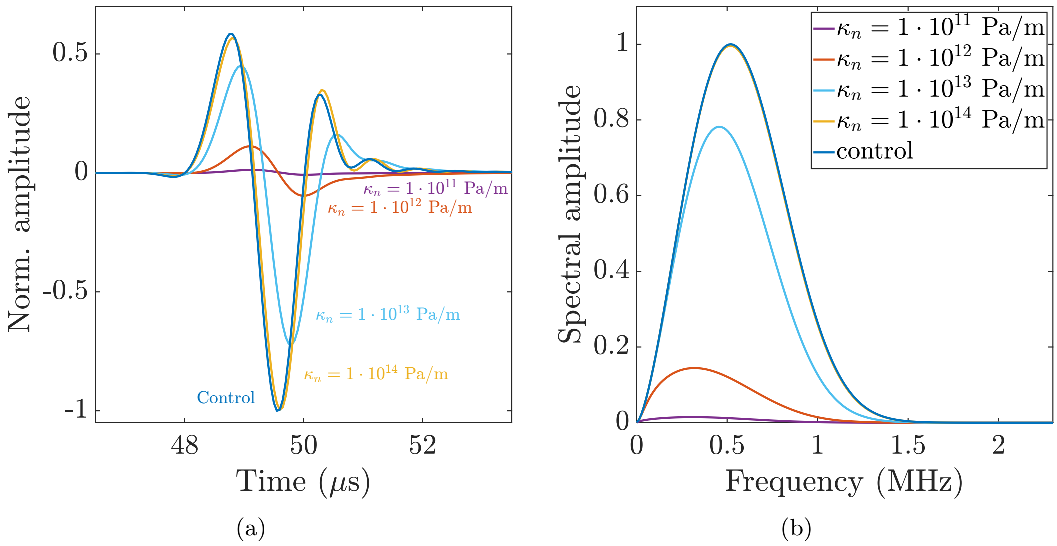

Figure 2.4: (a) Transmitted waveforms recorded at the receiver location (black triangles in Figures 2.5(a)-2.5(e)) for κ spanning from $\kappa = 1 \cdot 10^{11}$ Pa/m to $\kappa = 1 \cdot 10^{14}$ Pa/m, with the corresponding amplitude spectra (b).

the group time delay (t_g) of the transmitted wave. At normal incidence t_g becomes:

$$t_g = \frac{d\Theta_t}{d\omega} = \frac{2\left(\frac{\kappa_n}{Z_p}\right)}{4\left(\frac{\kappa_n}{Z_p}\right) + \omega^2}. \tag{2.4}$$

For arbitrary fracture orientation the time delay is also function of the shear fracture stiffness κ_s, and the angle of incidence.

Additionally, the equations (2.2) and (2.3) show characteristics of a low-pass filter with a cut-off frequency of $2\kappa/Z$ (Figure 2.4(b)), and also in case of not dissipative media $|T(\omega)|^2 + |R(\omega)|^2 = 1$ meaning that the energy is conserved (Pyrak-Nolte et al., 1990a).

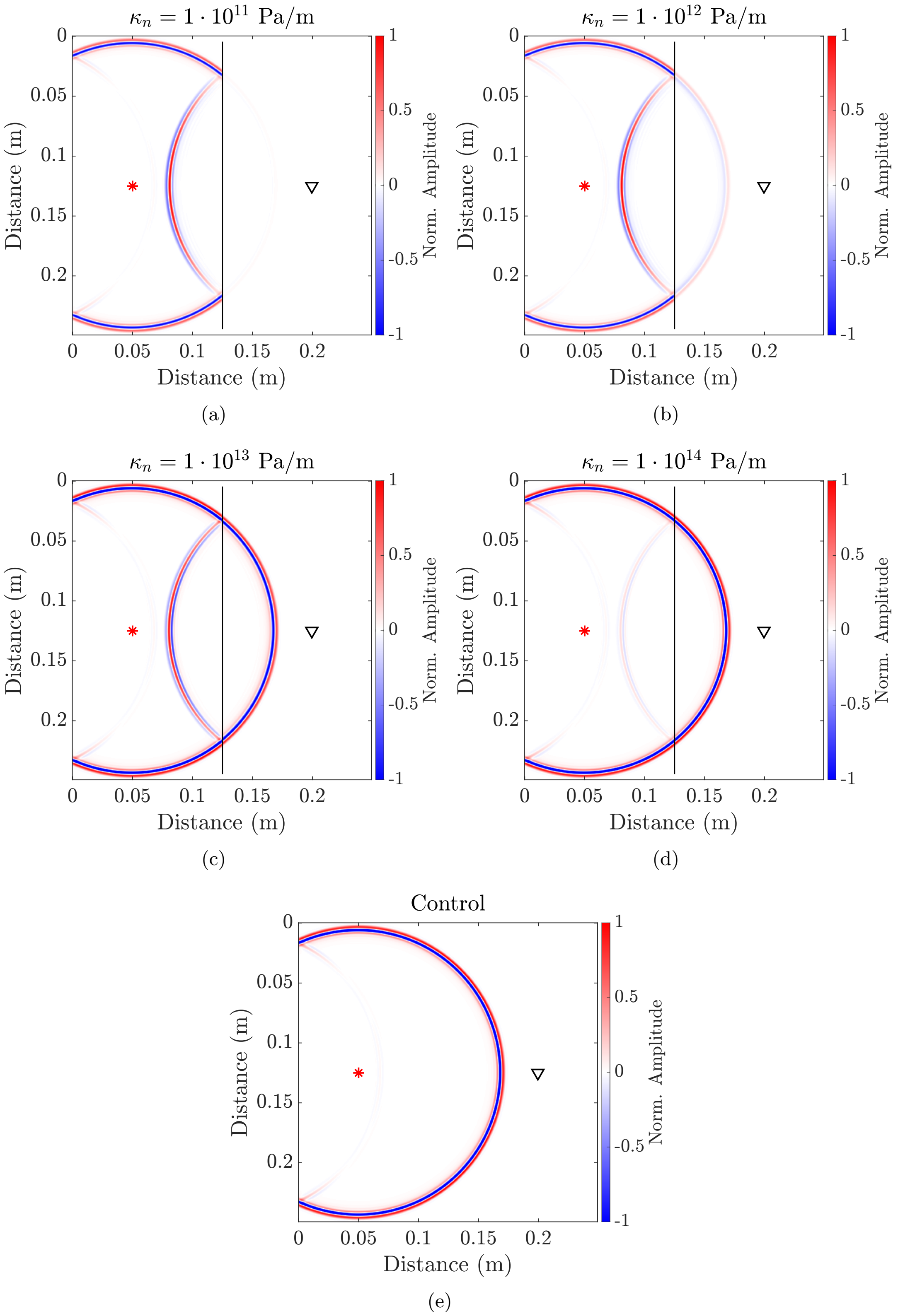

(a) (b) (c) (d) (e)

Figure 2.5: Wavefield-fracture interaction for a single vertical fracture of variable stiffness: (a) $\kappa = 1 \cdot 10^{11}$ Pa/m , (b) $\kappa = 1 \cdot 10^{12}$ Pa/m, (c) $\kappa = 1 \cdot 10^{13}$ Pa/m, (d) $\kappa = 1 \cdot 10^{14}$ Pa/m, (e) no fracture (control). The κ_n/κ_s ratio = 1. The colour scale indicates the normalised amplitude of the wavefield stress components $(\sigma_{11} + \sigma_{22})/2$

2.2.2 The displacement-discontinuity model: the effective medium theory

Due to the inherent limitation of seismic resolution that prevents a detailed knowledge of the rock masses which the seismic waves have passed, the explicit fracture model approach fails in characterising fractured rocks as whole. In fact, quantitative characterization of specific fracture stiffness has been mainly carried out in laboratory experiments (*e.g.* Pyrak-Nolte et al. (1990a), Pyrak-Nolte et al. (1990b), Lubbe et al. (2008), Jiang et al. (2009), Hedayat et al. (2014b), and Choi et al. (2014)) with only limited applications in the field. Recent successful field measurements of specific fracture stiffness have been carried out by Hunziker et al. (2020) and Barbosa et al. (2021).

In order to estimate the overall properties of cracked rocks and model the response of seismic waves, effective-medium (EM) theories are commonly used (Liu et al., 2000). These representations encapsulate the behaviour of a fractured rock within the elastic moduli, therefore they combine the effects of fractures and the host rock into a medium that potentially produces anisotropic material behaviour (Budiansky and O'Connell, 1976; Hudson, 1980; Schoenberg and Sayers, 1995; Liu et al., 2000). Therefore, EM theories provide a straightforward way to characterise a fractured medium when the size of the fractures, their spacing and opening are considerably smaller than the seismic wavelength.

In a series of papers from early 80s to mid-90s, Schoenberg and Sayers proposed an equivalent-medium theory (Schoenberg, 1983; Schoenberg and Douma, 1988; Schoenberg and Muir, 1989; Sayers and Kachanov, 1991; Schoenberg and Sayers, 1995) having the same root of the displacement-discontinuity theory for discrete cracks, reviewed in Section 2.2.1. Also this group of models are generically called linear slip-interface, or displacement-discontinuity fracture models, since they all share the same interface conditions: discontinuity of displacement and continuity of traction. Nevertheless, they express the effect of small imperfectly bonded interfaces upon the compliance matrix of the medium with the assumption of long wavelengths.

In the presence of fractures embedded in an elastic medium of volume V, the effective compliance matrix s^0_{ijkl} is written as

$$s_{ijkl} = s^0_{ijkl} + \Delta s^{(f)}_{ijkl} \tag{2.5}$$

where s^0_{ijkl} is the compliance matrix of the isotropic (elastic) host rock and $\Delta s^{(f)}_{ijkl}$ is the excess compliance matrix resulting from the fractures. The general form of the excess compliance matrix is (Schoenberg and Sayers, 1995; Liu et al., 2000)

$$\begin{aligned}
\Delta s^{(f)}_{ijkl} &= \frac{1}{4}\left(B_{ij}n_l n_j + B_{jk}n_l n_i + B_{il}n_k n_j + B_{jl}n_k n_i\right) = && (2.6)\\
&= \frac{N_f S_f}{4V}\left(Z_{ij}n_l n_j + Z_{jk}n_l n_i + Z_{il}n_k n_j + Z_{jl}n_k n_i\right) = && (2.7)\\
&= \frac{1}{4}\frac{1}{L}\left(Z_{ij}n_l n_j + Z_{jk}n_l n_i + Z_{il}n_k n_j + Z_{jl}n_k n_i\right) && (2.8)
\end{aligned}$$

where **B** is the fracture system compliance tensor (equivalent fracture compliance), **Z** is the specific fracture compliance tensor, n_i is the i-th component of the axis normal to the fractures, and N_f is the number of fractures, with mean area S_f, contained in V. The factor $\frac{N_f S_f}{V} = \frac{1}{L}$ represents the number of fractures per unit length and it is called fracture intensity (Bakulin et al., 2000) (Figure 2.6). L is the average fracture spacing.

Similarly, fracture intensity is also indicated as, e.g. (Liu et al., 2000),

$$D_f = \frac{1}{L} = \frac{N_f S_f}{V}. \tag{2.9}$$

For multiple fracture sets, the effective excess compliance matrix is the sum of $\Delta s^{(f)}_{ijkl}$ for each fracture orientation.

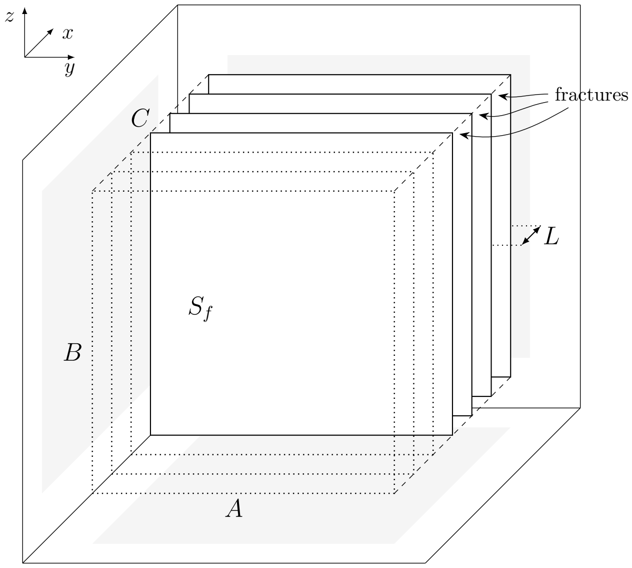

Figure 2.6: Schematic representation of a fractured medium containing a set of parallel fractures orthogonal to the x-axis in a volume $V = a \cdot b \cdot c$. Each fracture has a surface area of $S_f = a \cdot b$ and spacing L. This represents a horizontal transversely isotropic medium, or HTI medium.

If the medium contains only a set of parallel fractures invariant under rotations about $n = (1, 0, 0)$, i.e. the normal of fractures is parallel to the x-axis (Figure 2.6), the fractured medium can be characterised by just two terms: the equivalent normal fracture compliance B_n, and the equivalent tangential compliance B_s, with units of Pa^{-1} (Schoenberg and Sayers, 1995). Such a medium is transversely isotropic (TI), or more specifically it is a horizontal (since it is parallel to the x-axis) transversely isotropic medium, or abbreviated HTI.

From equation (2.6), with some tensor algebra, the excess compliance matrix becomes

$$\begin{aligned}\Delta s^{(f)}_{ijkl} =& \left[\frac{B_s}{4}\left(\delta_{ik}n_l n_j + \delta_{jk}n_l n_i + \delta_{il}n_k n_j + \delta_{jl}n_k n_i\right) + \right.\\ &\left.\left(B_n - B_s\right) n_i n_j n_k n_l\right].\end{aligned} \tag{2.10}$$

or equivalently

$$\begin{aligned}\Delta s^{(f)}_{ijkl} =& D_f\left[\frac{Z_s}{4}\left(\delta_{ik}n_l n_j + \delta_{jk}n_l n_i + \delta_{il}n_k n_j + \delta_{jl}n_k n_i\right) + \right.\\ &\left.\left(Z_n - Z_s\right) n_i n_j n_k n_l\right].\end{aligned} \tag{2.11}$$

where $Z_{n,s}$ is the fracture compliances with units of $\mathrm{m}\cdot\mathrm{Pa}^{-1}$, defined as

$$Z_{n,s} = \frac{B_{n,s}}{D_f}. \tag{2.12}$$

This can then be reduced to the conventional two-subscript condensed 6x6 compliance matrix form. In this notation $11 \rightarrow 1,\ 22 \rightarrow 2,\ 33 \rightarrow 3,\ 23 \rightarrow 4\ 13 \rightarrow 5,\ 12 \rightarrow 6$ (Schoenberg and Sayers, 1995). A factor of 2 is introduced when one of the matrix indices is 4, 5, or 6 (e.g. $s_{1,4}$, or $s_{5,2}$ and so on), while a factor of 4 is introduced when both of the matrix indices are 4, 5, or 6 (i.e. $s_{4,4}$, $s_{5,5}$, and $s_{6,6}$).

$$\Delta\mathbf{s}^{(f)} = \begin{pmatrix} B_n & 0 & 0 & 0 & 0 & 0 \\ 0 & 0 & 0 & 0 & 0 & 0 \\ 0 & 0 & 0 & 0 & 0 & 0 \\ 0 & 0 & 0 & 0 & 0 & 0 \\ 0 & 0 & 0 & 0 & B_s & 0 \\ 0 & 0 & 0 & 0 & 0 & B_s \end{pmatrix} \tag{2.13}$$

The factor 4 is absent in the 6×6 matrix form because $\Delta s_{5,5} = \Delta s_{6,6} = 4 \cdot \frac{B_s}{4} = B_s$.

Substituting equation (2.11) into equation (2.5) and inverting the compliance matrix yields the stiffness matrix $\mathbf{c}$ of the fractured medium (Schoenberg and Sayers, 1995; Bakulin et al., 2000)

$$\boldsymbol{c} = \left(\boldsymbol{s}^0 + \boldsymbol{\Delta s}^{(f)}\right)^{-1} =$$

$$= \begin{pmatrix} (\lambda+2\mu)(1-\Delta_n) & \lambda(1-\Delta_n) & \lambda(1-\Delta_n) & 0 & 0 & 0 \\ \lambda(1-\Delta_n) & (\lambda+2\mu)(1-r^2\Delta_n) & \lambda(1-r\Delta_n) & 0 & 0 & 0 \\ \lambda(1-\Delta_n) & \lambda(1-r\Delta_n) & (\lambda+2\mu)(1-r^2\Delta_n) & 0 & 0 & 0 \\ 0 & 0 & 0 & 0 & 0 & 0 \\ 0 & 0 & 0 & 0 & \mu(1-\Delta_s) & 0 \\ 0 & 0 & 0 & 0 & 0 & \mu(1-\Delta_s) \end{pmatrix} \tag{2.14}$$

with

$$r \equiv \frac{\lambda}{\lambda+2\mu} \tag{2.15}$$

$$\Delta_n = \frac{(\lambda+2\mu)B_n}{1+(\lambda+2\mu)B_n} = \frac{(\lambda+2\mu)Z_n}{L+(\lambda+2\mu)Z_n} = \frac{(\lambda+2\mu)\left(\kappa_n\right)^{-1}}{L+(\lambda+2\mu)\left(\kappa_n\right)^{-1}} \tag{2.16}$$

$$\Delta_s = \frac{B_s\mu}{1+B_s\mu} = \frac{Z_s\mu}{L+Z_s\mu} = \frac{\left(\kappa_s\right)^{-1}\mu}{L+\left(\kappa_s\right)^{-1}\mu} \tag{2.17}$$

where λ and μ are the Lamé parameters, and Δ_n and Δ_s are called normal and shear (or tangential) weaknesses (Bakulin et al., 2000). The stiffness matrix from equation (2.14) depends on only four independent quantities: μ, λ, Δ_n, Δ_s. Nevertheless, HTI models are generally described by five independent parameters, such as c_{11}, c_{33}, c_{13}, c_{44}, c_{55}. Therefore, there exists a constraint between the stiffness matrix elements that can be expressed as (Schoenberg and Sayers, 1995; Bakulin et al., 2000)

$$c_{11}c_{33} - c_{13}^2 = 2c_{44}(c_{11} + c_{13}) \tag{2.18}$$

Arbitrarily oriented fracture sets

For a more general case of a fracture set with an arbitrary orientation defined by the fracture dip, azimuth, and strike the effective stiffness tensor can be obtained by using the Bond transformation.

The Bond Transformation is an efficient technique for the change of coordinates of a stiffness (or compliance) tensor expressed as a 6 × 6 matrix, therefore it can be applied directly to the elastic constants given in 2-index notation (Mavko et al., 2020). The transformation is expressed by two 6 × 6 rotation matrices, **M** and **N**, given in terms of direction cosines defined for the stiffness tensor and compliance tensor, respectively, as

$$\mathbf{c'} = \mathbf{McM}^T \tag{2.19}$$

$$\mathbf{s'} = \mathbf{NsN}^T \tag{2.20}$$

$$\tag{2.21}$$

where

$$\mathbf{M} = \begin{pmatrix} \beta_{11}^2 & \beta_{12}^2 & \beta_{13}^2 & 2\beta_{12}\beta_{13} & 2\beta_{13}\beta_{11} & 2\beta_{11}\beta_{12} \\ \beta_{21}^2 & \beta_{22}^2 & \beta_{23}^2 & 2\beta_{22}\beta_{23} & 2\beta_{23}\beta_{21} & 2\beta_{21}\beta_{22} \\ \beta_{31}^2 & \beta_{32}^2 & \beta_{33}^2 & 2\beta_{32}\beta_{33} & 2\beta_{33}\beta_{31} & 2\beta_{31}\beta_{32} \\ \beta_{21}\beta_{31} & \beta_{22}\beta_{32} & \beta_{23}\beta_{33} & \beta_{22}\beta_{33} + \beta_{23}\beta_{32} & \beta_{21}\beta_{33} + \beta_{23}\beta_{31} & \beta_{22}\beta_{31} + \beta_{21}\beta_{32} \\ \beta_{31}\beta_{11} & \beta_{32}\beta_{12} & \beta_{33}\beta_{13} & \beta_{12}\beta_{33} + \beta_{13}\beta_{32} & \beta_{13}\beta_{31} + \beta_{11}\beta_{33} & \beta_{11}\beta_{32} + \beta_{12}\beta_{31} \\ \beta_{11}\beta_{21} & \beta_{12}\beta_{22} & \beta_{13}\beta_{23} & \beta_{12}\beta_{23} + \beta_{13}\beta_{22} & \beta_{13}\beta_{21} + \beta_{11}\beta_{23} & \beta_{11}\beta_{22} + \beta_{12}\beta_{21} \end{pmatrix} \tag{2.22}$$

and

$$\mathbf{N} = \begin{pmatrix} \beta_{11}^2 & \beta_{12}^2 & \beta_{13}^2 & \beta_{12}\beta_{13} & \beta_{13}\beta_{11} & \beta_{11}\beta_{12} \\ \beta_{21}^2 & \beta_{22}^2 & \beta_{23}^2 & \beta_{22}\beta_{23} & \beta_{23}\beta_{21} & \beta_{21}\beta_{22} \\ \beta_{31}^2 & \beta_{32}^2 & \beta_{33}^2 & \beta_{32}\beta_{33} & \beta_{33}\beta_{31} & \beta_{31}\beta_{32} \\ 2\beta_{21}\beta_{31} & 2\beta_{22}\beta_{32} & 2\beta_{23}\beta_{33} & \beta_{22}\beta_{33} + \beta_{23}\beta_{32} & \beta_{21}\beta_{33} + \beta_{23}\beta_{31} & \beta_{22}\beta_{31} + \beta_{21}\beta_{32} \\ 2\beta_{31}\beta_{11} & 2\beta_{32}\beta_{12} & 2\beta_{33}\beta_{13} & \beta_{12}\beta_{33} + \beta_{13}\beta_{32} & \beta_{13}\beta_{31} + \beta_{11}\beta_{33} & \beta_{11}\beta_{32} + \beta_{12}\beta_{31} \\ 2\beta_{11}\beta_{21} & 2\beta_{12}\beta_{22} & 2\beta_{13}\beta_{23} & \beta_{12}\beta_{23} + \beta_{13}\beta_{22} & \beta_{13}\beta_{21} + \beta_{11}\beta_{23} & \beta_{11}\beta_{22} + \beta_{12}\beta_{21} \end{pmatrix} \tag{2.23}$$

For rotations about the $x-$axis, the elements β_{ij} are, in matrix notation, defined as

$$\boldsymbol{\beta} = \begin{pmatrix} 1 & 0 & 0 \\ 0 & \cos(\phi) & \sin(\phi) \\ 0 & -\sin(\phi) & \cos(\phi) \end{pmatrix}_{x-\text{axis}} , \tag{2.24}$$

for rotation about the new $z-$axis, $\boldsymbol{\beta}$ takes the form

$$\boldsymbol{\beta} = \begin{pmatrix} \cos(\phi) & \sin(\phi) & 0 \\ -\sin(\phi) & \cos(\phi) & 0 \\ 0 & 0 & 1 \end{pmatrix}_{z-\text{axis}} , \tag{2.25}$$

and for rotation about the new $y-$axis, $\boldsymbol{\beta}$ takes the form

$$\boldsymbol{\beta} = \begin{pmatrix} \cos(\delta) & 0 & -\sin(\delta) \\ 0 & 1 & 0 \\ \sin(\delta) & 0 & \cos(\delta) \end{pmatrix}_{y-\text{axis}} . \tag{2.26}$$

Additionally, in the case of more than one set of fractures, the fracture system compliance tensor $\boldsymbol{\Delta s}^{(f)}$ can be obtained by summing the fracture compliance tensors of each fracture orientation (Schoenberg and Sayers, 1995).

Fracture stiffness ratio as a fluid indicator

The mechanical properties of fractures (fracture stiffnesses) can be, furthermore, utilised as an effective indicator of infilling fluids in fractures (Liu et al., 2000; Bakulin et al., 2000; Verdon and Wüstefeld, 2013; Choi et al., 2014). More specifically, κ_s/κ_n ratio is controlled by the presence or absence of fluids, and for dry cracks the ratio is equivalent to (Schoenberg and Sayers, 1995; Liu et al., 2000)

$$\frac{\kappa_s}{\kappa_n} = 1 - \frac{\nu}{2} \qquad \text{(for isolated cracks)} \tag{2.27}$$

or alternately (Liu et al., 2000; Lubbe et al., 2008)

$$\frac{\kappa_s}{\kappa_n} = \frac{1-\nu}{1-\nu/2} \qquad \text{(for a planar distribution of imperfect rough surfaces)} \tag{2.28}$$

where ν is the Poisson's ratio of the host rock.

Since the Poisson's ratio, for a variety of rocks, ranges typically from $0.1 \leq \nu \leq 0.35$, κ_s/κ_n the ratio approaches unity for dry cracks (or gas infill) and almost vanishes for fluid filled cracks ($\kappa_s \approx 0$) (Pyrak-Nolte et al., 1990b; Hsu and Schoenberg, 1993).

Although theoretically the κ_s/κ_n ratio has been shown to have a value approaching unity for dry cracks, experimentally (in both laboratory and field scale experiments) it has been found to have values reaching up to 3.0 (Choi et al., 2014).

2.3 WAVE3D: a program to model fractures numerically

WAVE3D was primarily created for modelling seismic waves recorded around excavations in mines and modelling the wave interaction with fractures (Hildyard, 2001). WAVE3D can model different phenomena such as wave mode conversion at oblique incidence with planes of discontinuities, fracture interface waves as Rayleigh-type wave propagating along the fault (Hildyard et al., 1995), as well as guided waves when they remain trapped within compliant parallel fractures. Despite that, it does not model cross-coupled waves due to shear stress applied to a fracture that converts, at normal incidence, shear waves in compressional waves and vice versa (Nakagawa et al., 2000). Those studies covered different problem scales: from a representation of dynamic fault slip and rockburst mechanisms in mines, to a representation of dynamic behaviour and wave propagation in fracture zones (Hildyard, 2007).

WAVE3D solves a system of first-order hyperbolic equations on a staggered grid using the finite difference method. The staggered grid scheme ensures a computational efficiency and a higher numerical accuracy (Virieux, 1986). WAVE3D implements a discrete representation of fractures as well as the EM approach (Cundall, 1992; Hildyard et al., 1995). Cracks are modelled as finite, and the displacements are continuous at the crack tips. WAVE3D also models additional mechanical phenomena such as frictional sliding, dynamic openness and closure of cracks, as well as variation of fracture specific stiffness along the crack (Hildyard, 2001). Recent developments have been made to introduce a hybrid approach between the EM and discrete fracture representation called localised effective medium (LEM) (Parastatidis et al., 2017; Parastatidis et al., 2021). This method models the fractures as grid cells containing equivalent anisotropic media and Parastatidis et al. (2021) showed that LEM approximates well the explicit fracture model when the thickness of the LEM layer is much smaller (~ 20 times) than the dominant wavelength.

2.3.1 Solving the wave equation through the finite difference method

The FD method is widely used to numerically solve the wave equation with a FD stencil to simulate seismic waves travelling through the subsurface. WAVE3D implements a velocity-stress formulation of the wave equation solving the system of two first order equations: a constitutive equation and an equation of motion. For a linear elastic isotropic material they are

$$\dot{\sigma_{ij}} = \delta_{ij}\left(K - \frac{2}{3}G\right)\partial\dot{e}_{kk} + 2G\dot{e}_{ij} \tag{2.29}$$

$$\rho\frac{\partial\dot{u}_i}{\partial t} = \frac{\partial\sigma_{ij}}{\partial x_j} \tag{2.30}$$

where σ_{ij} are the components of the stress tensor, e_{ij} are the components of the strain tensor, ρ is density, K and G are the bulk and shear moduli, respectively. The strain rates $\dot{e}_{ij}$ are calculated from

$$\dot{e}_{ij} = \frac{1}{2}\left[\frac{\partial\dot{u}_i}{\partial x_j} + \frac{\partial\dot{u}_j}{\partial x_i}\right]. \tag{2.31}$$

The system of equations (2.29)-(2.30) is solved numerically replacing the partial derivatives by finite differences by means of Taylor series (hence the origin of the method's name). Therefore, the continuum is discretised into a mesh at discrete points in time and space (Figure 2.7(a)). Specifically, WAVE3D uses a staggered grid where variables are separated by one half a grid length and each grid variable is computed at different positions in space (Figure 2.7(b)). It uses a central difference scheme with a second-order accuracy in time, and fourth-order in space. Nevertheless, the accuracy is reduced to the second order in the vicinity of mesh boundaries, cavities or cracks (Hildyard, 2001). Stresses are obtained from velocities using equation (2.29), while velocities from equation (2.30).

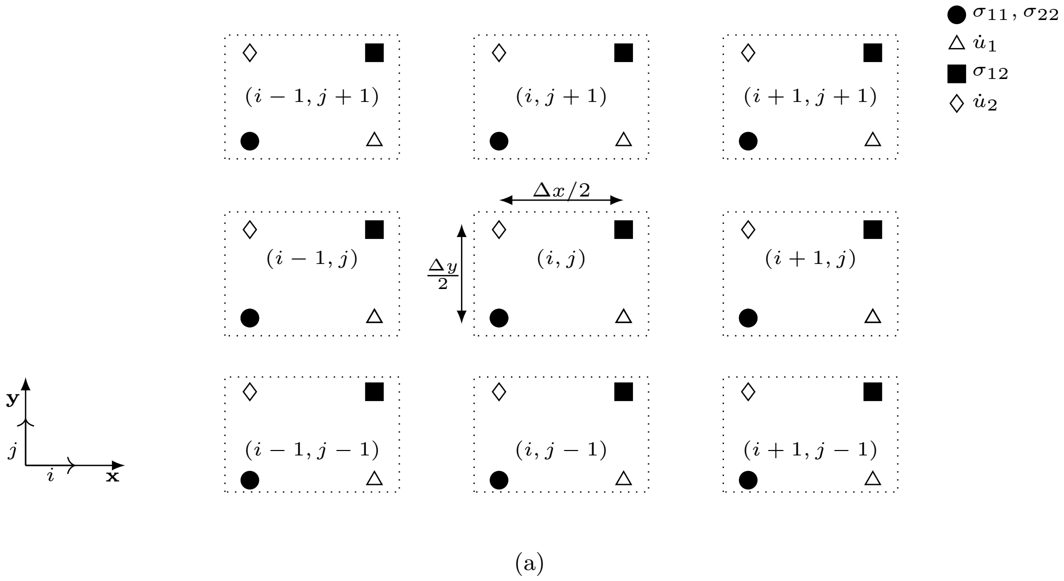

(a)

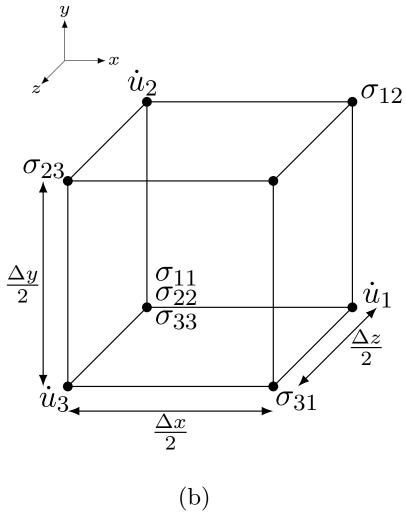

(b)

Figure 2.7: (a) A 2D portion of the WAVE3D mesh, showing the spatial positions for each variable. (b) A unit 3D cell in the WAVE3D staggered grid with the respective variables. Adapted from Hildyard (2007)

2.3.2 Numerical dispersion and numerical stability

The resulting space-time discretisation leads to non-physical phenomena such as numerical dispersion and numerical instability. The numerical solution of the wave equation is correct only if some stability and dispersion conditions are met, therefore limiting the range of values for the time-step interval and grid-spacing.

To prevent excessive grid dispersion, the spatial criterion imposed on the grid-spacing Δh for a fourth-order accuracy scheme recommends that the shortest wavelength is sampled by at least five grid-points per wavelength (Levander, 1988). WAVE3D follows this recommendation, however when there are large fractures or large numbers of fractures it is prudent to be more conservative and use 10 grid-points (Hildyard, 2001). Mathematically this means:

$$\Delta h \leqslant \frac{\lambda_{min}}{10} = \frac{1}{10}\frac{c_{min}}{f_{max}} \tag{2.32}$$

where c_{min} is the slowest velocity of all materials, λ_{min} the shortest wavelength, and f_{max} the highest modelled frequency. Note that, generally, the shortest wavelength is due to the S-wave velocity model, and therefore the shear velocity generally limits the grid spacing.

On the other hand, the grid spacing is coupled to the time-step interval (Δt) through the so called Courant–Friedrichs–Lewy (CFL) criterion. This describes how the temporal discretisation has to be satisfied to ensure the stability of the wave equation solution. It reads

$$\Delta t \leqslant \mathcal{C}\frac{\Delta h}{c_{max}} \tag{2.33}$$

where $\mathcal{C}$ is the Courant number (for fourth-order accuracy $\mathcal{C} = 0.606$ (Fichtner, 2010)), and c_{max} is the fastest velocity of all materials.

For fourth-order accuracy and in 3D, WAVE3D has a smaller value of $\mathcal{C}$ and uses $\mathcal{C} = 0.45$. Moreover, it allows for mixed sizes of dx, dy, and dz. It does not use the smallest value to compute the stability of the wave equation solution, and larger dy and dz increase the stable timestep.

2.3.3 Modelling fractures and fractured media in WAVE3D

In the mesh structure, discrete fractures are implemented as discontinuities and are expressed as zero-width thickness between two coincident surfaces with boundary conditions defined in Pyrak-Nolte et al. (1990b) and shown in Section 2.2.1. The orthogonal shear specific stiffness $\kappa_{s,y}$, as shown in Figure 2.2, assumes the same value of the shear stiffness $\kappa_{s,x}$ for all experiments throughout the manuscript. This representation has been shown to be valid for a wide range of seismic frequencies with fracture sizes and spacings both larger and smaller than the seismic wavelength (Hildyard, 2007).

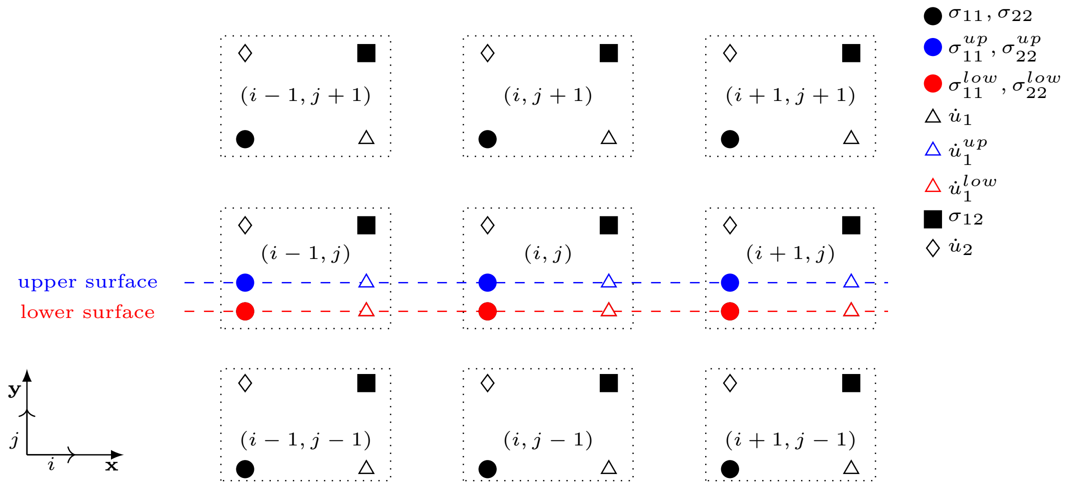

Figure 2.8: Representation of a 2-D horizontal fracture in the staggered mesh, in WAVE3D, showing surrounding grid variables and different values of σ_{11}, σ_{22}, and $\dot{u}_1$ for the upper and lower surface respectively. Adapted from Hildyard (2007).

For a two-dimensional horizontal crack case (Figure 2.8) the grid variables, coinciding with the crack surfaces, have an upper and lower value: σ_{22}^{up} and σ_{22}^{low}, σ_{11}^{up} and σ_{11}^{low}, $\dot{u}_1^{up}$ and $\dot{u}_1^{low}$, where for continuity $\sigma_{22}^{up} = \sigma_{22}^{low} = \sigma_{22}$, while σ_{11}^{up}, σ_{11}^{low}, $\dot{u}_1^{up}$, and $\dot{u}_1^{low}$ must be independently computed (Hildyard, 2007). Whereas, to model a medium containing fractures, WAVE3D implements the Schoenberg's equivalent fractured medium theory reviewed in Section 2.2.2.

Further descriptions of the numerical implementation of the displacement discontinuity theory can be found in Hildyard and Young (2002) and Hildyard (2007).

2.3.4 Crack assemblies in WAVE3D

To generate crack assemblies with a certain size and density, WAVE3D implements the conceptual model of fracturing as a collection of flat ellipsoidal openings introduced by Budiansky and O'Connell (1976). Here, a cracked medium is described through the crack density ϵ_0, a dimensionless parameter, defined as (for ellipsoidal open cracks)

$$\epsilon_0 = \frac{2N}{\pi}\left\langle \frac{A^2}{P} \right\rangle \tag{2.34}$$

where $N = N_f/V$ is the total number of elementary cracks (N_f) per unit volume V. A and P are the crack area and perimeter, respectively, and $\langle\cdot\rangle$ represents the average value. For circular open cracks equation (2.34) reduces to

$$\epsilon_0 = N \left\langle r^3 \right\rangle \tag{2.35}$$

with r the average crack radius.

Considering rectangular cracks with the i-th crack sides a_i and b_i, Hildyard (2007) defines ϵ, instead, as

$$\epsilon = \frac{1}{\pi V} \sum_{i=1}^{N_f} \frac{a_i^2 b_i^2}{a_i + b_i}. \tag{2.36}$$

If the cracks are square (i.e., $b_i = a_i$), equation (2.36) becomes

$$\epsilon = \frac{1}{2\pi V} \sum_{i=1}^{N_f} a_i^3 = \frac{N_f}{2\pi} \left\langle a^3 \right\rangle. \tag{2.37}$$

Equation (2.37) gives values of ϵ between the values of an inscribed circle and a circumscribed circle derived from equation (2.35) (Hildyard, 2007).

The interpretation of the crack density, however, gives rise to an inherent ambiguity. In fact, radically different fracture distributions may produce the same crack density. This is because a large number of small cracks (large N, small a) can have the same crack density as a few large cracks (small N, large a) (Lubbe and Worthington, 2006). Figure 2.9 shows an example of this behaviour, where two fractured models have the same crack density ϵ, distributed in the same fractured volume, but with different crack size. These two models, however, will have different fluid flow responses (e.g., (Pyrak-Nolte and Nolte, 2016)), as well as different anisotropic behaviours (Fuggi et al., 2021).

Using a specific WAVE3D plug-in, a discrete fracture zone is created within the numerical mesh by defining the crack size and crack density for each direction. Because of the orthogonal mesh, cracks can be generated only along the mesh grid points, i.e.,

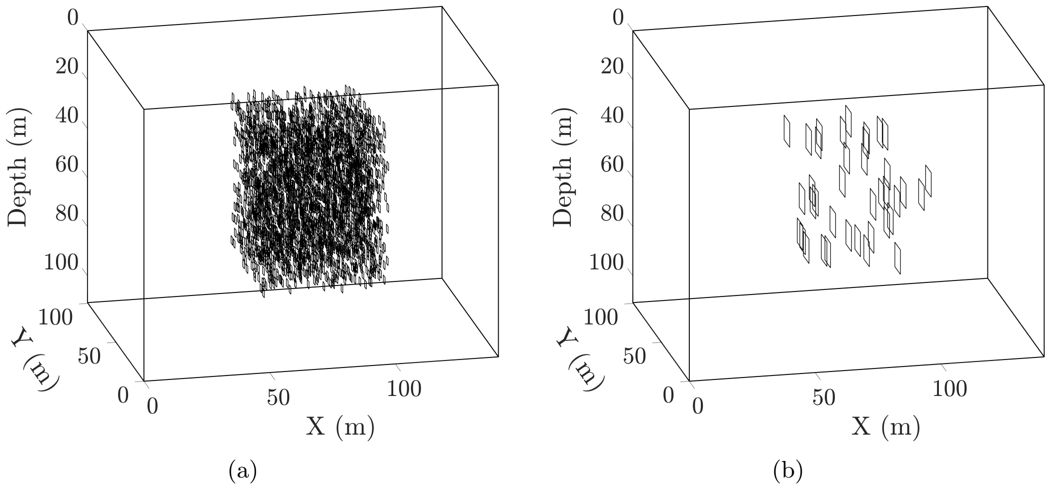

Figure 2.9: An example of the ambiguity of the crack density parameter. Two fracture models have the same crack density ($\epsilon = 0.025$), and same cracked volume ($V = 50 \times 67 \times 57$ m^3). However, in (a) crack size is $a^2 = 3 \times 3$ m^2, while in (b) crack size is $a^2 = 10 \times 10$ m^2.

parallel to the $x - y$ plane, $x - z$ plane, or $y - z$ plane (Figure 2.10).

It follows that, for a defined fractured volume, discrete cracks are progressively added (randomly distributed in space) until the crack density defined in equation (2.36), for each direction, is satisfied. Crack intersections are avoided.

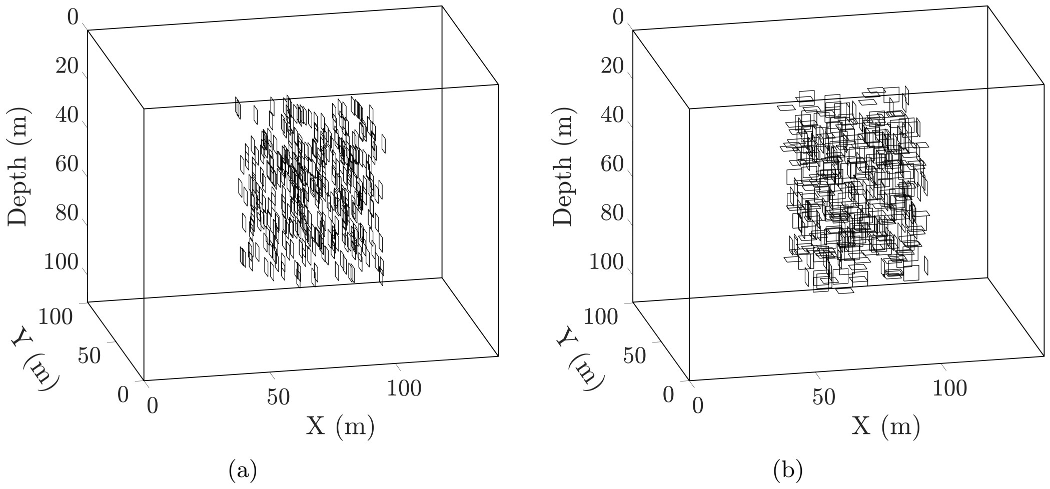

Figure 2.10: Two fracture models with the same crack density $\epsilon = 0.045$, crack size $a^2 = 6 \times 6$ m^2 and cracked volume $V = 50 \times 67 \times 57$ m^3, with different fracture orientations. In (a) the axis normal to the cracks is parallel to the x-axis, while in (b) the cracked medium is composed of three different sets of cracks orthogonal to each other. Each set has crack density $\epsilon = 0.015$, therefore, with a total crack density of $\epsilon = 0.045$.

Differently to Budiansky's model where cracks are considered open, in WAVE3D at each discrete crack is an associated (κ_n, κ_s) pair, i.e., they can be considered open, closed, or partially open depending on the stiffnesses values. This is the reason why in equations (2.34) and (2.35) crack density is named ϵ_0, whereas it is ϵ in equations (2.36) and (2.37).

2.3.5 Perfect Matched Layer (PML) as absorbing boundary conditions

Absorbing boundary conditions are used to simulate an infinite medium for wave propagation by implementing artificial boundaries at the edges of the computational domain. WAVE3D offers two solutions for this purpose: the absorbing boundary conditions (ABCs) and PML absorbing boundaries. PML was firstly developed and implemented in elecromagnetism, and only subsequently in seismology (Collino and Tsogka, 2001). Rather than using some local boundary conditions such as implemented by the ABCs, PML boundaries are designed to surround the domain of interest with artificial absorbing layers where waves are trapped and exponentially attenuated (Komatitsch and Tromp, 2003). Figure 2.11 shows a comparison between these two implementations in WAVE3D, highlighting that PML boundary conditions outperform the ABCs, attenuating the impinging waves approximately 20 times more (Figure 2.11(c)). Although they have a better performance, PML are also considerably more computationally demanding.

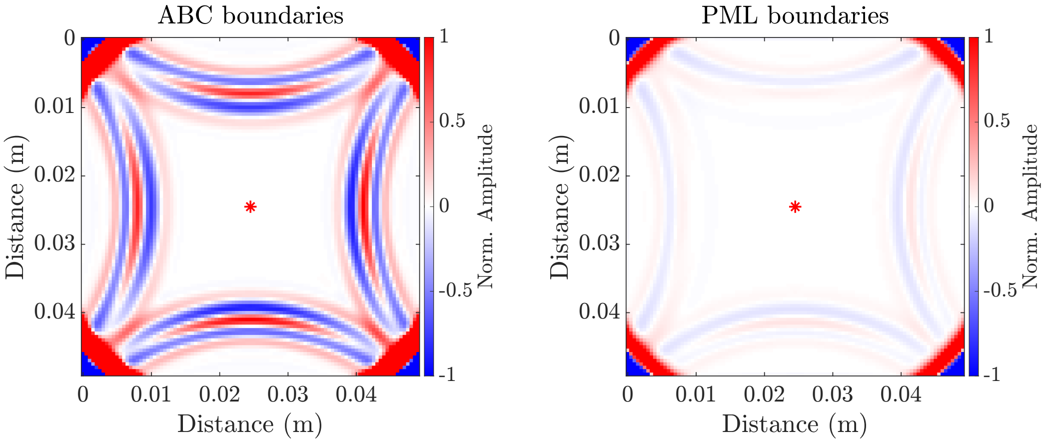

(a) Snapshots at 13 ms of a wavefield propagating in a medium with ABCs.

(b) Snapshots at 13 ms of a wavefield propagating in a medium with PML boundaries.

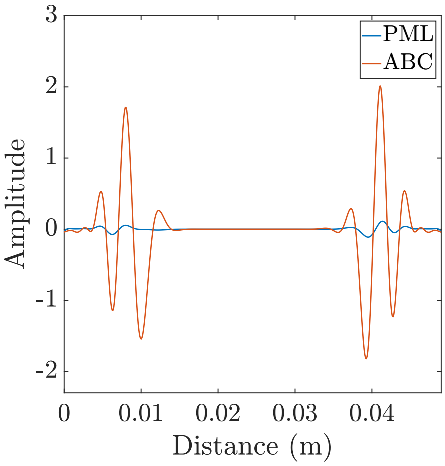

(c) Comparison between waveforms recoded in the medium in (a) (blue), and (b) (red).

Figure 2.11: Qualitative performance comparison between ABC (a) and PML (b) boundaries in WAVE3D. Red star is the source location. A Ricker wavelet was used to generate the propagating waves. (c) Waveforms recorded along a horizontal line of receivers passing through the source location. The spurious reflections from the model boundaries in the ABC case have amplitude approximately 20 times greater than the PML.

2.4 Surface seismic methodologies to characterise fractured rocks

There are a variety of techniques that are able to extract some fracture properties from surface seismic data. Most of them deal with the characterisation of anisotropy (of velocities or attenuation) in order to estimate, as an inverse process, physical properties of interest such as crack density (or fracture stiffnesses) and orientation (Chichinina et al., 2006; Willis et al., 2006; Clark et al., 2009; Moffat et al., 2010; Liu and Martinez, 2012). The main techniques can be split into two macro categories: travel time-based methods (e.g., Shear-wave Splitting (SWS) (Crampin, 1981), Azimuthal variation of normal moveout (NMO) velocity (Tsvankin, 1997)), and amplitude-based methods (e.g., Azimuthal Amplitude Variation with Offset (AzAVO or AVOAz) (Rüger, 1998), P-wave attenuation (Clark et al., 2009)).

2.4.1 Anisotropic parameters for TI media

In most elasticity theory applications, the elastic medium is assumed to be isotropic (Thomsen, 1986), therefore, the material properties are independent of direction. An isotropic medium can be defined by only two independent variables of the stiffness matrix, c_{11} and c_{44}, reduced from the 21 parameters needed to describe a more general case, the triclinic medium. It is common to describe an isotropic medium by using the Lamé parameters λ and μ, which have the following relations with the element of the stiffness matrix

$$c_{11} = \lambda + 2\mu, \qquad c_{44} = \mu, \tag{2.38}$$

and as functions of P-wave, S-wave velocities, and density, λ and μ are defined as

$$\begin{aligned} &\mu = \rho v_s^2 \qquad \text{(also called shear modulus), and} \\ &\lambda = \rho v_p^2 - 2\mu \end{aligned} \tag{2.39}$$

Nevertheless, in the presence of preferential alignment of minerals during deposition, flow, or ambient stress conditions (e.g., clay particles in shale formations), horizontal fine layering, or aligned fractures both the kinematic and the dynamic parameters of seismic wavefields are directionally dependent, so these media give rise to seismic anisotropy.

To describe explicitly the effect of anisotropy on the seismic wave propagation through a vertical transversely isotropic (VTI) medium – for instance a fine horizontal bedding – Thomsen (1986) defined dimensionless anisotropic parameters (ε, δ, γ

- hereafter Thomsen parameters) to separate the influence of the anisotropy from the isotropic parameters:

$$\varepsilon = \frac{c_{11} - c_{33}}{2c_{33}} \tag{2.40}$$

$$\delta = \frac{(c_{13} + c_{44})^2 - (c_{33} - c_{44})^2}{2c_{33}(c_{33} - c_{44})} \tag{2.41}$$

$$\gamma = \frac{c_{66} - c_{44}}{2c_{44}}. \tag{2.42}$$

In an analogy with the Thomsen parameters, Tsvankin (1997) and Rüger (1997) introduced a set of three anisotropic coefficients to describe HTI media, called $\varepsilon^{(V)}$, $\delta^{(V)}$, $\gamma^{(V)}$. The superscript $^{(V)}$ defines the parameters with respect to the vertical symmetry axis – the Thomsen parameters are defined with respect to the horizontal symmetry axis.

Using the elastic stiffness components c_{ij}, Tsvankin anisotropic parameters are defined as

$$\varepsilon^{(V)} = \frac{c_{11} - c_{33}}{2c_{33}} \tag{2.43}$$

$$\delta^{(V)} = \frac{(c_{13} - c_{55})^2 - (c_{33} - c_{55})^2}{2c_{33}(c_{33} - c_{55})} \tag{2.44}$$

$$\gamma^{(V)} = \frac{c_{66} - c_{44}}{2c_{44}}. \tag{2.45}$$

The parameter $\varepsilon^{(V)}$ is also defined as the P-wave anisotropy parameter since it expresses the difference between the P-wave velocity in the slowest and fastest direction, e.g., orthogonal and parallel to the fractures, respectively. $\delta^{(V)}$ is responsible for near-vertical P-wave velocity variation along the normal direction to the fractures, whereas $\gamma^{(V)}$ is also called the shear-wave splitting parameter because it governs the shear-wave splitting at vertical incidence. Both $\varepsilon^{(V)}$ and $\delta^{(V)}$ are negative.

The relationship between the anisotropic Tsvankin parameters and the fracture weaknesses Δ_n and Δ_s can be found by substituting the elastic stiffness components of equation (2.14) in equations (2.43)-(2.45). Bakulin et al. (2000) give their exact and approximated expressions, assuming weak anisotropy (i.e. $\varepsilon^{(V)} \ll 1$, $\delta^{(V)} \ll 1$ and $\gamma^{(V)} \ll 1$), as

$$\varepsilon^{(V)} = \frac{2g(1-g)\Delta_n}{1-\Delta_n(1-2g)^2} \approx -2g(1-g)\Delta_n \tag{2.46}$$

$$\begin{aligned}\delta^{(V)} &= -\frac{2g[(1-2g)\Delta_n+\Delta_s][1-(1-2g)\Delta_n]}{[1-\Delta_n(1-2g)^2]\left[1+\frac{1}{1-g}(\Delta_s-\Delta_n(1-2g)^2)\right]} \\ &\approx -2g[(1-2g)\Delta_n+\Delta_s]\end{aligned} \tag{2.47}$$

$$\gamma^{(V)} = -\frac{\Delta_s}{2}. \tag{2.48}$$

The parameter g is defined as $g = \frac{\mu}{\lambda+2\mu} = \frac{\bar{v}_s^2}{\bar{v}_p^2}$.

2.4.2 P-wave reflectivity in HTI media

The P-wave amplitudes (described by the AVOA attribute) and normal moveout (NMO) velocity are sensitive to the anisotropy of rock masses (Crampin et al., 1980; Tsvankin, 1997; Rüger, 1998). If the anisotropy is caused by vertical fractures, their strike and stiffness can be determined by the amplitude attributes (Rüger and Tsvankin, 1997).

Rüger and Tsvankin (1997) and Rüger (1998) proposed an analytical formulation to express the variation of the seismic amplitudes with angle in case of two HTI layers with the same orientation. The approximate reflection coefficient for compressional waves (R_{PP}^{HTI}), under the assumptions of small-to-moderate contrasts in rock properties and weak anisotropy between the upper and lower reflection interfaces, is given by Rüger and Tsvankin (1997):

$$\begin{aligned}R_{PP}^{HTI}(\theta,\varphi) = A^{ISO} \\ &+ \left(B^{ISO}+B^{HTI}(\varphi)\right)\sin^2\theta \\ &+ \left(C^{ISO}+C^{HTI}(\varphi)\right)\sin^2\theta\tan^2\theta\end{aligned} \tag{2.49}$$

where

$$\begin{aligned}
A^{ISO} &= \frac{1}{2}\left(\frac{\Delta Z}{\bar{Z}}\right)\\
B^{ISO} &= \frac{1}{2}\left(\frac{\Delta v_p}{\bar{v}_p} - 4g\frac{\Delta G}{\bar{G}}\right)\\
C^{ISO} &= \frac{1}{2}\left(\frac{\Delta v_p}{\bar{v}_p}\right)\\
B^{HTI}(\varphi) &= \frac{1}{2}\left[\left(\Delta\delta^{(V)} + 8g\Delta\gamma^{v}\right)\cos^2\varphi\right]\\
C^{HTI}(\varphi) &= \frac{1}{2}\left(\Delta\delta^{(V)}\sin^2\varphi\cos^2\varphi + \Delta\varepsilon^{(V)}\cos^4\varphi\right),
\end{aligned} \tag{2.50}$$

defined with θ and φ as the incident and azimuth angle (see Figure 2.12 for a graphical guide), respectively, the overline $\bar{}$ and Δ symbols represent the average and the difference values between the two media across the interface. $Z = \rho v_p$ is the acoustic impedance, $G = \mu = \rho v_s^2$ is the shear modulus.

Finally, substituting the Tsvankin parameters defined with respect to the fracture properties (equations (2.46)-(2.48)) into equation (2.49), rock physics fracture models are linked to the seismic AVOA attribute. In order to model the AVOA attribute for fracture-induced HTI layered media, Fuggi et al. (2020) introduced a correction to the isotropic parameters based on the elastic impedance formalism.

2.4.3 NMO velocity and traveltime in anisotropic media

Information about fractured rock volumes (e.g., fractured reservoirs) can also be obtained from the variation of NMO velocity with azimuth by inverting azimuthally-dependent reflection traveltimes (Bakulin et al., 2000) .

For a horizontal HTI layer having an arbitrary symmetry axis with respect to the x-axis (defined by the angle β) the reflection moveout of pure modes (non-converted) can be approximated by the hyperbolic equation (Tsvankin and Thomsen, 1994; Tsvankin, 1997; Grechka and Tsvankin, 1998):

$$t^2 = t_0^2 + \frac{x^2}{V_{nmo}^2(\varphi)} \tag{2.51}$$

where

$$V_{nmo}^{-2}(\varphi) = \frac{\cos^2(\varphi - \beta)}{V_{nmo,fast}^2} + \frac{\sin^2(\varphi - \beta)}{V_{nmo,slow}^2}. \tag{2.52}$$

$V_{nmo}(\varphi)$ is the azimuthally varying NMO velocity as a function of the shot-receiver azimuth φ (see Figure 2.12(a)), and V_{fast} and V_{slow} the fastest (direction parallel to the fracture strike) and slowest NMO velocities, respectively. The velocity V_{slow} is directly related to Tsvankin's parameter $\delta^{(V)}$ and V_{fast} by (Thomsen, 1986; Tsvankin, 1997)

$$V_{slow} = V_{fast}\sqrt{1 + 2\delta^{(V)}}. \tag{2.53}$$

By substituting equation (2.53) into equation (2.52), and considering the trigonometry identity $\cos^2(x) = 1 - \sin^2(x)$, equation (2.52) assumes the following form (Bakulin et al., 2000)

$$V_{nmo}^2(\varphi) = V_{fast}^2 \frac{1 + 2\delta^{(V)}}{1 + 2\delta^{(V)} \sin^2(\varphi - \beta)} \tag{2.54}$$

If equation (2.54) is plotted as a function of azimuth, the NMO velocity forms an ellipse with the semi-axes aligned with the vertical symmetry planes of the HTI layer. The semi-major axis of the NMO ellipse is defined by V_{fast}, whereas the semi-minor axis by V_{slow}.

An estimate of the magnitude of the anisotropy, which directly depends on $\delta^{(V)}$, is provided by the ratio (Thomsen, 1986)

$$anisotropy \approx \frac{V_{fast} - V_{slow}}{V_{fast}} = 1 - \sqrt{1 + 2\delta^{(V)}} \tag{2.55}$$

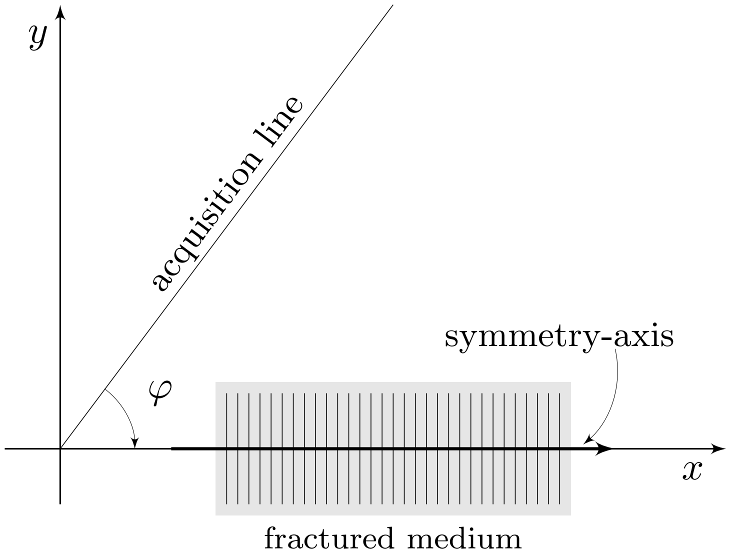

(a) The azimuth angle φ is defined as the difference between the acquisition line orientation and the symmetry-axis. In this case $\beta = 0$, since the symmetry-axis is parallel to the x-axis.

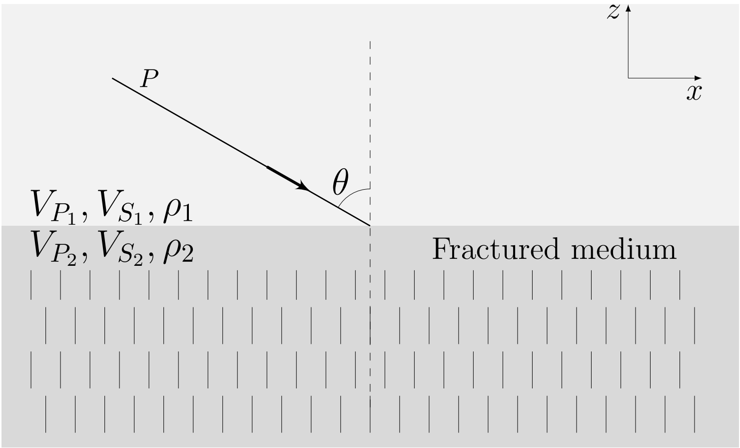

(b) The incident angle θ is defined with respect to the vertical axis z.

Figure 2.12: Graphical guide for the definition of the incident angle θ and the azimuth angle φ. Plan view in (a) and vertical cross-section view in (b) over a fractured medium containing aligned vertical fractures with the symmetry-axis along the x-axis.

2.4.4 Shear wave splitting

When a shear wave travels through an anisotropic medium it typically exhibits a physical phenomenon known as seismic birefringence, namely the incident shear wave splits into two polarized shear waves which travel as two separate orthogonal modes with different velocities, S1 and S2 components for fast and slow shear wave, respectively. In the case of a fractured HTI medium, both the polarization and the propagation of the faster split shear wave lies in the plane parallel to the strike of the cracks which is preserved, unchanged, even after it exits from the anisotropic region (Crampin, 1981). Therefore, once recorded, this shear wave mode can be used to infer the fracture orientation. The time delay (or time lag δt) between fast and slow shear waves is proportional to the strength of the anisotropy (Crampin, 1981), which is directly related to the Tsvankin parameter $\gamma^{(V)}$ (Tsvankin, 1997), and in turn to the shear weakness (Δ_s) of the fracture system (equation (2.48)). For dry or fluid-filled cracks, $\gamma^{(V)}$ also well approximates the crack density (Bakulin et al., 2000). Shear-wave splitting techniques were first used for fracture detection by Alford (1986).

In practice, by employing 3-component geophones, both the shear wave polarizations and δt can be measured. A fracture induced anisotropic medium is, therefore, characterised (Angus et al., 2009; Verdon et al., 2009; Wuestefeld et al., 2010; Verdon and Wüstefeld, 2013).

2.4.5 Attenuation due to aligned fractures

The amplitudes of seismic waves propagating in a fractured medium experience a decay in amplitude due to a variety of physical phenomena, such as solid friction, scattering, and transmission losses due to the energy partition at the fracture interfaces, generating reflected and transmitted waves. In addition to these, causes of seismic attenuation are also intrinsic attenuation, and geometrical spreading which are not necessary related to the presence of fractures. The strength of the attenuation is commonly quantified using the dimensionless quantity $\mathcal{Q}$, also called the *seismic quality factor.*

Rock volumes containing aligned cracks or fractures are prone to produce conduits for fluid flow or fluid storage, which may lead to a azimuth-dependent attenuation (Chichinina et al., 2006; Clark et al., 2009). Chichinina et al. (2006) analysed the variation of Q-factor with azimuth, calling the method QVOA in analogy with the azimuthal variation of AVO, and introducing new seismic attributes (QVO gradient and associated Q-intercept) to be linked to the parameters of the fractured medium, such as fracture-strike and crack density.

Some techniques described in this Section are beyond the scope of this work but they offer a broad overview of fracture characterisation. Some are further exploited and compared with the results obtained trough the inversion method developed and detailed in the next Chapter.

Chapter 3

Genetic algorithm full-waveform fracture inversion

In this chapter an alternative scheme is proposed that looks beyond the conventional local-optimisation FWI for velocity model building, investigating a two-step method involving a global optimisation technique, such as the genetic algorithm (GA), and uncertainties evaluation using the neighbourhood algorithm (NA) in order to estimate fracture properties directly from seismic waveforms.

The main task of the optimisation involves maximising or minimising of some misfit functionals with the aim of best fitting the observed (measured) seismic data with accurate models of seismic wave interactions with fractures. Therefore, the work presented in this chapter describes the theory and the implementation of the GA method along with the evolutionary operators that have been tested, and an introduction to the NA technique.

The evolutionary operators are briefly presented in section 3.3.3, and the appraisal of the model space through NA is presented in Section 3.4. In Section 3.5 the performance of the GA+NA approach in minimising and appraising analytical functions is also shown. A synthetic case of fracture characterisation in a simulated laboratory experiment is carried out in Section 3.6.

3.1 Preamble

In the context of discrete fractures characterisation, quantitative estimation of mechanical properties of fractures using waveform inversion techniques is very scarce. A recent study conducted by Hunziker et al. (2020) shows a successful application of a MCMC inversion of full-waveform tube-wave data recorded in a vertical seismic profiling (VSP) setting with the aim of estimating aperture and compliance of fractures in the underground Grimsel Test Site in the central Swiss Alps. Different to this project, their solution of the forward problem is based on a semi-analytic solution rather than a finite-difference solution of the elasto-dynamic equations.

A different approach to estimate fracture properties was followed by Rao and Wang (2009) who performed a waveform tomography on fractured media utilising a gradient-based (local) waveform inversion. The objective of this study was to investigate attenuation effects resulting from discrete fractures in subsurface media. In order to model the direct problem a finite difference approach was employed. The elastic wave equation was solved in the time domain and the discrete fractures were modelled using the displacement discontinuity approach proposed by (Coates and Schoenberg, 1995). The waveform inversion was performed in the frequency domain and in acoustic approximation by estimating the attenuation model ($\mathcal{Q}^{-1}$) due to fractures.

Other approaches for fracture characterisation which utilise waveform inversion methods deal with the estimation of fracture-induced anisotropy by means of the gradient-based (local) technique, e.g. (Bansal and Sen, 2010; Hou et al., 2013; Zhang et al., 2017).

To the author's knowledge, there are no attempts to estimate fracture properties explicitly through a stochastic seismic waveform inversion using a wave equation solver, such as the finite-difference technique. Therefore, this chapter lays the foundations, for the first time, of a more robust methodology in characterising fractures and fractured media by means of global waveform inversion.

3.2 An overview of Genetic Algorithms (GAs)

Genetic algorithms (GAs) are a subclass of evolutionary algorithms which mimic the evolution processes and the natural selection of a biological counterpart in an effort to solve complex multimodal optimisation problems (Goldberg, 1989; Sambridge and Drijkoningen, 1992). The GA optimisation process consists of a series of evolutionary operators, such as selection, crossover, mutation, and elitism, that operate in order to select the best candidate solutions, interpreted as individuals of a population, and through the evolution process (generations) find the optimum individual. The canonical GA framework, as known today, was conceived by Holland (1975) but since then different strategies and variations have been proposed and implemented to improve the exploration of the model space (e.g. Belding (1995), Aleardi and Mazzotti (2017), and Pierini et al. (2019)), the exploitation of the model space (e.g. Gonçalves et al. (2005) and Wan and Birch (2013)), and the convergence rate (e.g. Janikow and Michalewicz (1991)).

As a result of its flexibility and robustness, GA has had much success in a wide range of applications in real-world problems, covering subjects from chemistry to finance, from physics to image processing (Weise, 2009).

The first successful applications of GA to solve strongly non-linear geophysical problems were firstly presented by Gallagher et al. (1991) and Mallick (1995), and with a focus on waveform inversion and seismic tomography by Stoffa and Sen (1991), Sen and Stoffa (1992), and Sambridge and Drijkoningen (1992). However, these studies assumed one-dimensional geological models in an acoustic approximation in order to limit the large computational costs associated with the cost function calculation, unaffordable for that time. Nevertheless, due to the recent high rate growth of high-performance computing, many applications of GA for waveform inversion have been proposed, for instance, to derive 2D or 3D long-wavelength acoustic models of the subsurface (Sajeva et al., 2016; Mazzotti et al., 2016; Aleardi and Mazzotti, 2017), to recover acoustic and anisotropic parameters by combining local FWI and global inversion strategies (Debens, 2015; Tognarelli et al., 2020), or to characterise the shallow sediments of a seabed making use of ultra-high-frequency seismic reflection waveforms (Provenzano et al., 2018).

3.3 GA-FWFI method

Like a biological organism, each individual (also called, throughout this manuscript, model or candidate solution) is constituted by chromosomes which in turn are constituted by genes. A chromosome can therefore be represented as a $1 \times N$ vector where each vector element is a gene

$$\mathbf{chromosome}_i = (\text{gene}_1,\ \text{gene}_2, \ldots,\ \text{gene}_N)_i. \tag{3.1}$$

The j-th candidate solution of a model population can be defined as a collection of P chromosomes, or more compactly as a $P \times N$ matrix, as follows

$$\mathbf{individual}_j = \begin{pmatrix} \text{chromosome}_1 \\ \text{chromosome}_2 \\ \vdots \\ \text{chromosome}_P \end{pmatrix}_j = \begin{pmatrix} \text{gene}_{1,1},\ \text{gene}_{1,2}, \ldots,\ \text{gene}_{1,N} \\ \text{gene}_{2,1},\ \text{gene}_{2,2}, \ldots,\ \text{gene}_{2,N} \\ \vdots \\ \text{gene}_{P,1},\ \text{gene}_{P,2}, \ldots,\ \text{gene}_{P,N} \end{pmatrix}_j . \tag{3.2}$$

In the context of discrete fractures characterisation, each chromosome represents a fracture or the elastic properties of the background medium and each gene represents, in a general form, a fracture property such as κ_n, κ_s, size (l_{x_1}, l_{x_2}, along the x_1-axis and x_2-axis), and location (x_1, x_2, x_3). Thus, it follows that

$$\mathbf{model}_j = \begin{pmatrix} fracture_1 \\ fracture_2 \\ \vdots \\ fracture_M \\ \mathbf{v}_p \\ \mathbf{v}_s \end{pmatrix}_j = \begin{pmatrix} \kappa_{n,1},\ \kappa_{s,1},\ l_{x_1,1},\ l_{x_2,1},\ x_{1,1},\ x_{2,1},\ x_{3,1} \\ \kappa_{n,2},\ \kappa_{s,2},\ l_{x_1,2},\ l_{x_2,2},\ x_{1,2},\ x_{2,2},\ x_{3,2} \\ \vdots \\ \kappa_{n,M},\ \kappa_{s,M},\ l_{x_1,M},\ l_{x_2,M},\ x_{1,M},\ x_{2,M},\ x_{3,M} \\ \mathbf{v}_p \\ \mathbf{v}_s \end{pmatrix}_j . \tag{3.3}$$

In a more general case, background velocities can vary spatially, so they can assume different values for each model grid point. This is the reason why both $\mathbf{v}_p$ and $\mathbf{v}_s$ are expressed as vectors (bold). However, in the inversion experiments carried out in this work, the host rock is always assumed homogeneous, isotropic, and non-attenuative.

3.3.1 GA-FWFI work-flow

A key aspect for the success of the algorithm is how a physical model can be represented with a simple encoding. Under its initial formulation, the representation of the search space solutions was a fixed-length binary coded string (Sambridge and Drijkoningen, 1992; Sambridge and Mosegaard, 2002; Sen and Stoffa, 2013), where each gene is coded with a string of n bits, so with 2^n values allowed. Nevertheless, this representation did not seem adequate and particularly natural when optimisation problems with variables in continuous search spaces were tackled (Herrera et al., 1998). In fact, the real-coded (or floating-point) variable representation outperformed, especially in high-dimensional non-linear problems, the binary representation (Janikow and Michalewicz, 1991; Sajeva et al., 2016). In this work, consequently, a real-coded chromosome representation is implemented.

Figure 3.1 shows a flowchart of GA-FWFI implemented in this work, with all the operators involved. The GA procedure begins with a set of randomly generated models within a defined search area. This defines the “Generation 0” or initial population. A forward model is then solved through WAVE3D for each individual of the population, concurrently. To evaluate the *performance* of each individual a fitness functional is used, where the higher the value, the better the individual. This functional is inversely proportional to the misfit function which quantifies the discrepancy between the observed and modelled data (also referred to objective function throughout the thesis). According to the model fitness, the most successful individuals are selected and paired (*parents*) to produce new individuals (*offspring*). In this step, there is a recombination (or a crossover) of the model parameter values of both parents that are propagated to the offspring. Nevertheless, the crossover is not the only way to transfer genetic material across generations. The mutation operator acts over the entire model population, randomly choosing the chromosomes and slightly changing some of their genes to promote *genetic diversity*, i.e., higher degree of exploration of the search space. An optional strategy can be taken allowing a small fraction of the fittest parents to be preserved unchanged for the next generation. This strategy is named *elitism*. If this step is active, to maintain the desired number of individuals in the new generation the same amount of models needs to be rejected. The resulting individuals constitute the new generation, whom are in turn subject to their fitness evaluation, and the algorithm iterates through the generations until a convergence criterion is met. Finally, from the final generation the fittest model (also referred as the elite, or best model) is extracted.

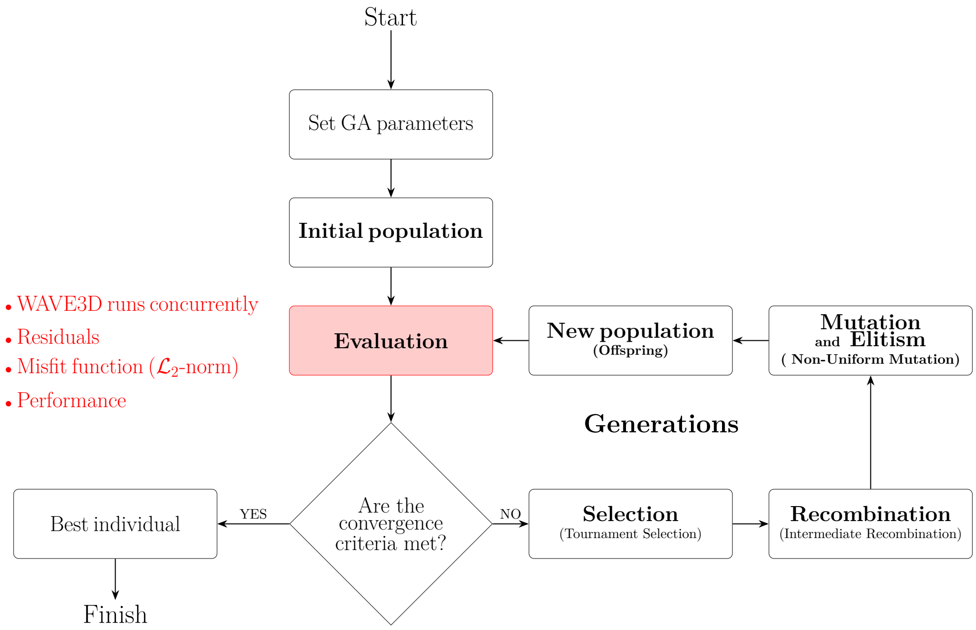

Figure 3.1: The GA-FWFI workflow implemented in this work

3.3.2 GA-FWFI implementation

The GA algorithm is written in Python and exclusively by the author. It embeds the forward modelling algorithm WAVE3D written predominantly in FORTRAN 90. The conversion of WAVE3D's output files into Python readable objects, such as *lists* or *numpy arrays*, is achieved by a series of python scripts and functions developed exclusively by the author (Fuggi et al., 2019).

In order to mitigate the computational burden given by solving thousands of forward problems, the algorithm has been parallelised over a computer cluster provided by the University of Leeds (ARC4) (*Operating system ARC4* 2021).

The Message Passing Interface (MPI), that is a standardised means to communicate between processes in distributed memory systems, has been adopted to distribute models of the GA population onto cores of the computer cluster nodes. At the end of each generation, the code waits until all GA models are submitted and terminated to calculate the corresponding misfit function values and apply the GA operators.

All compute nodes contain Intel Xeon Gold 6138 CPUs, the clock rate is 2.0 GHz, and the memory bandwidth per core is 800MHz. Each node contains 40 cores with 192 GB of memory each (*Operating system ARC4* 2021).

3.3.3 GA operators

Initialisation

Initialisation is a random process where the number of individuals and some user-selected minimum and maximum bounds are defined. Each model parameter (gene) of each candidate solution in the initial population is determined based on a uniform distribution within the multi-dimensional space solution

$$gene_{ijk} = r(gene_{ijk}^{high} - gene_{ijk}^{low}) + gene_{ijk}^{low} \tag{3.4}$$

where $gene_{ijk}$ is the i-th gene of the j-th chromosome of the k-th individual, r is a uniform random number in the interval $[0, 1]$, and $gene_{ijk}^{high}, gene_{ijk}^{low}$ are the upper and lower bound for the $gene_{ijk}$. If the gene corresponds to the location of an explicit fracture, equation (3.4) is rounded to the nearest integer to be implemented in the WAVE3D mesh.

A priori information can be included in the initialisation by using, for instance, a Gaussian distribution around some best-guess value for each model parameter.

Evaluation

The fitness for each model is evaluated by solving the forward problem in WAVE3D for each individual in the population. A misfit function is defined as the Euclidean distance ($\mathcal{L}_2$-norm) between the observed data (d^{obs}) and modelled data (d^{mod}), by comparing the two datasets trace:

$$S(\mathbf{m}) = \frac{1}{2}\sum_{s}^{ns}\sum_{r}^{nr}\sum_{t=0}^{t_{max}} \left|\left|d^{obs}(s,r,t) - d^{mod}(s,r,t)\right|\right|_2^2, \tag{3.5}$$

where nr and ns are the number of receivers and sources, respectively, and t_{max} is the maximum wave propagation time. Based on each individual's objective function value, fitness is evaluated to express how fit the model is.

Selection

There are a large variety of selection criteria which take into account different needs for specific problems. One of the most popular selection techniques in GA is the *Tournament Selection* (Shukla et al., 2015). From the actual population, the individuals compete in a series of "tournaments" to select the best ones. A *tournament size* determines the number of individuals – randomly chosen – that compete against each other. It is allowable to select the same model in different tournaments, meaning that it can be selected more than once. The Tournament size has an impact on the *diversity* of the next generations. The larger the tournament size, the greater is the probability of losing diversity (Pohlheim, 2005; Shukla et al., 2015).

The individual with the highest fitness value wins the tournament and gets selected, as parent, for generating the offspring. This process is repeated until the number of parents selected is equal to the size of initial population.

An example of how the Tournament Selection works is showed in Figure 3.2. Here, the initial population size is 10, whereas the tournament size is 3. In this case, Model 3 and Model 5 were randomly chosen two times, however only the latter won two tournaments and therefore selected twice. This implies that the same model as a parent can be found several times.

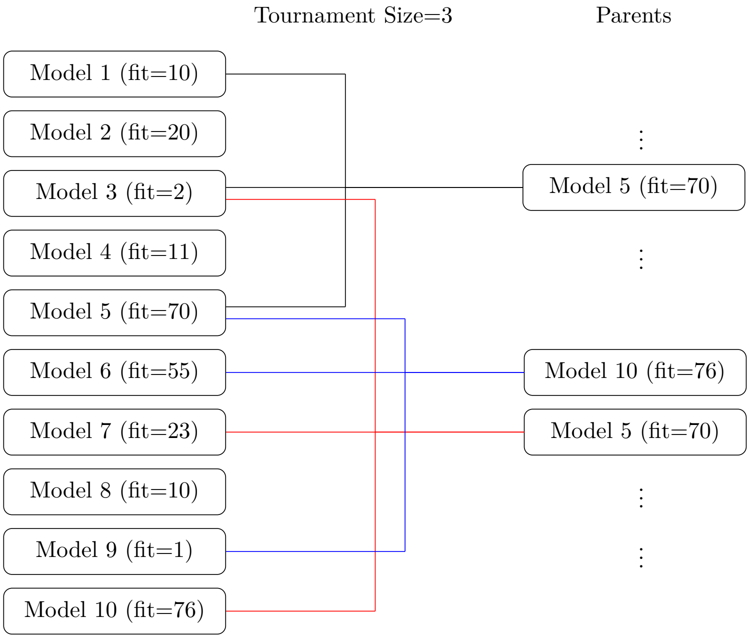

Figure 3.2: Example of Tournament Selection.

Mating

All the selected individuals (parents) from the previous stage, are paired for mating and through the recombination they produce the offspring, and each pair generates two new models to keep constant the number of final individuals. This mechanism allows the sharing of the genome between the two individuals.

There are several recombination operators which can generate the offspring. The *Arithmetic Crossover* is a family of operators that can be applied for the recombination of individuals (Ind) with real valued variables. An offspring is produced according to the following equation, that is a linear combination of the parents:

$$\mathrm{Ind}_{ij}^{off} = \alpha_j \mathrm{Ind}_{ij}^{par_1} + (1-\alpha_j)\mathrm{Ind}_{ij}^{par_2} \tag{3.6}$$

where $i \in [1, 2, \ldots, N_{ind}]$ (N_{ind} is the the number of initial individuals), j runs over the generations, α_j is a random value in the interval $[-d, 1+d]$ (d defines the size of the area for possible offspring, *e.g.* $d = 0.25$ means ±25% of the interval with respect to the extreme values), $\text{Ind}_{ij}^{par_1}$ and $\text{Ind}_{ij}^{par_2}$ are the two parents, and Ind_{ij}^{off} is the offspring individual.

If just one model parameter is considered for a given individual, the possible child's values lie in the red interval shown in the Figure 3.3. Therefore, all possible offspring's values lie in the segment that is bounded by two end points defined by the value d. The blue interval represents the area of the parents.

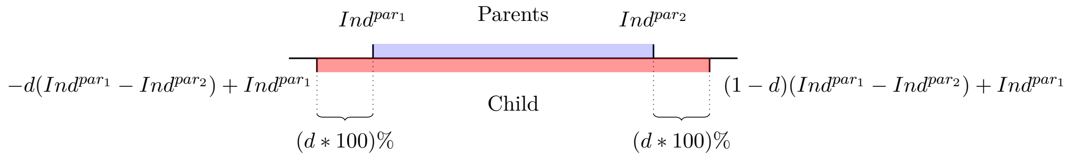

Figure 3.3: Graphical view of the Arithmetic Crossover. The Possible child's values lie in the red interval which is defined by the value d, *i.e.* between $(min(Ind^{par_1}, Ind^{par_2}) - (d * 100)\%|Ind^{par_2} - Ind^{par_1}|)$ and $(max(Ind^{par_1}, Ind^{par_2}) + (d * 100)\%|Ind^{par_2} - Ind^{par_1}|)$. Adapted from Pohlheim (2005).

Nevertheless, if two or more model parameters are considered, the *whole arithmetic crossover* approach is used (Figure 3.4(b); Pohlheim (2005)). This approach guarantees a better *genetic diversity* than the line operator, since it explores a larger model space with less probability of getting stuck in a local minimum (Pohlheim, 2005)

The *whole arithmetic crossover* uses different random values α_k (with k the k*th* gene) for each model parameter. This leads to producing the offspring within a hypercube (whose dimensions are equal to the number of genes) defined by the parents and the value d. An example with just two genes per individual is represented graphically for two genes for each individual, a graphical representation for the *Simple Arithmentic Crossover* and the *Whole Arithmentic Crossover* is given in Figure 3.4(a) and Figure 3.4(b) respectively.

Mutation

Mutation is a random process where one or more genes of a given chromosome are randomly altered. The mutation rate specifies the number of genes and chromosomes that are modified, and strongly affects the algorithm convergence as well as genetic diversity. For a high mutation rate the genetic diversity is higher, however the con-

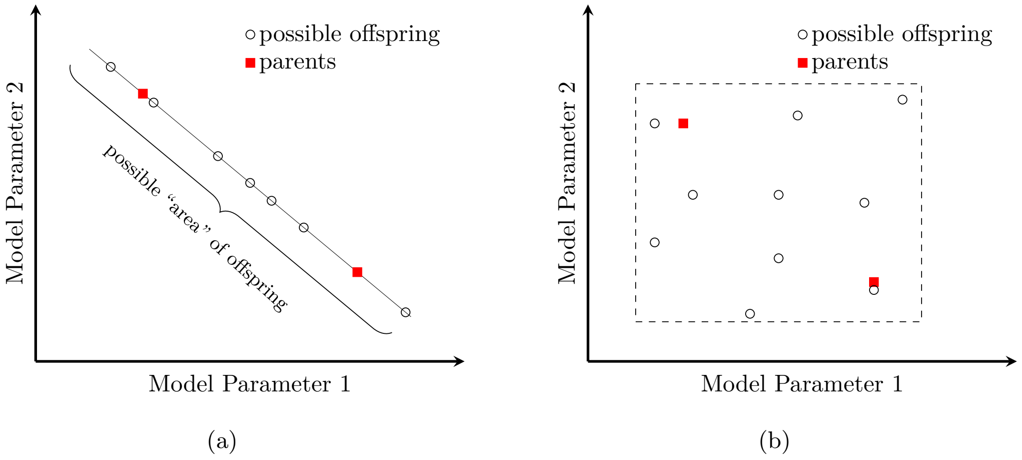

Figure 3.4: Graphical representation of the *simple arithmetic crossover* and *whole arithmetic crossover* in the case of 2 model parameters. Adapted from Pohlheim (2005).

vergence to the optimum solution may be delayed. On the contrary, a low mutation rate value limits the exploration of the model space, possibly leading the algorithm to converge to a local minimum.

An operator that has proven to be very useful in many test cases is *Non-Uniform Mutation (NUM)* (Michalewicz et al., 1994). This operator has a principal property of mutating a gene of a chromosome by exploring the model space uniformly in the first generations and more locally lately.

Through the operator NUM, a randomly selected gene g_k of a randomly selected chromosome is mutated into g'_k, according to the following equation

$$g'_k = \begin{cases} g_k + \Delta(G,\ \text{MaxVal} - g_k) & if\ R \leq 0.5 \\ g_k - \Delta(G,\ g_k - \text{MinVal}) & \text{otherwise} \end{cases} \tag{3.7}$$

where MinVal and MaxVal are the lower and upper bounds of g_k respectively, G is the actual generation, R is a random number uniformly distributed in $[0, 1]$, and $\Delta(G, y)$ is defined by:

$$\Delta(G, y) = y \cdot r \cdot \left(1 - \frac{G}{G_{TOT}}\right)^b \tag{3.8}$$

where G_{TOT} is the total number of generations, r is a random value in $[0, 1]$, and b

is called the *Non-Uniformity Degree* parameter which determines the strength of the mutation operator, a higher b gives faster convergence . The function $\Delta(G, y)$ returns a value in the range $[0, y]$ and it operates more and more locally as the number of generations increases (Figure 3.5(b)). A graphical representation of the NUM operator, for a chromosome composed of two genes, is shown in the Figure 3.5(a).

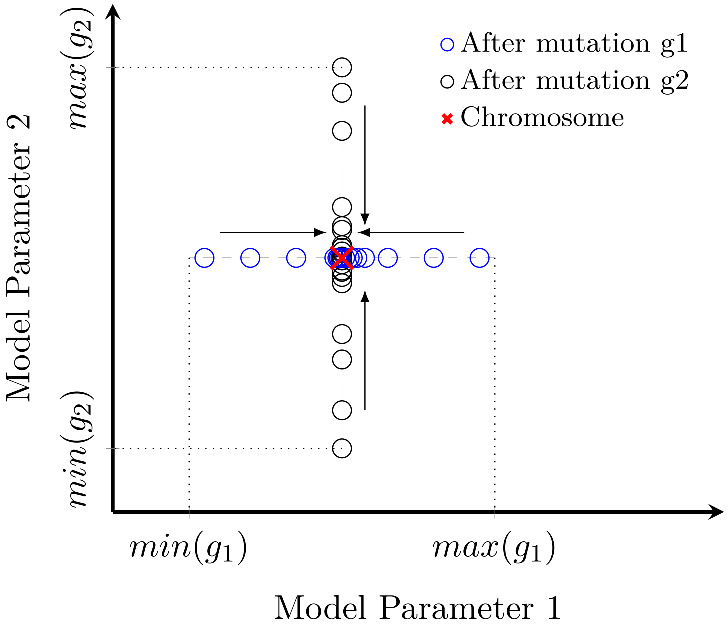

(a)

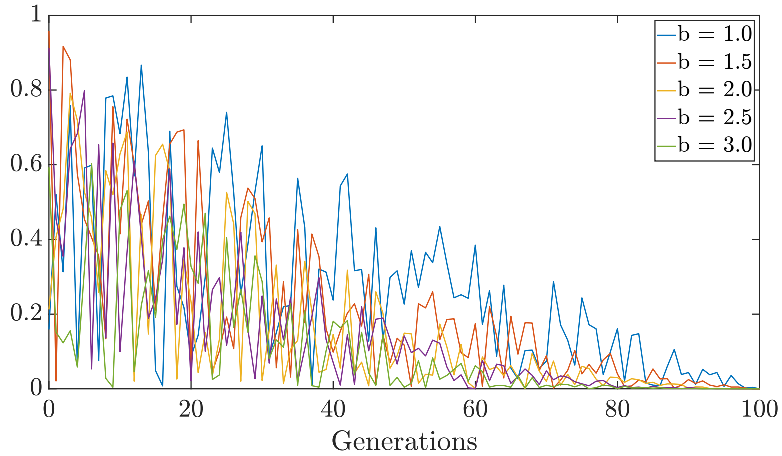

(b)

Figure 3.5: (a) Mutation of two genes $(g1, g2)$ of a given chromosome according to NUM. The circles show how the values of the two mutated genes change through the generations. Because of the function Δ, the mutated genes collapse toward the actual value at later stages. (b) Variation of the Δ function with the generations and the parameter $1 \leqslant b \geqslant 3$ (case with $y = 1$, and $G_{TOT} = 100$).

Elitism

The elitism operator involves copying a small proportion of the fittest candidates, unchanged, into the next generation. The reinsertion follows a fitness-based criterion in which the highest-fitness parents replace the lowest-fitness offspring. Elite chromosomes are also eligible for selection as parents and their number is defined in percentage of the entire population by the operator. This operator also influences the convergence rate of the algorithm.

3.3.4 Population size

The population size is an important parameter that directly influences the ability of exploring the model space and search for the optimum solution. Although a large number of models improves the model space sampling, increasing the probability that it contains a chromosome representing the optimal solution, it affects the computing time which increases exponentially (Fichtner, 2010). Whereas, if the population size is too small, the algorithm might converge too quickly to a local minimum of the misfit function (Sambridge and Mosegaard, 2002). Finding an optimum population size is not a trivial task due to its problem-dependent nature (Chen et al., 2012), and a trial-and-error method may be adopted. Nevertheless, studies have shown that a population size between 5 and 20 times the number of the search space dimension (number of unknowns) is a good compromise between GA efficiency and run time (Sambridge and Drijkoningen, 1992; Tran and Hiltunen, 2012; Sajeva et al., 2017).

3.3.5 Termination criteria

Two termination criteria were implemented in the algorithm: a pre-determined number of generations, and when the improvement of the average fitness over a given number of generations is negligible. Although the latter criterion might be more efficient, tests carried out by the author have not shown improvement in terms of total number of generations run. This is mainly due to the mutation operator which works locally at later generations, converging toward the global minimum. Therefore, the more simple criterion of a pre-determined number of iterations was used.

3.4 Uncertainty estimation by means of Neighbourhood Algorithm appraisal approach

As a stochastic optimiser, GA is implemented to explore the model space and locate the region, therein contained, where a best-fitting set of model parameters produces the lowest misfit data value. Conversely, from a statistical perspective, the solution of an inverse problem is not limited to a single set of estimated parameters but rather is represented by a probability density function (PDF), or posterior probability density (PPD) when normalised, on the model space. Therefore, the aim of inversion is not only to find a best-fitting set of model parameters but also to characterise the uncertainty in the inversion results as well as the the non-uniqueness of the solution (Sambridge and Mosegaard, 2002; Tarantola, 2005; Sen and Stoffa, 2013). Prior information, and the statistics of noise, can be incorporated into the inverse problem.

In this work, the statistical significance of the resulting ensemble of GA models is assessed through the Bayesian integration. To this end the Neighbourhood Algorithm (NA) appraisal approach is used. This process is also called NA-Bayes or NAB (Sambridge, 1999b)[1].

In order to estimate the PPD function for each model parameter and evaluate the Bayesian integrals, the distribution of the generated models needs to be known. However, GA is not a Markov-Chain Monte Carlo (MCMC) method and it provides a biased PPD if it is estimated directly from the GA-sampled models (Sambridge, 1999b; Sambridge and Mosegaard, 2002; Aleardi and Mazzotti, 2017). To circumvent this limitation, the first step of the NA appraisal method is to estimate an approximated PPD from the misfit values associated with the GA models using Voronoi cells (no additional forward models need to be solved in this step). Subsequently, the final PPD is computed making use of the Gibbs Sampler (GS) which generates a new set of samples whose distribution tends to the approximated PPD (Sambridge, 1999b). Schematically,

---

[1] The NA computer package is freely available on-line at http://www.iearth.org.au/codes/NA/.

$$\textbf{Misfit values (GA ensemble)} \xrightarrow{\text{voronoi cells}} \textbf{Approximated PPD} \xrightarrow{\text{GS}} \textbf{PPD}$$

Last, the Bayesian integrals can be evaluated using the final estimated PPD function. In the next section the NA appraisal approach is described, with a brief presentation of the Bayesian inference.

3.4.1 Bayesian inference for parameter estimation

The solution of the inverse problem within the Bayesian framework is the PPD on the model space, denoted by $P\left(\mathbf{m}|\mathbf{d}\right)$, namely the conditional probability of a set of models $\mathbf{m}$ given the data $\mathbf{d}$, also defined as posterior probability. Using Bayes' Theorem, the PPD is directly proportional to two terms: the likelihood function $L\left(\mathbf{m}|\mathbf{d}\right)$ which represents the fit of the models, and the prior $\rho(\mathbf{m})$ which represents the probability of the model independent of the data (Tarantola, 2005; Sen and Stoffa, 2013). It can be stated as

$$P\left(\mathbf{m}|\mathbf{d}\right) = kL\left(\mathbf{m}|\mathbf{d}\right)\rho(\mathbf{m}) \tag{3.9}$$

where $k = \frac{1}{p(\mathbf{d})}$ is a normalising factor. $p(\mathbf{d})$ does not depend on the model and can be considered as a constant in the inverse problem (Sen and Stoffa, 2013).

Assuming that the data measurement errors are Gaussian, the likelihood function $L\left(\mathbf{m}|\mathbf{d}\right)$ takes the form

$$L\left(\mathbf{m}|\mathbf{d}\right) = k\exp\left(-\frac{1}{2}\left(\mathbf{d}-\mathbf{g}(\mathbf{m})\right)^T C_D^{-1}\left(\mathbf{d}-\mathbf{g}(\mathbf{m})\right)\right) \tag{3.10}$$

where C_D is the data covariance matrix, and $\mathbf{d}-\mathbf{g}(\mathbf{m})$ the misfit vector between the observed data and those predicted by applying the forward operator. Consequently, $E(\mathbf{m}) = \left(\mathbf{d}-\mathbf{g}(\mathbf{m})\right)^T C_D^{-1}\left(\mathbf{d}-\mathbf{g}(\mathbf{m})\right)$ represents the misfit function minimised in the inverse process (Sambridge, 1999b; Tarantola, 2005).

Equation (3.9) and equation (3.10) provides a means of calculating the posterior probability of a particular set of model parameter $\mathbf{m}$. A general form of a Bayesian integral J, can be expressed as (Sambridge, 1999b; Sambridge and Mosegaard, 2002)

$$J = \int_{\mathcal{M}} \Gamma(\mathbf{m}) P\left(\mathbf{m}\right) d\mathbf{m} \tag{3.11}$$

where the domain spans over the entire model space $\mathcal{M}$. To simplify the notation the $|\mathbf{d}$ term in $P\left(\mathbf{m}|\mathbf{d}\right)$ is dropped, so $P\left(\mathbf{m}|\mathbf{d}\right)$ is substituted by $P\left(\mathbf{m}\right)$. The $\Gamma(\mathbf{m})$ term represents a generic function used to define each integrand.

For instance, the posterior mean model for the i-th parameter ($\overline{m_i}$), and the marginal PPD of a particular model parameter are, respectively, given by:

$$\overline{m_i} = \int_{\mathcal{M}} m_i P\left(m\right) dm, \tag{3.12}$$

and

$$P(m_i) = \int dm_1 \int dm_2 \ldots \int dm_{i-1} \int dm_{i+1} \ldots \int P\left(m\right) dm_M. \tag{3.13}$$

To quantify posterior uncertainty and thus solve the inverse problem, integrals in equations (3.12)-(3.13) need to be solved. The multi-dimensional integration over the model space $\mathcal{M}$ is generally not analytically tractable, hence numerical integration techniques, such as Monte Carlo, need to be employed to evaluate these integrals efficiently.

The discrete approximation of equation (3.11) to be used in a Monte Carlo integration technique, is expressed by (Sambridge, 1999b)

$$\hat{J} = \frac{1}{N} \sum_{k=1}^{N} \frac{\Gamma(\mathbf{m}_k) P(\mathbf{m}_k)}{h(\mathbf{m}_k)}, \tag{3.14}$$

where N indicates the number of Monte Carlo integration points, $\mathbf{m}_k$ and $h(\mathbf{m}_k)$ are the k-th model and its density distribution that is assumed normalised:

$$\int h(\mathbf{m}) d\mathbf{m} = 1. \tag{3.15}$$

A crucial aspect of evaluating the numerical integration of equation (3.14) is how the model space is sampled. When a Monte Carlo sampling is applied within a Bayesian framework, the samples are generated according to a particular distribution which usually follows the PPD function (Sambridge and Mosegaard, 2002).

Neverthless, as Sambridge (1999b), Sambridge and Mosegaard (2002), and Sen and Stoffa (2013) point out, in a case where the samples are generated with an unknown distribution the numerical integration can lead to biased results. This is also the case for the GA method.

To derive an unbiased PPD from an arbitrarily distributed ensemble, Sambridge (1999b) proposes an approach where the neighbourhood approximation (also utilised as an optimisation technique; Sambridge (1999a)) is applied. To this end, the NAB approach constructs an approximated PPD using the models generated by the GA algorithm and a multidimensional interpolant given by the Voronoi Cells. They are simply the nearest neighbour regions about each sample (model), and inside the whole of any individual Voronoi Cell the likelihood value of the model is set constant. The likelihood value is calculated using equation (3.10) with the GA models misfit values. The approximated PPD, also called neighbourhood approximation to the PPD, is defined as (Sambridge, 1999b)

$$P_{NA}(\mathbf{m}) = P(\mathbf{m}_i^{GA}) \tag{3.16}$$

where $\mathbf{m}_i^{GA}$ is the GA-sampled model in the input ensemble, which is closest to $\mathbf{m}$, a generic point in the multidimensional model space. Since the likelihood value of a model $\mathbf{m}_i$ is assigned to the whole of any individual Voronoi Cell, $P_{NA}(\mathbf{m})$ has a uniform probability inside that cell. The approximated PPD ($P_{NA}(\mathbf{m})$), thus, represents all the information gained from the input ensemble and can be used to compute the final PPD with the GS technique. Assuming an efficient exploration of the model space during the GA optimisation stage, $P_{NA}(\mathbf{m})$ can be considered as a rough approximation of the final PPD function $P(\mathbf{m})$ (Sambridge, 1999b; Aleardi and Mazzotti, 2017). So,

$$P_{NA}(\mathbf{m}) \approx P(\mathbf{m}). \tag{3.17}$$

The final PPD, consequently the Bayesian integrals, is then numerically evaluated by drawing a set of new MC samples in model space with a distribution asymptotically equivalent to $P_{NA}(\mathbf{m})$. This also means that $h(\mathbf{m}) \approx P_{NA}(\mathbf{m})$, which substituted in equation (3.14) leads to:

$$\hat{J}_{NA} = \frac{1}{\widetilde{N}} \sum_{k=1}^{\widetilde{N}} \Gamma(\widetilde{\mathbf{m}}_k) \tag{3.18}$$

where $\widetilde{\mathbf{m}}$ indicates the new set of $\widetilde{N}$ Monte Carlo models generated through the GS. In this form, Bayesian integrals become a simple average over the resampled ensemble.

3.5 GA performance on analytic objective functions

Before analysing the behaviour of seismic objective functions, a study of the performance of the GA+NA approach was carried out on analytical functions. The interest in the study of analytical functions lies in the fact they are assumed to have characteristics similar to the seismic objective functions. However, at a computational level, the resolution of the direct analytical problem is very much less expensive than the resolution of the corresponding seismic.

As a first test, the robustness of the GA algorithm with respect to a highly multimodal functional, such as the Rastrigin function, is evaluated. This test problem is also used to determine how the number of models impacts the convergence of the GA with respect to model space dimension (i.e., number of parameters). In a second test, a more simple function (the *peaks* function) was used to estimate the PPD through the NA approach.

3.5.1 The Rastrigin function

In a n-dimensional space, the Rastrigin function is defined by:

$$f(x_1, \ldots, x_n) = An + \sum_{i=1}^{n} \left[x_i^2 - A\cos(2\pi x_i)\right] \tag{3.19}$$

where $A = 10$, and $x_i \in [-5.12, 5.12]$.

This function is a typical example of a non-convex function, which contains a large number of local minima (increasing exponentially as 11^n in the range $[-5.12, 5.12]^n$), and a global minimum in $(0, \ldots, 0)$ with $f(0, \ldots, 0) = (0, \ldots, 0)$ (Sajeva et al., 2017). Figures 3.6(a) and 3.6(b) show the Rastrigin function with $n = 2$ in three dimensions, and as a 2D projection, respectively.

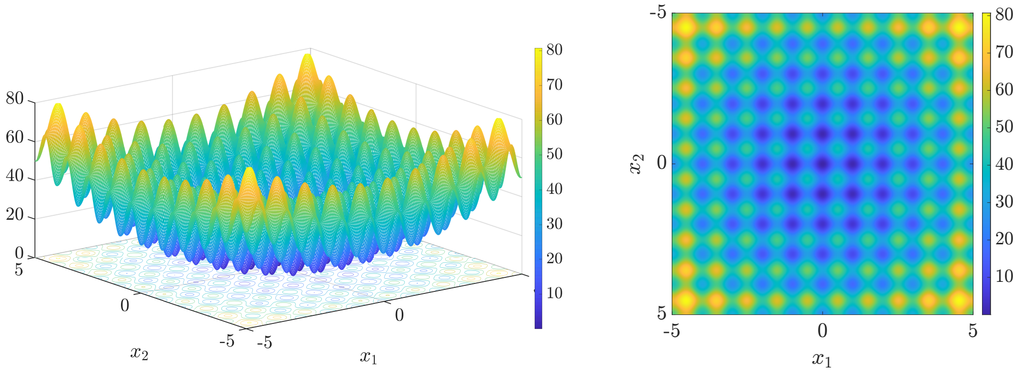

(a) (b)

Figure 3.6: Rastrigin function with $n = 2$, (a) as a three dimensional surface, and (b) as a 2D projection.

Due to its complexity, this function is often used as a performance test problem for global optimisation algorithms, since for a local optimisation method, such as the steepest descent or other gradient methods (see also Figure 1.3), is practically impossible to obtain a successful convergence to the global minimum (Dieterich and Hartke, 2012; Weise, 2009; Sajeva et al., 2017).

Optimisation Rastrigin function with $n = 2$

Figure 3.7 shows the evolution of the individuals to optimise the Rastrigin function with $n = 2$ from a random population of models (red dots) (Figure 3.7(a)). The GA parameters used in this test are listed in Table 3.1. With a high mutation ratio (70% of the models are mutated), and with no elitism operator, a wide exploration of the model space is obtained.

The wide exploration can be indirectly observed in Figure 3.7(f), where the average value (red line) of all models remains roughly stable between generation 10 and generation 70. It only converges to the optimum solution during the last generations

GA parameters	**Values**
Population size	500
Generations	100
Tournament size	2
Mutation ratio	0.7
b	2
d	0.3
Elitism	0

Table 3.1: GA inversion parameters for the optimisation of the Rastrigin function.

where the NUM operators constraint the search algorithm to explore the model space more locally. Figure 3.7(e) shows generation 100 where all models have converged to the global minimum.

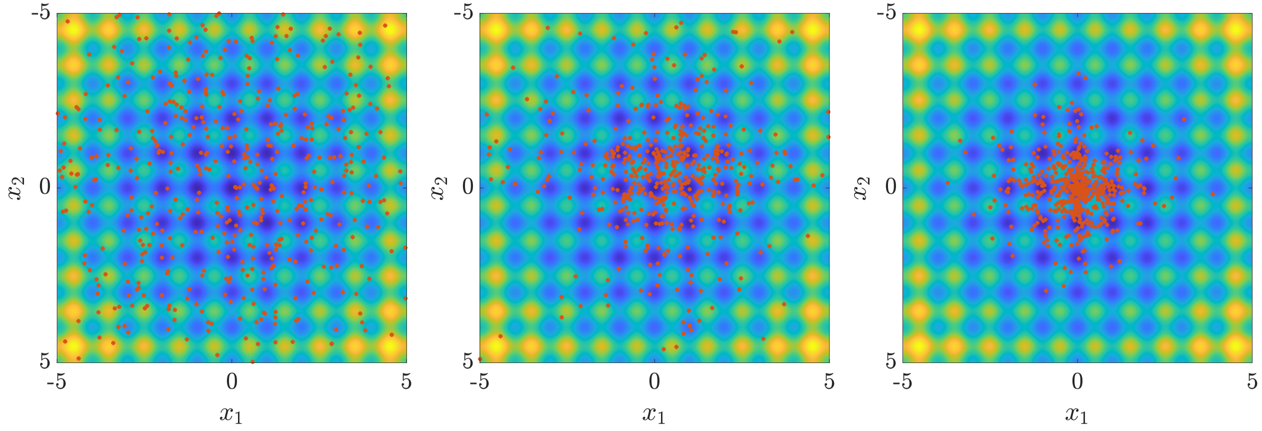

(a) Generation 1.

(b) Generation 15.

(c) Generation 66.

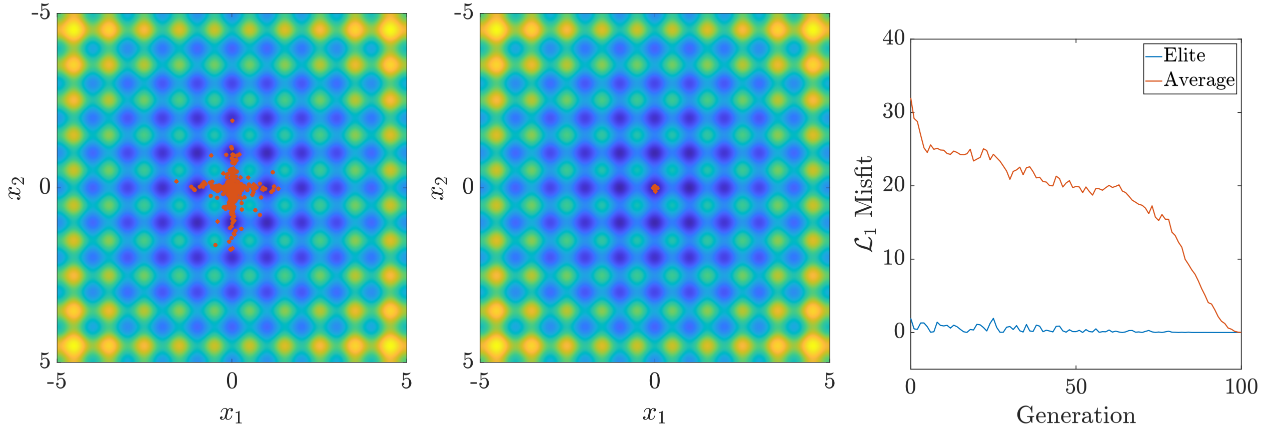

(d) Generation 87.

(e) Generation 100.

(f)

Figure 3.7: Evolution of the model population constituted by 500 individuals through 100 generations in order to minimise the Rastrigin function. Before converging to the global minimum in $f(0, 0) = 0$, the models explore the whole space without being trapped in one of the numerous local minima. This shows the robustness of a global optimisation technique such as the GA, to optimise a multi-modal functional. In (f) is shown how the data misfit evolves as function of GA generation.

Analysis of population size vs space dimension: constant space dimension

The previous section has shown a simple example of optimising a function (Rastrigin) of only two parameters. The potential of this algorithm has been highlighted, both for exploring the model space and searching for the best solution. But how does the correct convergence relate to the population size? Section 3.3.4 stressed the importance of this parameter, as well as that the optimum number of models is problem-dependent. Nevertheless, testing a highly multimodal function, such as the Rastrigin function, can be considered as a guide to set the population size for the next inversion experiments.

The tests are carried out using the same GA parameters of Table 3.1 except for the population size, which takes values of 10, 50, 200, 500. They correspond to a ratio R between the population size and the number of parameters inverted of $R = 5$, $R = 25$, $R = 100$, $R = 250$, respectively. For each population size the inversion is repeated 6 times. Figures 3.8(a)-3.8(d) show the evolution of the function value referred to the elite model with the generations and the population size.

Optimising the Rastrigin function using only 10 individuals ($R = 5$) (Figure 3.8(a)) leads to a convergence toward a local minimum for four out of six tests (purple line and green line represent successful optimisations). On the contrary, for population size of 50, 200, and 500 the GA algorithm successfully finds the global minimum in all six cases.

Analysing the value of the elite models, it can be observed there is no improvement between the case of 50 and 200 models, and a slight improvement if compared to 500. Therefore, the higher computational cost of evaluating the latter cases makes them not convenient and unnecessary. The ratio $R \geqslant 25$ results to be a good compromise between efficiency and computing time.

Analysis of population size vs space dimension: constant population size

Differently than the previous section where it was analysed the success of the optimisation of the Rastrigin function with $n = 2$ with respect of the population size, in this experiment the optimisation it is semi-quantitatively analysed by increasing the space

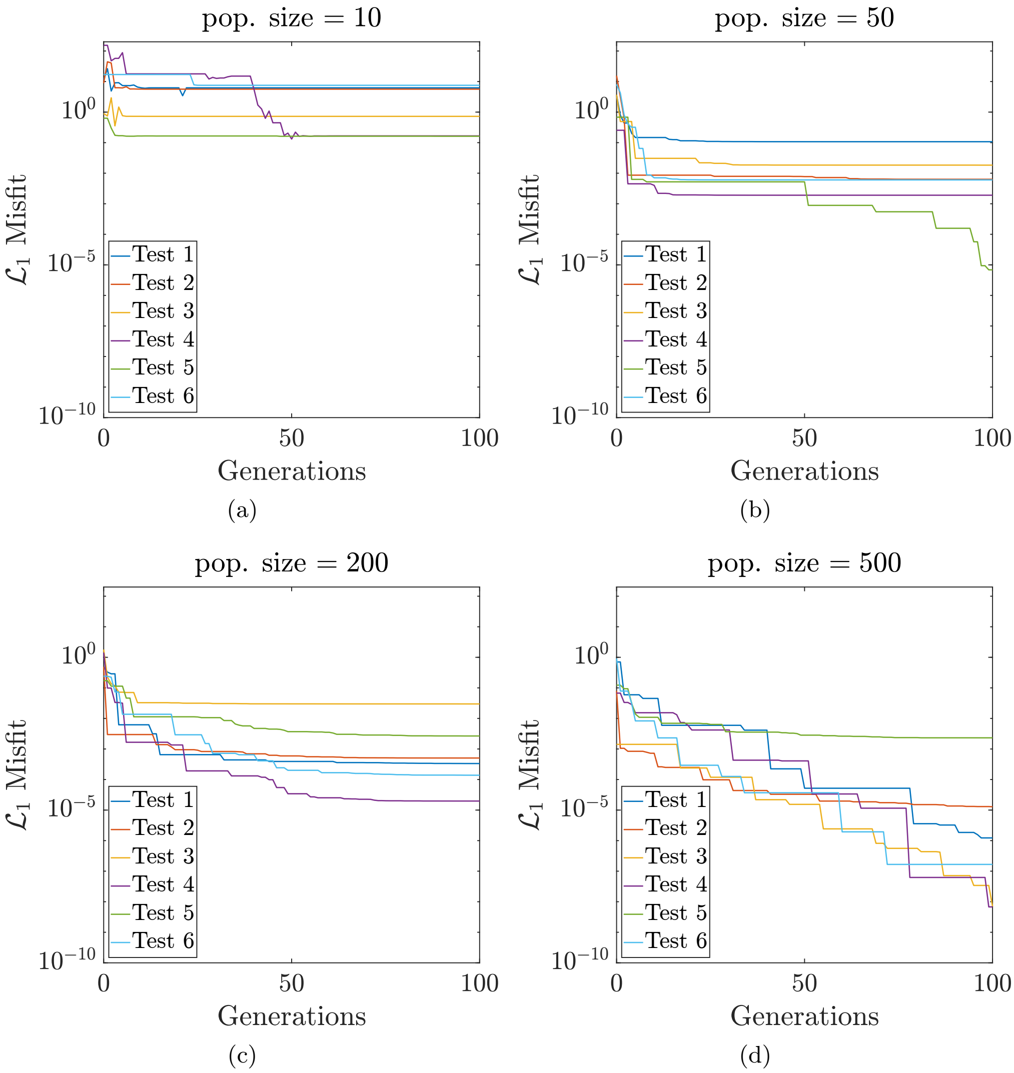

(a) (b) (c) (d)

Figure 3.8: Misfit evaluation for the same analytical function (Rastrigin function) in two dimensions ($n = 2$), but different population size. (a) population size of 10 models, (b) population size of 50 models, (c) population size of 200 models, and (d) population size of 500 models. For each population size, the inversion is repeated 6 times (Test 1 , ..., Test 6). For all cases with more than 50 individuals, the optimisation of the Rastrigin function is successful. Only with a population size of 10 individuals the minimisation of the function fails. Nevertheless, from 50 to 500 models there is not a huge improvement in the efficacy of the algorithm, however the computational cost is 10 times more if it is not done in parallel programming. $R \leq 25$ offers a good compromise between efficiency and computing time.

dimension of the Rastrigin function from $n = 5$ to $n = 50$ (equation 3.19), fixing the population size to 500. Therefore, the ratio R between the population size and model space dimension spans $R_{n=2} = 250$ to $R_{n=50} = 10$. In this case

The parameters used in the GA optimisation are listed in Table 3.1 (as the previous tests) for all model space dimensions analysed. The optimisation is repeated only once for each case.

Figure 3.9 shows the evolution of the $\mathcal{L}_1$-misfit as a function of the generation with respect to the dimension of the Rastrigin model space n. As expected the convergence rate decreases as the model space dimension increases, and the convergence to the global minimum is only attained in cases from $n = 5$ to $n = 20$, so up to $R_{n=20} = 25$. This result is consistent to that obtained in the previous section where $R \leq 25$ showed a good compromise between efficiency and running time.

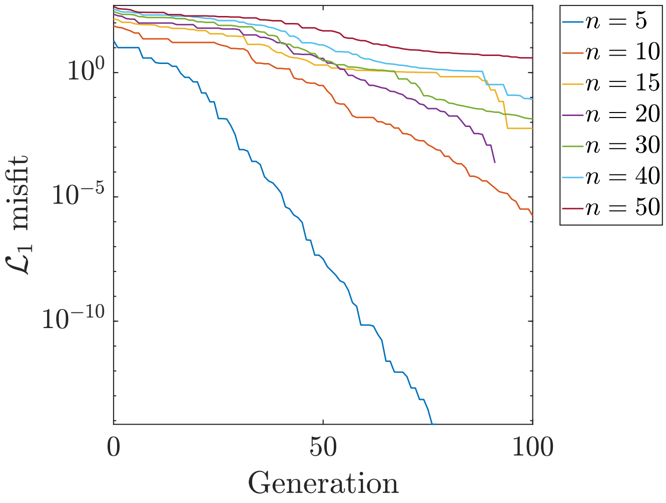

Figure 3.9: Data misfit as function of GA generation with respect to the dimension of the model space (number of model parameters). The population size remains constant at 500 individuals throughout the tests. The correct convergence to the optimum model is attained up to the model space dimension $n = 20$, therefore $R \leq 25$.

3.5.2 The *peaks* function

Peaks is a built-in MATLAB function of two variables obtained by translating and scaling Gaussian distributions, and defined by:

$$\begin{aligned} f(x_1, x_2) =& 3(1 - x_1)^2 e^{-x_1^2 - (x_2+1)^2} \\ & - 10 \left(\frac{x_1}{5} - x_1^3 - x_2^5 \right) e^{-(x_1^2 + x_2^2)} \\ & - \frac{1}{3} e^{-(x_1+1)^2 - x_2^2}. \end{aligned} \tag{3.20}$$

It is a simple function, which contains only one local minimum in $(x_1^{(l)}, x_2^{(l)}) = (-1.3473, 0.2045)$, and one global minimum in $(x_1^{(g)}, x_2^{(g)}) = (0.2283, -1.6255)$ with

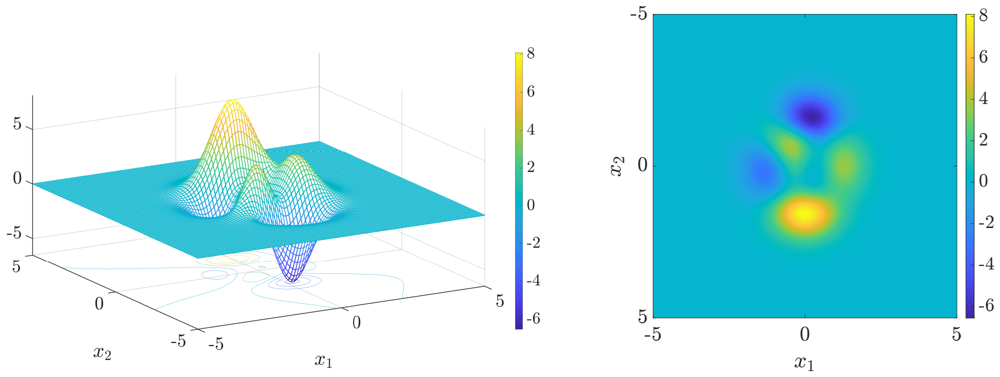

(a) (b)

Figure 3.10: *Peaks* function defined in equation (3.20) as a three dimension surface in (a), and as a 2D projection in (b).

$f(x_1^{(g)}, x_2^{(g)}) = -6.5511$ as illustrated in Figure 3.10(a). The *peaks* function is used to evaluate the convergence of the GA algorithm, and to assess the NAB approach for sampling the related PPD function. Table 3.2 summarises the control parameters of the GA algorithm utilised for optimising the peaks function.

GA parameters	**Values**
Model population size	300
Generations	30
Tournament size	2
Mutation ratio	0.4
b	2
d	0.3
Elitism	0

Table 3.2: GA control parameters used in the optimisation of the peaks function.

The $\mathcal{L}_1$-norm $= |f(x_1^{GA}, x_2^{GA})| - |f(x_1^{(g)}, x_2^{(g)})|$ is utilised to quantify the misfit between the peak function evaluated at the GA model's coordinates (x_1^{GA}, x_2^{GA}) and the global minimum. Figure 3.11 shows how the best and the average values of the misfit (blue and red line, respectively) evolve with the generations. The convergence is accurately reached by all employed models by the 30th generation.

Using the whole ensemble of models (equivalent to $300 \times 31 = 9300$ models) as shown in Figure 3.12(a), the marginal PPDs for both variables (x_1 and x_2) are calculated (Figure 3.12(c)). As expected, the exploration of the GA algorithm is focused on the

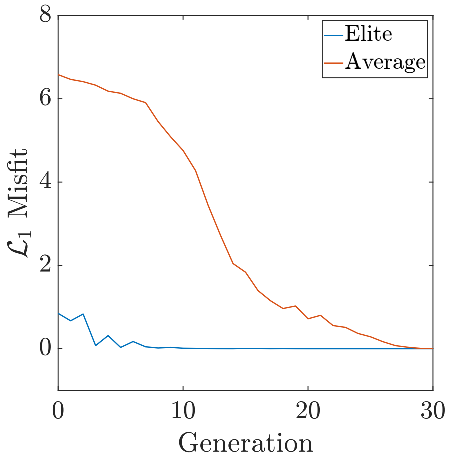

Figure 3.11: Misfit evolution with GA generation for the *peaks* function.

upper left corner where the two valleys are located, and in turn, the Voronoi cells, which divide the entire model space explored by GA, are much denser where the global minimum is placed. Finally, the marginal PPD, which is a projection of the joint PPD to a given parameter axis and obtained by integrating out all the other parameters (equation (3.13)), is correctly characterised as displayed in Figure 3.12(c).

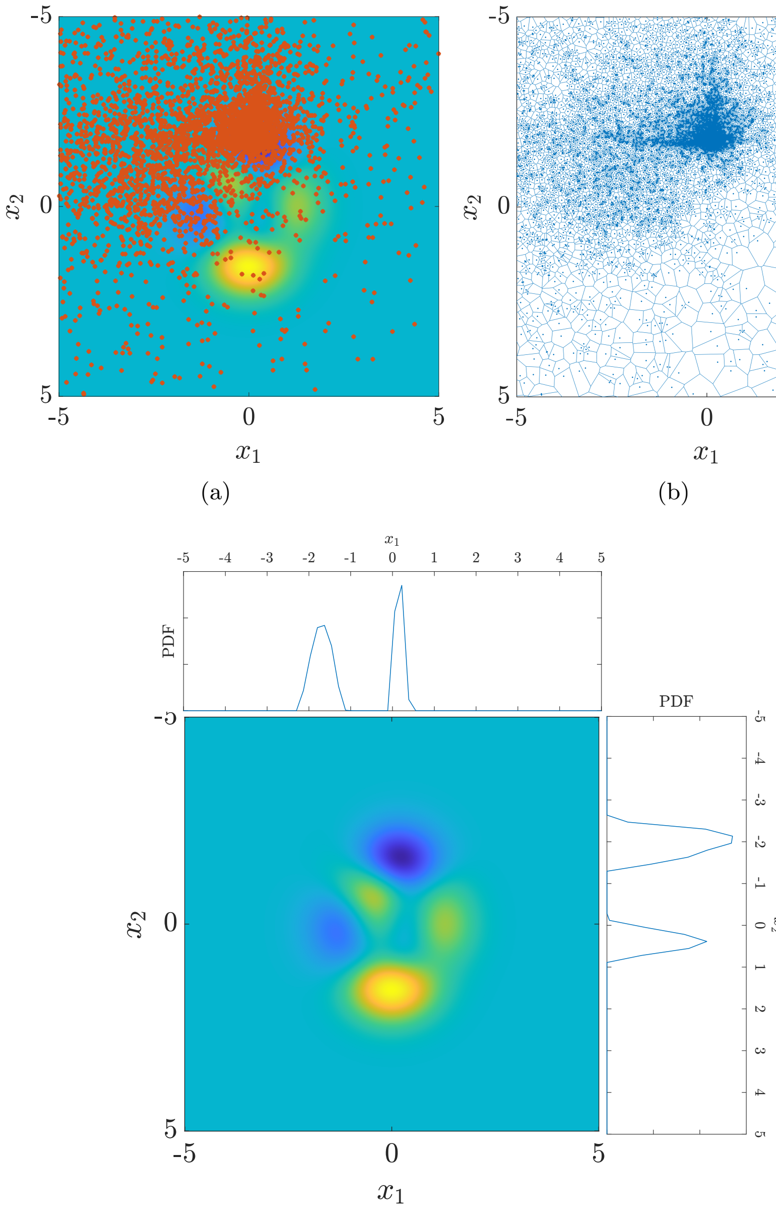

(a) (b) (c)

Figure 3.12: (a) The 9300 models (red dots) sampled during the genetic algorithm optimisation. This represents the whole GA model ensemble generated throughout the generations. The majority of the models explore the top left portion of the space, due to the presence of two minima: a global and a local minimum. (b) The model space explored during the genetic algorithm step is divided into Voronoi cells, and the fitness associated with each model is assigned to the whole cell. This builds an interpolant (in this case a 2D interpolant) of the search space. The Neighbourhood Algorithm step approximates the posterior probability distribution, and using the Gibbs Sampler method it estimates the PPD of each variable. (c) displays the 1D marginal distributions for the variable x_1 and x_2, which show a good degree of correlation with the two minima.

3.6 GA-FWFI to characterise fracture properties: a synthetic case

Elastic wave measurements such as seismic, sonic or ultrasonic data can be an efficient tool for non-invasive detection and characterisation of physical properties of fractures (Liu and Martinez, 2012). The presence of fractures causes attenuation and delay of the seismic waves when they propagate through the medium. Analysing the group travel time (equation 2.4) as well as the amplitudes of transmitted and reflected waves, can lead to an estimate of the specific stiffness of the fractures (Pyrak-Nolte et al., 1990a). The magnitude of the transmission coefficient for a wave propagating across a set of N parallel fractures at the normal incidence is $|T|^N$, where $|T|$ is the transmission coefficient due to a single interface. $|T|$ is dependent on the specific stiffness of the interface and the frequency of the propagating wave (Pyrak-Nolte et al., 1990a; Pyrak-Nolte et al., 1990b) and the effective group time delay for oblique incidence for the same medium with N parallel fractures can be determined from (Pyrak-Nolte et al., 1990a)

$$t_{eff} = \frac{L}{U}\cos(\theta) + Nt_g \tag{3.21}$$

where L is the total path length normal to the fracture planes, U is the group velocity in intact rock, θ the incidence angle, and t_g is the time delay caused by a single fracture (equation 2.4). Assumptions are made to simplify the model such as ignoring the multiple reflections, fracture spacing, and considering a uniform stress state. Hildyard (2007) addressed the limitation of assuming homogeneous stress distribution and showed that it is an important factor to take into account in wave propagation.

Such an analytical approach is therefore only applicable in simple cases. Furthermore, this approach does not provide an estimate of model parameter uncertainties as well as equally likely possible multiple solutions. The data-driven approach presented here, such as GA-FWFI, alleviates these limitations by proposing a more automated method that takes into account the entire wavefield to characterise explicitly mechanical properties of fractures and estimates the PPD function of the model parameters analysed.

Here, the GA-FWFI was applied to quantify the fracture-specific stiffnesses (both normal and shear stiffness) of each fracture in a set of parallel discontinuities, their spatial location and the background material properties. The focus was on inverting transmitted and reflected waves mimicking ultrasonic laboratory experiments on a 2-D isotropic and homogeneous sample containing 5 parallel fractures orthogonal to the wave propagation. Hence, the so-called *observed data* was generated by using known material and fracture properties through WAVE3D, whereas the inverse problem was solved by estimating the fracture specific stiffnesses $\kappa_{n,s}$ of each fracture, their location, and the P-wave of the background medium, by best-fitting the observed data. In the inverse process WAVE3D was used to generate the so called *modelled data*.

3.6.1 Synthetic 2-D sample with 5 vertical fractures

The two-dimensional synthetic square sample has side length of 14.7 cm, and contains 5 parallel and equidistant fractures (Figure 3.13). The fractures cut the sample vertically from one side to the other. The fracture spacing is 1.5 cm and the fracture length 14.7 cm. They are located at 2.9 cm, 4.4 cm, 5.9 cm, 7.4 cm, and 8.9 cm from the source location, corresponding to the sample's left side.

The host medium is purely isotropic and homogeneous, with material density of $\rho = 1560$ kg/m^3, P-wave velocity $v_p = 3230$ m/s, and S-wave velocity $v_s = 1910$ m/s. The material properties are equal to the gypsum elastic properties in the experiments of Hedayat (2013) and Hedayat et al. (2014b), discussed in Chapter 5.

In order to minimise spurious reflections and boundary effects, the model edges were shifted further away from the interest zone and the absorbing boundary conditions were applied. In Figure 3.13 the actual synthetic sample is represented by the dashed red line. Here it is also illustrated the acquisition geometry which is composed of one single P-wave source on the left of the block (red star) and three lines of continuous receivers with an offset of 0.1 cm, placed around the block represented by the blue triangles. They record the dilatational components of stress given by $\bar{\sigma} = \frac{\sigma_1 + \sigma_2}{2}$.

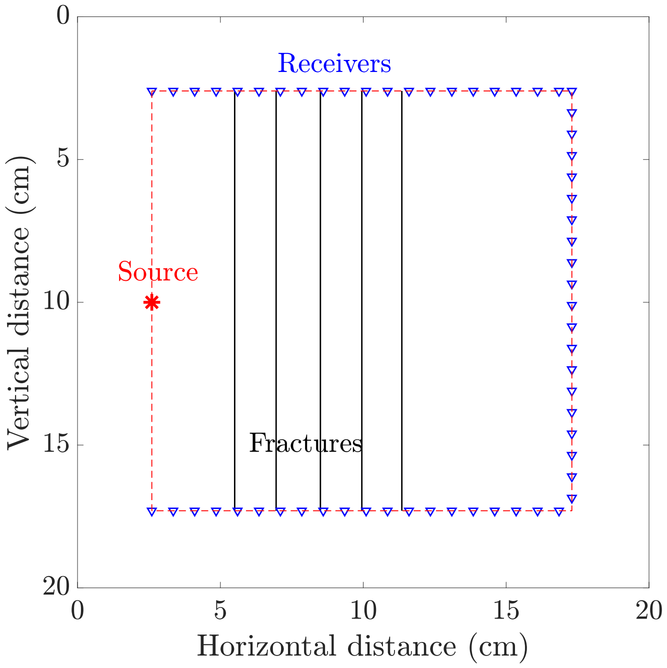

Figure 3.13: Fractured model used to compute the observed data (Figure 3.15) and the snapshots displayed in Figure 3.14. See the text for the elastic properties of the background material, and the mechanical properties of the fractures. The red star is the source, the blue triangles the receivers, and the dashed red line represents the simulated sample edges.

The medium is discretised in space through a regular grid of 400 × 400 elements. The source signature is a Ricker wavelet with a peak frequency of 0.5 MHz. To generate minimal numerical dispersion and ensure the numerical stability of WAVE3D everywhere in the medium, the grid spacing is set to $dx = dy = 5 \cdot 10^{-4}$ m (= 0.5 mm), and the time-step to $dt = 5 \cdot 10^{-8}$ s (= 50 ns). The dominant compressional wavelength is thus $\lambda_p = 6.5 \cdot 10^{-3}$ m which roughly corresponds to 0.43 times the fracture spacing, while the dominant shear wavelength is $\lambda_s = 3.8 \cdot 10^{-3}$ m corresponding to 0.25 times the fracture spacing. The normal fracture stiffness is $\kappa_n = 7 \cdot 10^{12}$ Pa/m, identical for all discontinuities, as well as the shear specific stiffness which is fixed to $\kappa_s = \kappa_n/2 = 3.5 \cdot 10^{12}$ Pa/m for all fractures.

Some snapshots of the seismic wave propagation through this medium at $t_1 = 10$ μs, $t_2 = 20$ μs, $t_3 = 30$ μs, $t_4 = 40$ μs, $t_5 = 50$ μs, $t_6 = 60$ μs can be visualised in Figures 3.14(a)-3.14(f), respectively. Figures 3.15(a)-3.15(b) show the observed data recorded by the top, right, and bottom receivers lines, respectively.

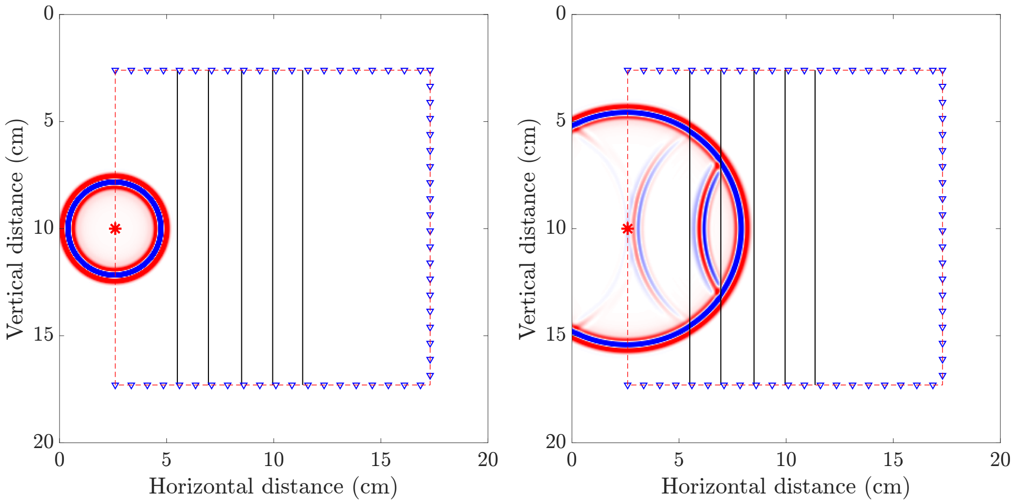

(a) Snapshot at $t_1 = 10\ \mu$s.

(b) Snapshot at $t_2 = 20\ \mu$s.

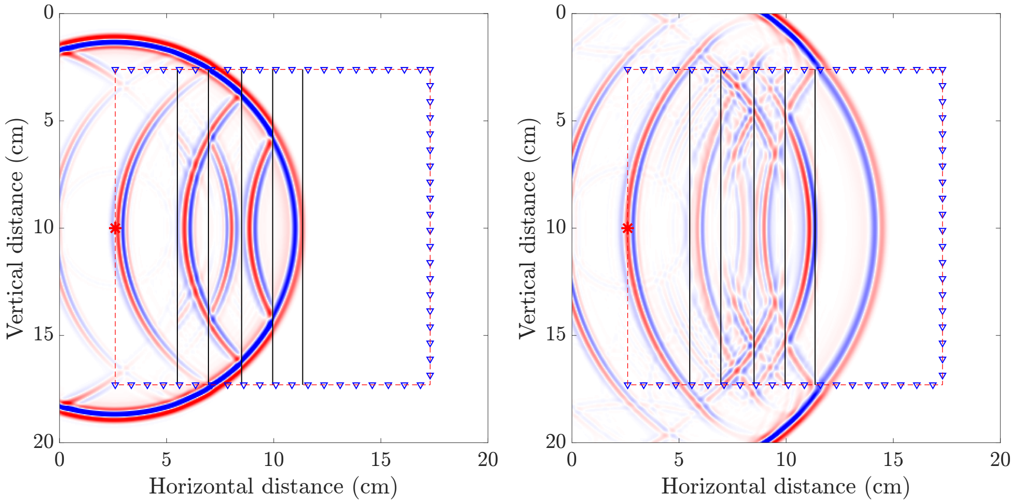

(c) Snapshot at $t_3 = 30\ \mu$s.

(d) Snapshot at $t_4 = 40\ \mu$s.

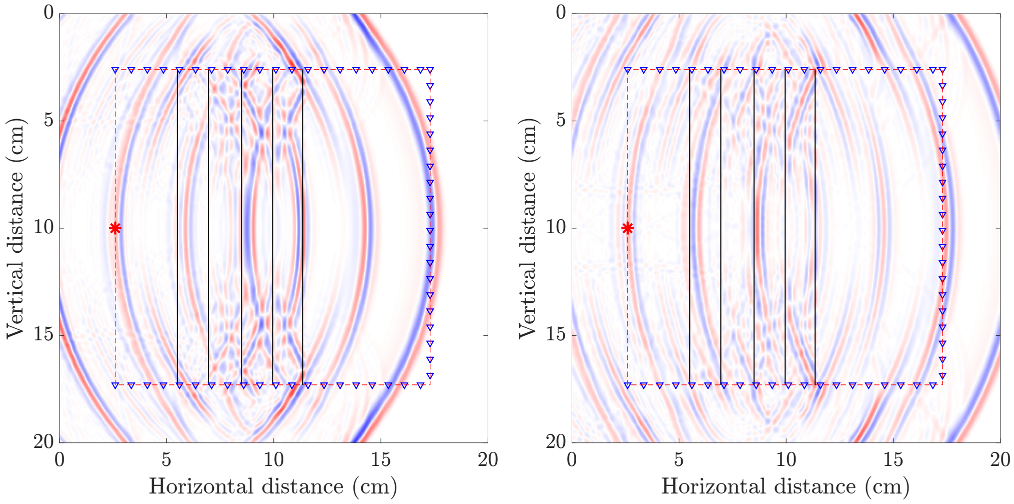

(e) Snapshot at $t_5 = 50\ \mu$s.

(f) Snapshot at $t_6 = 60\ \mu$s.

Figure 3.14: Wavefield snapshots taken at six different time steps which propagate through the fractured medium containing 5 parallel fractures. It represents the isotropic component of stress $\widetilde{\sigma}$.

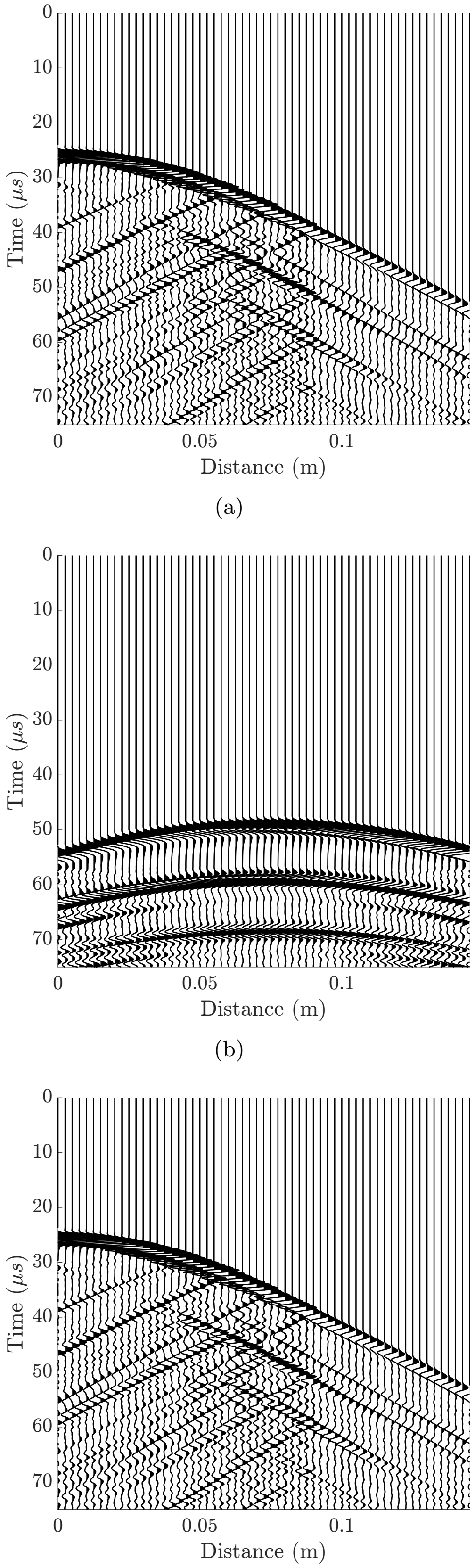

(a)

(b)

(c)

Figure 3.15: From top to bottom, seismograms related to the top, right and bottom receiver lines of Figure 3.13, respectively. The traces show the isotropic component of stress $\widetilde{\sigma}$.

3.6.2 GA-FWFI results

The GA-FWFI stochastic inversion approach was applied to estimate the specific stiffnesses (both κ_n and κ_s) of the 5 fractures simultaneously (so 10 mechanical parameters in total), as well as their spatial location along the $x-$axis, and the P-wave velocity of the background material. Consequently, the model representation, following equation (3.3), becomes

$$\mathbf{model}_j = \begin{pmatrix} \text{fracture}_1 \\ \text{fracture}_2 \\ \text{fracture}_3 \\ \text{fracture}_4 \\ \text{fracture}_5 \\ v_p \end{pmatrix}_j = \begin{pmatrix} \kappa_{n,1},\ \kappa_{s,1},\ x_1 \\ \kappa_{n,2},\ \kappa_{s,2},\ x_2 \\ \kappa_{n,3},\ \kappa_{s,3},\ x_3 \\ \kappa_{n,4},\ \kappa_{s,4},\ x_4 \\ \kappa_{n,5},\ \kappa_{s,5},\ x_5 \\ v_p \end{pmatrix}_j \tag{3.22}$$

where x_i represents the coordinate of the $i-$th fracture along the $x-$axis. The total number of inverted parameters is 16.

The ranges of the search space, for each model parameter inverted, are listed in Table 3.3, where the boundaries for the fracture specific stiffnesses κ_n and κ_s are equal for all fractures. The source signature is assumed known, as well as the density, and S-wave background velocity. To avoid intersection between fractures in the modelling (WAVE3D does not support fracture intersection), the GA search bounds for the fracture locations do not overlap. This is also the reason why the number of fractures in the inversion is kept fixed.

The control parameters used in the GA inversion are summarised in Table 3.4. The observed data were inverted without any post-processing; however in order to have an overall amplitude balancing, appropriate weights were applied to the waveforms of the three receiver lines, the same for both observed and modelled data.

The evolution of the elite and average normalised misfits as function of the GA generation is illustrated in Figure 3.16. The inversion's convergence is gradual, although it seems to stabilise after 40 generations.

Model parameter	Range	Unit
Normal specific stiffness of the discontinuity (κ_n)	$[1 \cdot 10^{12}, 5 \cdot 10^{13}]$	Pa m^{-1}
Shear specific stiffness of the discontinuity (κ_s)	$[5 \cdot 10^{11}, 2.5 \cdot 10^{13}]$	Pa m^{-1}
Background P-wave velocity (v_p)	$[3000, 3400]$	m s^{-1}
Fracture location along x	$x_1 \in [2.5,\ 3.3]$	cm
	$x_2 \in [4.0,\ 4.8]$	cm
	$x_3 \in [5.5,\ 6.3]$	cm
	$x_4 \in [7.0,\ 7.8]$	cm
	$x_5 \in [8.5,\ 9.3]$	cm

Table 3.3: Free parameters in the inversion with their search boundaries.

GA parameters	Values
Population	400
Generations	50
Tournament size	3
Mutation ratio	0.4
b	2
d	0.3
Elitism	0.05

Table 3.4: GA inversion parameters used for optimising the objective function in the case of 5 parallel fractures.

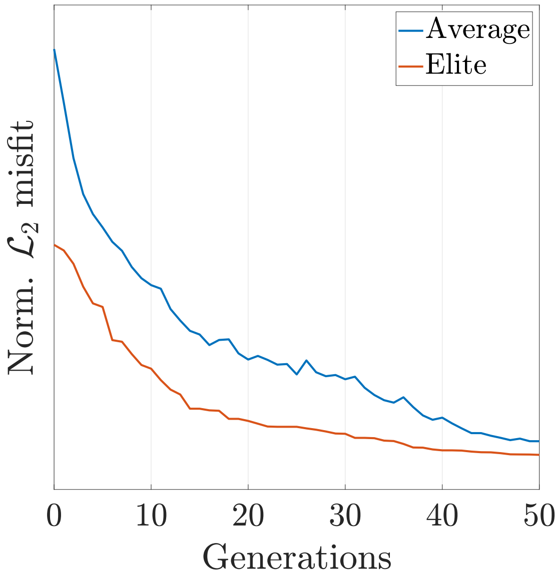

Figure 3.16: Normalised data misfit as a function of GA generation. The blue and red lines represent the average and elite misfits for the population, respectively. The misfit at the last generation corresponds to the optimum model parameters listed in Table 3.5.

The model parameters obtained from the inversion, displayed in Table 3.5, resemble with high accuracy the true values used for generating the observed data. As it can be observed, the location of all fractures match exactly the true locations, as well as the background compressional velocity.

	κ_n^{GA} (κ_n^{true}) (Pa/m)	κ_s^{GA} (κ_n^{true}) (Pa/m)	x location (true) (cm)	v_p (true) (m/s)
Frac. 1	$7.4 \cdot 10^{12}$ $(7.0 \cdot 10^{12})$	$3.3 \cdot 10^{12}$ $(3.5 \cdot 10^{12})$	2.900 (2.90)	3229.3 (3230.0)
Frac. 2	$7.1 \cdot 10^{12}$ $(7.0 \cdot 10^{12})$	$3.6 \cdot 10^{12}$ $(3.5 \cdot 10^{12})$	4.40 (4.40)	
Frac. 3	$7.3 \cdot 10^{12}$ $(7.0 \cdot 10^{12})$	$3.3 \cdot 10^{12}$ $(3.5 \cdot 10^{12})$	5.90 (5.90)	
Frac. 4	$7.6 \cdot 10^{12}$ $(7.0 \cdot 10^{12})$	$3.6 \cdot 10^{12}$ $(3.5 \cdot 10^{12})$	7.40 (7.40)	
Frac. 5	$7.1 \cdot 10^{12}$ $(7.0 \cdot 10^{12})$	$2.2 \cdot 10^{12}$ $(3.5 \cdot 10^{12})$	8.90 (8.90)	

Table 3.5: Optimum GA model as defined in equation (3.22). The true model parameter values, utilised to generate the observed data, are stated in parentheses. The fracture location on the x-axis is referred to the distance between the source location and fractures.

The success of the inversion can be also recognised by the good match between the observed and the modelled data, for the three receiver lines, in Figures 3.17(a), 3.17(c), and 3.17(e). Their corresponding difference is shown in Figures 3.17(b), 3.17(d), and 3.17(f), respectively. The ratio between the maximum amplitude of the observed data and the corresponding difference is around 15 times for top and bottom receivers, and around 8 times for the receivers on the right.

The posterior probability distributions for each inverted parameter, as computed by Bayesian integration through NA-Bayes, are plotted in Figure 3.18. Here the prior probability distribution is set to be uniform within the parameter space boundaries, assuming that all parameters in the parameter space are equally likely but also being careful to avoid impossible solutions (e.g. dividing by zero, negative fracture stiffness values). Nevertheless, the uniform prior has little impact on the posterior distribution because it makes minimal assumptions about the model. The marginal distributions show that all parameters are well constrained by the inversion, except for the shear specific stiffness κ_s related to the fracture 5 (the furthest fracture from the source), where the optimum model results are underestimated with respect to the ground truth model by a factor of about 1.6. The shear specific fracture stiffness is sensitive to the shear waves so in this case, because the source is dilatational and the 'recorded traces' are the isotropic stress, then the data include compressional waves converted to S-waves and then reconverted to P. Therefore, the offset between expected and inverted value may be due to a lack of converted waves at that discontinuity.

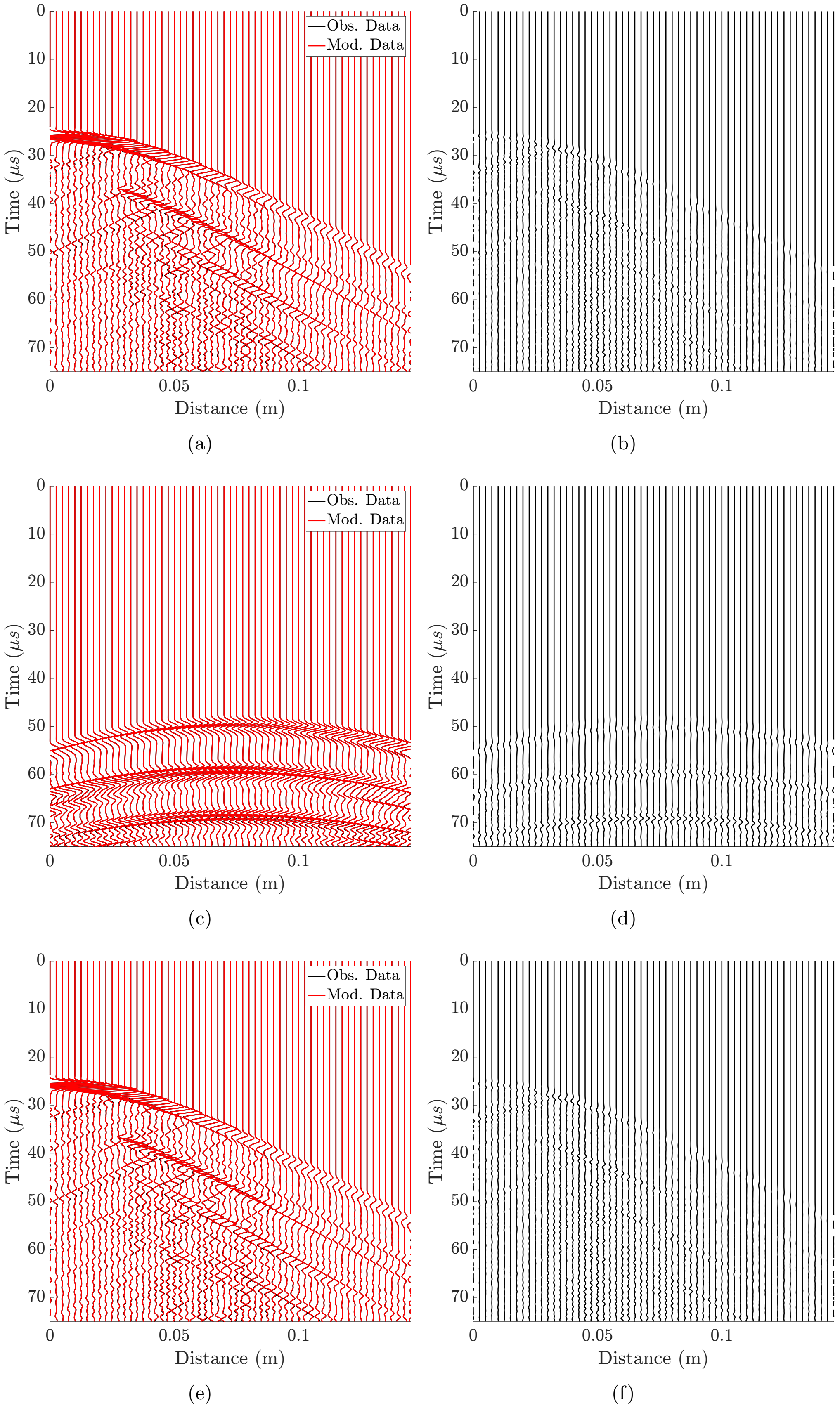

(a) (b) (c) (d) (e) (f)

Figure 3.17: In (a), (c), and (e) comparison between the observed (black) and modelled data (red) for the top, right, and bottom line of receivers, respectively. The corresponding difference between these two datasets is shown in (b), (d), and (f), respectively. The amplitude of the difference is around 15 times smaller than the observed data in case (a) and (e), around 8 times in case (c).

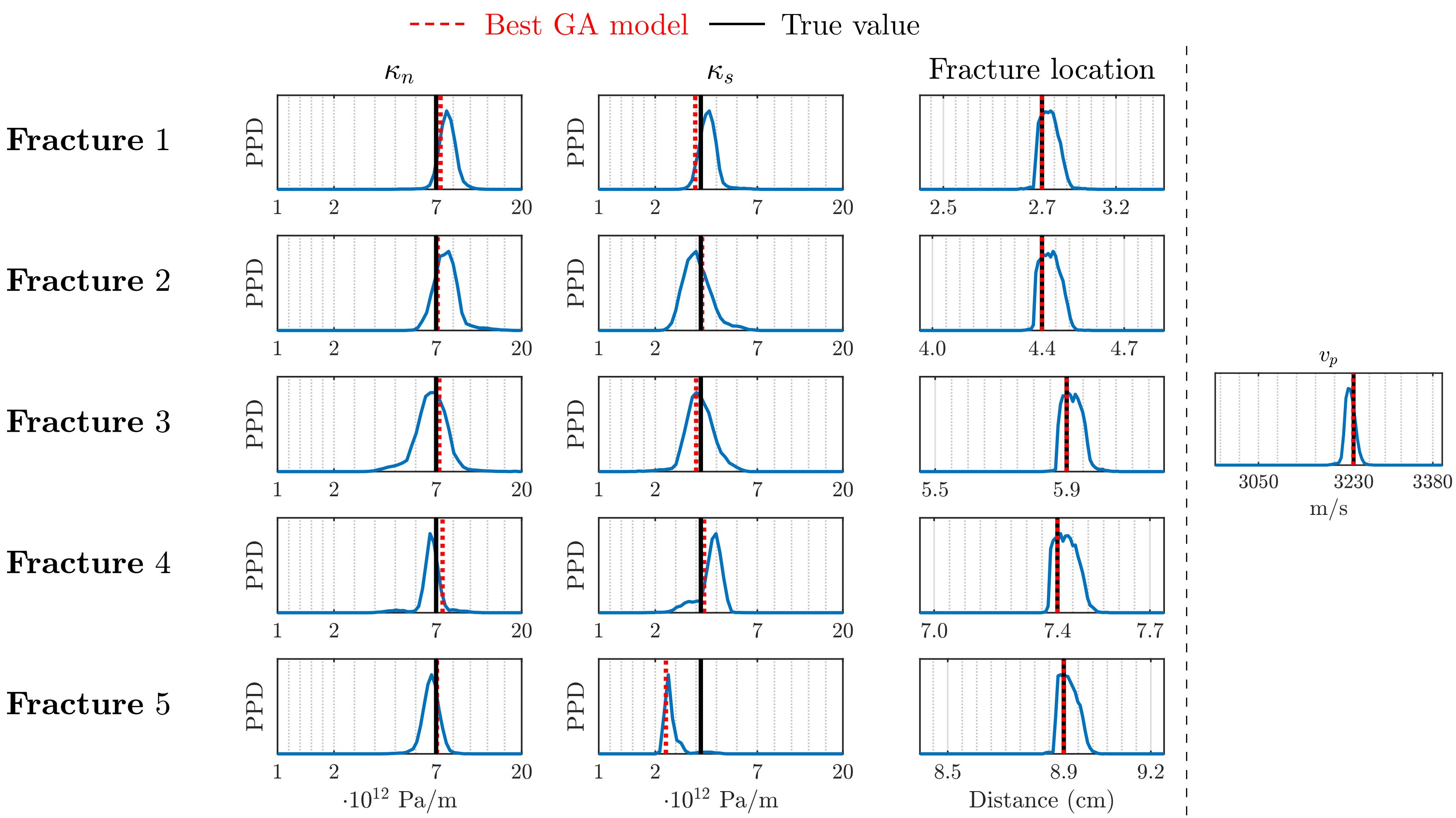

Figure 3.18: Normalised marginal PPD functions estimated through the NA-Bayes method by using the models sampled during the GA optimisation (blue curve). The continuous black line represents the the true model parameter, while the dashed red line the elite model predicted by the GA inversion.

3.7 Summary and Discussion

Characterising mechanical properties of discrete fractures along with their spatial distribution is of primary importance in applications such as stability investigations and rock damage, CO_2 sequestration, geothermal energy exploration, nuclear waste monitoring and hydrocarbon recovery. Analytical equations can be used to estimate such properties by measuring the group time delay (equation (3.21)), or the variation of the seismic amplitude. Nevertheless, the theoretical assumptions behind the equations limit their applicability to relatively simple fracture models. Moreover, such analytical approaches require extensive manual processing of the data and they do not take into account possible scenarios which could be equally likely. For these pathological cases, numerical strategies need to be employed.

The stochastic approach GA-FWFI+NA, developed exclusively by the author and presented in Section 3.3, overcomes these limitations. The proposed global waveform inversion technique employs the GA method in the optimisation step and embeds WAVE3D to solve the direct problem to infer the stiffness of individual fractures, their location and the background medium velocity simultaneously by best-fitting the observed data (Section 3.6). Hence, this provides a potential alternative to local approaches for multi-parameter inversion within the framework of FWI. In fact, unlike the local optimisation techniques (e.g. conventional FWI) which exploit only a restricted region of the model space, a global inversion method (such as GA) avoids the calculation of the first- and second-order derivatives and the optimisation strategy is less dependent on the initial models. Moreover, the models generated by this method can be used to appraise the ensembles through NAB in order to estimate the posterior probability distributions in model space.

A limitation of the GA-FWFI lies in the extremely high computational cost of the optimisation step. This makes it impractical, at present, for large scale data or problems in high-dimensional spaces; such a phenomenon is also known as the *curse of dimensionality* (Sambridge and Mosegaard, 2002; Fichtner, 2010). For this reason, the choice of the GA control parameters is paramount for thoroughly exploring the model space and at the same time having a reasonable model population size, or in other words, a good balance between computational feasibility and correct convergence towards the optimum model.

The robustness of the algorithm and the appraisal stage have been tested in Section 3.5 by processing a highly multi-modal analytical function (the Rastrigin function) and the *peaks* function. For the more complex Rastrigin function the relation between the population size and the correct convergence to the elite model was also analysed. Although finding an optimal population size is not a trivial task due to its problem-dependent nature, such analyses helped to evaluate how the algorithm behaves in optimising such a complicated multi-modal function designing the subsequent implementation in fracture inversion experiments. These tests have highlighted that a population size 25 times the space dimension ($R \approx 25$) gives a good compromise between efficiency and computing time. This value was then used to set the size of the model population (400 models for 16 parameters) in the waveform inversion case in Section 3.6. In this synthetic experiment a two-dimensional square sample, containing 5 parallel and equidistant fractures, was characterised by inverting transmitted and reflected compressional waves mimicking an ultrasonic laboratory experiment. Here, the specific stiffnesses (normal and shear) of each fracture, their location along the x-axis, and the background velocity were estimated by only means of seismic waves. The fractures cut the sample vertically and they are orthogonal to the wave propagation. The *observed data* was generated by using known material and fracture properties through WAVE3D. The model parameters obtained from the GA inversion have shown a very high degree of accuracy with respect to the true values used for generating the observed data. The PPD functions have also shown that all parameters are well constrained by the inversion and they do not exhibit cross-talk. The only parameter which was underestimated by the inversion was the shear specific stiffness of the fracture 5 (the furthest fracture from the source). This could be due to the scarce presence of converted waves caused by that fracture from the compressional source that weakly constrains the shear specific stiffness.

The application of the GA-FWFI work-flow on real laboratory datasets (3D inversion) in order to characterise a single discontinuity during a shearing experiment is presented in Chapter 4.

Chapter 4

GA-FWFI of active ultrasonic measurements

4.1 Preamble

This chapter investigates the suitability of the global inversion scheme GA-FWFI for a series of laboratory active ultrasonic measurements. The laboratory experiments (Hedayat, 2013; Hedayat et al., 2014a; Hedayat et al., 2014b) were carried out with the primary objective of investigating the mechanical and geophysical processes that occur during shear failure of rock joints by analysing the amplitude variation of pulses transmitted through and reflected off the discontinuities.

The raw seismograms were processed and analysed by the author following the analytical procedure showed in Hedayat (2013) and Hedayat et al. (2014b). Successively, the GA-FWFI method was applied Here, the variation of the mechanical properties of the discontinuity, along with the elastic parameters of the rock specimen, was estimated by taking into account the entire seismic waveforms. The objectives of this chapter are two-fold. First, it seeks to show whether inferences from this novel approach resembles with a good accuracy those from the conventional approaches. These laboratory experiments provide an excellent test-bed of this inversion scheme on real waveforms due to the reduced number of unknowns of the problem. Second, it aims to develop a robust and flexible approach to be applied in less constrained processes such as cases with variation of seismic velocities, or unknown distribution of the discontinuities.

4.2 Laboratory experiment

In order to investigate the slip process along a frictional discontinuity, a series of direct shear experiments was performed on gypsum specimens by (Hedayat, 2013; Hedayat et al., 2014a; Hedayat et al., 2014b). During the shearing process the joint was monitored using both compressional and shear waves.

4.2.1 Specimen characteristics

The specimen was composed of two prismatic blocks with perfectly mated contact surfaces. The final dimensions of each block were 152.4 mm long, 127 mm wide, and 25.4 mm thick. The gypsum material is isotropic and homogeneous (Hedayat, 2013) with measured material properties summarised in Table 4.1.

The contact surfaces consisted of two areas of equal size with distinct frictional characteristics: a smooth area with low frictional strength ($\mu \sim 0.7$) on the lower half, and a rough area with high frictional strength ($\mu \sim 1.2$) on the upper half. The sides of the specimen were polished to obtain flat, smooth, and perfectly planar surfaces to avoid any stress concentrations, to enable uniform compression loading along the fracture surface, and to apply shear stresses parallel to the discontinuity.

Properties	**Values**
Density	1560 kg/m^3
Average P-wave velocity	3230 m/s
Average S-wave velocity	1910 m/s
Unconfined Compressive Strength (UCS)	36 MPa
Young's modulus	6 GPa
Poisson's ratio	0.15

Table 4.1: Material properties of the gypsum specimen.

4.2.2 Experimental setup

Figure 4.1(a) shows the experimental setup which consists of a flatjack, loading platens that encase the specimen and sensors, steel rods, and plates. A biaxial compression apparatus, consisting of two independent loading frames, was used to apply both normal and shear stresses to the contact surface between the two gypsum blocks (Figure 4.1(a)). The normal stress of $1 - 4$ MPa, perpendicular to the fracture plane, was supplied by a horizontal loading frame, and a standard loading machine was used to apply the shear stress at a constant shearing rate of 8 μm/s. The average vertical displacement of the specimen was recorded by two linear variable differential transformers (LVDT), while the shear load was applied by a cell in the loading machine. To minimise the vertical friction and ensure that the vertical load was directly transferred to the interface between the gypsum blocks, a series of steel balls (rollers) was placed between the loading platen and the steel plate (Figure 4.1(b)).

During the shearing process a data acquisition system enabled the measurements of transmitted and reflected full waveforms to monitor continuously the shear failure along the joint. This was carried out by using two arrays placed facing each other and in contact with two opposite faces of a sample as shown schematically in Figure 4.1(b). Each array involves thirteen broadband piezoelectric transducers, housed in specially designed load platens. Six of these sensors (2P, 4P, 5P, 6P, 11P, 13P) were P-wave transducers, while seven were S-wave transducers polarised parallel to the direction of shear (1S, 3S, 7S, 8S, 9S, 10S, 12S). Figure 4.1(c) shows their layout (mirrored arrangement) along with the polarisation direction of S-wave transducers that was used for seismic measurements. The transducers were broadband with a central frequency of 1MHz (Panametrics V103-RM for P-waves and V153-RM for S-waves). Two pulser-receivers (Panametrics 5077PR), one in transmission mode and one in reflection mode, were used to generate square wave pulses with a repetition rate of 5 kHz, amplitude of 100 V and a gain of +10 dB. A sampling rate of 20 Million samples/sec (0.05 μs per point) was used to record full waveforms in real time. Although the transducers can either work as sources or as receivers, only normal incident waveforms were recorded.

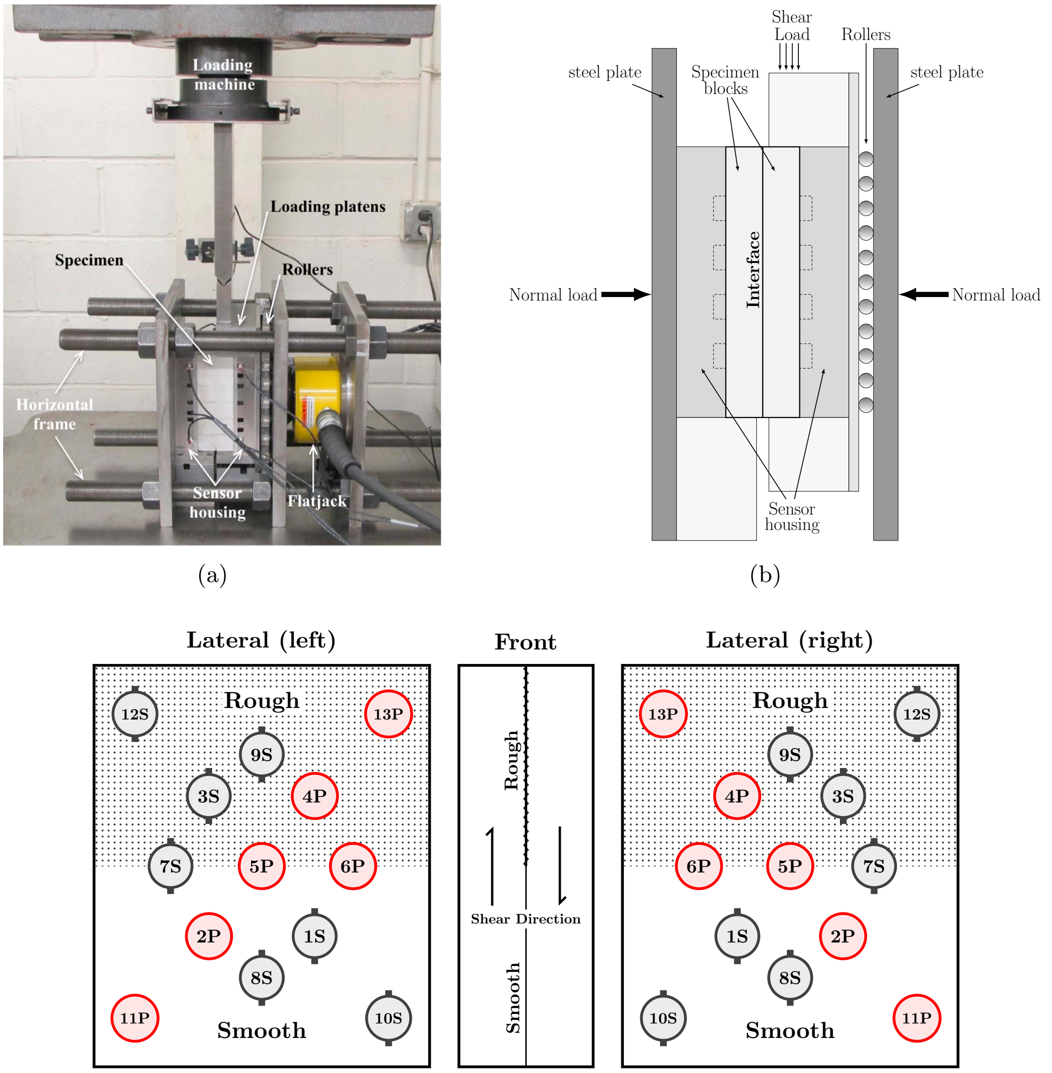

(a) (b)

(c)

Figure 4.1: (a) Photo of the biaxial compression apparatus (Hedayat et al., 2014b), and its schematic setup (b) (adapted from (Hedayat et al., 2014a)). (c) Transducer layouts. The vertical segments indicate the polarisation direction of the S-wave transducers (adapted from (Hedayat et al., 2014a)).

Therefore, only the mirrored source-receiver pairs (e.g. 1S-1S, 2P-2P, etcetera) were consecutively activated to record the waveforms. To increase the signal-to-noise ratio the signals were averaged over 30 measurements for each transducer.

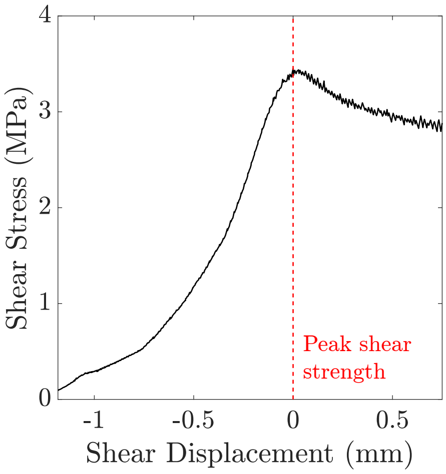

Figure 4.2: Shear stress-displacement curve for the non-homogeneous specimen.

4.2.3 Experimental results - seismic ultrasonic monitoring of shear failure

Figure 4.2 displays the shear stress versus shear displacement for the gypsum specimen at a normal stress of 2.3 MPa. It can be noted that after the initial seating deformation of the specimen, from -1.20 mm to -0.75 mm of shear displacement, the shear stress increased rapidly with shear displacement until it reached the peak shear strength of the discontinuity (red dashed curve). The shear displacement values are referenced with respect to the displacement at which the peak shear stress (shear failure) occurred. Therefore, negative values of shear displacement define the status before the failure occurs.

Figure 4.3 shows a comparison of representative transmitted (Figure 4.3(a)-4.3(d)) and reflected (Figure 4.3(e)-4.3(h)) raw waveforms at two shear displacement values ($\Delta u_z = -0.81$ mm, and $\Delta u_z = -0.25$ mm). They represent the compressional transducer pairs such as the 2P-2P (Figure 4.3(a), and 4.3(e)) and the 4P-4P (Figure 4.3(b), and 4.3(f)), and shear transducer pairs 8S-8S (Figure 4.3(c), and 4.3(g)) and 9S-9S (Figure 4.3(d), and 4.3(h)).

As the shear displacement evolves with respect to the shear stress applied, seismic waveforms change accordingly. Figure 4.4 shows the variation of the transmitted and reflected amplitude with the shear displacement for all P-wave (4.4(a), 4.4(b)) and S-

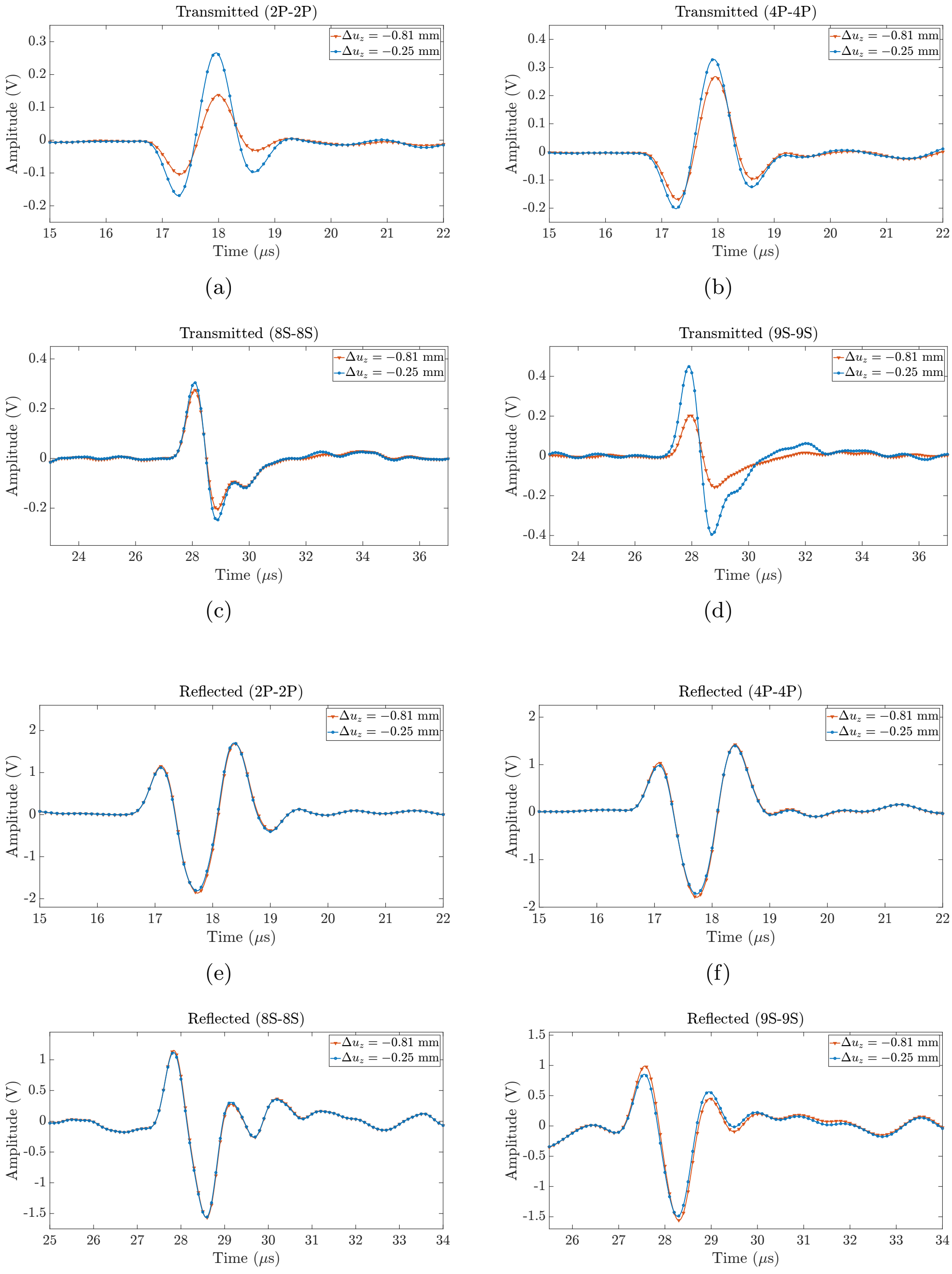

(a) (b) (c) (d) (e) (f) (g) (h)

Figure 4.3: Comparison of representative raw waveforms at two shear displacement values ($\Delta u_z = -0.81$ mm, and $\Delta u_z = -0.25$ mm). (a) Transmitted compressional waves of the transducer pair 2P-2P. (b) Transmitted compressional waves of the transducer pair 4P-4P. (c) Transmitted shear waves of the transducer pair 8S-8S. (d) Transmitted shear waves of the transducer pair 9s-9S. (a) Reflected compressional waves of the transducer pair 2P-2P. (b) Reflected compressional waves of the transducer pair 4P-4P. (c) Reflected shear waves of the transducer pair 8S-8S. (d) Reflected shear waves of the transducer pair 9S-9S.

wave transducers (4.4(c), 4.4(d)). For a better comparison, the peak-to-peak amplitude values were normalised with respect to their initial values before the shearing. The variability in amplitude transmission and reflection across the specimen, with respect to shear displacement, is significantly affected by the surface roughness that changes the local contact area as well as the stress concentration.

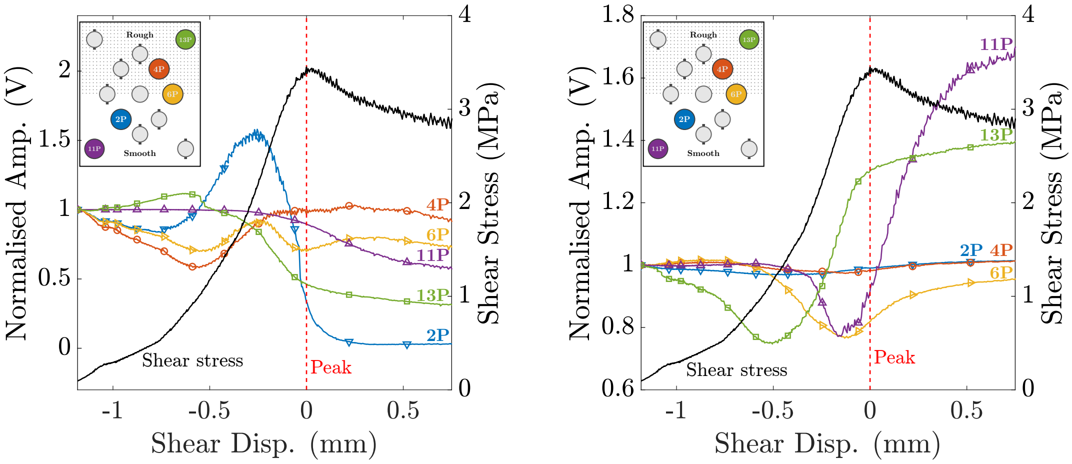

(a) Compressional transducers. Normalised amplitude for the transmitted waves.

(b) Compressional transducers. Normalised amplitude for the reflected waves.

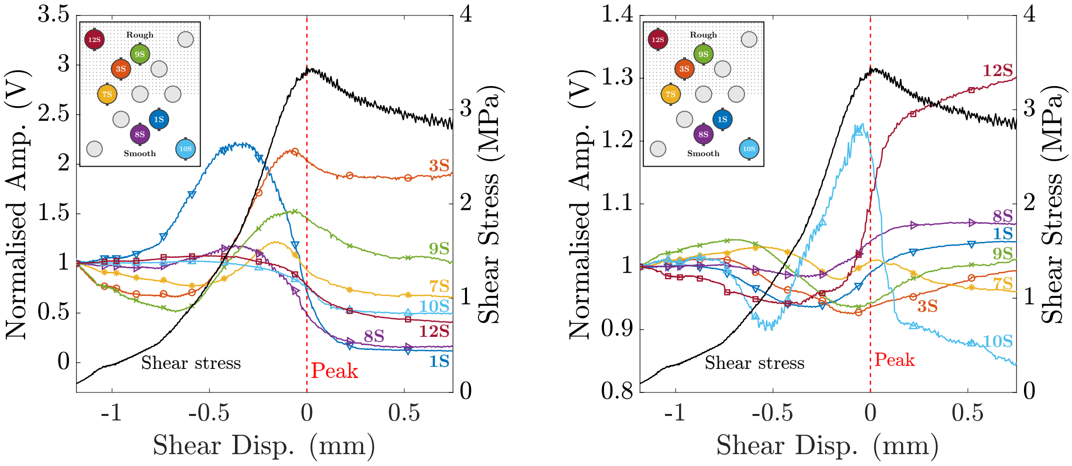

(c) Shear transducers. Normalised amplitude for the transmitted waves.

(d) Shear transducers. Normalised amplitude for the reflected waves.

Figure 4.4: Variation of the normalised shear and compressional amplitudes, for both reflected and transmitted waves, as function of the shear stress applied to the sample.

Because compressional wave transducers are sensitive to the change in interface's normal stiffness and shear wave transducers are sensitive to the shear stiffness of the interface, the analysis carried out in this section focuses on the effect of shearing on the waveforms recorded by the compressional transducer pair 2P-2P (Figure 4.5) and by the shear transducer pair 8S-8S (Figure 4.6).

Compressional waveforms: transducer pair 2P-2P

Twelve compressional full waveform measurements (six in transmission and six in reflection), collected by the transducers 2P-2P during the direct shear experiment, were extracted at six shear displacement measures: -1.15 mm, -0.81 mm, -0.50 mm, -0.25 mm, -0.08 mm, 0.07 mm (Figures 4.5(c), 4.5(d)). These values sample the peak-to-peak amplitude curves of the seismic traces at the main events (Figures 4.5(a), 4.5(b)): initial values, troughs, peaks, just before and just after the shear failure. Their corresponding amplitude spectra are shown in Figures 4.5(c), 4.5(d).

The amplitude of the transmitted compressional waves increased as the shear load was transferred to the specimen (Figure 4.5(a)). A distinct peak in the transmitted wave amplitude occurred prior to the peak shear strength and it was identified as an ultrasonic precursor indicating the imminent shear failure of the discontinuity (Hedayat et al., 2014b). The maximum in amplitude was followed by a steep drop as slip occurred due to the reduction of the joint's normal specific stiffness induced by a damage and loss of contact at the interface.

Conversely, the amplitude of the reflected compressional waves (Figure 4.5(b)) followed the opposite trend of the transmitted waves, although the change is small relative to the amplitude. The amplitude of the reflected signals decreased as the shear load was transferred to the contact surface reaching a minimum value prior the shear slip occurred and then increasing after failure. The minimum in the amplitude of the reflected waves corresponded to the maximum of the amplitude of the transmitted waves. This is also clearly observed in the amplitude spectra in Figure 4.5(e), where the shear displacement $\Delta u_z = -0.25$ mm has amplitude greater than the other measurements in the entire frequency band (purple curve). Conversely, the minimum energy is contained in the transmitted waves at shear displacement $\Delta u_z = 0.07$ mm (light blue curve). Since the difference in amplitude between the reflected waves is very little (Figure 4.5(d)), this also reflects in a minimum difference in the amplitude spectra too (Figure 4.5(f)).

Shear waveforms: transducer pair 8S-8S

The main features observed and described for the compressional transducer pair 2P-2P (Figure 4.5), were also observed for the shear transducer pair 8S-8S (Figure 4.6). A distinct maximum in the transmitted wave amplitude was likewise detected: in this case at the shear displacement $\Delta_z = -0.35$ mm, (Figure 4.6(a)), also visible in the time and frequency domain in Figure 4.6(c) and Figure 4.6(e), respectively.

The minimum in the peak-to-peak amplitude plot (Figure 4.6(b)) was detected and corresponds to the maximum of the transmitted wave (Figure 4.6(a)). This can be also observed both in Figure 4.6(d) (recorded reflected waveforms) and in Figure 4.6(f) (corresponding amplitude spectra). This is a clear indication of a change in the discontinuity's shear stiffness.

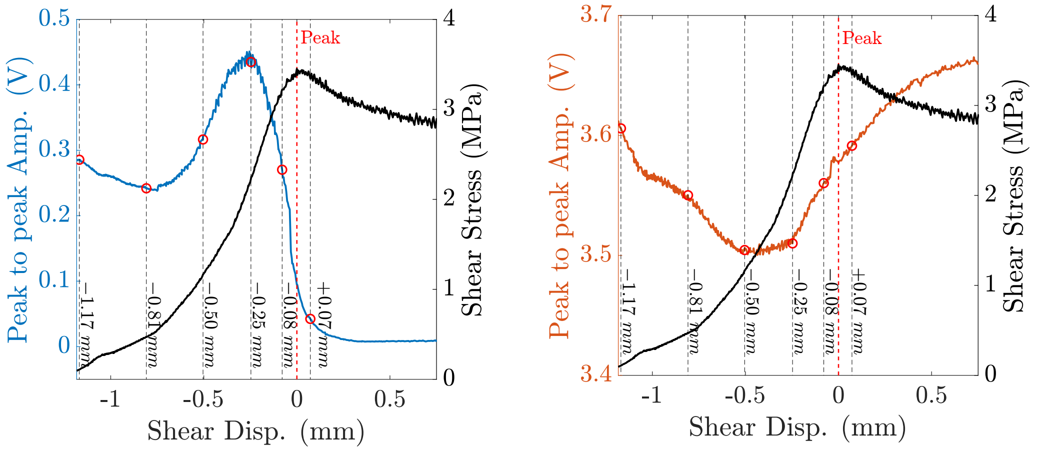

(a) Shear stress displacement and compressional peak-to-peak amplitude of transmitted waves using transducer pair 2P-2P.

(b) Shear stress displacement and compressional peak-to-peak amplitude of reflected waves using transducer pair 2P-2P.

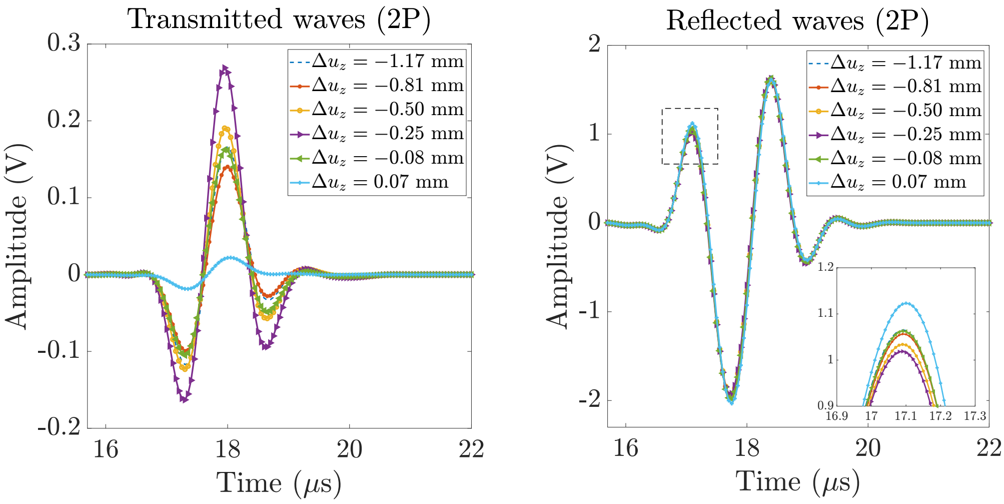

(c) Transmitted compressional wave (2P-2P).

(d) Reflected compressional wave (2P-2P).

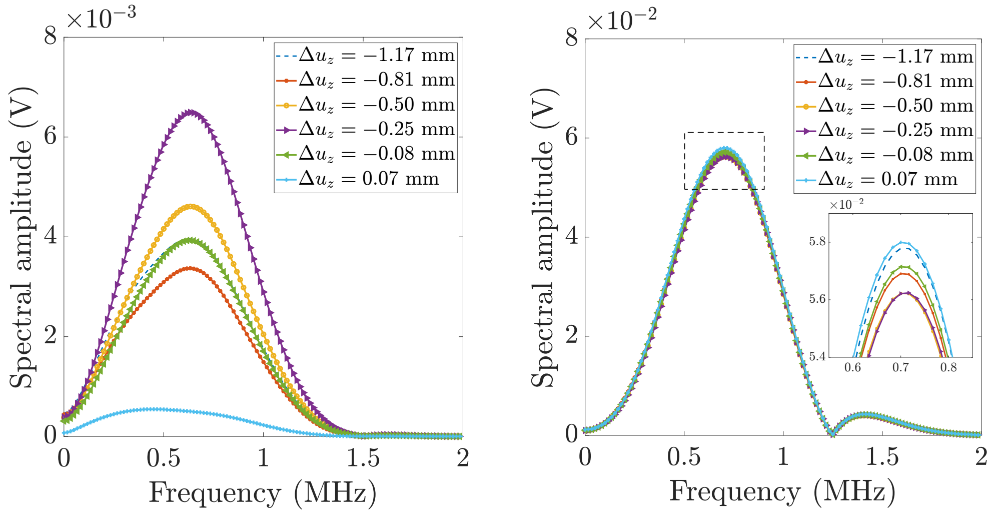

(e) Transmitted compressional wave spectra (2P-2P).

(f) Reflected compressional wave spectra (2P-2P).

Figure 4.5: The figures on the left column, (a), (c), and (e), show the variation of the transmitted wave peak-to-peak amplitude as function of the shear displacement, the transmitted waveforms, and the corresponding frequency amplitude spectra for the transducer pair 2P-2P, respectively. The figures on the right column, (b), (d), and (f), are referred to the reflected waves of the transducer pair 2P-2P.

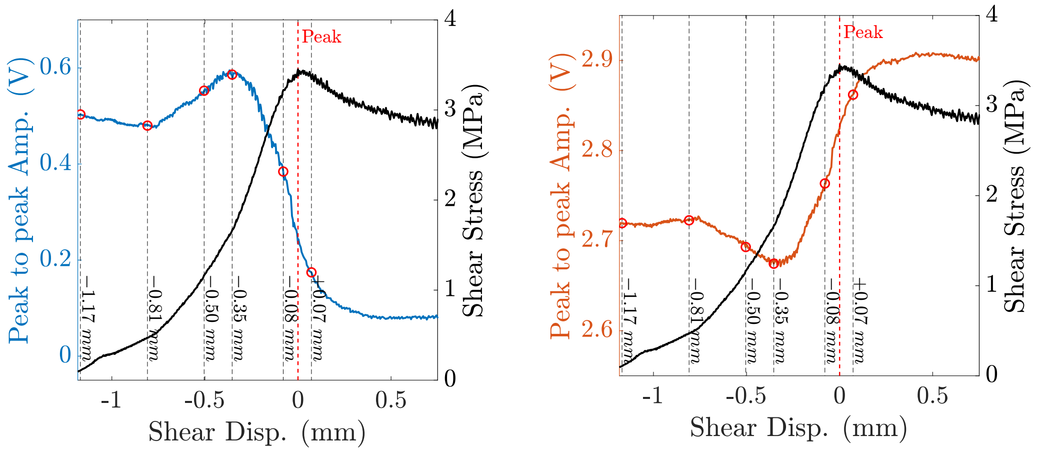

(a) Shear stress displacement and shear peak-to-peak amplitude of transmitted waves using transducer pair 8S-8S.

(b) Shear stress displacement and shear peak-to-peak amplitude of reflected waves using transducer pair 8S-8S.

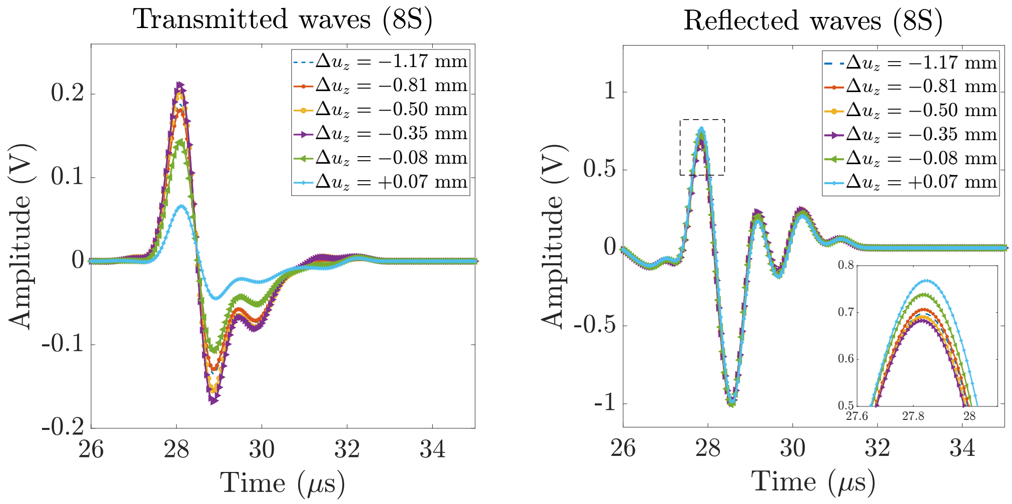

(c) Transmitted shear waves (8S-8S).

(d) Reflected shear waves (8S-8S).

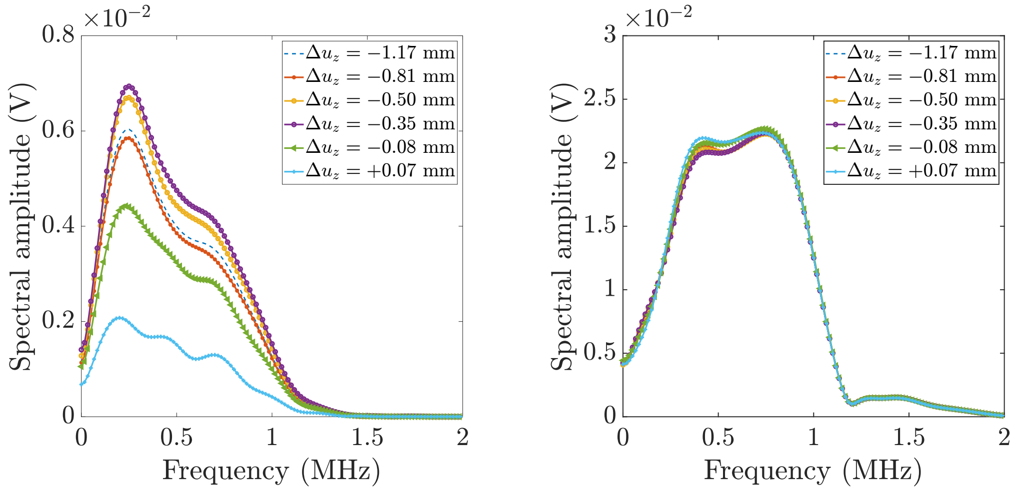

(e) Transmitted shear wave spectra (8S-8S).

(f) Variation of shear fracture stiffness with shear displacement for the 8S-8S pair transducers.

Figure 4.6: The figures on the left column, (a), (c), and (e), show the variation of the transmitted wave peak-to-peak amplitude as function of the shear displacement, the transmitted waveforms, and the corresponding frequency amplitude spectra for the transducer pair 8S-8S, respectively. The figures on the right column, (b), (d), and (f), are referred to the reflected waves of the transducer pair 8S-8S.

4.2.4 Computation of fracture stiffness

The seismic response of a fracture can be theoretically evaluated using the displacement discontinuity model (Schoenberg, 1980; Schoenberg, 1983; Pyrak-Nolte et al., 1990b; Pyrak-Nolte, 1996). Changes in the amplitude of transmitted and reflected waves are associated with changes in the specific stiffnesses (normal or tangential) of the discontinuity. For waves propagated at normal incidence the latter are calculated from the following equations (Hedayat et al., 2014b; Choi et al., 2014):

$$\kappa_n(\omega, \Delta u_z) = \frac{\omega \rho v_p}{2} \left| \frac{T_P(\omega, \Delta u_z)}{R_P(\omega, \Delta u_z)} \right|, \tag{4.1}$$

$$\kappa_s(\omega, \Delta u_z) = \frac{\omega \rho v_s}{2} \left| \frac{T_S(\omega, \Delta u_z)}{R_S(\omega, \Delta u_z)} \right|, \tag{4.2}$$

where κ_n and κ_s are the normal and shear stiffness of the joint, respectively, ρ the gypsum density, v_p and v_s the gypsum compressional and shear wave velocity, respectively, Δu_z the shear displacement, and ω the angular frequency. The subscripts $_P$ and $_S$ are referred to the P- and S-wave amplitude, respectively.

The variation of normal and shear fracture stiffness during the direct shear experiment, calculated using equation (4.1) and (4.2), is illustrated in Figure 4.7(a) (transducer pair 2P-2P) and Figure 4.7(c) (transducer pair 8S-8S). Due to the frequency-dependent nature of specific stiffness (Pyrak-Nolte and Nolte, 1992), the blue and black curve correspond to the maximum and minimum value of fracture stiffness within the frequency band $0.4 - 1$ MHz as shown in Figure 4.7(b) and Figure 4.7(d). As observed in the amplitude trends, the fracture specific stiffnesses showed a gradual increase with shear stress until they reach a maximum preceding the shear failure (the precursor), after which a sharp drop followed.

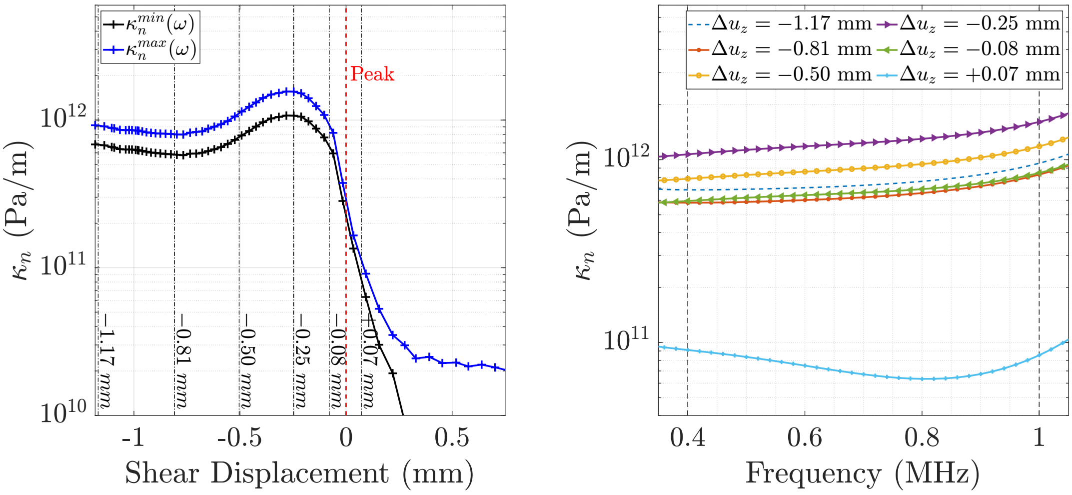

(a) Variation of normal fracture stiffness during the direct shear experiment for the transducers pair 2P-2P.

(b) Variation of normal fracture stiffness with frequency for the transducers pair 2P-2P at the selected shear displacement values.

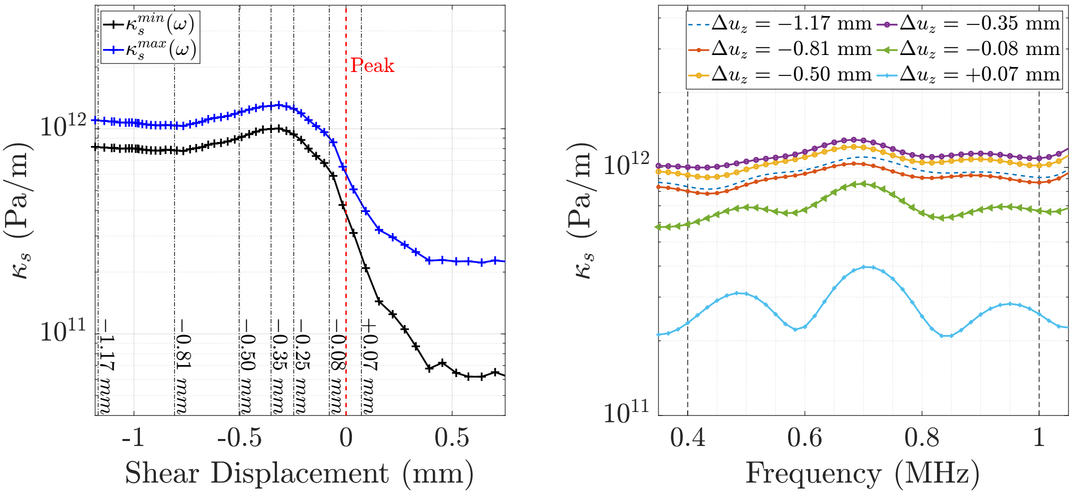

(c) Variation of shear fracture stiffness during the direct shear experiment for the transducers pair 8S-8S.

(d) Variation of shear fracture stiffness with frequency for the transducers pair 8S-8S at the selected shear displacement values.

Figure 4.7: Comparison between the variation of the normal in (a) and shear specific fracture stiffness in (c) for the transducers pair 2P-2P and 8S-8S, respectively. The blue and black curves correspond to the maximum and minimum values of the fracture stiffnesses in the frequency interval [0.4, 1] MHz, as shown in (b) and (d).

4.3 Application of GA-FWFI to the laboratory waveforms

4.3.1 Estimation of the source wavelet

In the experiment an excitation signal (a voltage pulse) is applied to a transducer to generate a stress wave which propagated through the gypsum specimen. The transmitted waves ($o_{exp}(t)$), recorded by the receiver on the opposite side, represent a signal which combines the effect of the transducers and the effect of the sample material upon the input pulse. In mathematical terms this translates in the convolution operation between the input pulse shape $i_{exp}(t)$ and the system transfer function $h(t)$ (or Green's function likewise), as (e.g. Claerbout (1976))

$$\underbrace{o_{exp}(t)}_{\text{output}} = \overbrace{i_{exp}(t)}^{\text{input}} * \underbrace{h(t)}_{\substack{\text{transfer}\\\text{function}}} \quad . \tag{4.3}$$

To decouple these effects, the shape of the input pulses (both compressional and shear wave sources) needed to be estimated numerically from the control experiment (intact gypsum specimen). Then, these inverted sources were applied to the fractured models. The estimation of the experimental source function is, in fact, the first step needed to model the laboratory waveforms successfully. Figure 4.8 illustrates the procedure followed. The control experiment was modelled in three dimensions, through WAVE3D, using a test input source $i_{mod}(t)$ (Figure 4.8(c)) which propagated in a material with the same elastic parameters of the gypsum sample. The modelled response $o_{mod}(t)$ (Figure 4.8(d)) to the input $i_{mod}(t)$ can be expressed by the relation

$$o_{mod}(t) = i_{mod}(t) * h(t). \tag{4.4}$$

It was assumed that the modelled system transfer function was equivalent to the experiment transfer function.

Taking the Fourier transform ($\mathcal{F}(\cdot)$) of equations (4.3) and (4.4), and rearranging with respect to the unknown source function, $I_{exp}(\omega)$ can be calculated as

$$I_{exp}(\omega) = \frac{O_{exp}(\omega)}{O_{mod}(\omega)} I_{mod}(\omega), \tag{4.5}$$

where ω is the angular frequency, $i(t) \xrightarrow{\mathcal{F}} I(\omega)$, and $o(t) \xrightarrow{\mathcal{F}} O(\omega)$. The required source was derived from equation (4.5) after applying the inverse Fourier transform.

Note that, any inelastic behaviour (such as $\mathcal{Q}$) of the gypsum material itself were included in the source function – and hence accounted for in both the control and fracture experiment. Moreover, were assumed equal:

- the P- and S-wave velocities of intact and fractured specimens;
- the distance between the sources and receivers in the two cases (intact and fractured sample);
- the sources in the two specimens are synchronised, i.e. they explode at the same time zero, i.e. no phase change is assumed.

Although in field measurements this inversion procedure needs to be used with caution especially due to inherent limitations of knowledge of material properties, in controlled laboratory experiments the uncertainties related to material properties or source-receiver geometry can be neglected.

The model shear and compressional wave sources involved a smooth excitation in the σ_{xy} component of stress and a dilatation stress ($\sigma_{xx} = \sigma_{yy} = \sigma_{zz}$), respectively. Velocity sources (v_y for the S-wave source and v_x for the P-wave source) were also tested, however the results were very similar for both cases to the stress sources.

Basic pre-processing was applied to the laboratory control waveforms to obtain a more stable solution. It included removal of the DC component from the signal and a cosine taper to blank out the later-arriving waves isolating, consequently, only the first arrival. Post-filtering was also necessary to suppress high frequency noise to avoid numerical dispersion.

Different tapers were evaluated to determine which one would give the best representation of the spectral energy of the first pulse. The main criteria in selecting the shape and duration of the taper was to ensure that the taper does not change the spectrum of the pulse and preserve the low frequency content of the signal without too much distortion in the high frequency range. The same procedure was also followed for the main experiments (e.g. Figure 4.10).

Figures 4.9(c) and 4.9(a) show the inverted S-wave and P-wave sources, respectively, after applying the inverse Fourier transform to equation (4.5). Their corresponding simulated responses were compared to the experimental waveforms in Figures 4.9(d) and 4.9(b), respectively. The latter also show that the match between the waveforms is remarkably good, confirming the success of the inversion procedure. It needs to be considered that for the purposes of this study, the relationship between voltage and actual modelled stress is arbitrary.

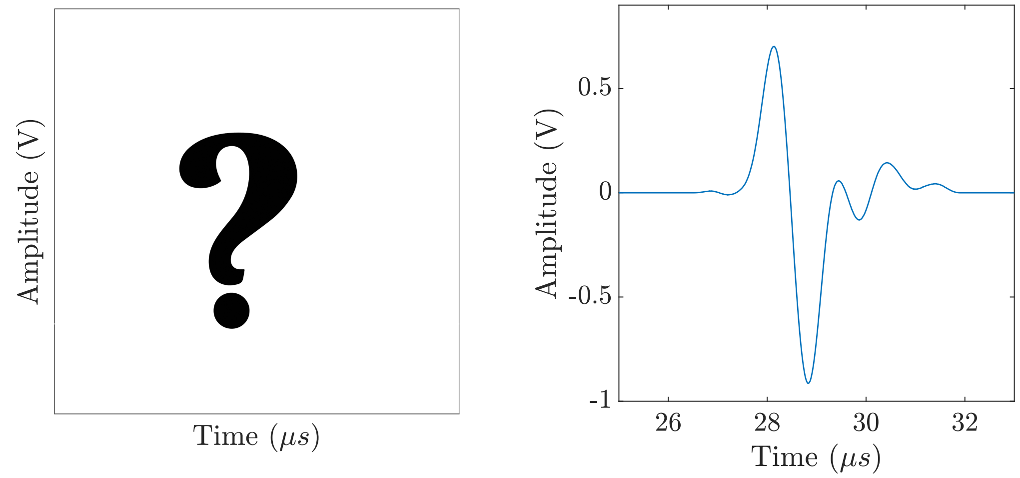

(a) Unknown experimental input source ($i_{exp}(t)$).

(b) Control experiment response ($o_{exp}(t)$).

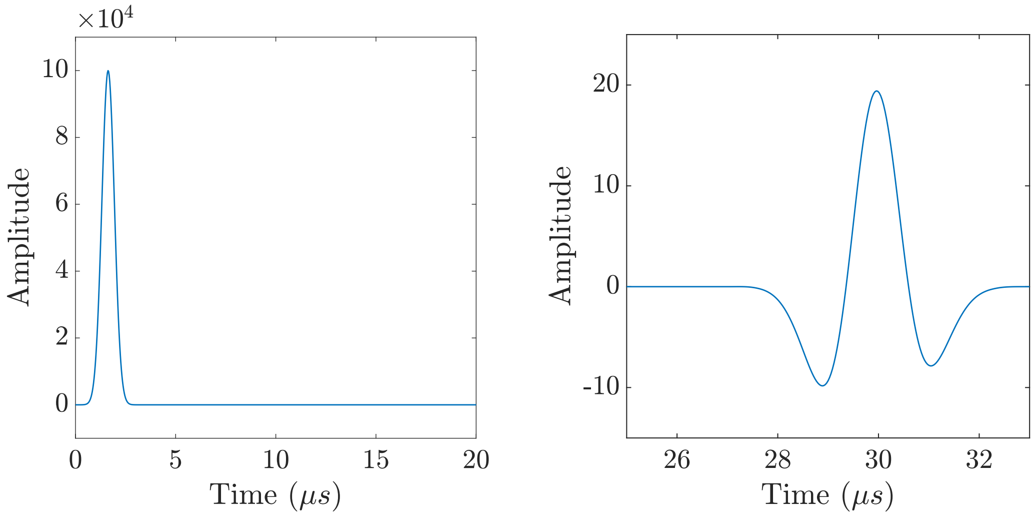

(c) Test input source ($i_{mod}(t)$).

(d) Simulated response ($o_{mod}(t)$) to the test source.

Figure 4.8: Procedure followed to estimate the unknown experimental input source (in this case the source for the compressional wave experiment) in (a). The test source $i_{mod}(t)$ in (c) is injected into the model representing the intact gypsum specimen, to obtain the simulated response (d). By taking the Fourier Transform of this response, the test source and the experimental response, a source function can be found using equation 4.5.

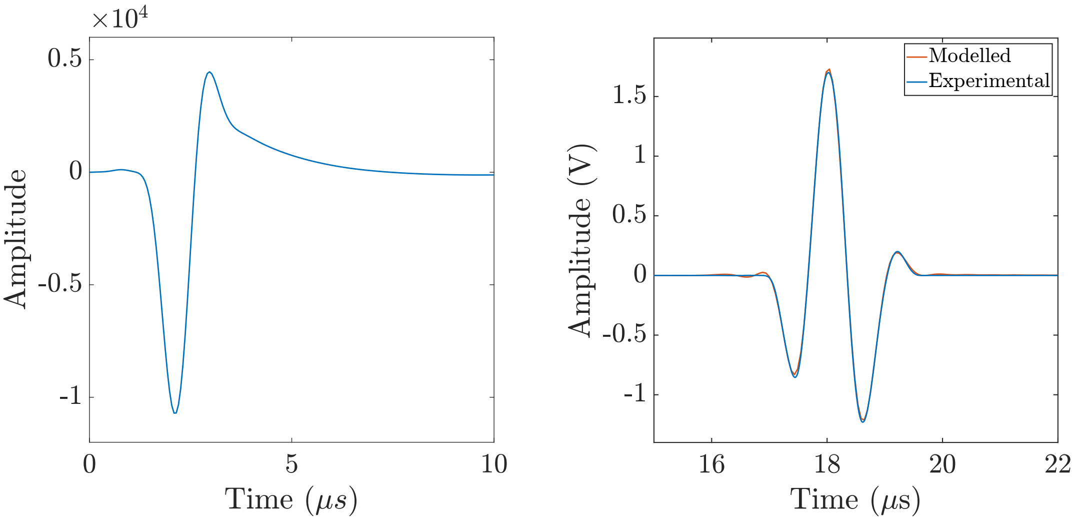

(a) Inverted P-wave stress source.

(b) Modelled response to the inverted P-wave source compared to the recorded data.

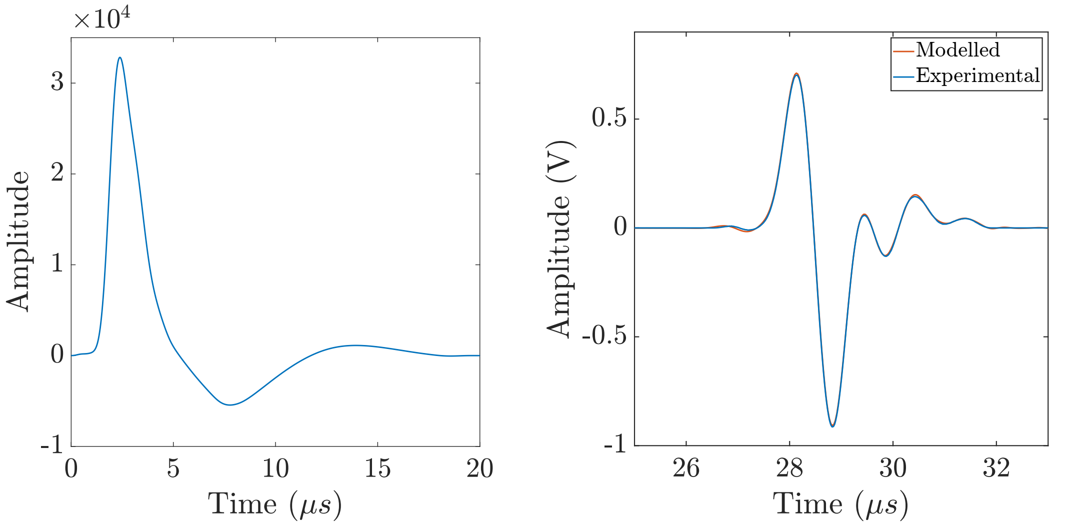

(c) Inverted S-wave stress source.

(d) Modelled response to the inverted S-wave source compared to the recorded data.

Figure 4.9: Compressional and shear wave stress sources after inversion in (a) and (c), respectively, and their corresponding WAVE3D outputs in (b), and (d), respectively.

4.3.2 Transmitted waveform inversion

The GA-FWFI+NA method was applied to characterise the discontinuity in terms of its mechanical properties and to explore the possibility of detecting seismic precursors to shear failure. To this end, the proposed multi-parameter FWI strategy used, as input, the whole transmitted P- and S-wave fields with minimal pre-processing (DC removal, cosine taper to isolate the main arrival, and filtering) (Figure 4.10) to invert for the P- and S-wave velocity of the background material, the shear and normal specific stiffness of the discontinuity, and its location. In order to estimate the joint location it was required to constrain the inversion by using both the reflected and the transmitted waves. Finally, the Neighbourhood Algorithm was employed to infer uncertainties associated with the retrieved parameters from the entire ensembles of GA models.

Although the P-wave velocity, S-wave velocity and fracture location are known, fewer constraints were included in the data fitting in order to generalise the inversion and to show the potential of this methodology in cases where analytical solutions could fail. Furthermore, the shear and normal fracture stiffness were also included in the inversion of the compressional and shear seismic waveforms, respectively, as control. In fact, P-waves at normal incidence (for a single fracture) are not sensitive to the shear fracture stiffness, just as S-waves at normal incidence are not sensitive to the normal fracture stiffness.

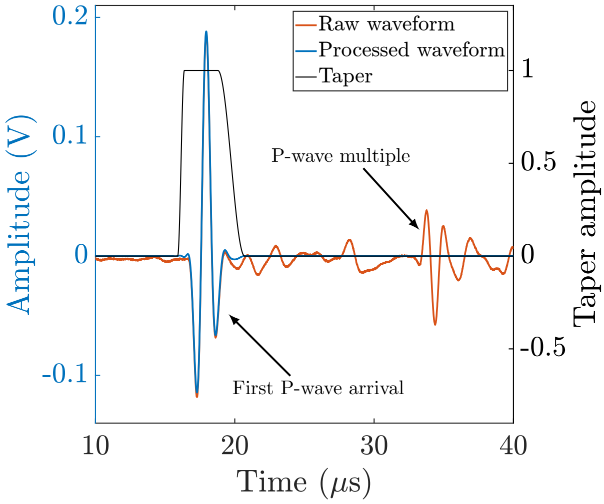

Figure 4.10: Comparison between raw and post-processed waveform of transducer pair 2P-2P.

The analysis was performed on compressional waves recorded by the transducer pair 2P-2P, at the displacement measures of -1.15 mm, -0.81 mm, -0.50 mm, -0.25 mm, -0.08 mm, and $+0.07$ mm as shown in Figure 4.5(c), and on shear waves recorded by the transducer pair 8S-8S at the displacement measures of -1.15 mm, -0.81 mm, -0.50 mm, -0.35 mm, -0.08 mm, and $+0.07$ mm as shown in Figure 4.6(c).

4.3.3 Compressional waveforms inversion

Numerical simulations were performed over 3-D models. The model, with the background material isotropic and homogeneous, was discretised in space using a regular 3-D grid of 190 × 170 × 170 elements, and 30 cells (1.27 cm) of absorbing boundary layers were added to each model boundary, bringing the total number of grid points to nearly 9 millions. The numerical dispersion and stability criteria that apply to the FD scheme, constrain the temporal and spatial sampling of the model. Using the elastic properties of the gypsum material (Table 4.1) at maximum frequency of the source signal, a time-step of $dt = 55$ ns and a grid spacing of $dx = dy = dz = 0.423$ mm generated minimal numerical dispersion and ensured the stability of WAVE3D everywhere. With 400 time steps, the total recording time was 22 μs.

The P-wave source function estimated in the intact gypsum (Figure 4.9(a)) was used in this inversion procedure. The genetic algorithm evaluated a total population of 840 models within the multi-dimensional model space expressed by the parameter vector

$$\mathbf{m} = \{\kappa_n, \kappa_s, v_p, x_{joint}\}, \tag{4.6}$$

preconditioned by the number of discontinuities (one in this case), and its orientation (orthogonal to the $x-$axis). The principal control parameters used in the GA inversion are summarised in Table 4.2, and the misfit function was defined as the Euclidean distance ($\mathcal{L}_2$-norm) between the recorded waveforms and the modelled waveforms.

The model space was bounded in each dimension by the search boundaries of each parameter (Table 4.3). The GA ranges for the fracture specific stiffnesses (both κ_n and κ_s) are consistent with the experimental values found by Pyrak-Nolte et al. (1990b),

GA parameters	Values
Population	40
Generations	20
Tournament size	3
Mutation ratio	0.4
Elitism	0.05

Table 4.2: GA inversion parameters for the compressional waves inversion.

Lubbe et al. (2008), and Verdon and Wüstefeld (2013).

Model parameters	Range	Unit
Normal specific stiffness of the discontinuity (κ_n)	$[1 \cdot 10^{11}, 5 \cdot 10^{12}]$	Pa m^{-1}
Shear specific stiffness of the discontinuity (κ_s)	$[1 \cdot 10^{11}, 5 \cdot 10^{12}]$	Pa m^{-1}
Background P-wave velocity (v_p)	$[3000, 3400]$	m s^{-1}
Location of the discontinuity along x (x_{joint})	$[1.5, 3.5]$	cm

Table 4.3: Free parameters for the compressional waves inversion with their search boundaries.

From the inversion of the transmitted waveforms, six model parameter vectors (equation 4.7) were determined: one set of model parameters for each shear displacement value analysed:

$$\begin{bmatrix} m_1 \\ m_2 \\ m_3 \\ m_4 \\ m_5 \\ m_6 \end{bmatrix} = \begin{bmatrix} \kappa_{n1}, \ \kappa_{s1}, \ v_{p_1}, \ x_{joint_1} \\ \kappa_{n2}, \ \kappa_{s2}, \ v_{p_2}, \ x_{joint_2} \\ \kappa_{n3}, \ \kappa_{s3}, \ v_{p_3}, \ x_{joint_3} \\ \kappa_{n4}, \ \kappa_{s4}, \ v_{p_4}, \ x_{joint_4} \\ \kappa_{n5}, \ \kappa_{s5}, \ v_{p_5}, \ x_{joint_5} \\ \kappa_{n6}, \ \kappa_{s6}, \ v_{p_6}, \ x_{joint_6} \end{bmatrix}. \tag{4.7}$$

The variation of the fittest GA models of the normal fracture stiffness with the shear displacement can be seen in Figure 4.11(a). Here, the inverted models (red asterisks) were superimposed on the analytical curves (Figure 4.7) obtained from equation (4.1) using $\omega_{min} = 400KHz$ and $\omega_{max} = 1000KHz$ and plotted in Figure 4.11(a). A very good degree of matching between the predicted and inverted results can be noticed. The GA models, in fact, fall within the range of κ_n values, following precisely the analytical trend. The peak prior to failure and the subsequent sharp drop are clearly reproduced. Figure 4.11(b) shows the average data misfits, normalised to their maximum value, as a function of GA generation for each inverted model. The inversion converges gradually but stabilises after 15 generations.

Δu (mm)	-1.17	-0.81	-0.50	-0.35	-0.08	+0.07
κ_n (Pa/m)	$6.91 \cdot 10^{11}$	$5.96 \cdot 10^{11}$	$8.08 \cdot 10^{11}$	$1.13 \cdot 10^{12}$	$6.78 \cdot 10^{11}$	$9.84 \cdot 10^{10}$
κ_s (Pa/m)	$1.13 \cdot 10^{11}$	$1.48 \cdot 10^{11}$	$3.13 \cdot 10^{11}$	$2.25 \cdot 10^{11}$	$4.68 \cdot 10^{11}$	$9.43 \cdot 10^{10}$
Joint location (cm)	2.50	2.54	2.54	2.50	2.50	2.54
v_p (m/s)	3229.0	3229.2	3227.7	3228.8	3228.2	3235.6

Table 4.4: Optimum GA model as defined in equation (4.7) for compressional waves, where each model is represented by the set of parameters κ_n, κ_s, v_p, x_{joint}. The true model parameter values are $v_p = 3230$ m/s, and $x_{\text{joint}} = 2.54$ cm. The fracture location on the x-axis is referred to the distance between the source location and fractures.

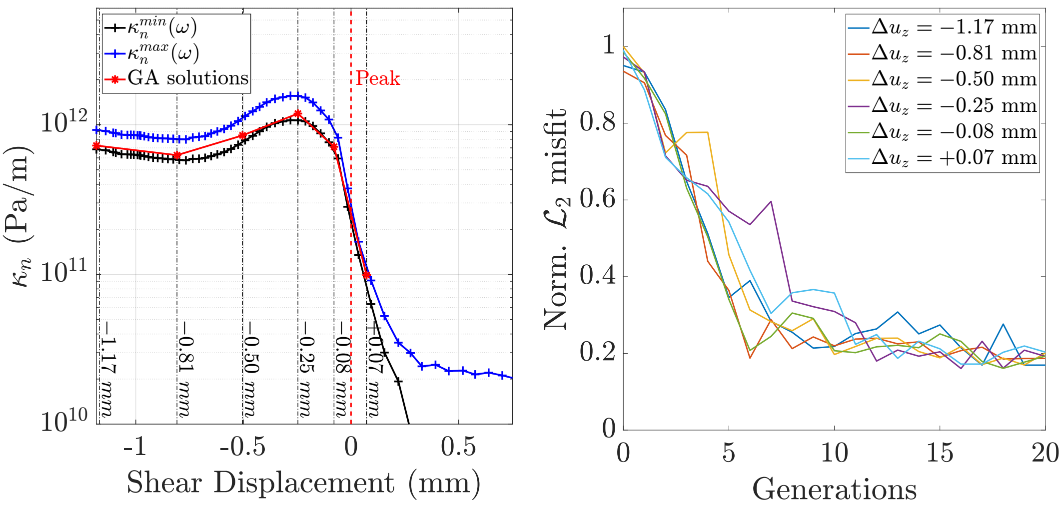

(a) (b)

Figure 4.11: (a) GA inverted normal specific stiffness of the discontinuity (red stars) superimposed to the analytical curves shown in Figure 4.7.(b) Misfit evolution as a function of generations.

In Figure 4.12 the waveforms modelled using the elite GA models are overlaid on the laboratory ones at the shear displacement values analysed. In all cases, not only is the peak-to-peak amplitude well retrieved but the overall fit between the waveforms is also extremely good. The good agreement between the modelled and experimental data is also highlighted in the frequency domain (Figure 4.13).

The PPD for each model parameter, as computed through NA, are plotted in Figure 4.14. The plots also show, as reference, the best GA models (dashed red curves) and the true values (solid black curve), such as the measured v_p and the joint location along x. The estimates of these model parameters agree with the corresponding true values and their PPDs are characterised by a peaked appearance. This means that only a restricted range of values is able to explain the experimental data and there is not any cross-talk between the model parameters inverted. The same behaviour can be observed for the parameter κ_n, where the results are very well constrained to a unique best solution. In contrast, the specific shear stiffness κ_s suffers multimodality meaning that multiple solutions can have the same data misfit. This is due to the insensitivity of compressional waves at normal incidence to the discontinuity to the variation of the shear fracture stiffness, and is therefore in agreement with the expected behaviour.

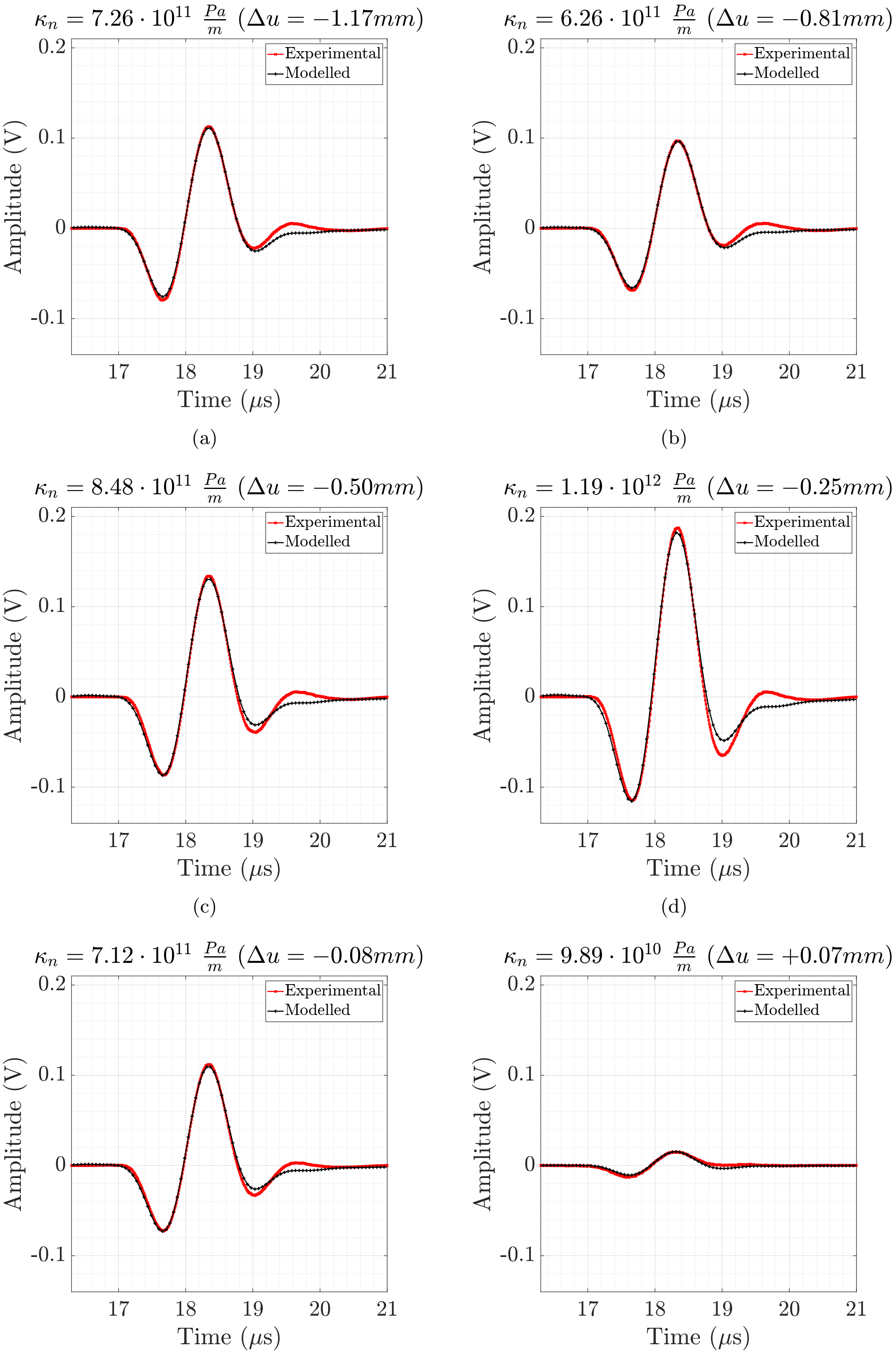
$\kappa_n = 7.26 \cdot 10^{11}\ \frac{Pa}{m}\ (\Delta u = -1.17mm)$

$\kappa_n = 6.26 \cdot 10^{11}\ \frac{Pa}{m}\ (\Delta u = -0.81mm)$

(a)

(b)

$\kappa_n = 8.48 \cdot 10^{11}\ \frac{Pa}{m}\ (\Delta u = -0.50mm)$

$\kappa_n = 1.19 \cdot 10^{12}\ \frac{Pa}{m}\ (\Delta u = -0.25mm)$

(c)

(d)

$\kappa_n = 7.12 \cdot 10^{11}\ \frac{Pa}{m}\ (\Delta u = -0.08mm)$

$\kappa_n = 9.89 \cdot 10^{10}\ \frac{Pa}{m}\ (\Delta u = +0.07mm)$

(e)

(f)

Figure 4.12: Comparison between the compressional waveforms (2P-2P) modelled using the optimum GA model (black) with the respective experimental waveforms (red) for each shear displacement (Δu) value analysed. In (a) $\Delta u = -1.17$ mm, in (b) $\Delta u = -0.81$ mm, in (c) $\Delta u = -0.50$ mm, (d) $\Delta u = -0.25$ mm, in (e) $\Delta u = -0.08$ mm, and in (f) $\Delta u = +0.07$ mm.

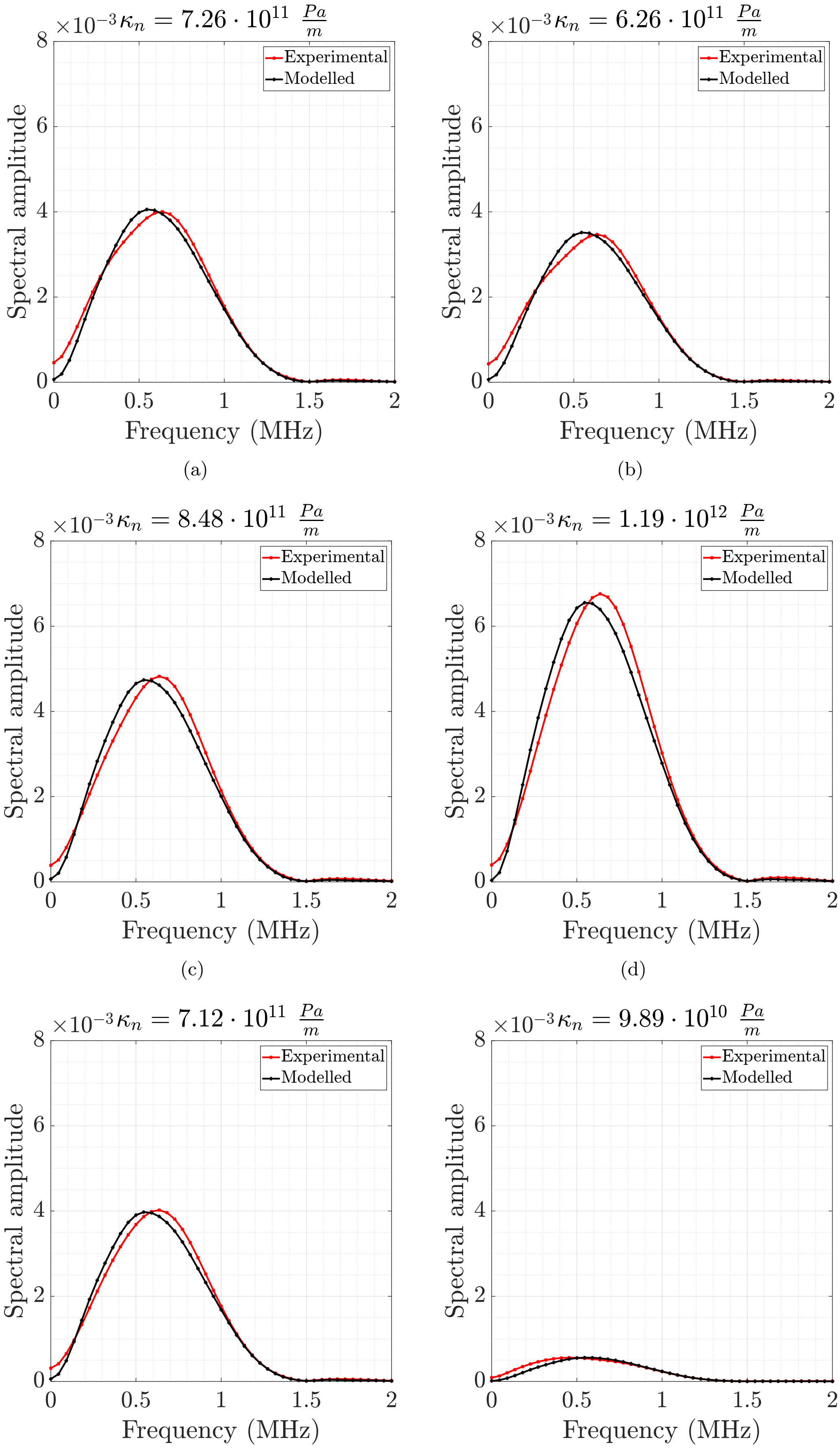

(a) (b) (c) (d) (e) (f)

Figure 4.13: Comparison of the amplitude spectra between modelled and laboratory waveforms shown in Figure 4.12.

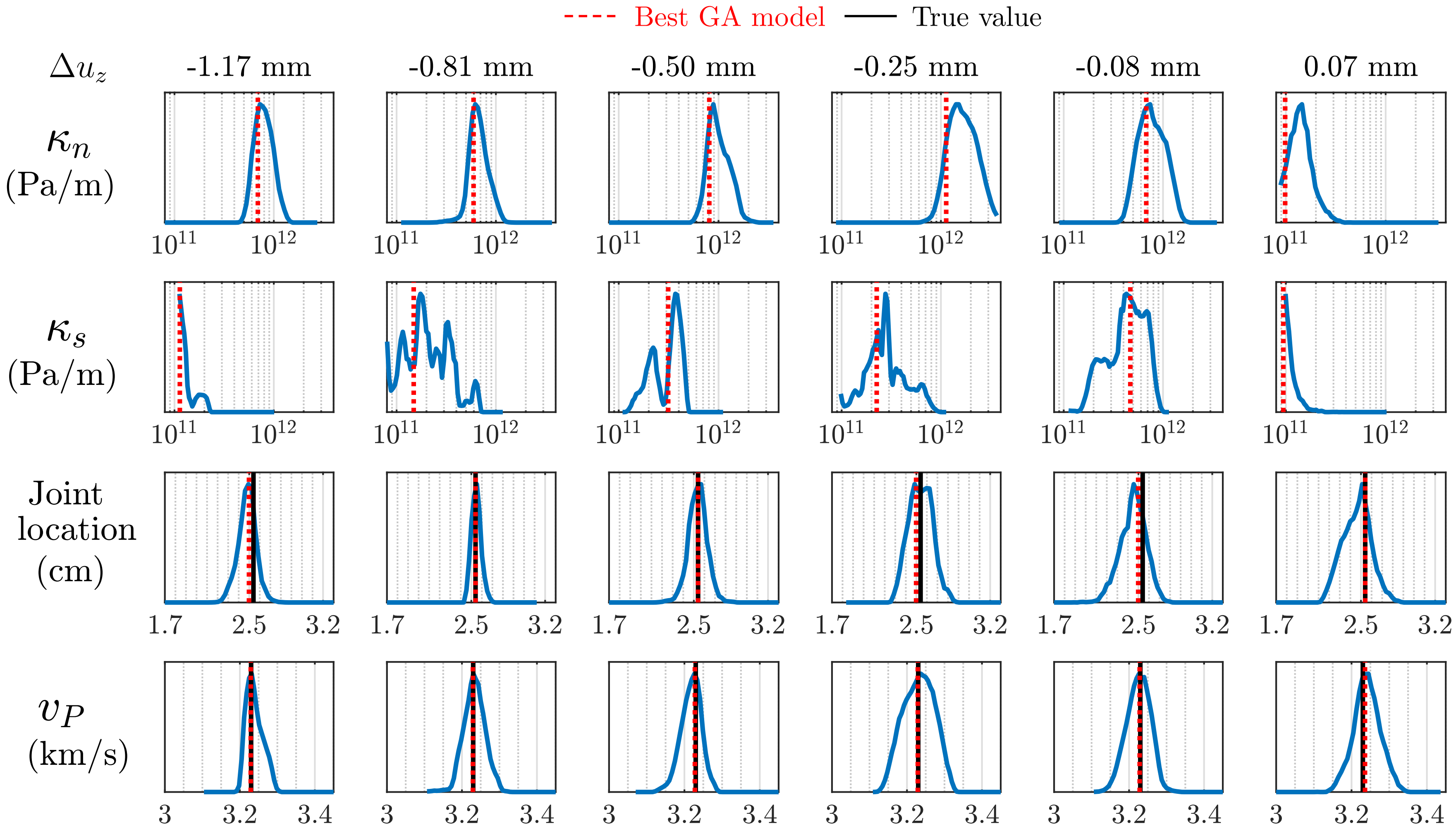

Figure 4.14: Marginal Posterior probability density (PPD) function for each model parameter inverted (compressional case) and for each shear displacement value, through the NA approach.

4.3.4 Shear waveforms inversion

To simulate the S-wave propagation, the model geometry needed to be modified to honour the new numerical dispersion and stability criteria. Although the maximum frequency modelled was similar to the previous case, S-wave velocity is slower than the P-wave, therefore the grid spacing had to be smaller to sample correctly the shear wavefields. A value of $dx = dy = dz = 0.21$ mm was chosen to satisfy the dispersion criterion. In turn, to keep equal the model dimensions and to avoid numerical instability, the model was discretised in space using a regular 3-D grid of $300 \times 210 \times 210$ elements, and a time-step of $dt = 29$ ns. Also the total time steps increased to 1150 cycles, with a record time length of 33.35 μs. To reduce slightly the computational time, yet limiting spurious reflections from the boundaries, the width of the PML zones was reduced from 30 cells to 20 cells.

The S-wave source function estimated in the intact gypsum (Figure 4.9(c)) was used in this inversion procedure. Like the compressional waveforms inversion, GA evaluated a total population of 840 models within the multi-dimensional model space

$$\mathbf{m} = \{\kappa_n, \kappa_s, v_s, x_{joint}\}\,, \tag{4.8}$$

to find the optimum solution $\mathbf{m}^{best} = \left\{\kappa_n^{best}, \kappa_s^{best}, v_s^{best}, x_{joint}^{best}\right\}$ which best fits the experimental waveforms. The GA parameters employed in these numerical experiments were kept unchanged (see Table 4.2), while the number of discontinuities and orientation were fixed during the inversion. Table 4.5 shows the search boundaries for each model parameter.

Model parameter	Prior range	Unit
Normal specific stiffness of the discontinuity (κ_n)	$1 \cdot 10^{11} - 5 \cdot 10^{12}$	Pa m^{-1}
Shear specific stiffness of the discontinuity (κ_s)	$1 \cdot 10^{11} - 5 \cdot 10^{12}$	Pa m^{-1}
Background S-wave velocity (v_s)	$1500 - 2500$	m s^{-1}
Location of the discontinuity along x (x_{joint})	$1.5 - 3.5$	cm

Table 4.5: Free parameters in the shear waves inversion with their search boundaries.

Δu (mm)	-1.17	-0.81	-0.50	-0.35	-0.08	+0.07
κ_n (Pa/m)	$8.98 \cdot 10^{11}$	$6.20 \cdot 10^{11}$	$1.19 \cdot 10^{12}$	$1.85 \cdot 10^{12}$	$8.21 \cdot 10^{11}$	$4.05 \cdot 10^{10}$
κ_s (Pa/m)	$9.99 \cdot 10^{11}$	$9.75 \cdot 10^{11}$	$1.13 \cdot 10^{12}$	$1.15 \cdot 10^{12}$	$7.30 \cdot 10^{11}$	$3.05 \cdot 10^{10}$
Joint location (cm)	2.50	2.58	2.54	2.54	2.54	2.50
v_s (m/s)	1914.1	1920.8	1923.4	1924.1	1915.3	1918.5

Table 4.6: Optimum GA model as defined in equation (4.7) for shear waves, where each model is represented by the set of parameters κ_n, κ_s, v_s, x_{joint}. The true model parameter values are $v_s = 1910$ m/s, and $x_{\text{joint}} = 2.54$ cm. The fracture location on the x-axis is referred to the distance between the source location and fractures.

Figure4.15(a) illustrates the inverted discontinuity's shear stiffness (red asterisks) compared with the predicted analytical values. Again, the best solutions of fracture shear stiffnesses (κ_s^{best}) fall into the interval defined by the frequency band 400-1000 KHz and it follows the shape of the curve accurately. The precursor to the shear failure (peak of the shear stiffness) is also correctly characterised. The convergence to the optimal solutions can be observed between generation 15 and 20 (see Figure 4.15(b)) which shows the evolution of the average misfit with the generations and for each shear displacement tested).

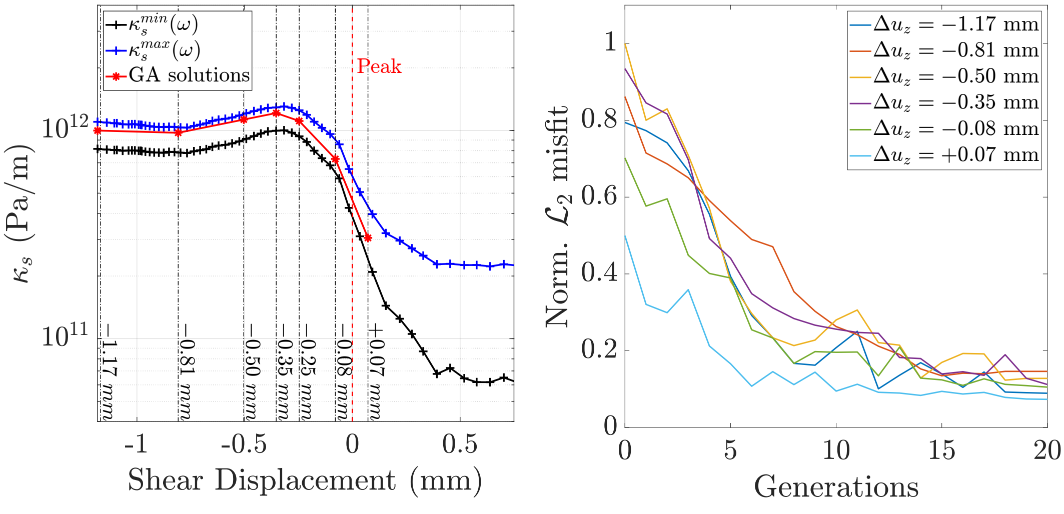

(a) (b)

Figure 4.15: (a) GA inverted normal specific stiffness of the discontinuity (red stars) superimposed to the analytical curves shown in Figure 4.7. (b) Misfit evolution as a function of generations.

The optimal GA solutions ($\mathbf{m}^{best}$) were used to forward model the transmitted waveforms at different shear displacement steps. Figures 4.16 and Figure 4.17 compare the modelled waveforms with the respective experimental ones and the corresponding amplitude spectra. These show that a high degree of accuracy was achieved.

A quantitative Bayesian analysis of the entire multi-dimensional model space was also carried out to infer the posterior probability density function for each model parameter and each inversion, by taking the entire ensemble of GA solutions (Figure 4.18). As observed in the compressional wave inversion, where the wave propagation at normal incidence was insensitive to the shear stiffness, here the wave propagation is insensitive to the the normal stiffness parameter. This behaviour is vividly displayed in Figure 4.19(a) and Figure 4.19(b) which show the projection of all GA models and their corresponding misfit values on the $\kappa_n - \kappa_s$ plane in the case of the compressional and shear waveform inversion. These show elongated valleys of minima parallel to the κ_s-axis for compressional wave inversion and κ_n-axis for shear wave inversion. This is clearly due to the insensitivity of P- and S-wave propagation to these two parameters.

In the case of the shear waveform inversion, this leads to a multimodal or flatter PPD function for κ_n within the range analysed (Figure 4.18 top row) meaning that multiple values are equally likely. On the other hand, κ_s was correctly estimated and constrained to a narrow range of probable values. This can be observed in Figure 4.18 in the second row, where the marginal PPD functions exhibit sharp peaks at the best-fitting GA values.

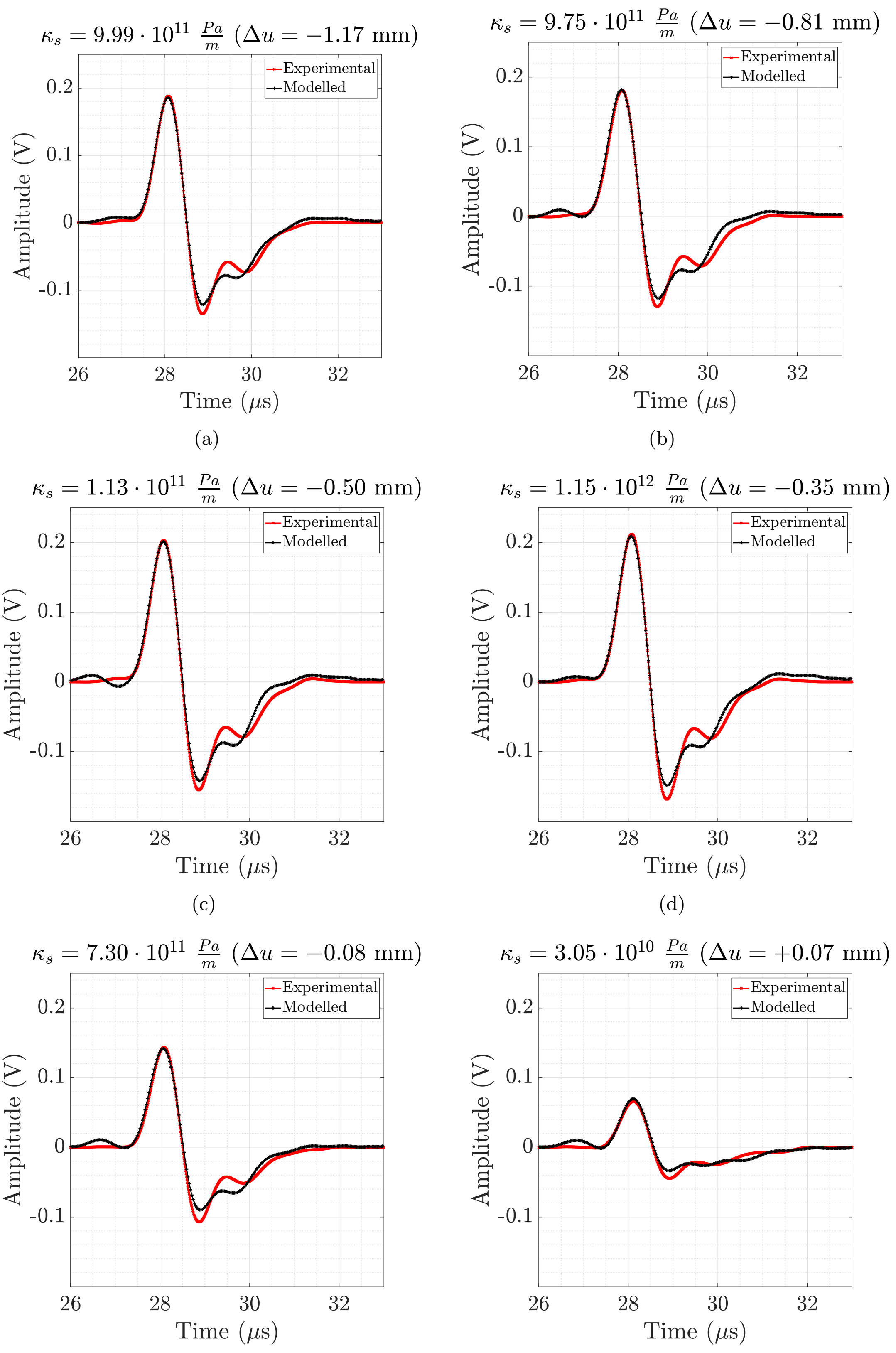

(a) (b) (c) (d) (e) (f)

Figure 4.16: Comparison between the shear waveforms (8S-8S) modelled using the optimum GA model (black) with the respective experimental waveforms (red) for each shear displacement (Δu) value analysed. In (a) $\Delta u = -1.17$ mm, in (b) $\Delta u = -0.81$ mm, in (c) $\Delta u = -0.50$ mm, (d) $\Delta u = -0.35$ mm, in (e) $\Delta u = -0.08$ mm, and in (f) $\Delta u = +0.07$ mm.

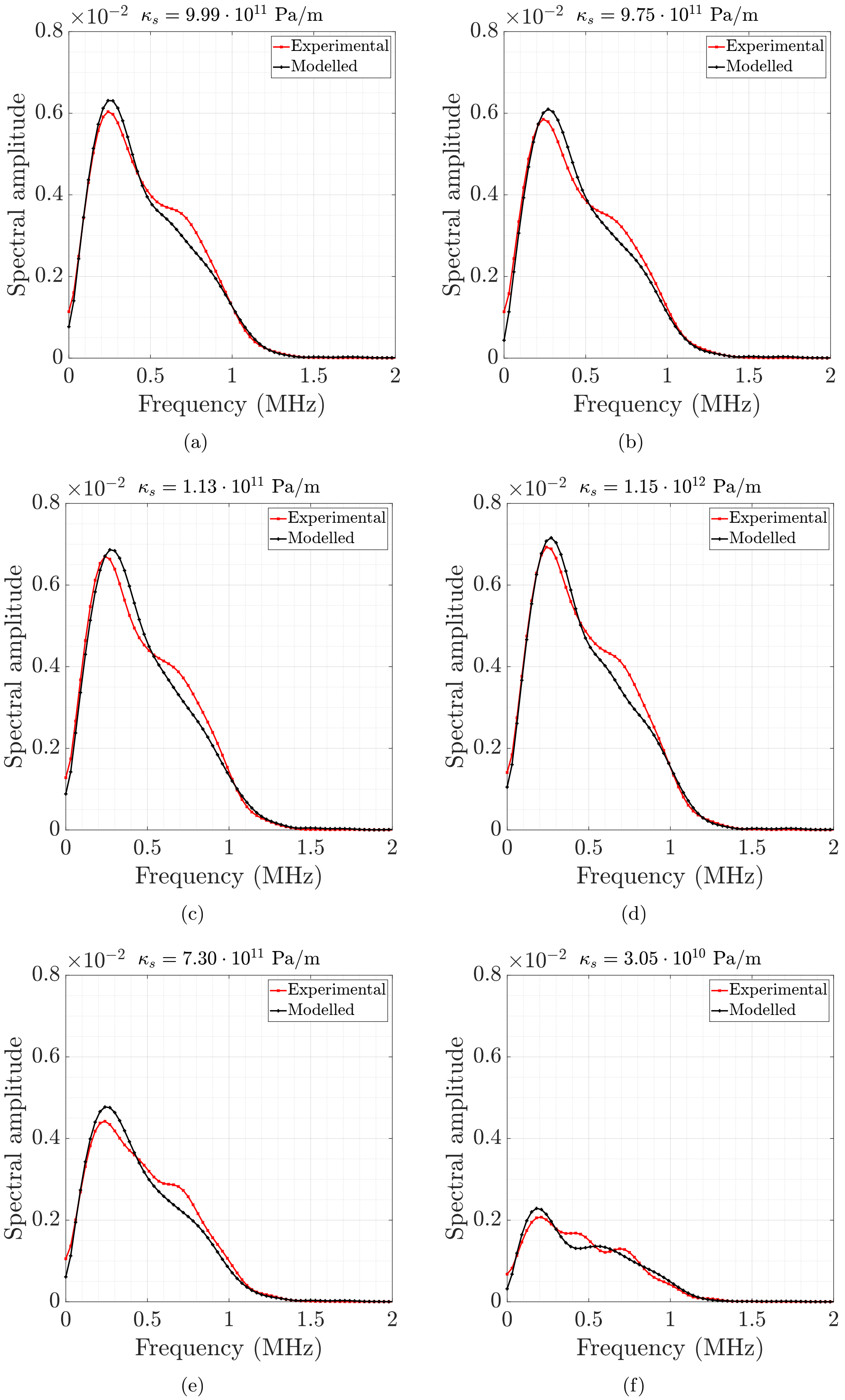

(a) (b)

(c) (d)

(e) (f)

Figure 4.17: Comparison of the amplitude spectra between modelled and laboratory waveforms shown in Figure 4.16.

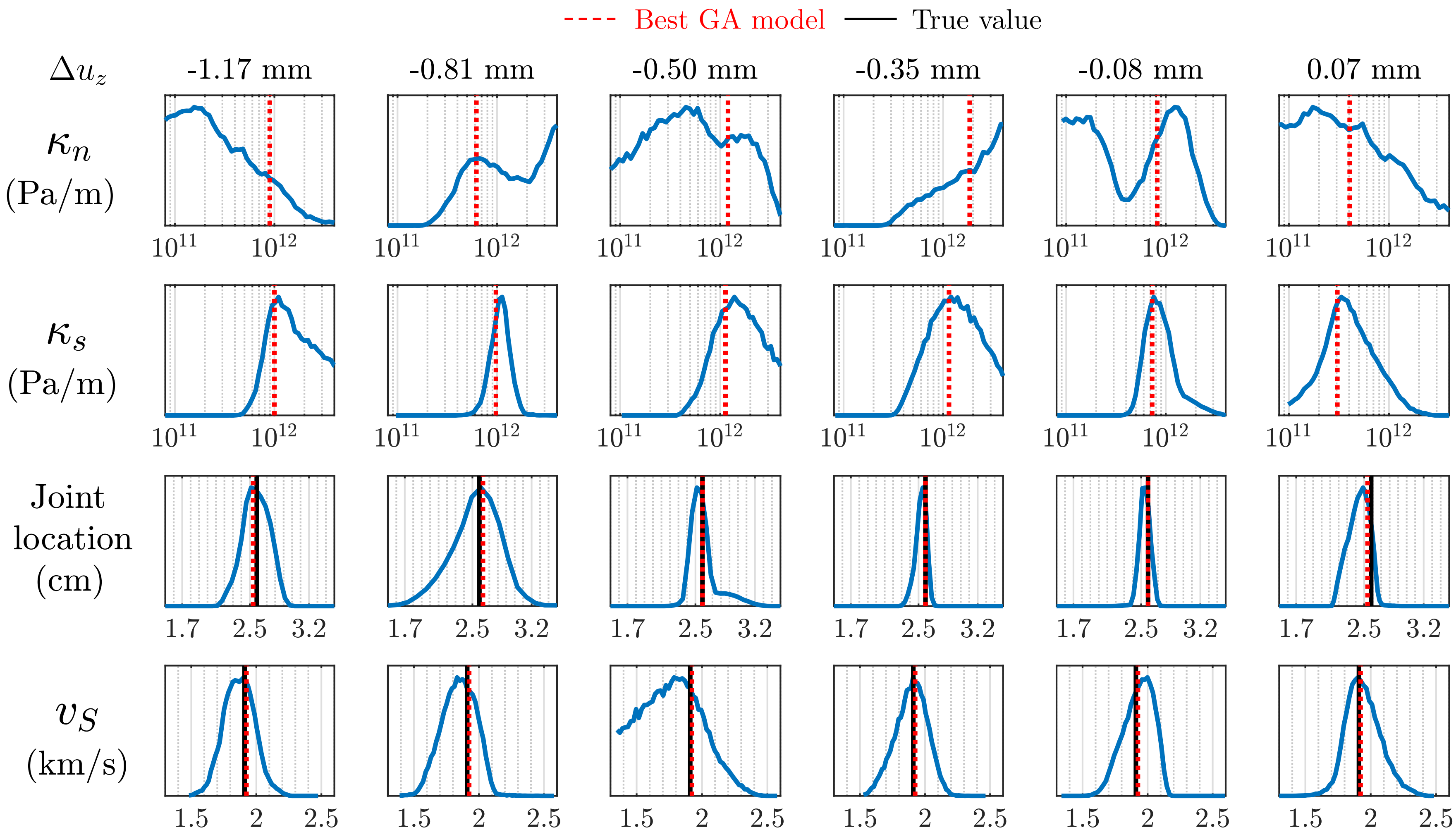

Figure 4.18: Marginal Posterior probability density (PPD) function for each model parameter inverted (shear case) and for each shear displacement value, through the NA approach.

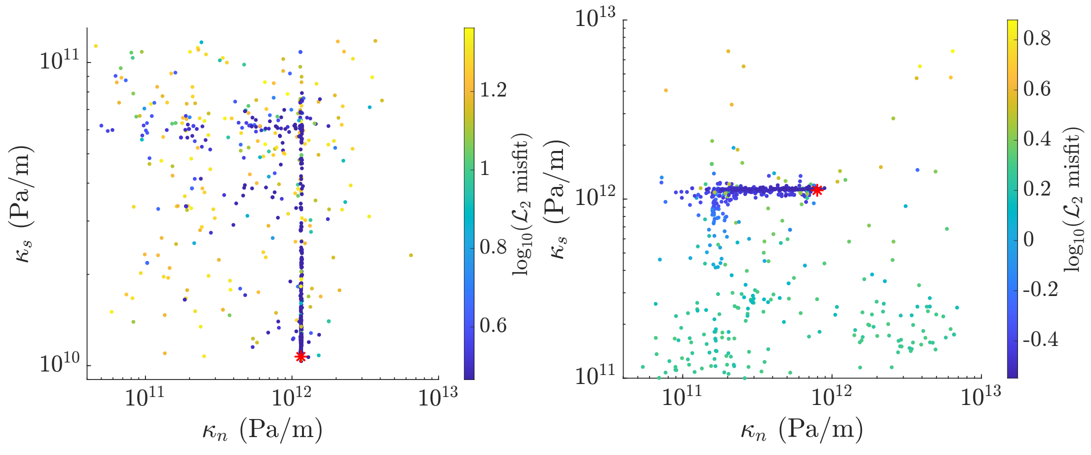

(a) (b)

Figure 4.19: Representative examples of the GA model ensemble related to the shear displacement $\Delta u = -0.25$ mm and transducer pair (2P-2P), and (8S-8S) in (a) and (b), respectively, projected on the plane $\kappa_n - \kappa_s$. Each point represents a GA model, while the color represents its misfit value. The red stars represent the fittest models. In (a) the misfit function contains an elongated minimum valley orthogonal to the κ_n axis. This is due to the insensitivity of compressional waves, at normal incidence of the discontinuity, to the κ_s variation. (b) shows similar behaviour but the elongated valley is parallel to the κ_n axis, i.e. insensitivity with respect to κ_n.

4.4 Reflected waveforms for the transducer pair 2P-2P and 8S-8S

The best GA models ($\mathbf{m}^{\text{best}}$) for both the compressional and shear waves, were used to forward model the reflected waveforms at different shear displacement values analysed. Figure 4.20 shows a comparison between the experimental (red) and the modelled (black) compressional waveforms for the transducer pair 2P-2P. Although there is a relatively good match in shape and amplitude between these two sets of waveforms, the experimental waveforms seem to show a lack of high frequencies. This is confirmed by the amplitude spectra displayed in Figure 4.21 which is attenuated for high frequency.

The reflected shear waves for the transducer pair 8S-8S are compared in Figure 4.22. In this case, the match between the experimental and modelled (red and black, respectively) is very good, albeit that there can be observed a slight mismatch in frequency domain between 400 and 700 KHz. Nevertheless, the high frequency attenuation does not occur. A principal reason could be due to the a slightly narrower frequency range

($f_{max} < 1.3$ MHz) than the P-wave case, within the transducer frequency response range. As explained in Section 2.2.1, due to irregular geometry of the asperities between the two sides of the discontinuity the propagating wavefield experiences attenuation by scattering which might not be captured by the receivers. In these cases the displacement discontinuity theory may not estimate correctly the dynamic of the wavefields and consequently the energy is not conserved, i.e $|T(\omega)|^2 + |R(\omega)|^2 \neq 1$. Moreover, the phenomenon of *cross-coupled waves* due to the conversion of P- and S- waves in shear and compressional waves, respectively, at normal incidence during shearing cannot be explained by the displacement-discontinuity theory (Nakagawa et al., 2000).

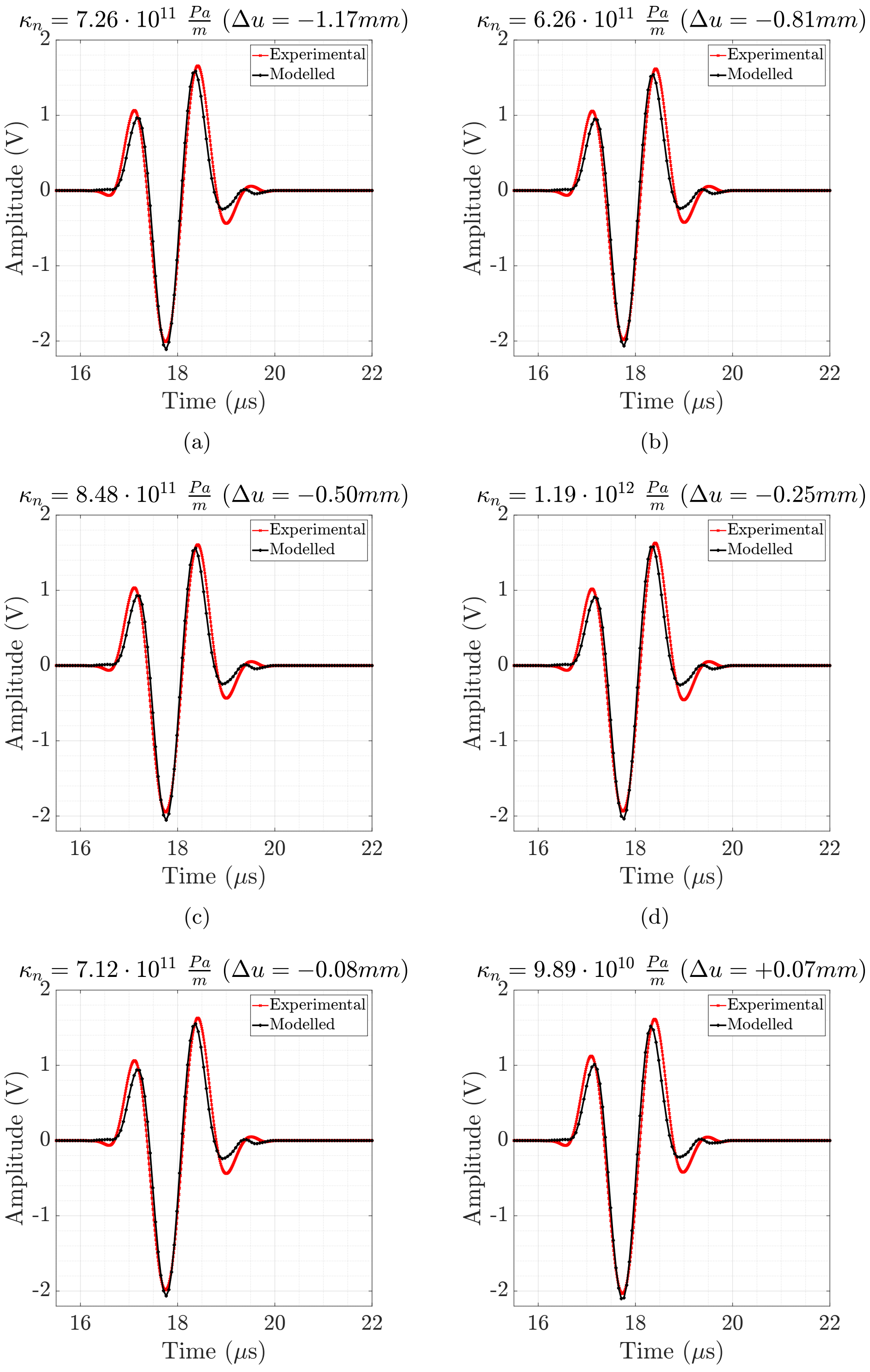

(a) (b) (c) (d) (e) (f)

Figure 4.20: Comparison between the reflected compressional waveforms modelled (black) using the optimum GA model (Table 4.4) with the respective experimental waveforms (red) for each shear displacement (Δu) value analysed (transducer pair 2P-2P). In (a) $\Delta u = -1.17$ mm, in (b) $\Delta u = -0.81$ mm, in (c) $\Delta u = -0.50$ mm, (d) $\Delta u = -0.25$ mm, in (e) $\Delta u = -0.08$ mm, and in (f) $\Delta u = +0.07$ mm.

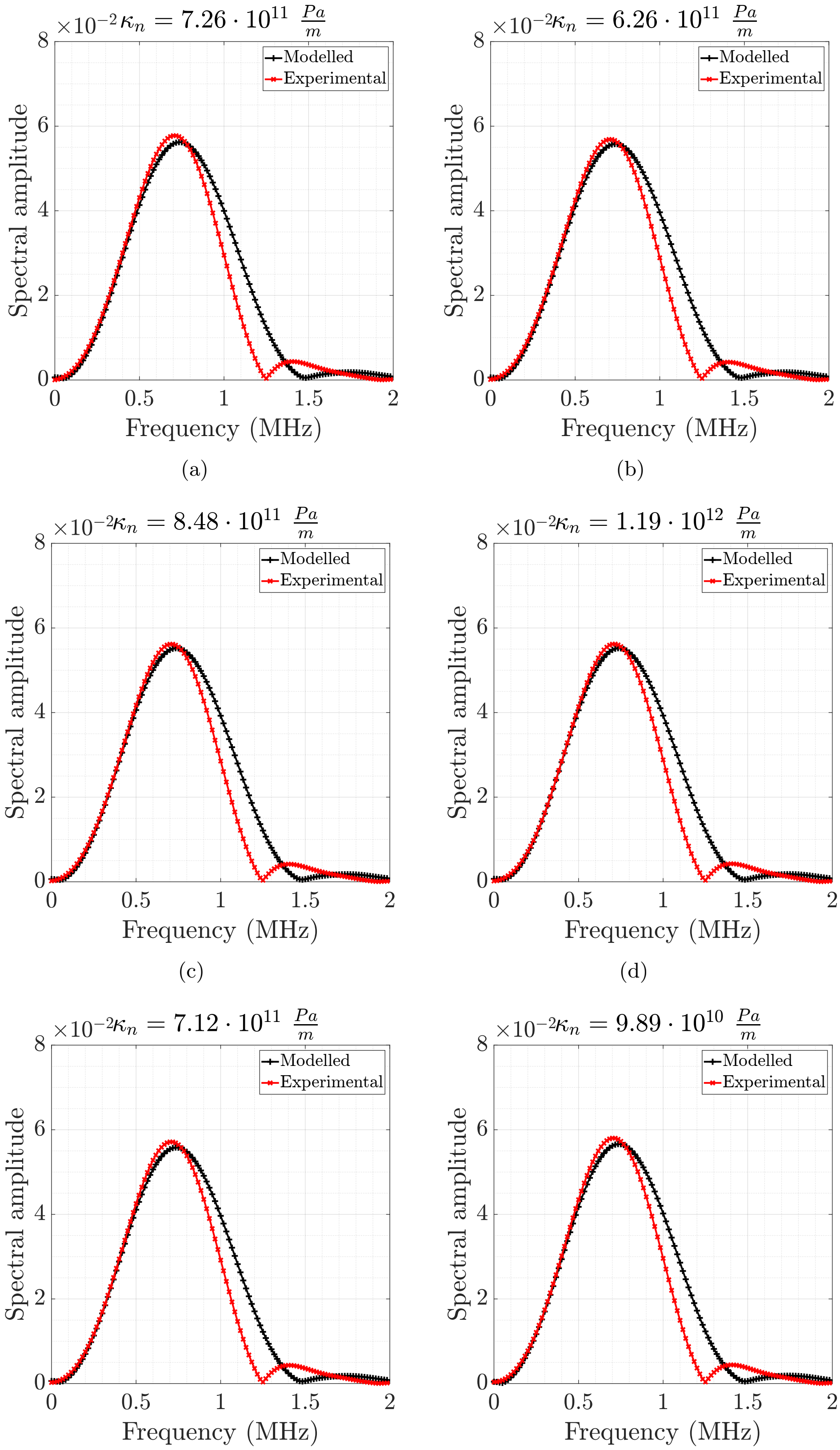

(a) (b) (c) (d) (e) (f)

Figure 4.21: Comparison between the amplitude spectra of modelled and laboratory reflected compressional waves shown in Figure 4.20. The experimental waveforms show a lack of high frequencies probably due to the transducers response.

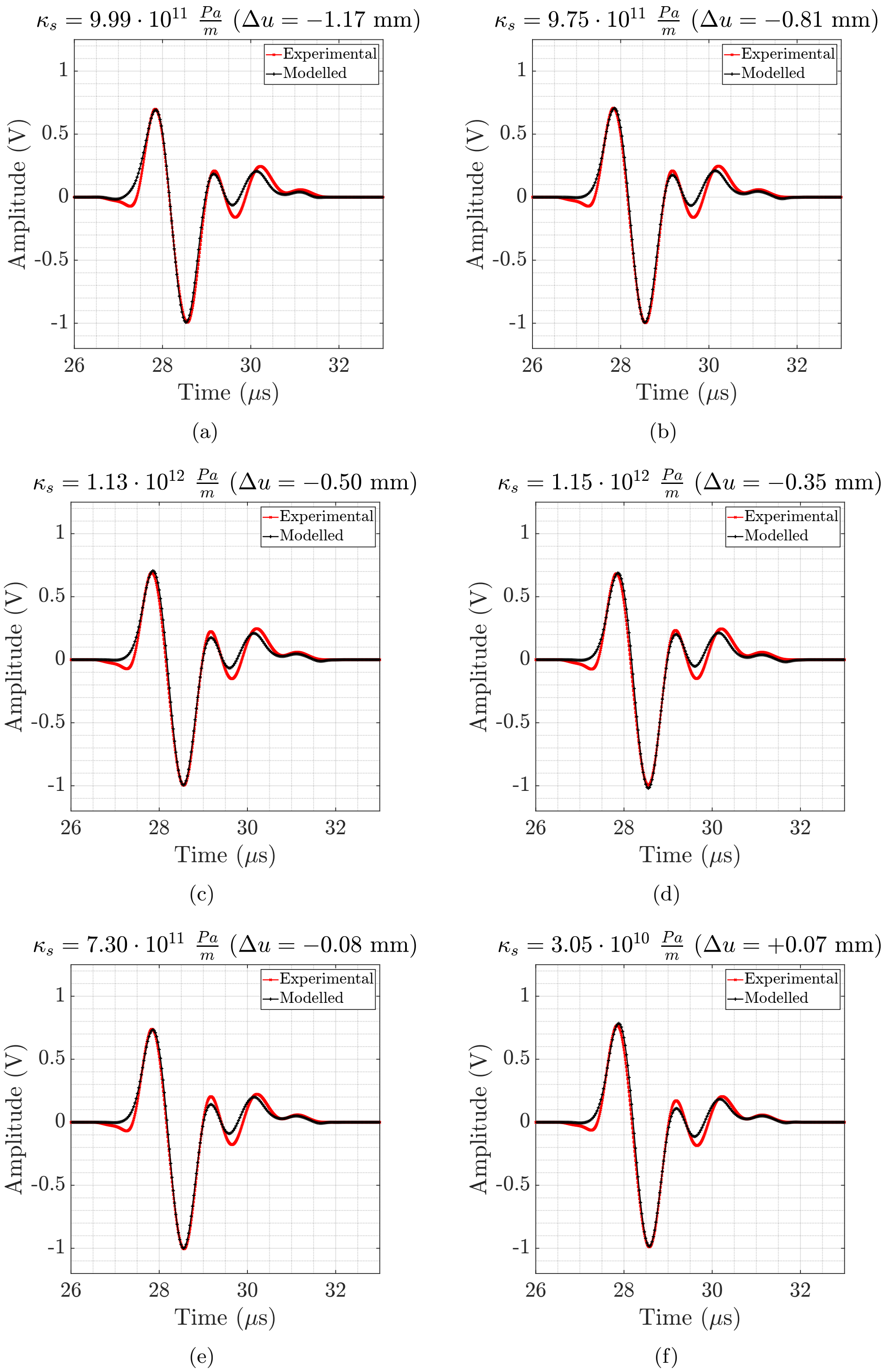

$\kappa_s = 9.99 \cdot 10^{11}\ \frac{Pa}{m}$ ($\Delta u = -1.17$ mm)

(a)

$\kappa_s = 9.75 \cdot 10^{11}\ \frac{Pa}{m}$ ($\Delta u = -0.81$ mm)

(b)

$\kappa_s = 1.13 \cdot 10^{12}\ \frac{Pa}{m}$ ($\Delta u = -0.50$ mm)

(c)

$\kappa_s = 1.15 \cdot 10^{12}\ \frac{Pa}{m}$ ($\Delta u = -0.35$ mm)

(d)

$\kappa_s = 7.30 \cdot 10^{11}\ \frac{Pa}{m}$ ($\Delta u = -0.08$ mm)

(e)

$\kappa_s = 3.05 \cdot 10^{10}\ \frac{Pa}{m}$ ($\Delta u = +0.07$ mm)

(f)

Figure 4.22: Comparison between the reflected shear waveforms modelled (black) using the optimum GA model (Table 4.6) with the respective experimental waveforms (red) for each shear displacement (Δu) value analysed (transducer pair 8S-8S). In (a) $\Delta u = -1.17$ mm, in (b) $\Delta u = -0.81$ mm, in (c) $\Delta u = -0.50$ mm, (d) $\Delta u = -0.35$ mm, in (e) $\Delta u = -0.08$ mm, and in (f) $\Delta u = +0.07$ mm.

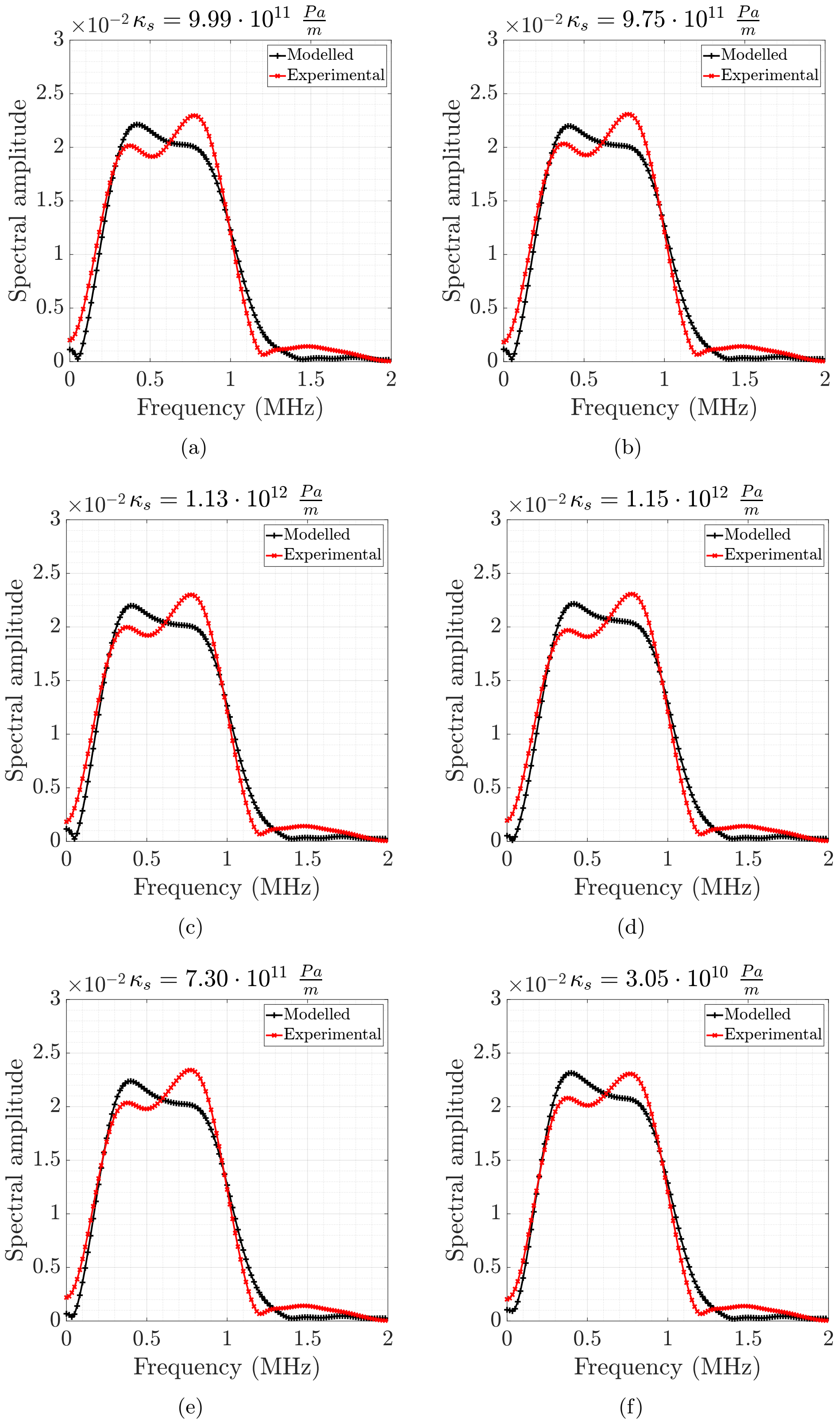

(a) (b)

(c) (d)

(e) (f)

Figure 4.23: Comparison between the amplitude spectra of modelled and laboratory reflected shear waves shown in Figure 4.22.

4.5 Discussion and Conclusions

In this chapter a novel approach has been proposed to characterise mechanically a rock joint during shear failure, at the laboratory scale. The laboratory experiments were conducted by Hedayat (2013). The novelty of this work is the application of the stochastic waveform inversion method (GA-FWFI) to invert active ultrasonic measurements. In particular, the inversion was performed for both P- and S-waves, at normal incidence with respect to the joint, to investigate the mechanical and geophysical processes that occur during shear failure by monitoring the variation of fracture specific stiffnesses.

The acquisition layout (Figure 4.1(c)) used to record transmitted and reflected waveforms, makes it possible to estimate analytically the mechanical properties (specific stiffnesses) of the joint, through the equation (4.1) and (4.2), as shown by Hedayat et al. (2014a) and Hedayat et al. (2014b). However, they are only valid for wave propagation at normal incidence and single fracture with the assumption of homogeneous background medium, taking into account only the ratio between the amplitude of reflected and transmitted waveforms. Therefore, the analytical approach can be employed only for limited cases. In order to characterise a more complex fractured medium, numerical wave modelling strategies need to be implemented, and consequently a waveform inversion approach can help with this regard. Moreover, since the 3D forward solver (WAVE3D) takes into account all the physical phenomena that are occurring in the medium, there is no need to post-process heavily the seismic data or for correction due to, for example, the geometrical spreading. It is known, in fact, that the geometrical spreading plays a major role in the observed attenuation from seismic data and needs to be taken into account for the characterisation of fractured media (Barbosa et al., 2019; Bourne et al., 2021).

With respect to the model parameters, the P- and S-wave velocity of the gypsum (sample's material), and the joint location along the x-axis, although known from other measurements, were added as free parameters in the inversion for two reasons. First, a relaxation of constraints leads to a more robust and effective inversion for cases where the analytical solution could not be applied (e.g. complex fracture geometry). Second, a possible cross-talk between the inverted model parameters can be analysed by Bayesian inference through NA.

The GA-FWFI method was applied to characterise the discontinuity in terms of its mechanical properties (κ_s and κ_n) by best fitting the experimental transmitted S- and P-waves with the modelled ones. To this end, six experimental waveforms, for each wave type, were selected at six different shear displacement values, before and after the joint failure, to sample coherently the stiffness-displacement curve (Figure 4.7(a), 4.7(c)). The shear displacement values selected, for both P- and S-waves, span from 1.17 mm before to 0.08 mm after the peak shear stress. For both compressional and shear wave inversion, the match between the experimental and modelled transmitted waveforms was very good (Figure 4.12, 4.16). The inverted normal and shear stiffness values followed with a high degree of accuracy the analytical trends (Figure 4.11(a), 4.15(a)), and the corresponding PPDs, estimated by the NA technique, showed a single peak close to the elite models, meaning that the solution was well constrained. Since the wave propagation occurs at normal incidence to the joint, transmitted compressional waves are not sensitive to the shear fracture stiffness, whereas the shear waves are not sensitive to the normal fracture stiffness. This is clearly observed in Figures 4.14 and 4.18, which show multimodal marginal PPDs for κ_s and κ_n, respectively.

Simultaneously with the fracture stiffnesses, the background velocities and the the joint location were also estimated. For both P- and S-waves, the estimates of these model parameters agreed with the corresponding true values, and they were also confirmed by the Bayesian analysis which showed that the PPDs were well constrained (Figures 4.14 and 4.18). In both inversion experiments the prior probability density distribution is set to be constant over the parameter space.

Using the elite GA models of the waveform inversion of both transducer pairs 2P-2P and 8S-8S, the reflected wavefields were modelled at the different shear displacement values analysed. From the comparison between all observed and modelled waveforms (Figure 4.20 and Figure 4.22) it is clear that the match is extremely good although the observed compressional waveforms are lacking in high frequency (Figure 4.21). This could be due to the amplitude response of the P-wave transducer which acted as a low-pass filter.

The results presented in this chapter demonstrate that this novel approach can provide reliable estimate of the mechanical characteristics (stiffnesses) of an individual fracture, its location and the background medium velocities from ultrasonic wave measurements at laboratory scale.

Chapter 5

Application of GA-FWFI to estimate the effective medium parameters of DFN models

This chapter uses the GA-FWFI method to assess the effectiveness of the equivalent medium (EM) theory for discrete fracture networks (DFNs). More specifically, it analyses how the discrete crack parameters, such as crack density, crack stiffness, crack size, and crack orientation, influence the equivalent properties of a cracked medium. To this end, two main experiments were carried out. In a first experiment, GA-FWFI is applied to synthetic seismic data generated in simulated multi-azimuth cross-hole experiments in order to recover the equivalent medium fracture stiffness along with the effective fracture strike ϕ and fracture dip δ. In a second experiment, GA-FWFI is applied to quantify the extent that discrete crack properties impact the overall elastic properties of a HTI material containing randomly distributed parallel cracks.

5.1 Introduction

Crack density and fracture intensity are two geometrical properties of fractured rocks that are routinely employed in various formulations of cracked media as measure of the degree of fracturing. Both parameters are closely related to the crack size that plays a crucial role in characterising the mechanical and hydraulic behaviour of a fractured medium. Crack size impacts not only on the mechanical stability of rock masses, but has indeed a great importance in understanding the fluid flow in the subsurface quantified by the concept of permeability. For parallel plates - permeability is in fact proportional to the crack aperture squared, which is in turn related to the crack size (Lubbe and Worthington, 2006).

Inclusion-based theories, such as those proposed by Budiansky and O'Connell (1976), Hudson (1980), Crampin (1984), and Liu et al. (2000), use crack density to relate the seismic wave propagation in a fractured rock to the anisotropy magnitude. A different approach is followed by the displacement discontinuity fracture models (Schoenberg and Douma, 1988; Schoenberg and Muir, 1989; Schoenberg and Sayers, 1995) where fractures are modelled as planes of weakness, and the degree of fracturing is quantified by the volumetric fracture intensity which provides a non-directional intrinsic measure of fracturing by incorporating both fracture size and fracture spacing (Rogers et al., 2015). Other direct measures of fracture intensity using e.g. boreholes/scanlines or outcrop mapping, in fact, provide a directionally and location biased data with respect to orientation of boreholes/photogrammetry in relation to the orientation of fractures and sampling location (see Section 5.1.3).

Nevertheless, the volumetric fracture intensity only gives an estimate of fracture spacing (which must in some way relate to crack density, see Section 5.1.1), and to be able to characterise the whole fractured medium, this parameter needs to be coupled to the compliance of individual fractures (Schoenberg and Sayers, 1995; Worthington, 2008). Consequently, the equivalent fractured medium compliances $B_{n,s}$ for a fractured medium consisting of a set of N_f parallel fractures with area S_f, distributed in a rock volume V, and with fracture compliances $Z_{n,s}$, are equal to (see equations 2.12, 2.9, Chapter 2)

$$B_{n,s} = \frac{N_f S_f}{V} Z_{n,s}. \tag{5.1}$$

Using the definition of fracture intensity, as stated in equation (2.9),

$$D_f = \frac{N_f S_f}{V}, \tag{5.2}$$

equation (5.1) can be compactly rewritten as

$$B_{n,s} = D_f Z_{n,s}. \tag{5.3}$$

Although EM theories provide a straightforward way to characterise a fractured medium, either using the crack density parameter or the equivalent medium compliance, there are limitations and inherent ambiguities in their application (as noted in Section 2.3.4 for crack density). Vlastos et al. (2003) and Lubbe and Worthington (2006) warn to use them with caution when interpreting seismic data. In fact, frequency range, low concentration of cracks, details of their spatial distribution, and the inability to distinguish between micro-cracks and meso-scale fractures, limit the applicability of these approaches (Lubbe and Worthington, 2006).

Hence, fractured media within different theoretical frameworks, are conceptually described by different discrete fracture parameters, and their influence influence upon the effective fracture parameters has not been fully explored.

5.1.1 Fracture intensity vs crack density

For a collection of rectangular cracks of sides a_i and b_i, crack density ϵ is given by (Hildyard, 2007) (see Section 2.3.4, equation (2.36))

$$\epsilon = \frac{1}{\pi V} \sum_{i=1}^{N_f} \frac{a_i^2 b_i^2}{a_i + b_i}, \tag{5.4}$$

whereas, fracture intensity D_f is given by (see equation (2.9))

$$D_f = \frac{1}{V} \sum_{i}^{N_f} a_i b_i. \tag{5.5}$$

Taking the ratio between equation (5.4) and (5.5), it is possible to express one quantity as function of the other:

$$\frac{\epsilon}{D_f} = \frac{1}{\pi}\sum_{i=1}^{N_f}\frac{a_i^2 b_i^2}{a_i + b_i}\Bigg/\sum_{i}^{N_f} a_i b_i. \tag{5.6}$$

where N_f is the number of cracks/fractures in the volume V.

For identical square fractures with side length a, equation (5.5) becomes

$$D_f = \frac{1}{V} N_f a^2, \tag{5.7}$$

that is equivalent to equation (5.2), while equation (5.6) reduces to

$$\frac{\epsilon}{D_f} = \frac{a}{2\pi}, \tag{5.8}$$

which corresponds to a linear relationship between the crack density and fracture intensity.

5.1.2 Fractures as distribution of individual cracks

Supposing that a fracture set is not simply composed of continuous interfaces (Figure 5.1(a)) but rather a distribution of individual cracks (Figure 5.1(b)) with surface S_c, how the equivalent cracked medium compliances are related to the compliances of the single crack?

Worthington (2007) and Worthington (2008) showed that the effective compliance of the whole medium needs to be scaled by the effective area of all cracks in the volume. Namely, the reduction of the effective (bulk) compliance due to the transition from a continuous fracture planes (with fracture intensity D_f) to individual cracks decreases by a factor η, is given by

$$\eta = \frac{D_c}{D_f} = \frac{N_c S_c}{V}\frac{V}{N_f S_f} = \frac{N_c S_c}{N_f S_f} \tag{5.9}$$

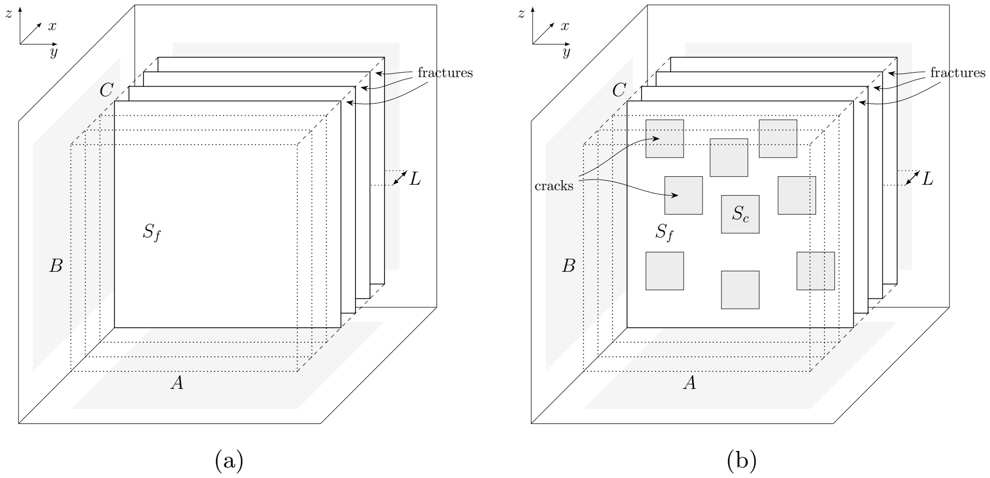

(a) (b)

Figure 5.1: Schematic representation of a fractured medium in (a) and its evolution in a cracked medium in (b). The fractured medium contains a set of parallel fractures orthogonal to the x-axis in a volume $V = ABC$. Each fracture has a surface area of $S_f = AB$ and spacing L. Whereas, in (b) the fractured medium is represented as a collection of N_c small cracks, each with area S_c.

therefore

$$D_c = \eta D_f \tag{5.10}$$

where D_c is the volumetric fracture intensity due to cracks.

For a medium containing isolated cracks with specific compliances $Z^{(c)}_{n,s}$, the equivalent cracked medium compliances, expressed by equation (5.3), become

$$B^{(c)}_{n,s} = D_c Z^{(c)}_{n,s}, \tag{5.11}$$

substituting equation (5.10) into equation (5.11), $B^{(c)}_{n,s}$ becomes:

$$B^{(c)}_{n,s} = \eta D_f Z^{(c)}_{n,s}. \tag{5.12}$$

Equation (5.12) represents therefore a linear relationship between the compliances of a single crack and the effective medium compliances. Worthington (2008) shows a similar relationship, although the inverse of D_f becomes the average crack spacing in a direction orthogonal the crack strike.

The effective compliance matrix $\mathbf{s}$ of the cracked medium is then calculated by adding up the excess compliance matrix due to cracks $\Delta s^{(c)}$ to the isotropic background medium compliance $\mathbf{s}^0$:

$$\mathbf{s} = \mathbf{s}^0 + \Delta\mathbf{s}^{(c)}. \tag{5.13}$$

where $\Delta s^{(c)}$ is defined as (see equation (2.13), Chapter 5)

$$\Delta\mathbf{s}^{(c)} = \begin{pmatrix} B_n^{(c)}/\eta & 0 & 0 & 0 & 0 & 0 \\ 0 & 0 & 0 & 0 & 0 & 0 \\ 0 & 0 & 0 & 0 & 0 & 0 \\ 0 & 0 & 0 & 0 & 0 & 0 \\ 0 & 0 & 0 & 0 & B_s^{(c)}/\eta & 0 \\ 0 & 0 & 0 & 0 & 0 & B_s^{(c)}/\eta \end{pmatrix}. \tag{5.14}$$

To yield the stiffness matrix $\mathbf{c}$ equation (5.13) can be simply inverted. Nevertheless, to model the equivalent cracked medium (quantified in the equivalent fracture stiffness, or volumetric fracture stiffness $\kappa_{n,s}^{vf}$), WAVE3D requires as input the specific stiffness $\kappa_{n,s} = Z_{n,s}^{-1}$ of the fracture plane that contains the smaller cracks, along with the fracture intensity D_f that corresponds to the inverse of the fracture spacing L (see Section 5.1.3). Hence, from equation (5.3) follows:

$$\kappa_{n,s}^{vf} = (B_{n,s})^{-1} = \frac{1}{D_f}\kappa_{n,s} = L\kappa_{n,s}. \tag{5.15}$$

To take into account the stiffness increment of the whole medium due to the transition from a continuous fracture plane to individual cracks, the effective medium stiffnesses $\kappa_{n,s}^{vf}$ is derived from equation (5.12) as

$$\kappa_{n,s}^{vf} = \frac{1}{\eta D_f}\kappa_{n,s}^{(c)} \equiv \frac{L}{\eta}\kappa_{n,s}^{(c)} \tag{5.16}$$

where $\kappa_{n,s}^{(c)} = \eta\kappa_{n,s}$.

5.1.3 Linear vs volumetric intensity for cracked media

A classification scheme for the fracture intensity parameter have been proposed to quantitatively describe fractured rock masses for different scales and dimensions (Dershowitz and Herda, 1992; Rogers et al., 2015).

This scheme is known as the P_{ij} system where the subscript i represents the dimension of the sample ($i = 1$ for 1D borehole, $i = 2$ for 2D map, and $i = 3$ for 3D volume), whereas the subscript j indicates the dimensions of the measure, e.g. dimensionless measure ($j = 0$), length ($j = 1$), area ($j = 2$), introduced by Dershowitz (1998). Hence, according to this system, the fracture intensities are measured in terms of P_{10}, P_{21}, P_{32}. Nevertheless, in order to be consistent with the definition of fracture intensity expressed in Section 5.1.1, the corresponding multi-dimensional fracture intensities are defined as follows:

1. *Linear fracture intensity*, D_f^{1D} ($\equiv P_{10}$), is usually measured from borehole data or scan lines. It counts the number of fractures per unit length (units 1/m);

2. *Surface fracture intensity*, D_f^{2D} ($\equiv P_{21}$), is derived by mapping outcrop or tunnel walls, and it measures the length of fractures per unit area (units m/m^2);

3. *Volumetric fracture intensity*, D_f^{3D} ($\equiv P_{32}$) or simply D_f throughout the Chapter. It is not always possible to be directly measured since it is extremely difficult to observe the internal geometry of fractures. However, it can be estimated from the linear and surface fracture intensity (Dershowitz and Herda, 1992). It measures the area of fractures per unit volume (units m^2/m^3).

Volumetric fracture intensity yields a more comprehensive indication of rock volume fracturing and it is used as an input parameter to generate DFN models (Rogers et al., 2015). However, the linear fracture intensity is the easiest to measure and it can be used to have an estimate of the average crack spacing (Lu et al., 2017).

Although linear fracture intensity can produce biased estimates of crack spacing with respect to orientation of boreholes in relation to the orientation of fractures and sampling location, it can be converted to non-directional intensity property, i.e. the volumetric intensity (Rogers et al., 2015; Lu et al., 2017).

Figure 5.2(a) shows a comparison between the linear (blue curve) and volumetric fracture intensity (red curve) for the cracked models displayed later in Figures 5.14(a), 5.14(b), and 5.14(c). In these models the crack length is 3 m, and the crack density corresponds to $\epsilon = 0.01,\ 0.025$, and 0.05, respectively. The volumetric fracture intensity, for all crack density cases, is computed using equation (5.8), whereas the linear fracture intensity is estimated by counting the number of cracks that intersect random generated scanlines normal to the crack plane, and taking their arithmetic mean values. The distribution of the number of cracks counted along the scanlines for each crack density value, with its mean value are shown in Figures 5.2(b), 5.2(c), 5.2(d). Since the cracks are randomly generated in the volume, the crack distribution is roughly symmetric around the arithmetic mean value. The linear fracture intensity is linearly related to the crack density and it is roughly 4 times larger than the volumetric fracture intensity.

As just shown, fracture intensities of different dimensionality cannot have the same values for the same fractured volume (Lu et al., 2017). However, a special case of fracture model having the same fracture intensity is a set of fractures composed of identical, parallel, and aligned fractures as shown in Figure 5.1(a), where the three fracture intensity parameters degenerate to an equivalent case. Here the fracture volume is $V = ABC$ and the area of a single fracture plane is $S_f = AB$. The fracture intensity parameters are thus as follows

1. $D_f^{1D} = \frac{N_f}{C} = \frac{1}{L}$
2. $D_f^{2D} = \frac{N_f A}{AC} = \frac{1}{L}$
3. $D_f^{3D} = \frac{N_f AB}{ABC} = \frac{1}{L}$

Therefore, $D_f^{1D} \equiv D_f^{2D} \equiv D_f^{3D} = \frac{1}{L} = D_f^0$

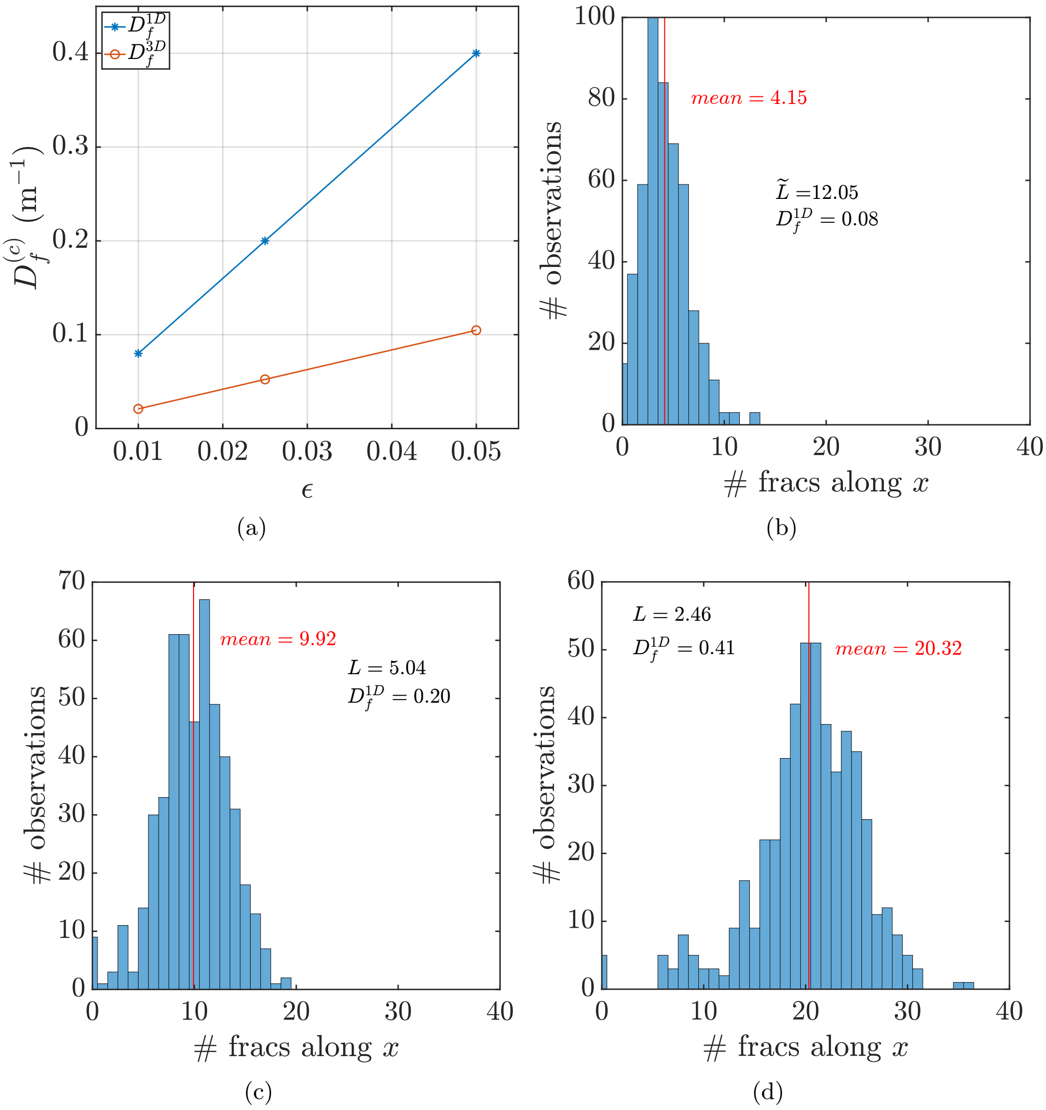

Figure 5.2: (a) Comparison between the linear (blue curve) and volumetric fracture intensity (red curve) for the cracked models displayed in Figures 5.14(a), 5.14(b), and 5.14(c). (b), (c), and (d) are distribution of the number of cracks counted along the scanlines, randomly generated, for crack density $\epsilon = 0.01,\ 0.025,\ 0.05$, respectively. The red lines show the arithmetic mean values of the number of cracks along the x-axis.

5.1.4 Effective crack length in numerical models

Crack length is a very important parameter for crack generators since the crack density depends on the cube of the length (equation (5.4)). In fracture modelling codes crack length is usually defined as the distance between the two end grid nodes. However, (Hildyard et al., 1995; Hildyard and Young, 2002) have shown that, for a crack under static load, the WAVE3D solution converges to the correct one for an effective crack length shorter than the actual length. Hildyard (2001) has empirically calculated that the positions of the crack tips span from 0.3 to 0.4 elements from the end nodes.

This observation has been implemented in the calculation of the crack density ϵ, where the crack length l is substituted by the effective crack length $\widetilde{l}$ that is defined as (Hildyard, 2001)

$$\widetilde{l} = (n - 0.7)\Delta h = l - 0.7\Delta h \tag{5.17}$$

where n is the number of elements in the crack, and Δh is the grid spacing.

5.2 From a discrete fracture model to the effective medium model

In this section the relationship in equation (5.15) is tested by using GA-FWFI to estimate the effective fractured media stiffness, and equivalent fracture sets orientation, from synthetic waveforms generated for known fracture networks. The numerical experiments simulate a cross-hole seismic acquisition having a single point source outside the cracked medium, and 198 3-component receivers, evenly distributed in three vertical boreholes with an interborehole spacing of 20 m, placed outside the cracked volume on the opposite side of the source location (Figure 5.3).

To model realistic cracked media, the explicit fracture approach (DFN approach) is employed (Figure 5.3(a)), and the “observed” data is generated. For the inverse process the EM model (Figure 5.3(b)) is utilised, allowing the bulk fractured medium properties to be estimated by best fitting the observed seismic data.

To model the equivalent cracked medium, as explained in Section 5.1.2, WAVE3D requires as input parameters:

- specific stiffnesses $\kappa_{n,s}$ of the fracture planes containing the smaller cracks;
- fracture intensity D_f corresponding to the inverse of fracture spacing L;
- fracture strike ϕ and fracture dip δ to define the fracture set orientation.

The volumetric fracture stiffness is the calculated using equation (5.15).

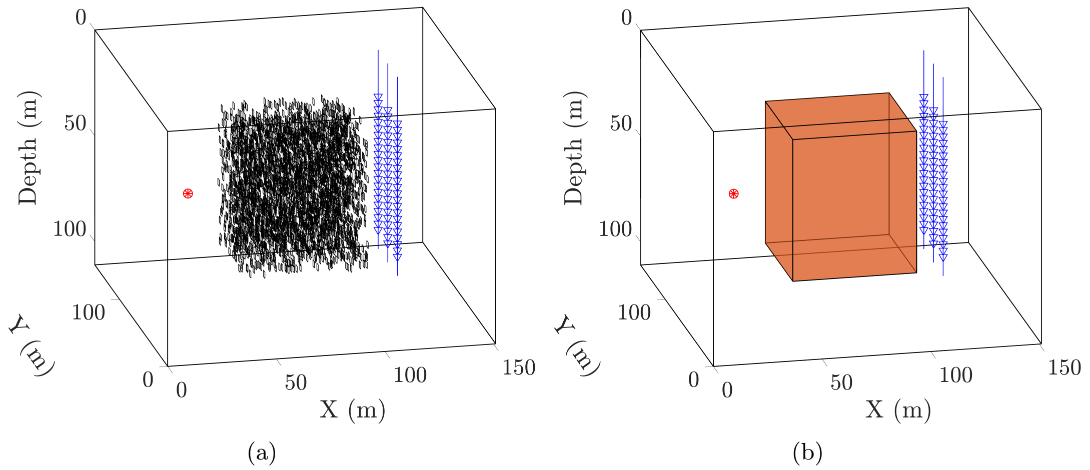

Figure 5.3: A simulated cross hole seismic acquisition across a fractured medium modelled as a distribution of small isolated cracks (DFN approach) in (a), and as an fracture-induced anisotropic medium (EM approach) in (b). In order to estimate the fracture-induced anisotropic parameters, the EM approach is used in the waveform inversion method to best fit the observed data generated through the DFN model.

Two main experiments were carried out. Firstly, GA-FWFI was applied to assess whether the effective fracture strike (ϕ) and dip (δ) angles could be correctly recovered from acquisition at different azimuths in a cracked medium containing vertical cracks. In a second numerical experiment, the waveform inversion was performed to investigate to what extent discrete crack properties such as crack size, crack stiffness, and crack density impact the overall elastic properties of a HTI material containing randomly distributed cracks.

5.3 Application of GA-FWFI to a multi-azimuth acquisition

The base fracture model consists of vertical square cracks normal to the x-axis, embedded in a purely isotropic background medium with P-wave velocity $v_p = 5200$ m/s, S-wave velocity $v_s = 3160$ m/s, and density $\rho = 2700$ Kg/m^3. Cracks are identical with size 3×3 m^2, crack density $\epsilon = 0.025$, and normal crack stiffness $\kappa_n = 1 \cdot 10^9$ Pa/m. Shear crack stiffness is half of the normal stiffness. Cracks are randomly distributed along parallel planes which are 1 m apart, thus $L = 1$ m. The dimension of the cracked zone is $(x, y, z) = (57\text{m},\ 57\text{m},\ 67\text{m})$ placed within a model with overall dimension of

$(x, y, z) = (150\text{m},\ 150\text{m},\ 110\text{m})$ as displayed in Figure 5.3(a) and Figure 5.4.

Compressional and shear waves are generated from a single point source by a smooth excitation in the σ_{12} component of stress. The dominant source frequency (f_{peak}) is approximately 175 Hz corresponding to a dominant wavelength of $\lambda_P \approx 30$ m, and $\lambda_s \approx 18$ m. The dominant wavelength was chosen much longer than the crack size to meet the theoretical requirement of a DFN model for successful analysis with an effective medium approach. The grid spacing is set to $\Delta h = 1$ m to sample correctly the S-waves (shorter wavelength), and the time step to $\Delta t = 70$ μs to satisfy the stability criterion of the wave equation solution. To minimise the spurious reflections from the model edges the PML absorbing condition is used with a layer thickness of 20 elements.

To record the seismic data at different azimuths, the source-receiver geometry is rotated clockwise by angles of $\phi = 0°,\ 15°,\ 30°,\ 60°$ with respect to the x-axis and about the centre of the cracked volume. For all cases, the cracked zone remains unchanged. Figure 5.4 shows a plan view of the cracked zone and the source-receiver geometry at different azimuth angles, from $\phi = 0°$ in Figure 5.4(a), to $\phi = 60°$ in Figure 5.4(d). The recorded x and y components of velocity, referred to the middle receiver line, are shown in Figures 5.5 and 5.6, respectively. These seismograms, along with the z component of velocity (Figure 5.7) and the other two receiver lines not showed here, comprise the observed data which feed the GA-FWFI algorithm.

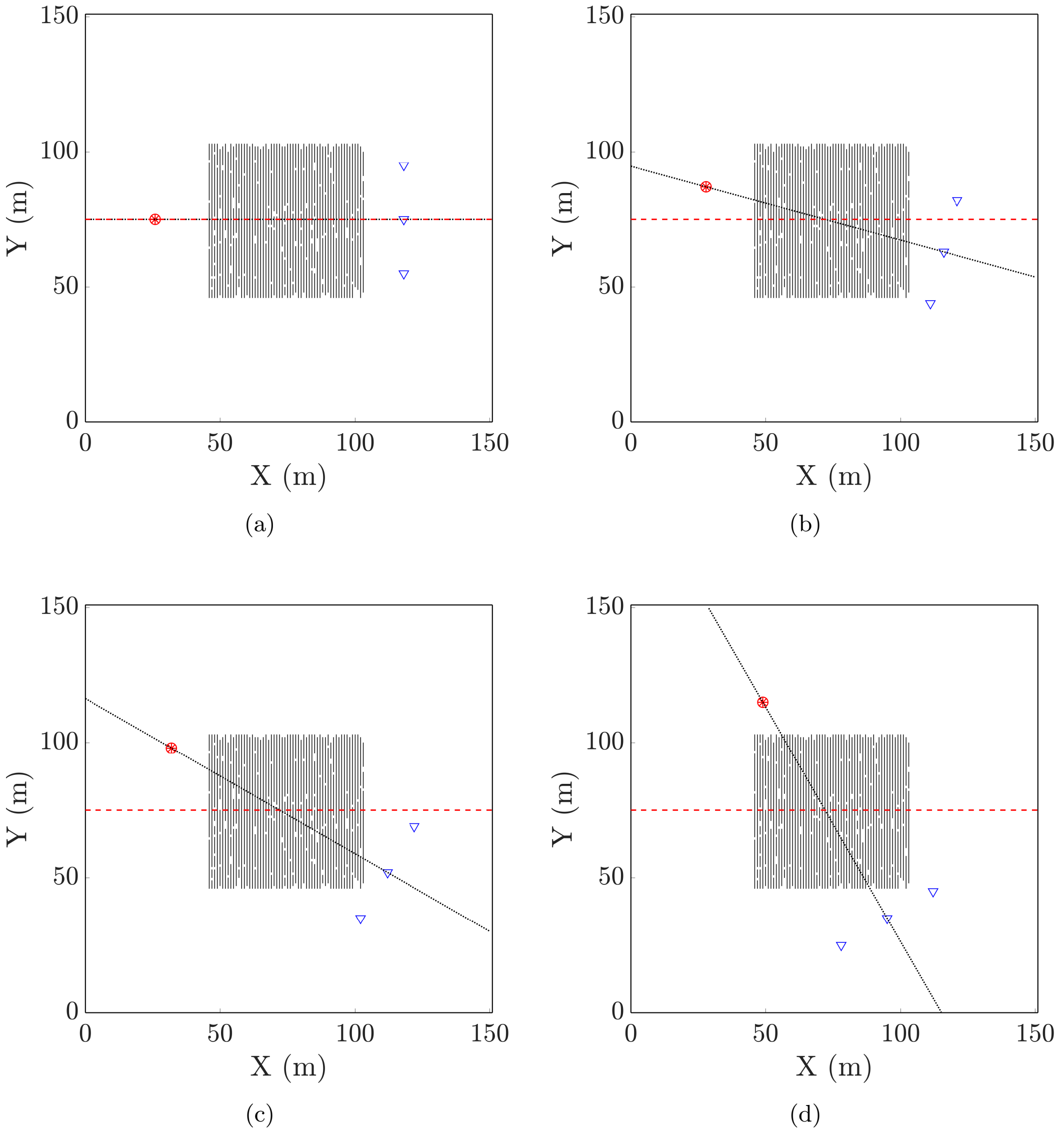

Figure 5.4: Plan view of the cracked medium shown in Figure 5.3(a) at different azimuth angles acquisition. (a) at $\phi = 0°$, (b) at $\phi = 15°$, (c) at $\phi = 30°$, (d) at $\phi = 60°$ with respect to the $x-$axis. Due to the model geometry, ϕ also corresponds to the fracture strike in the coordinate system source-(middle) receiver line (black line). The red dashed line is the symmetry axis of the fractured medium.

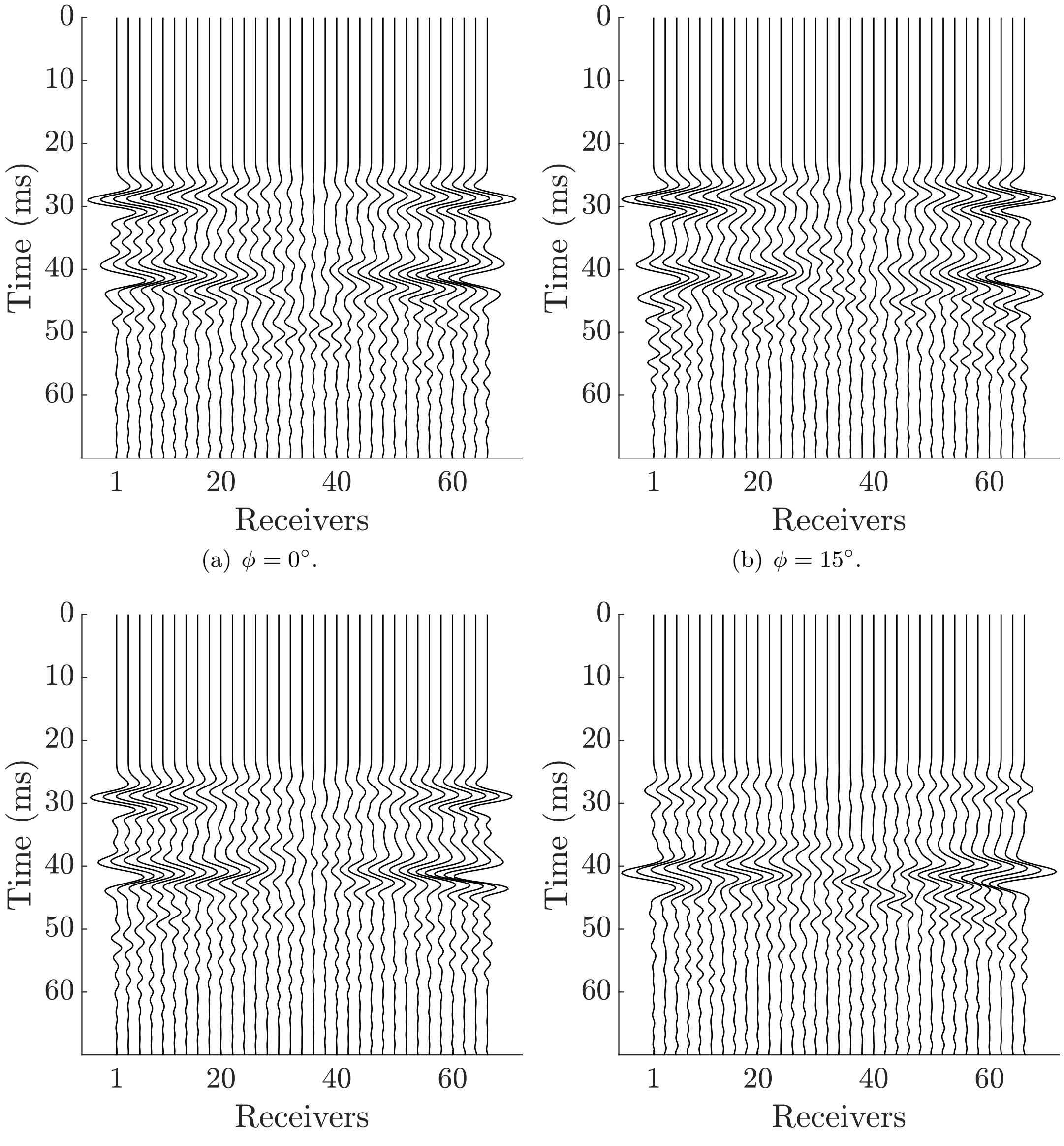

(a) $\phi = 0°$.

(b) $\phi = 15°$.

(c) $\phi = 30°$.

(d) $\phi = 60°$

Figure 5.5: Raw data (observed data) of velocity component x recorded by the line receiver 2 (middle) at four azimuth angles: (a) $\phi = 0°$, (b) $\phi = 15°$, (c) $\phi = 30°$, (d) $\phi = 60°$.

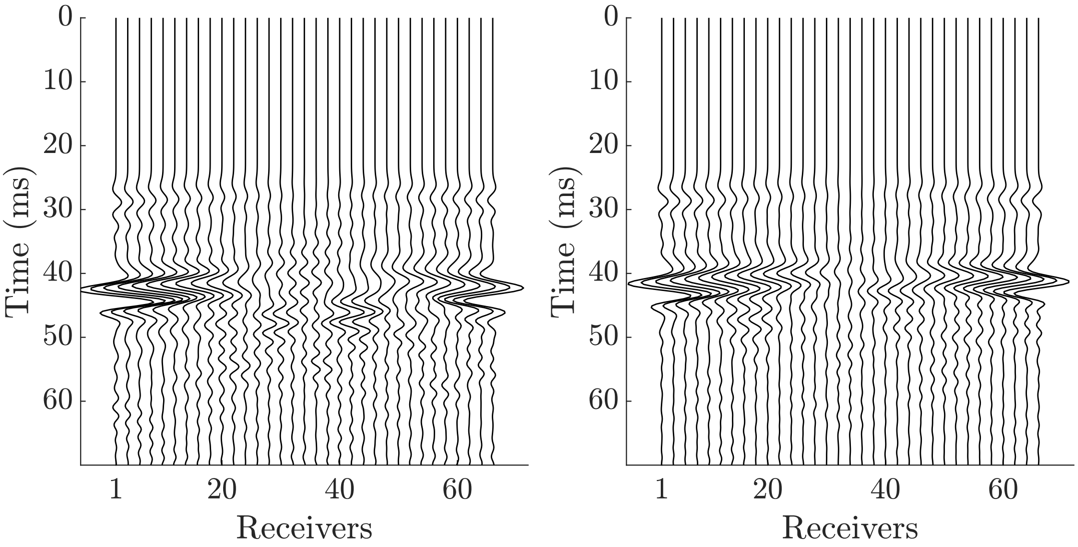

(a) $\phi = 0°$.

(b) $\phi = 15°$.

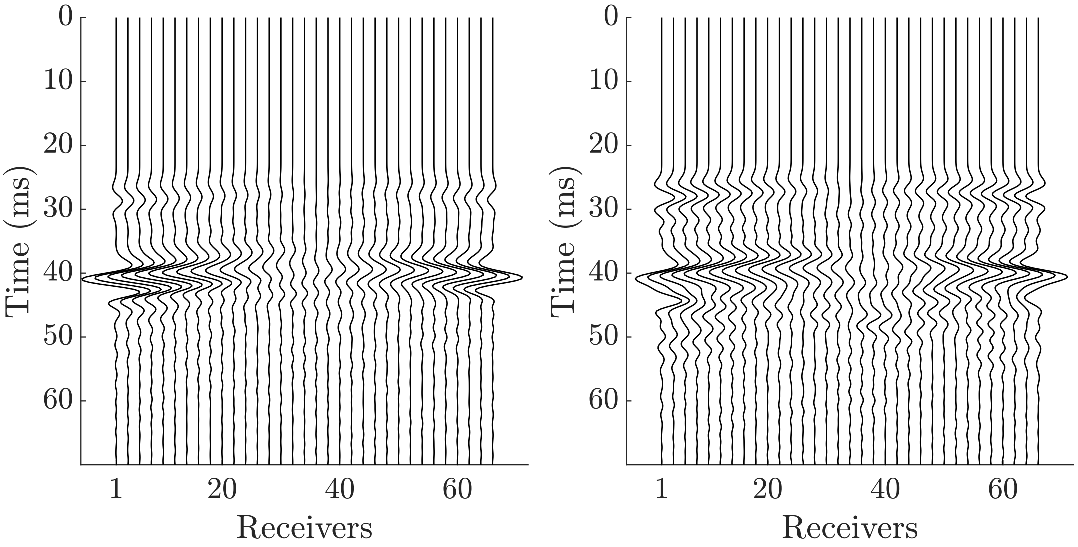

(c) $\phi = 30°$.

(d) $\phi = 60°$.

Figure 5.6: Raw data (observed data) of y velocity component recorded by the line receiver 2 (middle) at four azimuth angles: (a) $\phi = 0°$, (b) $\phi = 15°$, (c) $\phi = 30°$, (d) $\phi = 60°$.

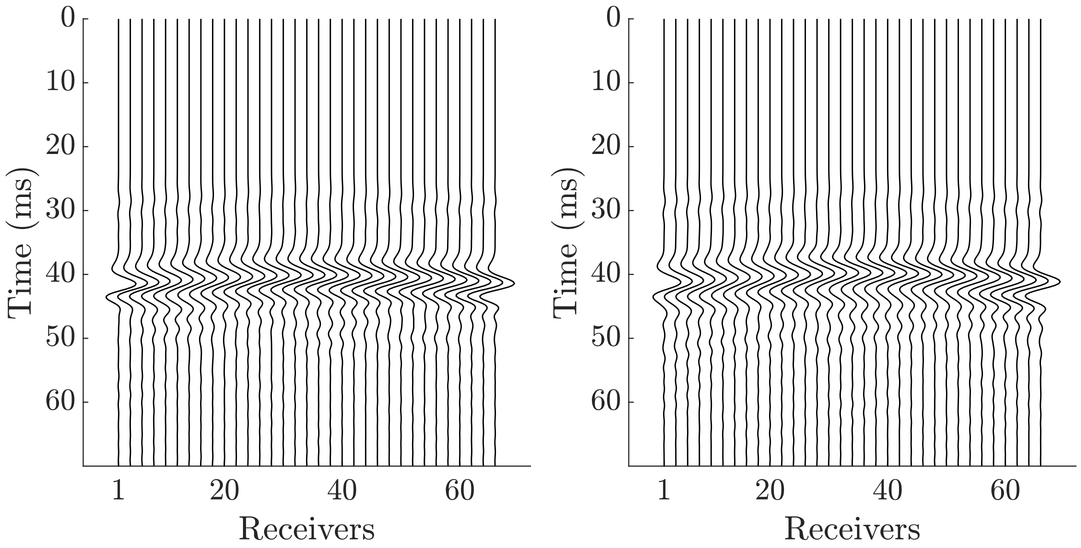

(a) $\phi = 0°$.

(b) $\phi = 15°$.

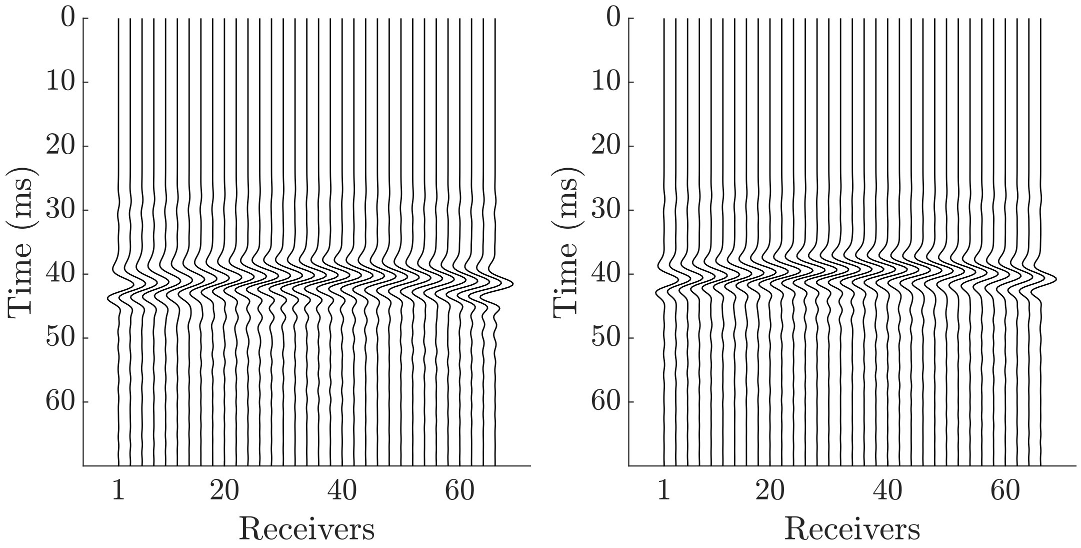

(c) $\phi = 30°$.

(d) $\phi = 60°$.

Figure 5.7: Raw data (observed data) of z velocity component recorded by the line receiver 2 (middle) at four azimuth angles: (a) $\phi = 0°$, (b) $\phi = 15°$, (c) $\phi = 30°$, (d) $\phi = 60°$.

5.3.1 GA inversion results and the Bayesian analysis

The genetic algorithm operates on the multi-parameter space, preconditioned by the exact background elastic properties (v_p, v_s, and ρ), the same used for the DFN models. It exploits a random population of 80 models, that evolve through 30 generations according to a misfit function defined as the $\mathcal{L}_2-$norm between the observed data and the modelled data (here, the EM approach is used). The source function is assumed known. Table 5.1 summarises the control parameters of the GA algorithm.

GA parameters	**Values**
Model population size	80
Generations	30
Tournament size	3
Mutation ratio	0.4
b	2
d	0.3
Elitism	0.05

Table 5.1: GA control parameters used in this numerical experiment.

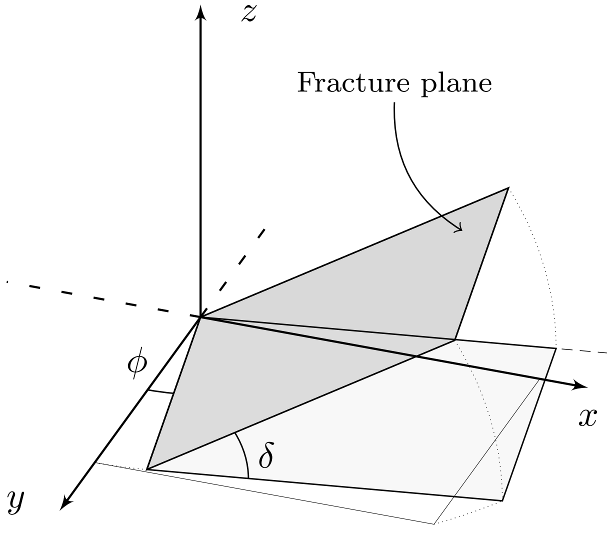

Figure 5.8: Schematic illustration of a fracture plane. The angle δ represents the fracture dip, so the angle between the horizontal plane and the fracture plane. The angle ϕ represents the fracture strike, so the angle that forms the intersection of the fracture plane with the $x-y$ plane, and the y axis.

The EM model, that needs to be estimated through GA-FWFI, can be described by the parameter vector $\mathbf{m} = \{\kappa_n^{vf}, \phi, \delta\}$ where the angle ϕ represents the fracture strike with respect to the y-axis, and δ is the fracture dip (angle between the fracture plane and the $x-y$ plane) as depicted in Figure 5.8. Due to the model geometry, the fracture strike corresponds to the azimuth angle. The shear fracture stiffness κ_s^{vf} is fixed in the inverse process assuming the value $\kappa_s^{vf} = \kappa_n^{vf}/2$. The fracture intensity $D_f = 1/L$ is also fixed at the arbitrary value of $1/L = 0.001$ m^{-1}, such that the volumetric fracture stiffness $\kappa_{n,s}^{vf}$ is calculated from equation (5.15)). Therefore, the stiffness matrix of such a medium can be defined as (equation (2.14), Chapter 2):

$$\boldsymbol{c} = \begin{pmatrix} (\lambda+2\mu)(1-\Delta_n) & \lambda(1-\Delta_n) & \lambda(1-\Delta_n) & 0 & 0 & 0 \\ \lambda(1-\Delta_n) & (\lambda+2\mu)(1-r^2\Delta_n) & \lambda(1-r\Delta_n) & 0 & 0 & 0 \\ \lambda(1-\Delta_n) & \lambda(1-r\Delta_n) & (\lambda+2\mu)(1-r^2\Delta_n) & 0 & 0 & 0 \\ 0 & 0 & 0 & 0 & 0 & 0 \\ 0 & 0 & 0 & 0 & \mu(1-\Delta_s) & 0 \\ 0 & 0 & 0 & 0 & 0 & \mu(1-\Delta_s) \end{pmatrix} \tag{5.18}$$

with

$$\begin{aligned} r &\equiv \frac{\lambda}{\lambda+2\mu} \\ \Delta_n &= \frac{(\lambda+2\mu)\,(L\kappa_n)^{-1}}{1+(\lambda+2\mu)\,(L\kappa_n)^{-1}} \\ \Delta_s &= \frac{2\,(L\kappa_s)^{-1}\,\mu}{1+2\,(L\kappa_s)^{-1}\,\mu} \end{aligned}$$

The stiffness matrix in equation (5.18) is then transformed using the tensor rotation (or Bond transformation) according to the angle ϕ around the $z-$axis, followed by a rotation of an angle δ around the new $y-$axis (equations (2.25), (2.26), Chapter 2).

Figure 5.9(b) shows the compressional velocity as function of angle (the fracture strike ϕ) comparing the expected theoretical values calculated from the inverted stiffness matrix in equation (5.18), namely $v_p = \sqrt{c_{33}/\rho}$, and the manual picking of the P-wave arrivals (Figure 5.9(a)). The P-wave anisotropy parameter (Tsvankin parameter $\varepsilon^{(V)}$)

calculated from the inverted stiffness matrix is

$$\varepsilon^{(V)} = \frac{c_{11} - c_{33}}{2c_{33}} = -0.0625. \tag{5.19}$$

The elastic parameters used in this simulation correspond to the isotropic background medium defined previously, and the equivalent medium stiffness $\kappa_n^{vf,GA}$ found via GA-FWFI. The waveforms are extracted from a single receiver in the central borehole having the same depth as the source, forming the angles with respect to the $x-$axis from 0° to 90°, as shown in Figure 5.4.

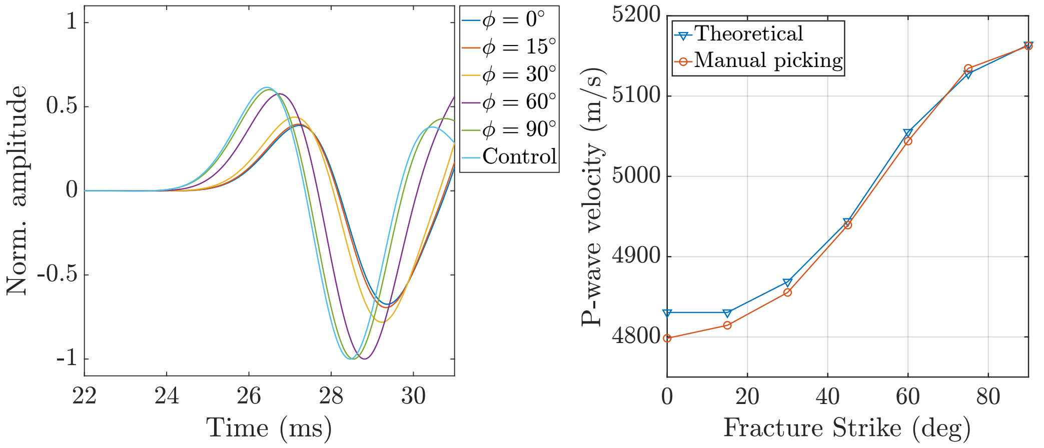

(a) (b)

Figure 5.9: (a) First P-wave arrivals at different azimuth angles ϕ. (b) Compressional velocity as function of the angle ϕ. Blue curve is calculated using the stiffness matrix of equation (5.18) and the Bond transformation to rotate the coordinate system according to ϕ. Red curve is obtained by picking the first arrivals of the compressional waves shown in (a).

The search boundaries for the inverted parameters are listed in Table 5.2. The maximum frequency inverted is 200 Hz, which corresponds to a wavelength of $\lambda_p \approx 26$ m, and $\lambda_s \approx 16$ m, therefore approximately 9 times the crack length for P-waves, and 6.5 times for S-waves.

The successful application of the waveform inversion can be seen in the good match between the observed (black) and modelled data (red) in Figures 5.10-5.12 of representative seismic data (three components of the velocity for the middle line of receivers). These correspond to the same seismograms showed in Figures 5.5-5.7, after applying a low-pass filter with cutoff frequency of 200 Hz.

Model parameter	**Range**	**Unit**
Normal fracture stiffness (κ_n^{vf})	$[1 \cdot 10^{10}, 5 \cdot 10^{13}]$	Pa
Fracture strike (ϕ)	$[-15°,\ 40°]$	
Fracture dip (δ)	$[70°,\ 110°]$	

Table 5.2: Free parameters in the inversion with their search boundaries.

The best GA models for each azimuth case, are listed in Table 5.3. Finally, the posterior probability density function is estimated through the NA method, and the marginal probability distributions, for each inverted model parameter, are shown in Figure 5.13. All parameters are well constrained by the inversion and they well depict the ground truth represented by the solid black line.

	$\kappa_n^{vf,GA}$	δ^{GA}	ϕ^{GA}
Case 1 ($\phi = 0°$)	$3.20 \cdot 10^{11}$ Pa	89.5°	-1.2
Case 2 ($\phi = 15°$)	$3.26 \cdot 10^{11}$ Pa	91.5°	16.5
Case 3 ($\phi = 30°$)	$3.24 \cdot 10^{11}$ Pa	90.2°	32.1
Case 4 ($\phi = 60°$)	$3.28 \cdot 10^{11}$ Pa	90.5°	61.9

Table 5.3: Best GA models for the 4 cases analysed.

As shown in Table 5.3, the effective fracture set orientation is extremely well retrieved, for both dip and strike angle in all inversion cases. Cracks in the DFN models are vertical, so $\delta = 90°$, and orthogonal to the $x-$axis, therefore $\phi = 0°$. Nevertheless, in the coordinate system of the acquisition geometry, that is rotated with respect to the $x-$axis, ϕ corresponds to the actual angle between the source-middle receivers line direction and the $x-$axis. The dip angle, on the contrary, remains unchanged.

The inverted values of the effective fracture stiffness $\kappa_n^{vf,GA}$, with respect to the azimuth angles, show coherently the same value that is approximately $3.2 \cdot 10^{11}$ Pa. The expected value of bulk stiffness κ_n^{vf} for the medium is given by equation (5.16):

$$\kappa_n^{vf} = \frac{L}{\eta}\kappa_n^{(c)} \approx 1.5 \cdot 10^{10} \text{ Pa} \tag{5.20}$$

with

$$L = 1 \text{ m} \tag{5.21}$$

$$\eta = \frac{N_c S_c}{N_f S_f} = \frac{2811 \cdot (3 - 0.7)^2 \text{m}^2}{58 \cdot (57 \cdot 67) \text{ m}^2} = 0.0671 \tag{5.22}$$

$$\kappa_n^{(c)} = 1 \cdot 10^9 \text{ Pa/m}. \tag{5.23}$$

Comparing the expected value κ_n^{vf} with the inverted value $\kappa_n^{vf,GA}$, it can be noted that the latter is approximately 20 times larger than the predicted theoretical value. This unexpected result leads to the second series of numerical experiments which aim to reveal the direct relationship between discrete crack parameters and the corresponding best-fit effective medium parameters.

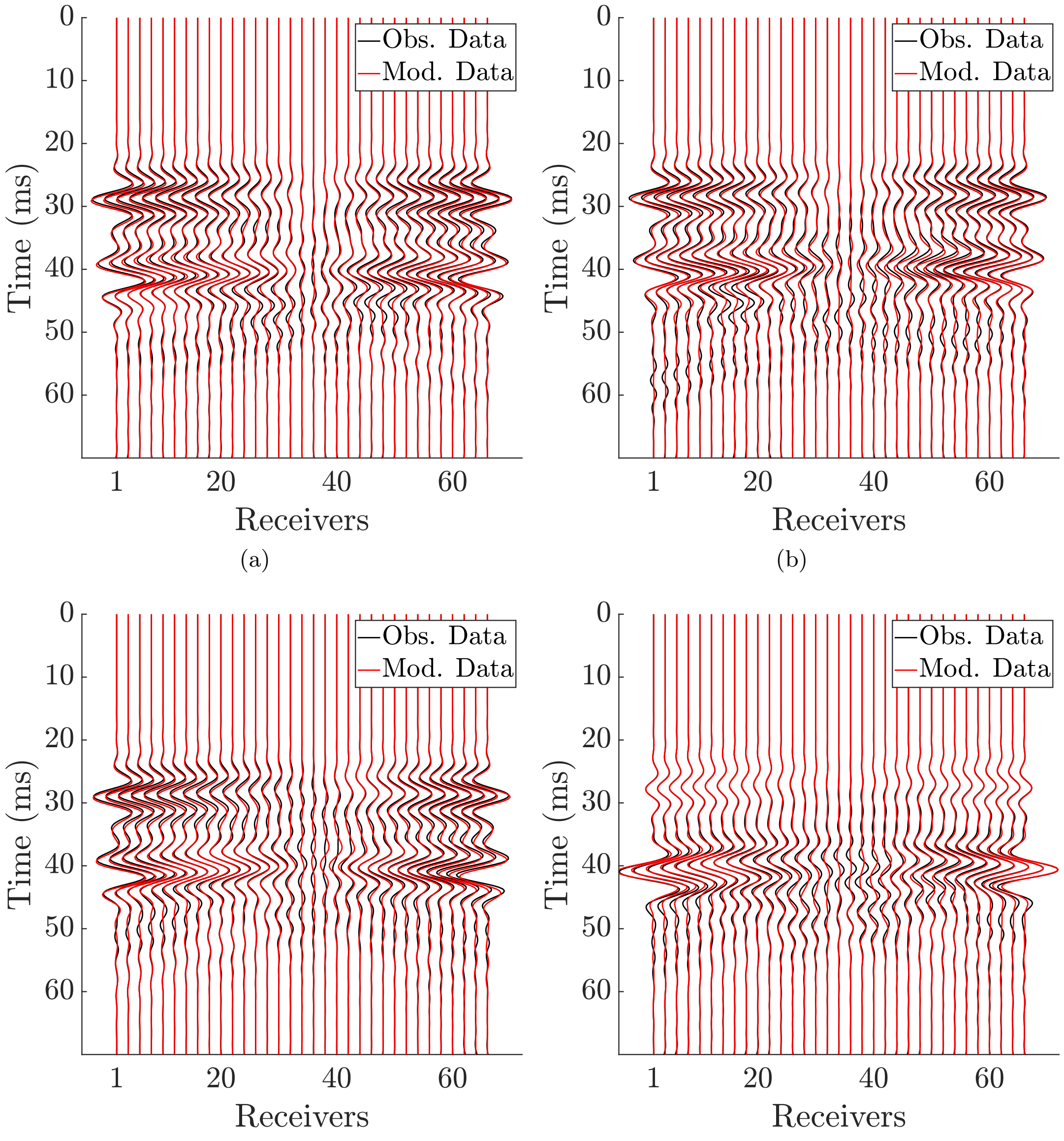

(a) (b)

(c) (d)

Figure 5.10: Comparison between the observed data (black) and the best predicted seismograms (red) through the waveform inversion of x component of velocity for azimuth angles of $\phi = 0°$ in (a), $\phi = 15°$ in (b), $\phi = 30°$ in (c), $\phi = 60°$ in (d). A low-pass filter with cutoff frequency of 200 Hz has been applied to all cases in both datasets.

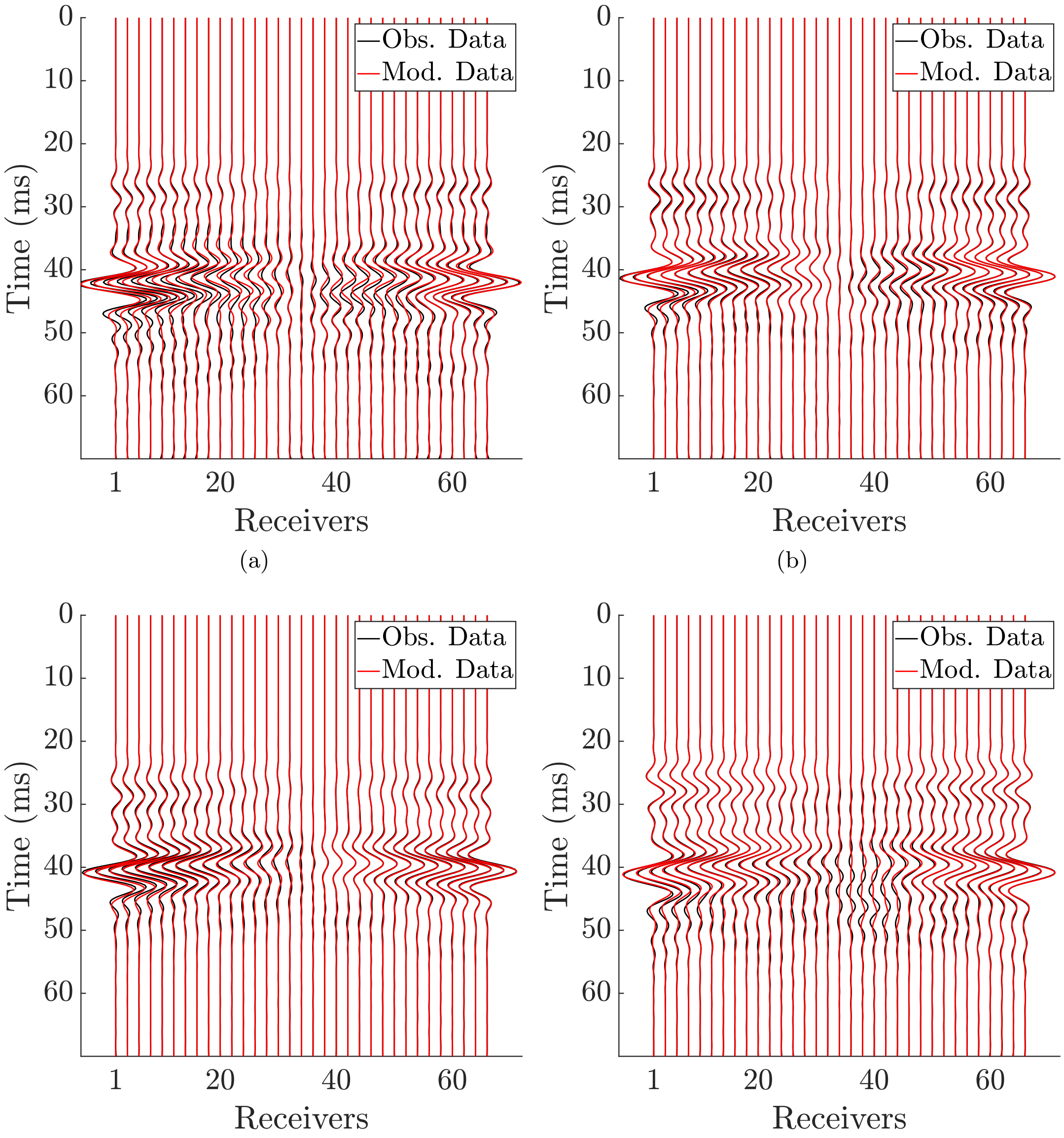

(a) (b)

(c) (d)

Figure 5.11: Comparison between the observed data (black) and the best predicted seismograms (red) through the waveform inversion of y component of velocity for azimuth angles of $\phi = 0°$ in (a), $\phi = 15°$ in (b), $\phi = 30°$ in (c), $\phi = 60°$ in (d). A low-pass filter with cutoff frequency of 300 Hz has been applied to all cases in both datasets.

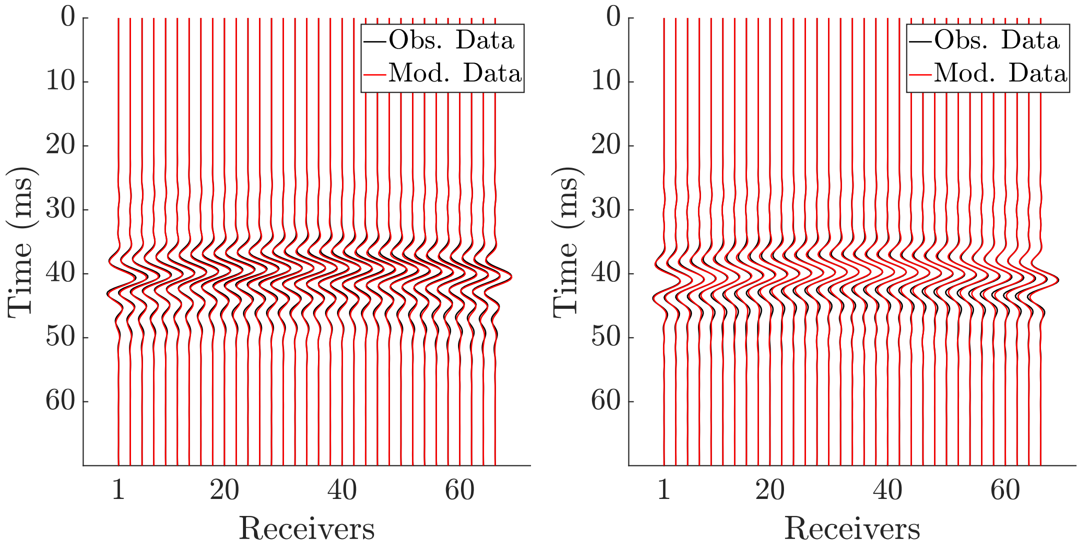

(a) $\phi = 0°$ velocity component x.

(b) $\phi = 15°$ velocity component x.

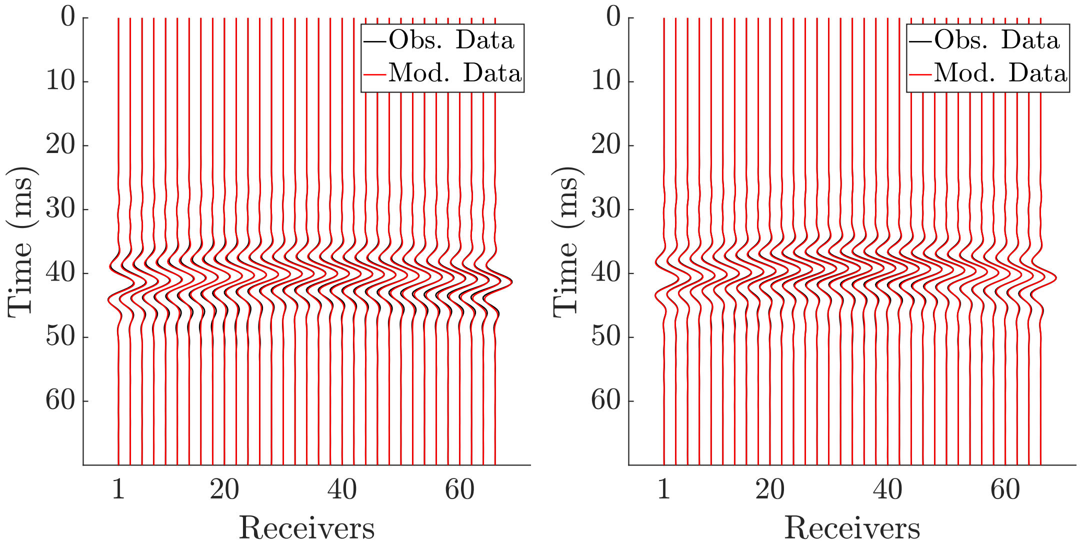

(c) $\phi = 30°$ velocity component x.

(d) $\phi = 60°$ velocity component x.

Figure 5.12: Comparison between the observed data (black) and the best predicted seismograms (red) through the waveform inversion of z component of velocity for azimuth angles of $\phi = 0°$ in (a), $\phi = 15°$ in (b), $\phi = 30°$ in (c), $\phi = 60°$ in (d). A low-pass filter with cutoff frequency of 300 Hz has been applied to all cases in both datasets.

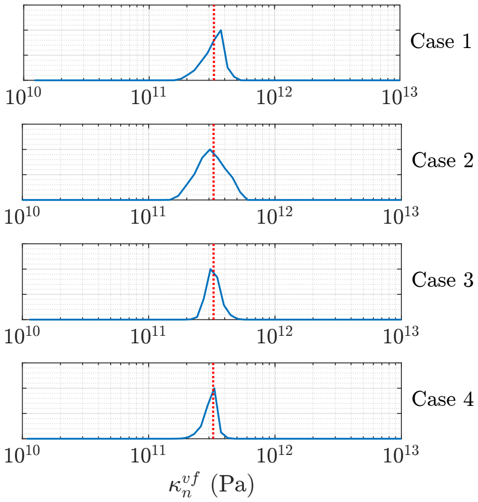

(a) Effective medium stiffness κ_n^{vf}

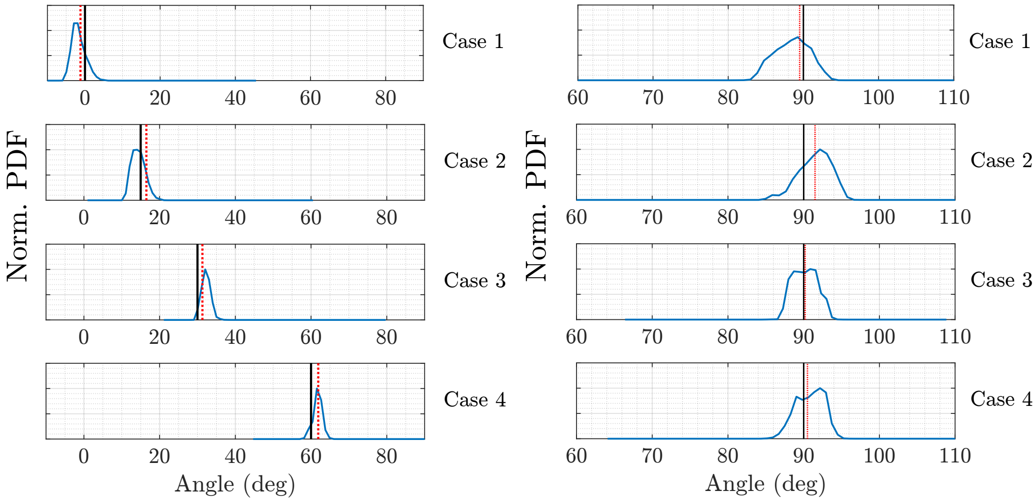

(b) Effective fracture strike ϕ.

(c) Effective fracture dip δ.

Figure 5.13: Marginal PPDs computed by the NAB algorithm using the GA model ensembles. (a) shows the marginal PPD of the effective medium stiffness κ_n^{vf}, (b) the marginal PPD of the strike angle ϕ, and (c) the marginal PPD of the dip angle δ. The solid black line represents the ground truth, whereas the dashed red line the best GA inverted parameter.

5.4 Waveform inversion to assess the effectiveness of the EM models

The first numerical experiment (Section 5.3) has shown the successful application of GA-FAWFI to retrieve both fracture orientation and volumetric fracture stiffness in a simulated multi-azimuth acquisition. However, the inverted values of volumetric fracture stiffness do not follow the theoretical derived values of equation (5.16).

A second series of numerical experiments was therefore designed to analyse how the discrete crack parameters, such as crack density, crack stiffness, and crack size, influence the effective properties of a cracked medium. In all cases seismic wavelengths are much longer than the crack length, so that the effective medium approach still applies.

To this end, a set of 54 different DFN scenarios consisting of vertical cracks orthogonal to the $x-$axis in an isotropic background medium are generated. Cracks are randomly distributed along parallel planes which are 1 m apart, thus $L = 1$ m. The isotropic medium properties are the same as the previous experiment, so $v_p = 5200$ m/s, $v_s = 3160$ m/s, and $\rho = 2700$ Kg/m^3. The explicit crack parameters are in turn changed while keeping the other two constant. Crack density takes values of $\epsilon = (0.01,\ 0.025,\ 0.05)$, crack length of $l = (3,\ 4,\ 10)$ m, and normal crack stiffness of $\kappa_n^{(c)} = (1,\ 2,\ 5,\ 10,\ 50,\ 100)$ GPa/m. The ratio $\kappa_n^{(c)}/\kappa_s^{(c)}$ is set to 2 for all cases, and the acquisition geometry is kept fixed. Figure 5.14 illustrates the cracked media involved in this study for all crack density and crack size values: each row shows the cracked media with the same crack size, but with crack density increasing from left to right. The DFN models can be described, consequently, by the parameter vector $\mathbf{m} = \{\epsilon,\ \kappa_n^{(c)},\ l\}$. The fracture strike ϕ and fracture dip δ are set to 0° and 90°, respectively, and they remain fixed throughout the experiment.

Compressional and shear waves are generated from a single point source by a smooth excitation in the σ_{12} component of stress. The source signature is a Ricker wavelet. All cases were designed to fit within the Rayleigh scattering regime (i.e. $\lambda_S/l \gg 1$).

For $l = 3$ m, and $l = 4$ m the dominant source frequency (f_{peak}) is approximately 175 Hz. The corresponding dominant wavelength is $\lambda_P \approx 30$ m, and $\lambda_S \approx 18$ m which is approximately 8-10 times the crack length for P-waves, and roughly 5-6 times for S-waves. For $l = 10$ m the dominant source frequency is reduced to 90 Hz in order to meet the long wavelength requirement for the EM approach ($\lambda_S/l > 3$ leads to a valid approximation of a cracked medium through the EM theory (Yousef and Angus, 2016)). In fact, in this case, $\lambda_P \approx 57$ m and $\lambda_S \approx 38$ m which is approximately 6 and 4 times the crack length for P-waves and S-waves, respectively. Representative raw data (observed data) of x, y and z components of velocity (middle borehole) for all crack size cases are displayed in Figure 5.15, and Figure 5.16.

Again, in order to minimise the spurious reflections from the model edges the PML, absorbing condition is used with a layer thickness of 20 elements.

The grid spacing is set to $\Delta h = 1$ m, and the time step to $\Delta t = 70$ μs to satisfy the stability criterion of the wave equation solution.

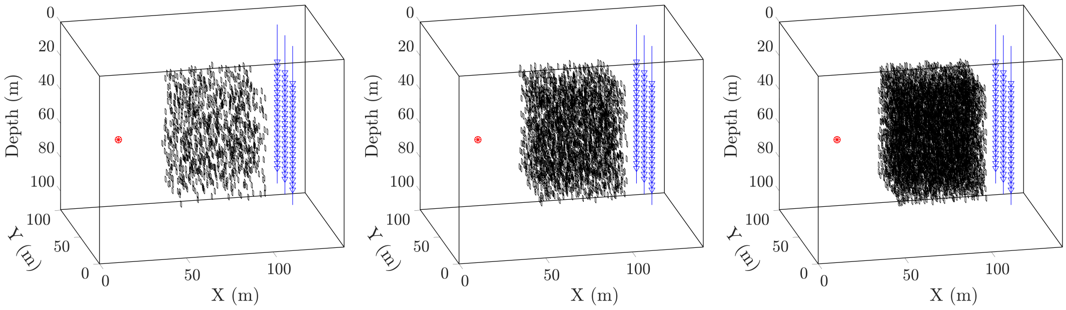

(a) Crack 3×3 m^2, $\epsilon = 0.01$. (b) Crack 3×3 m^2, $\epsilon = 0.025$. (c) Crack 3×3 m^2, $\epsilon = 0.05$.

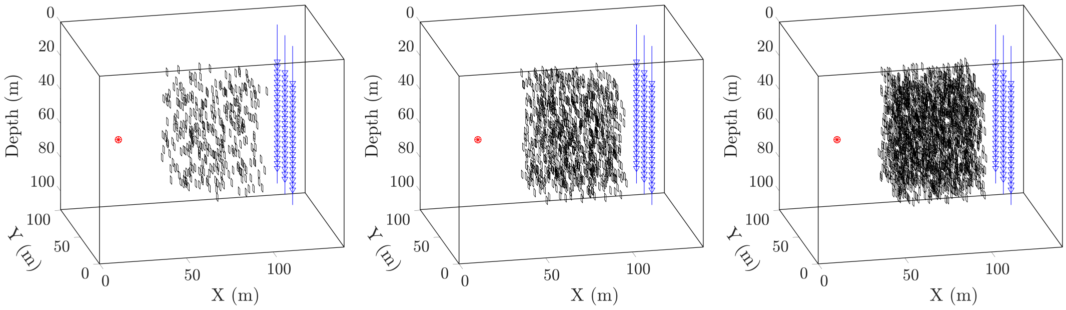

(d) Crack 4×4 m^2, $\epsilon = 0.01$. (e) Crack 4×4 m^2, $\epsilon = 0.025$. (f) Crack 4×4 m^2, $\epsilon = 0.05$.

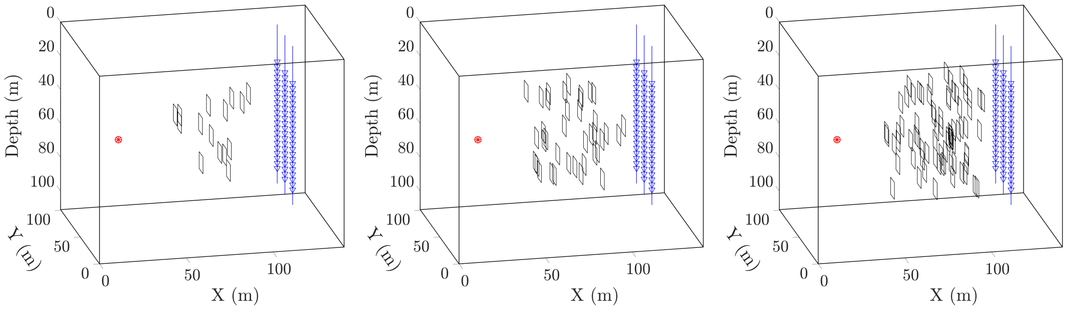

(g) Crack 10×10 m^2, $\epsilon = 0.01$. (h) Crack 10×10 m^2, $\epsilon = 0.025$. (i) Crack 10×10 m^2, $\epsilon = 0.05$.

Figure 5.14: Cracked models used to generate the observed data, where the red star is the source and the blue triangles are the receivers. Each row represents a set of three models with the same crack size but with crack density increasing from left to right. Respectively, from top to bottom crack size of 3×3 m^2, 4×4 m^2 and 10×10 m^2, and from left to right crack density of $\epsilon = 0.01$, $\epsilon = 0.025$, $\epsilon = 0.05$.

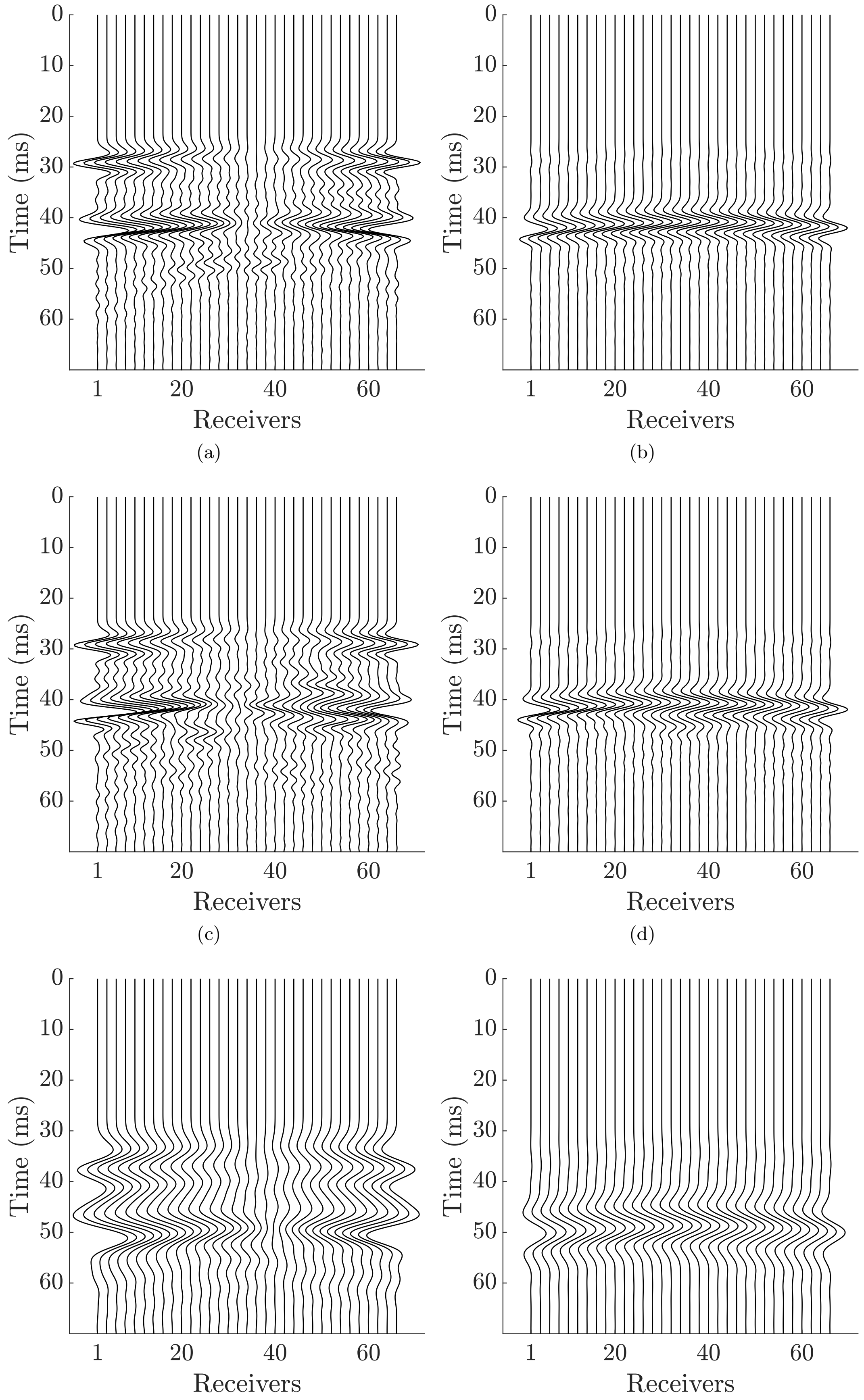

(a) (b)

(c) (d)

(e) (f)

Figure 5.15: Raw data (observed data) of x and z components of velocity, first and second column, respectively, for crack size of 3×3 m^2, 4×4 m^2 and 10×10 m^2 from top to bottom, respectively. The dominant source frequency f_{peak} for 3×3 m^2, and 4×4 m^2 cracks is 175 Hz, whereas $f_{peak} = 90$ Hz for 10×10 m^2 cracks.

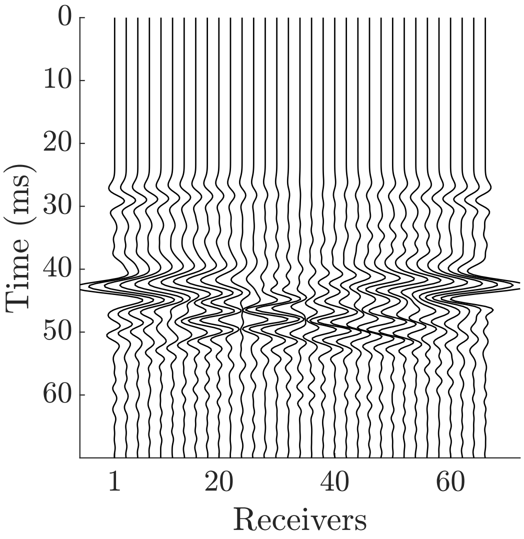

(a) $\phi = 15°$ velocity component x.

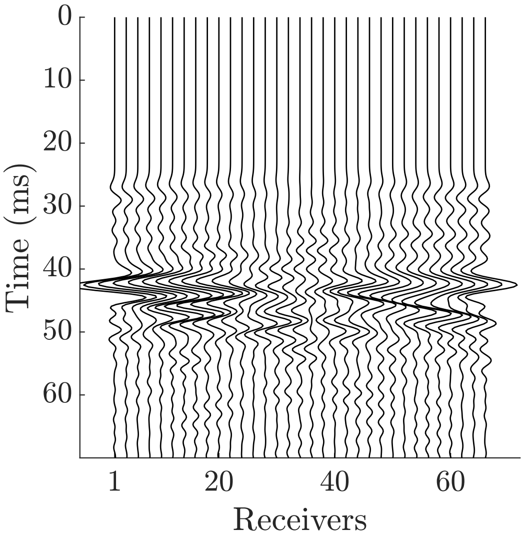

(b) $\phi = 30°$ velocity component x.

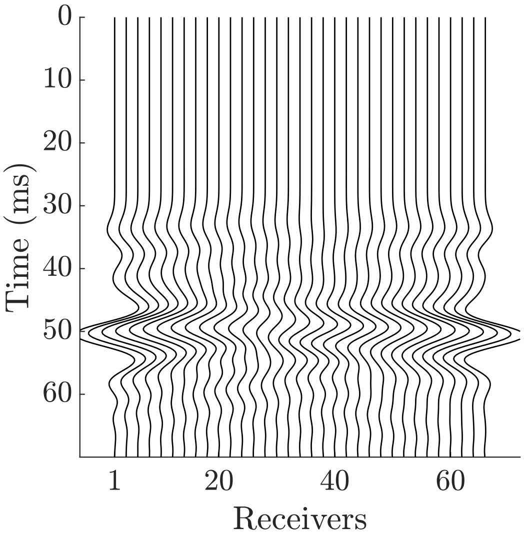

(c) $\phi = 60°$ velocity component x.

Figure 5.16: Raw data (observed data) of y component of velocity for crack size of 3×3 m^2, 4×4 m^2 and 10×10 m^2 from top to bottom, respectively. The dominant source frequency f_{peak} for 3×3 m^2, and 4×4 m^2 cracks is 175 Hz, whereas $f_{peak} = 90$ Hz for 10×10 m^2 cracks.

The values for κ_n^{vf} predicted by the linear relationship expressed in equation (5.15) with respect to parameters involved (ϵ, $\kappa_n^{(c)}$, l), are plotted against the crack stiffness $\kappa_n^{(c)}$ in Figure (5.17). The dashed lines are results for three different crack densities (0.01, 0.02, 0.05). Figure 5.17(a), 5.17(b), 5.17(c) are for 3×3 m^2 cracks, 4×4 m^2 cracks, and 10×10 m^2 cracks, respectively. There is a linear relationship with a slope of L/η. Taking logarithms of equation (5.16) gives

$$\log(\kappa_n^{vf}) = \underbrace{\log(L)}_{=0} - \underbrace{\log(\eta)}_{<0} + \log(\kappa_n^{(c)}), \tag{5.24}$$

and hence plotted on a logarithmic scale (Figure 5.17) the lines are parallel with a shift given by $\log(\eta)$ which only depends on the crack density. The predicted values are independent of crack size as observed by comparing Figure 5.17(a), 5.17(b), and 5.17(c).

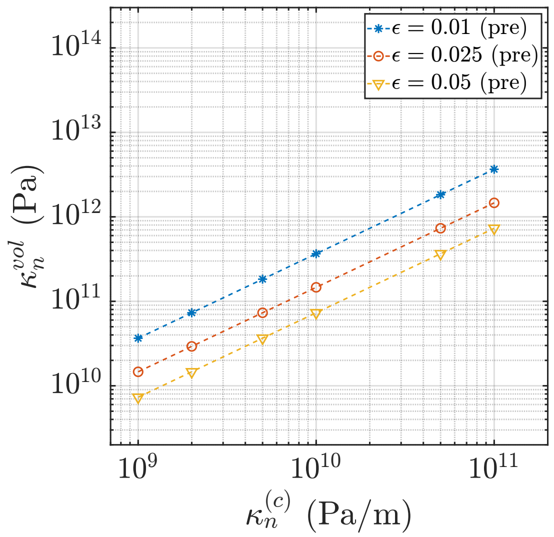

(a) Crack size 3×3 m^2

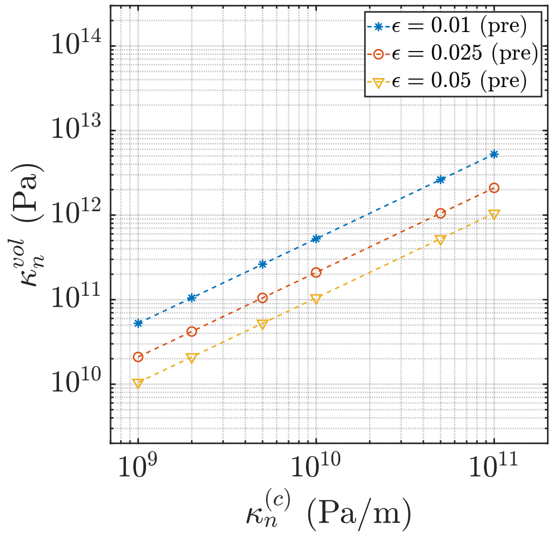

(b) Crack size 4×4 m^2

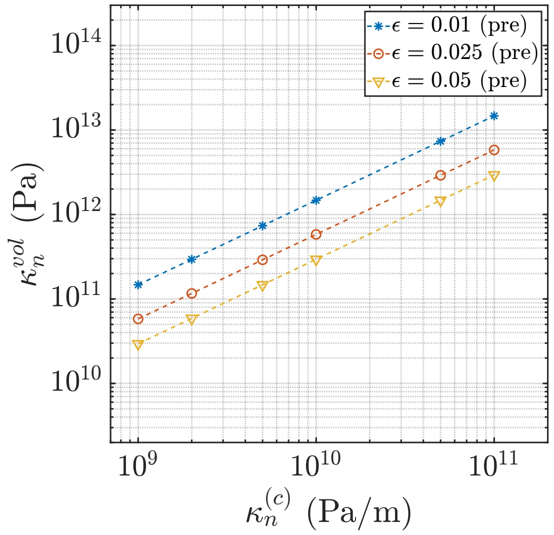

(c) Crack size 10×10 m^2

Figure 5.17: Predicted values of κ_n^{vf} as function of specific crack stiffness $\kappa_n^{(c)}$ implied by the linear relationship expressed in equation (5.15), with respect of crack density ϵ, and crack size. In (a) the crack length is $l = 3$ m, in (b) $l = 4$ m, in (c) $l = 10$ m.

5.4.1 GA inversion results and the Bayesian analysis

Each of the 54 DFN models was inverted using GA-FWFI. The host rock properties (v_p, v_s, and ρ) are assumed known, therefore they are kept fixed during the inversion process, as well as the source wavelet. Hence, the global waveform inversion operates on the space defined by $\mathbf{m} = \{\kappa_n^{vf}, \phi, \delta\}$ for each of the 54 DFN model scenarios. Each inversion used a population of 80 models, approximately 25 times the model dimension (3 parameters). This population size has shown good performance in both exploration and convergence. The models evolve through 30 generations to minimise the cost function defined as the $\mathcal{L}_2-$norm between the observed data and the modelled data. Table 5.4 summarises the control parameters used by the GA algorithm, and Table 5.5 shows the search range of each inverted model parameter.

GA parameters	**Values**
Model population size	80
Generations	30
Tournament size	3
Mutation ratio	0.4
b	2
d	0.3
Elitism	0.05

Table 5.4: GA control parameters used in the experiment.

Model parameter	**Range**	**Unit**
Normal fracture stiffness (κ_n^{vf})	$[1 \cdot 10^{10}, 5 \cdot 10^{14}]$	Pa
Fracture strike (ϕ)	$[-15°,\ 30°]$	
Fracture dip (δ)	$[70°,\ 110°]$	

Table 5.5: Free parameters in the inversion with their search boundaries.

For $l = 3$ m, and $l = 4$ m the maximum frequency inverted is 200 Hz, which corresponds to a wavelength of compressional waves of $\lambda_p \approx 26$ m, therefore approximately 9 times the smaller crack length, and 6.5 times the case of $l = 4$ m. For shear waves $\lambda_s \approx 16$ m, so 5 and 4 times longer than the crack lengths.

For the case of crack length $l = 10$ m, the inversion process involves frequencies up to

100 Hz, and wavelength approximately 5 times the crack size for P-wave, and 3 times for S-waves.

Figures 5.19-5.20 show a comparison between the inverted (red) and observed waveforms (black) of representative seismic data for the three velocity components. The examples shown are for the DFN models with $\epsilon = 0.025$, $\kappa_n^{(c)} = 10$ GPa, and for crack length of $l = 3$ m, $l = 4$ m, and $l = 10$ m, respectively. For a correct comparison, the synthetics modelled with crack length 3 m and 4 m have been low-pass filtered with a cutoff frequency of 200 Hz (maximum inverted frequency), while in the seismograms modelled with crack length of 10 m all frequencies above 100 Hz have been filtered out. All cases show that an excellent match is obtained between the modelled and observed data for all velocity components. This result, coupled with the good estimates of fracture orientation (Table 5.6), means that the waveform inversion has correctly found the global minimum of the misfit function.

A more complete description of the misfit function for all DFN scenarios are displayed in Figures (5.21)-(5.29) where the marginal distributions of all inverted parameters are displayed. Each figure inverts for the equivalent medium fracture stiffness (κ_n^{vf}), fracture strike, and dip, left, middle and right hand columns respectively, with crack stiffness ($\kappa_n^{(c)}$) increasing top to bottom. In all cases the PPDs associated to the equivalent medium stiffness κ_n^{vf} is well constrained, although they widen for larger and stiffer cracks (e.g. Figure (5.21) left column, top to bottom), and for larger cracks (e.g. LH column in Figures (5.21), (5.24) and (5.27)). On the contrary, the PPDs related to the equivalent fracture set orientation (fracture strike and dip) suffer from multimodality, indicating that multiple values of these parameters generate seismograms with almost identical data misfit, when the cracks become stiffer. This verifies especially for cases of $\kappa_n^{(c)} = 5 \cdot 10^{10}$ Pa/m and $\kappa_n^{(c)} = 1 \cdot 10^{11}$ Pa/m), and for low crack density ($\epsilon = 0.01$), e.g. Figure (5.21), and Figure (5.24). Generally, the fracture dip is better constrained than the fracture strike (central and right-hand columns of Figures (5.21)-(5.29)). This can be due to the geometry acquisition where the aperture is wider (Figure 5.18). In fact, the angle α which represents the maximum aperture about the depth axis (vertical axis) (Figure 5.18(a)) is $\alpha \approx 24°$, while the maximum aperture β about the Y-axis is $\beta \approx 40°$. This behaviour becomes even more evident in case of 10×10 m^2 cracks (Figure (5.27), and Figure (5.28)) where the PPDs are mostly flat within the intervals considered. Conversely, for higher crack density ($\epsilon = 0.05$) and smaller cracks, the PPD functions are characterised by a more spiky appearance meaning that the range of possible solutions narrows.

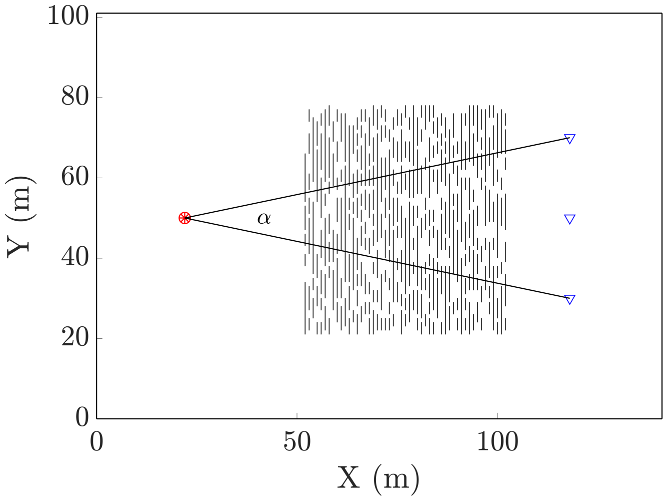

(a)

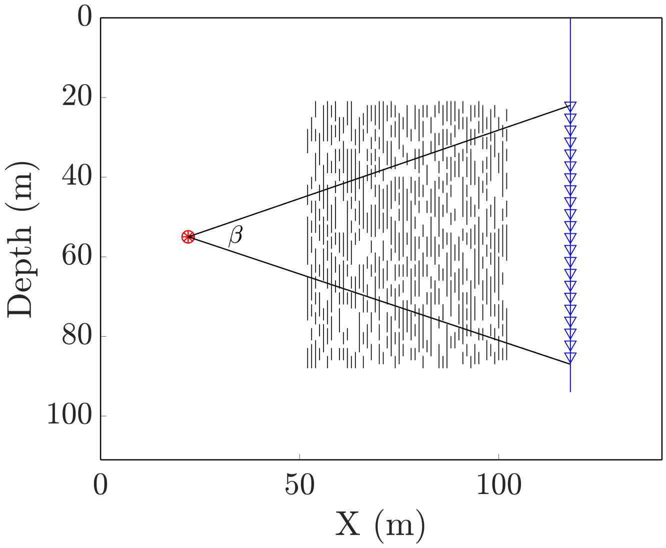

(b)

Figure 5.18: (a) Plan view of the fracture model of Figure 5.14(b) showing the maximum aperture (α) about the depth axis. (b) Vertical 2D projection of the fracture model of Figure 5.14(b) showing the maximum aperture (β) about the Y-axis. The red star is the source and the blue triangles the receivers. $\alpha \approx 24°$, and $\beta \approx 40°$.

	$\kappa_n^{(c)} = 1$ GPa/m			$\kappa_n^{(c)} = 2$ GPa/m			$\kappa_n^{(c)} = 5$ GPa/m			$\kappa_n^{(c)} = 10$ GPa/m			$\kappa_n^{(c)} = 50$ GPa/m			$\kappa_n^{(c)} = 100$ GPa/m		
	$\kappa_n^{vf,GA}$ (GPa)	ϕ (°)	δ (°)	$\kappa_n^{vf,GA}$ (GPa)	ϕ (°)	δ (°)	$\kappa_n^{vf,GA}$ (GPa)	ϕ (°)	δ (°)	$\kappa_n^{vf,GA}$ (GPa)	ϕ (°)	δ (°)	$\kappa_n^{vf,GA}$ (GPa)	ϕ (°)	δ (°)	$\kappa_n^{vf,GA}$ (GPa)	ϕ (°)	δ (°)
3×3																		
$\epsilon = 0.01$	88.2	1.3	92.6	91.7	-0.63	90.6	104.4	1.4	90.5	118.6	-1.7	91.5	247.0	-0.5	87.5	369.8	-1.8	88.0
$\epsilon = 0.025$	35.9	-1.1	90.4	37.7	-1.2	90.4	43.3	-2.0	90.4	48.2	-0.8	90.4	116.1	-2.0	90.5	204.5	-0.3	88.7
$\epsilon = 0.05$	18.8	1.6	89.1	19.7	1.6	89.0	22.9	1.5	89.1	27.5	1.1	89.1	78.3	-1.0	89.6	193.3	0.8	87.3
4×4																		
$\epsilon = 0.01$	100.0	-6.1	91.3	111.3	2.7	91.2	127.2	3.2	87.5	153.7	-3.8	90.8	327.3	4.5	88.6	543	-7.6	93.0
$\epsilon = 0.025$	39.1	-3.9	90.6	42.9	1.7	91.4	48.7	2.6	93.0	59.3	-3.7	91.2	151.7	-9.7	93.1	252.2	-8.1	90.7
$\epsilon = 0.05$	18.8	3.4	88.6	20.5	-2.3	88.5	23.9	2.7	91.7	29.8	3.1	89.1	81.6	-0.8	88.5	124.7	1.9	88.6
10×10																		
$\epsilon = 0.01$	147.2	-2.1	70.9	144.3	-1.9	109.9	163.2	10.6	92.4	227.1	7.1	91.5	785.7	-2.2	71.3	1619.2	0.1	88.2
$\epsilon = 0.025$	46.3	4.7	93.9	50.2	-3.2	91.8	69.2	4.7	91.5	102.2	3.3	92.9	289.9	-0.3	87.2	561.8	-6.6	91.2
$\epsilon = 0.05$	26.0	1.6	92.0	32.7	-1.6	89.1	37.9	1.5	89.5	58.6	-3.9	99.1	166.6	-0.9	94.6	331.4	2.8	92.3

Table 5.6: Best GA models for all 54 DFN scenarios analysed.

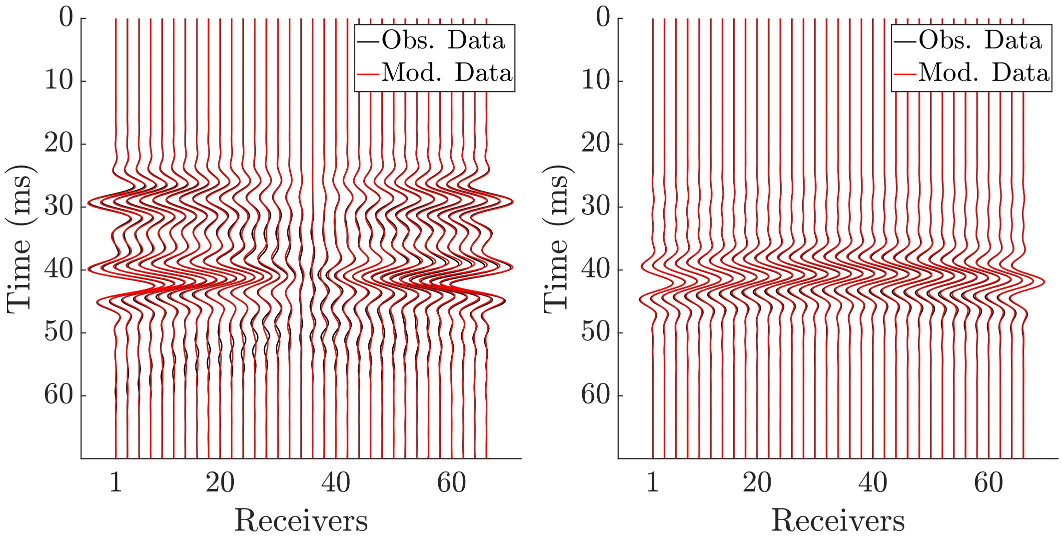

(a) $\phi = 15^{\circ}$ velocity component x.

(b)

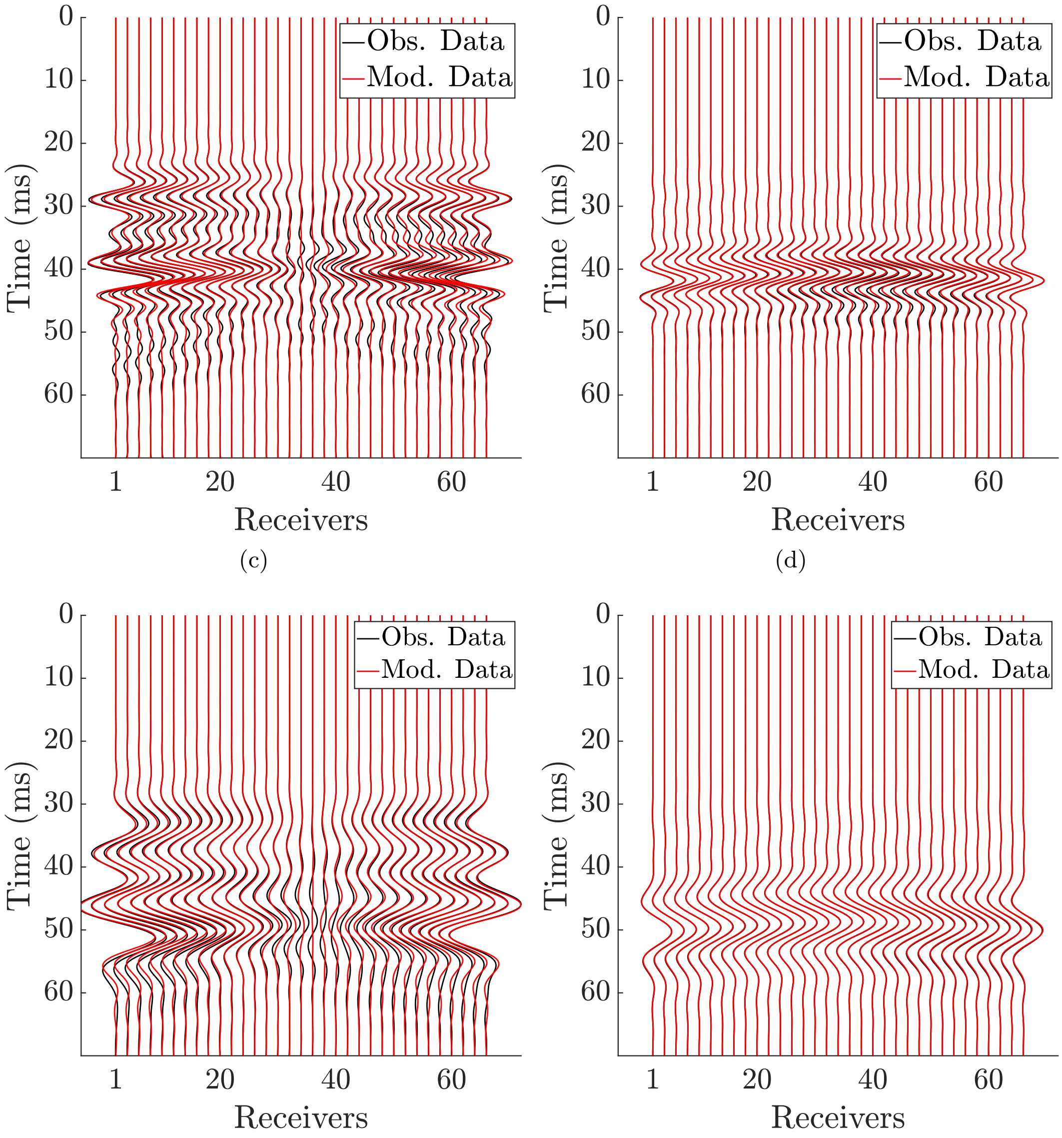

(c)

(d)

(e)

(f)

Figure 5.19: Comparison between the observed data (black) (Figure 5.15) and the best predicted seismograms (red) of the x and y components of velocity (left and right column, respectively), and for crack size of 3×3 m^2, 4×4 m^2 and 10×10 m^2 from top to bottom, respectively. For all cases $\epsilon = 0.025$, and $\kappa_n^{(c)} = 1 \cdot 10^{10}$. Both observed and modelled data has been low-pass filtered with a cutoff frequency of 200 Hz.

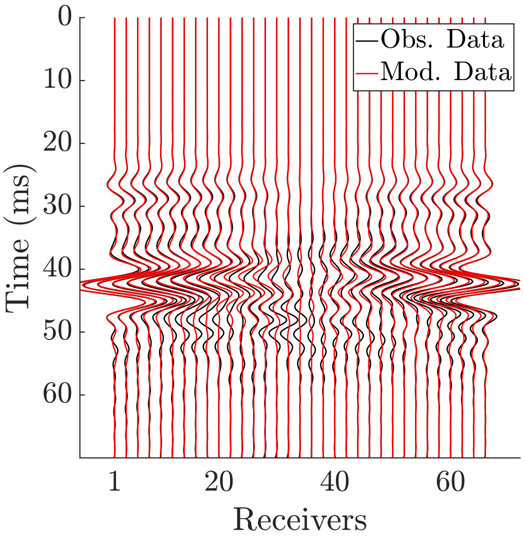

(a)

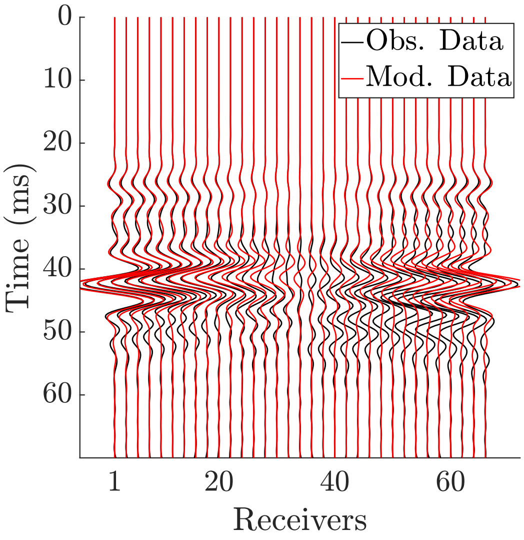

(b)

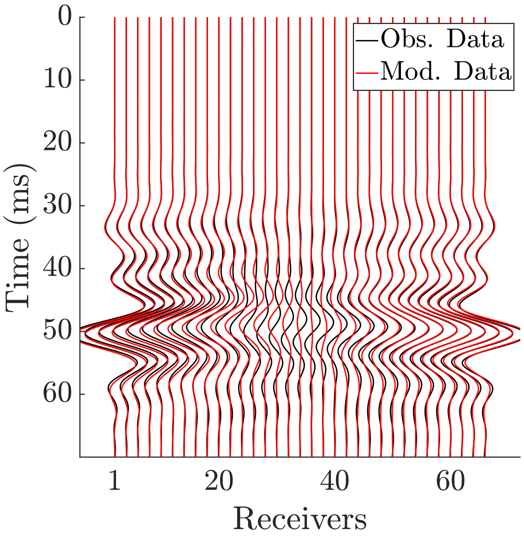

(c)

Figure 5.20: Comparison between the observed data (black) (Figure 5.16) and the best predicted seismograms (red) of the z component of velocity. From top to bottom $l = 3$, $l = 4$, $l = 10$, respectively. For all cases $\epsilon = 0.025$, and $\kappa_n^{(c)} = 1 \cdot 10^{10}$. Both observed and modelled data has been low-pass filtered with a cutoff frequency of 200 Hz.

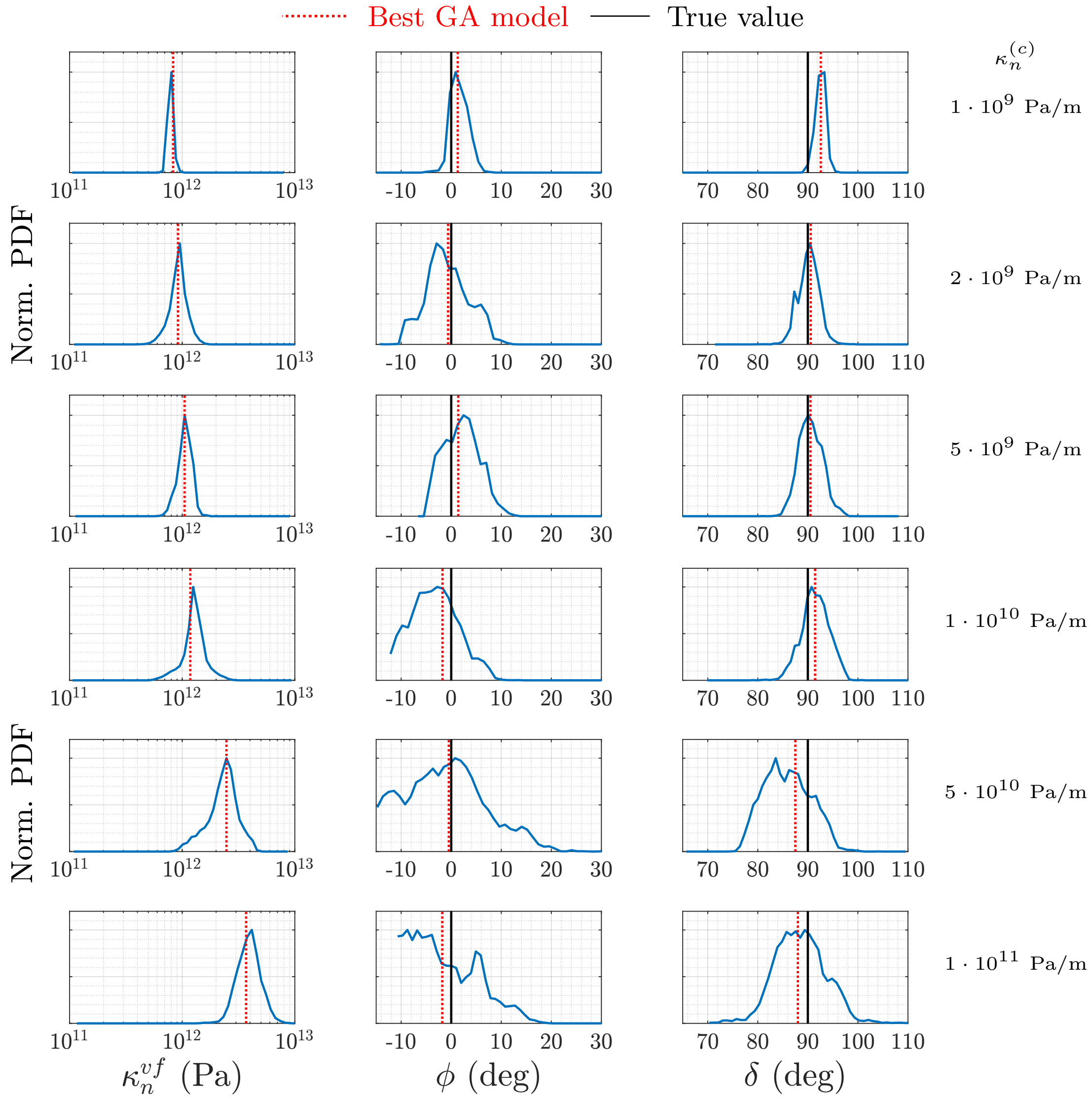

Figure 5.21: The normalised marginal PPD functions for the case $l = 3$ m, and $\epsilon = 0.01$ are represented from top to bottom for the six inverted normal crack stiffness ($\kappa_n^{(c)}$) values. The equivalent medium stiffness κ_n^{vf}, the equivalent fracture strike ϕ, and the equivalent fracture dip δ values are represented in the left, central, and right columns, respectively. The continuous black line represents the the true model parameter, while the dashed red line the elite model predicted by the GA inversion.

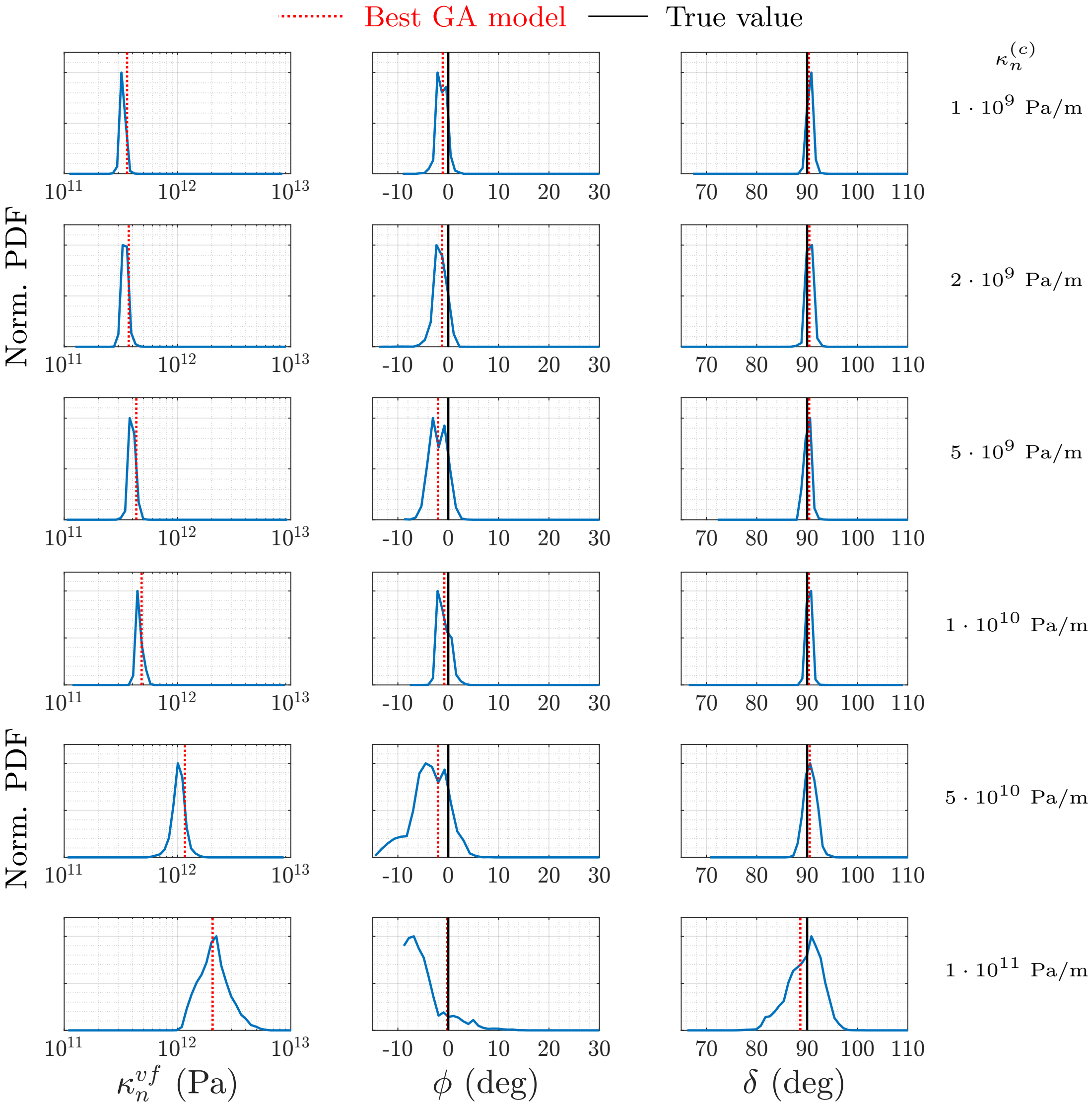

Figure 5.22: The normalised marginal PPD functions for the case $l = 3$ m, and $\epsilon = 0.025$ are represented from top to bottom for the six inverted normal crack stiffness ($\kappa_n^{(c)}$) values. The equivalent medium stiffness κ_n^{vf}, the equivalent fracture strike ϕ, and the equivalent fracture dip δ values are represented in the left, central, and right columns, respectively. The continuous black line represents the the true model parameter, while the dashed red line the elite model predicted by the GA inversion.

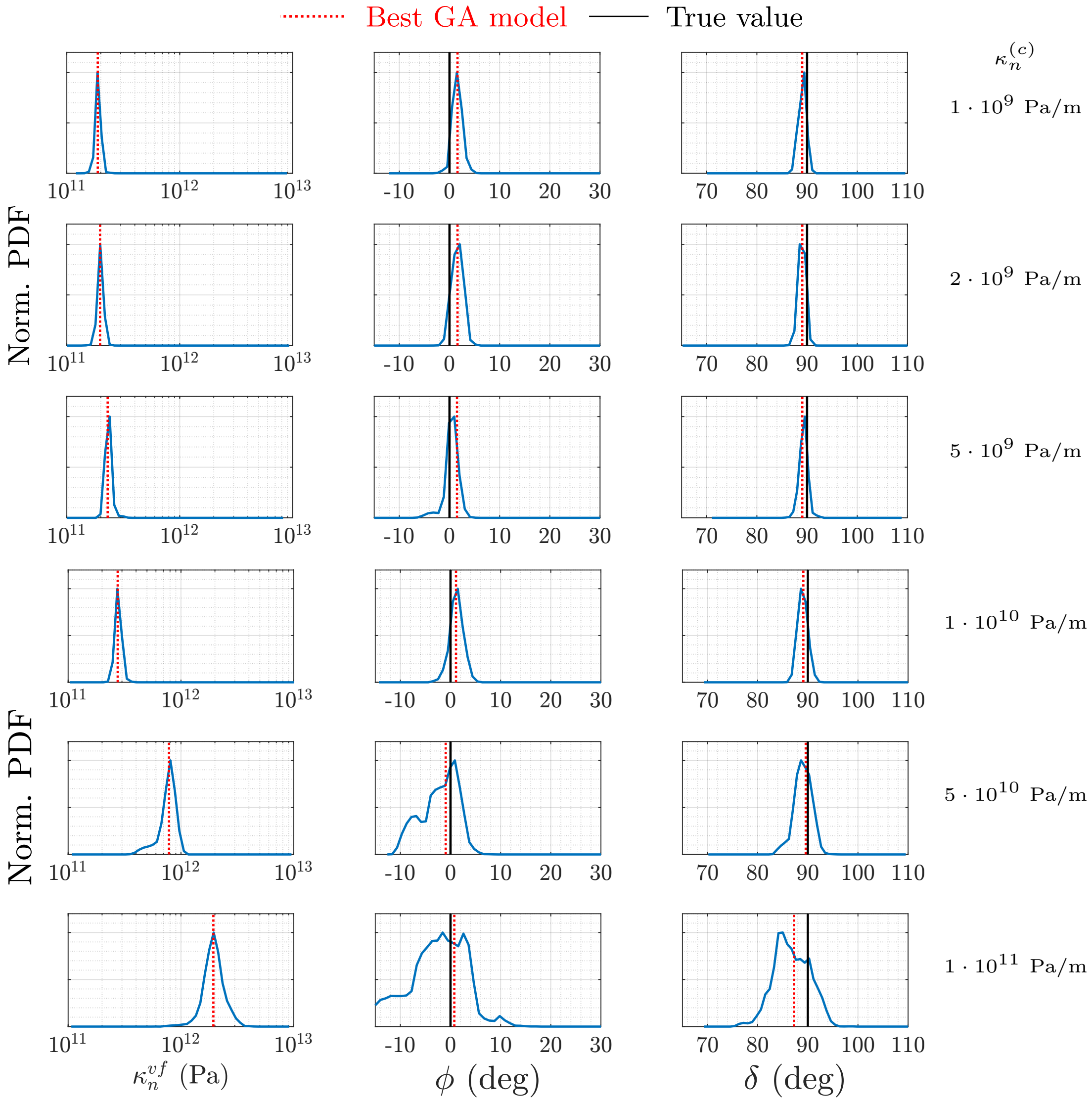

Figure 5.23: The normalised marginal PPD functions for the case $l = 3$ m, and $\epsilon = 0.05$ are represented from top to bottom for the six inverted normal crack stiffness ($\kappa_n^{(c)}$) values. The equivalent medium stiffness κ_n^{vf}, the equivalent fracture strike ϕ, and the equivalent fracture dip δ values are represented in the left, central, and right columns, respectively. The continuous black line represents the the true model parameter, while the dashed red line the elite model predicted by the GA inversion.

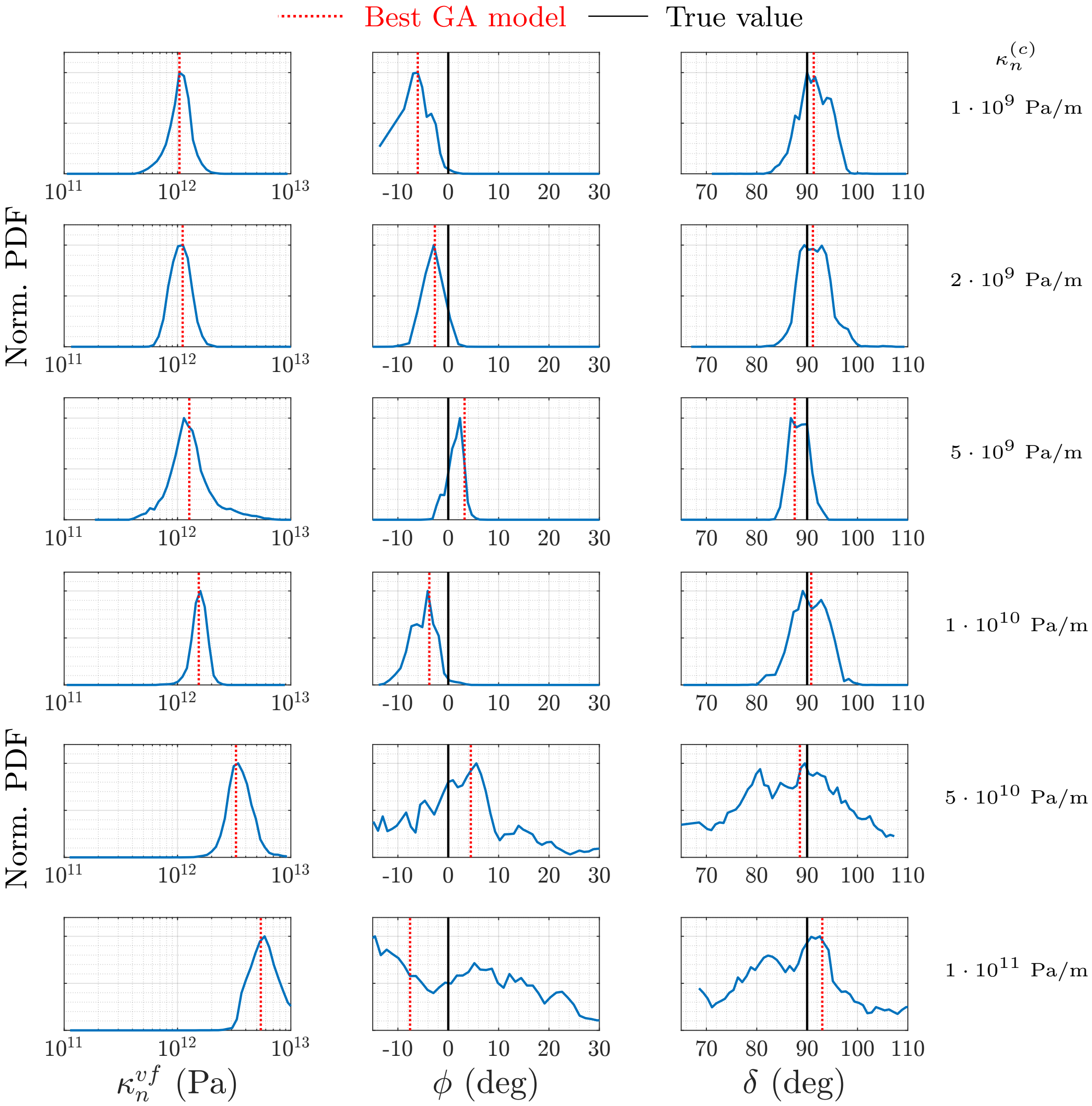

Figure 5.24: The normalised marginal PPD functions for the case $l = 4$ m, and $\epsilon = 0.01$ are represented from top to bottom for the six inverted normal crack stiffness ($\kappa_n^{(c)}$) values. The equivalent medium stiffness κ_n^{vf}, the equivalent fracture strike ϕ, and the equivalent fracture dip δ values are represented in the left, central, and right columns, respectively. The continuous black line represents the the true model parameter, while the dashed red line the elite model predicted by the GA inversion.

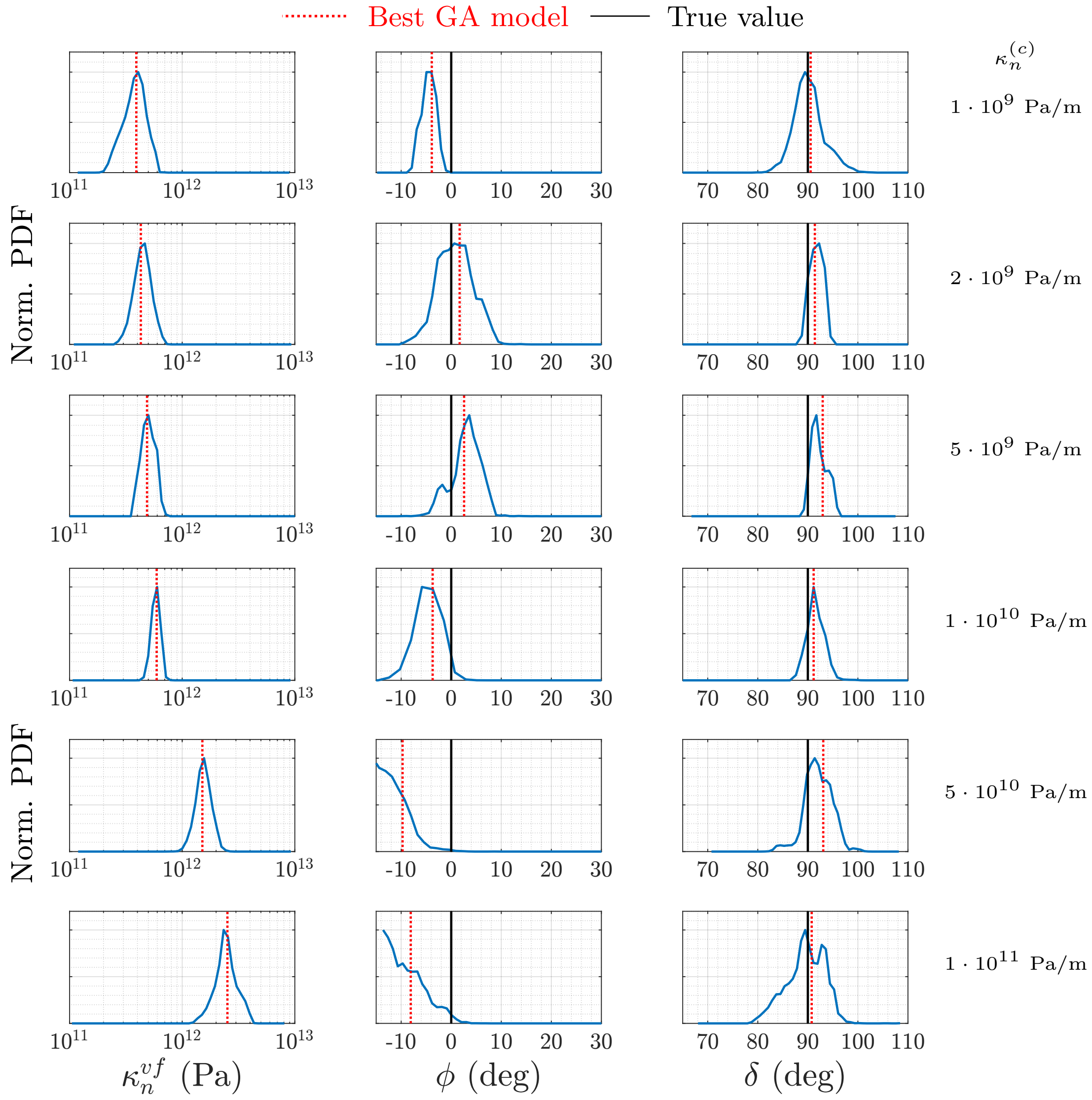

Figure 5.25: The normalised marginal PPD functions for the case $l = 4$ m, and $\epsilon = 0.025$ are represented from top to bottom for the six inverted normal crack stiffness ($\kappa_n^{(c)}$) values. The equivalent medium stiffness κ_n^{vf}, the equivalent fracture strike ϕ, and the equivalent fracture dip δ values are represented in the left, central, and right columns, respectively. The continuous black line represents the the true model parameter, while the dashed red line the elite model predicted by the GA inversion.

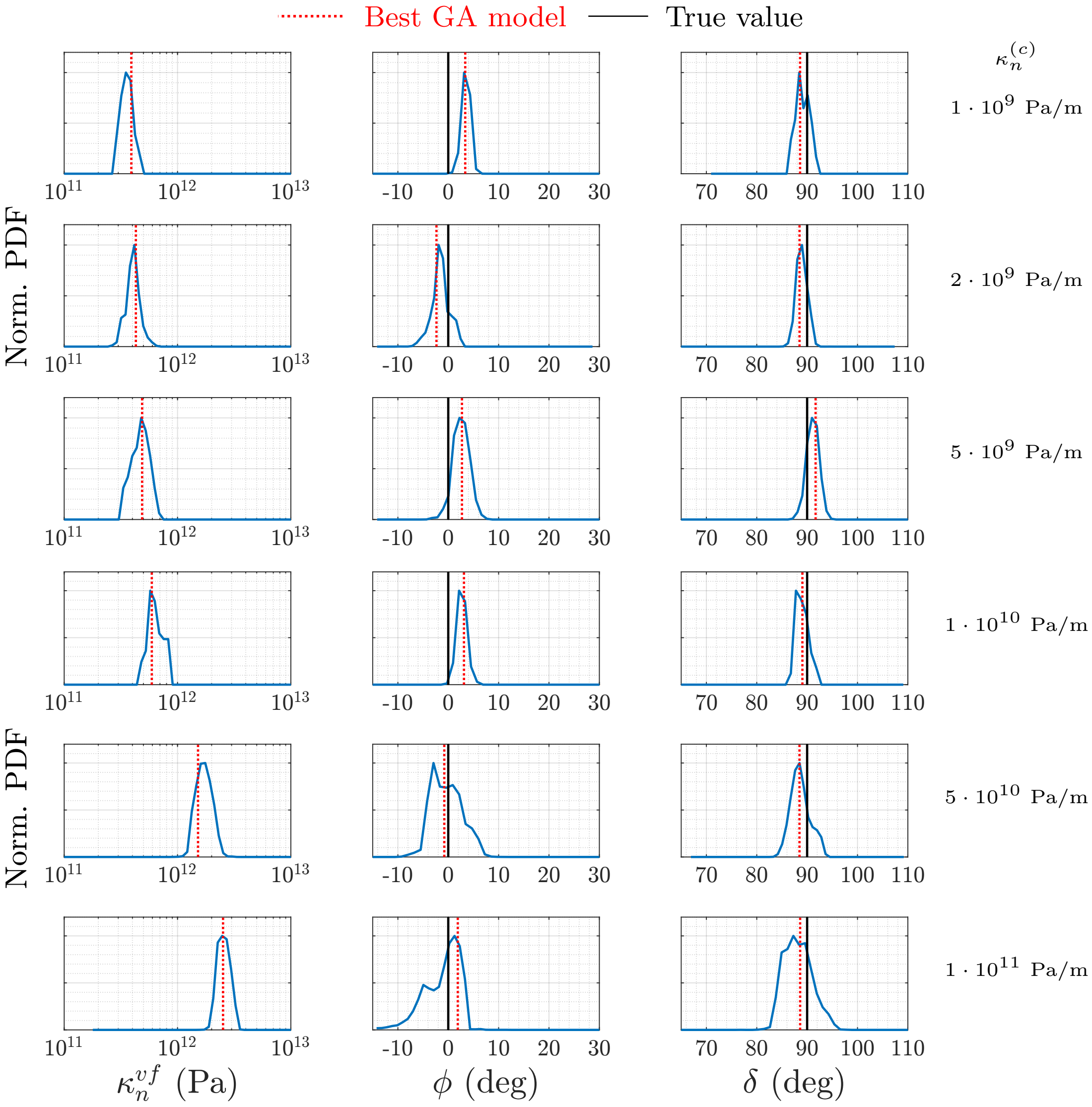

Figure 5.26: The normalised marginal PPD functions for the case $l = 4$ m, and $\epsilon = 0.05$ are represented from top to bottom for the six inverted normal crack stiffness ($\kappa_n^{(c)}$) values. The equivalent medium stiffness κ_n^{vf}, the equivalent fracture strike ϕ, and the equivalent fracture dip δ values are represented in the left, central, and right columns, respectively. The continuous black line represents the the true model parameter, while the dashed red line the elite model predicted by the GA inversion.

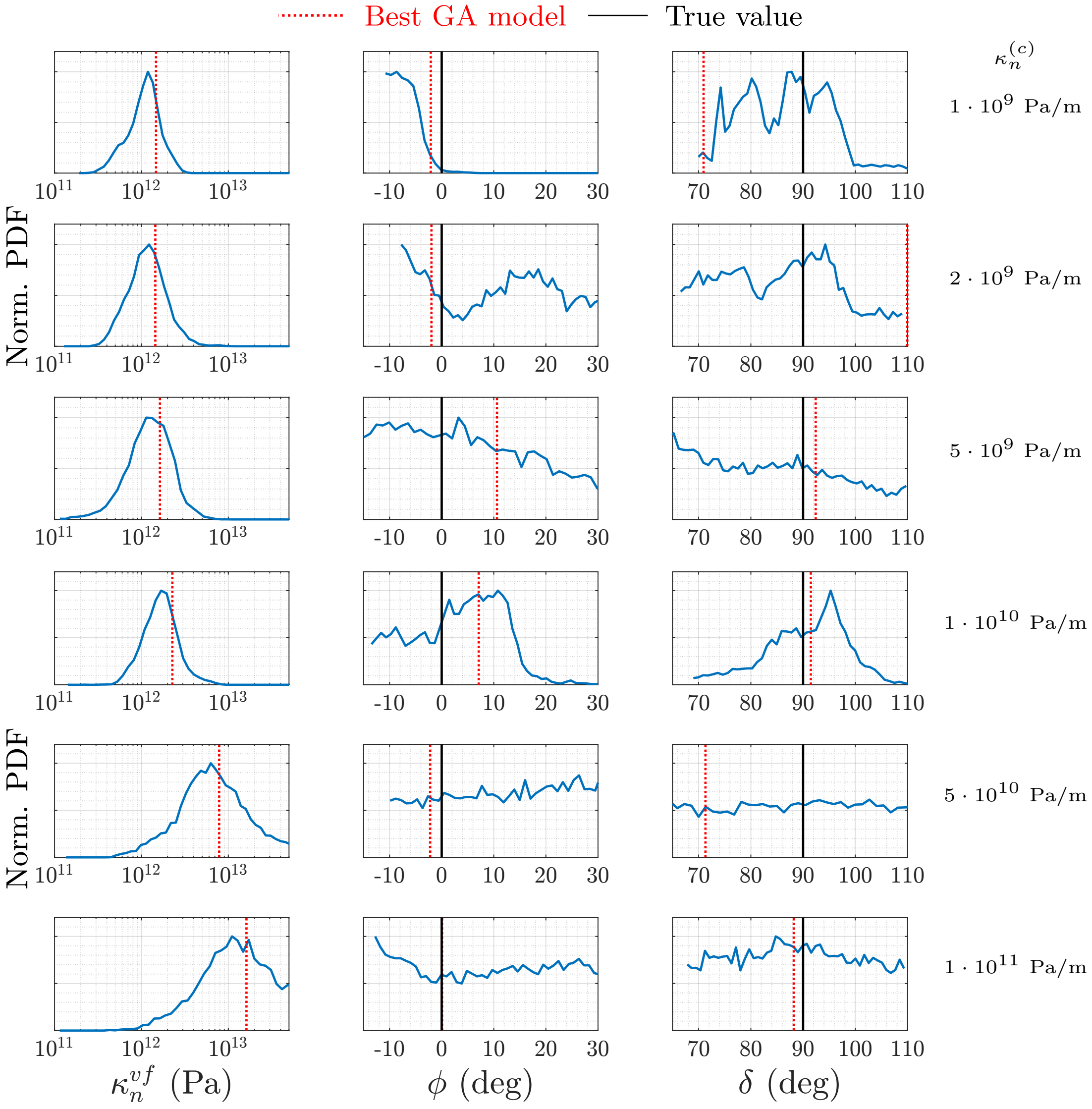

Figure 5.27: The normalised marginal PPD functions for the case $l = 10$ m, and $\epsilon = 0.01$ are represented from top to bottom for the six inverted normal crack stiffness ($\kappa_n^{(c)}$) values. The equivalent medium stiffness κ_n^{vf}, the equivalent fracture strike ϕ, and the equivalent fracture dip δ values are represented in the left, central, and right columns, respectively. The continuous black line represents the the true model parameter, while the dashed red line the elite model predicted by the GA inversion.

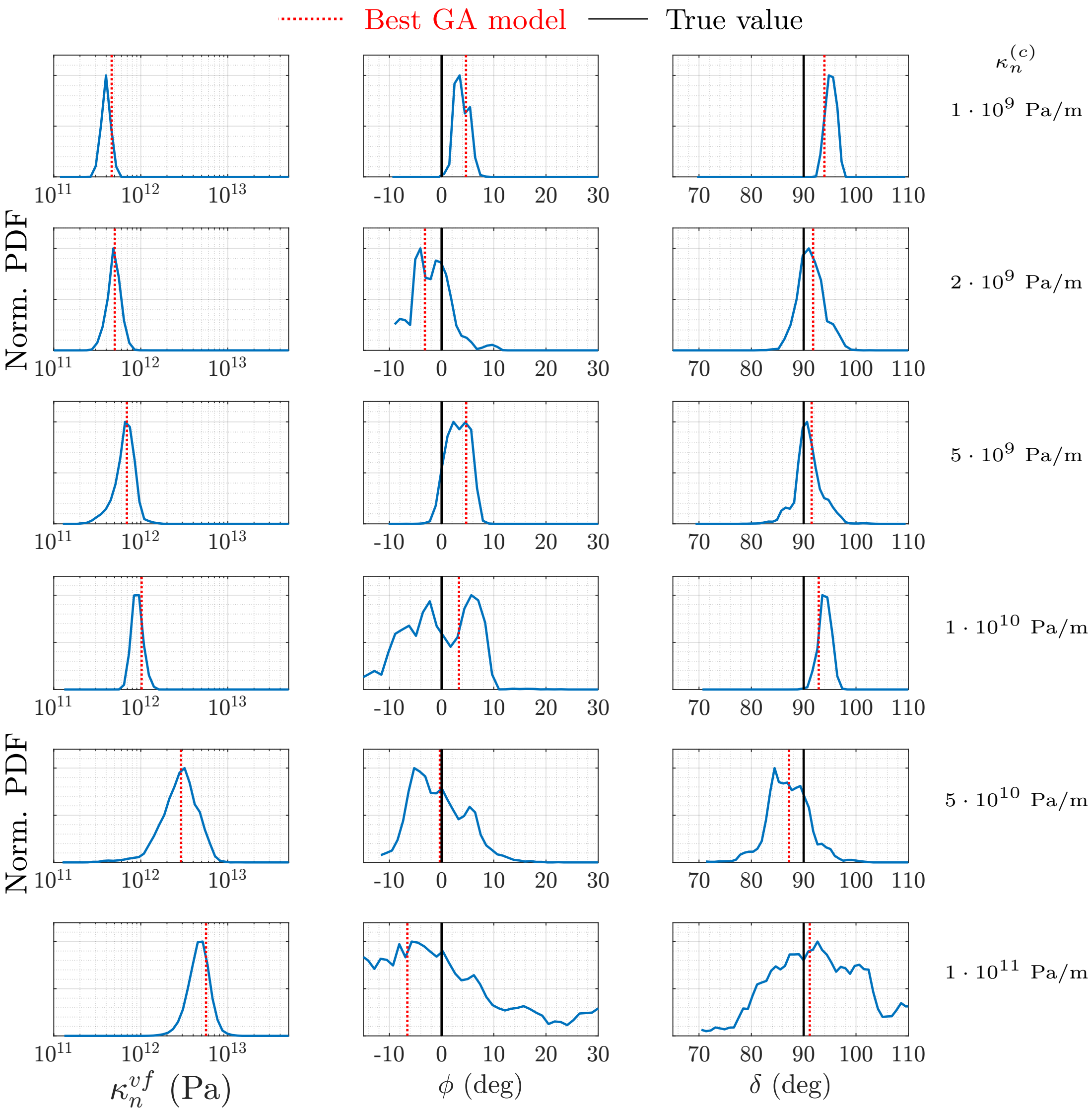

Figure 5.28: The normalised marginal PPD functions for the case $l = 10$ m, and $\epsilon = 0.025$ are represented from top to bottom for the six inverted normal crack stiffness ($\kappa_n^{(c)}$) values. The equivalent medium stiffness κ_n^{vf}, the equivalent fracture strike ϕ, and the equivalent fracture dip δ values are represented in the left, central, and right columns, respectively. The continuous black line represents the the true model parameter, while the dashed red line the elite model predicted by the GA inversion.

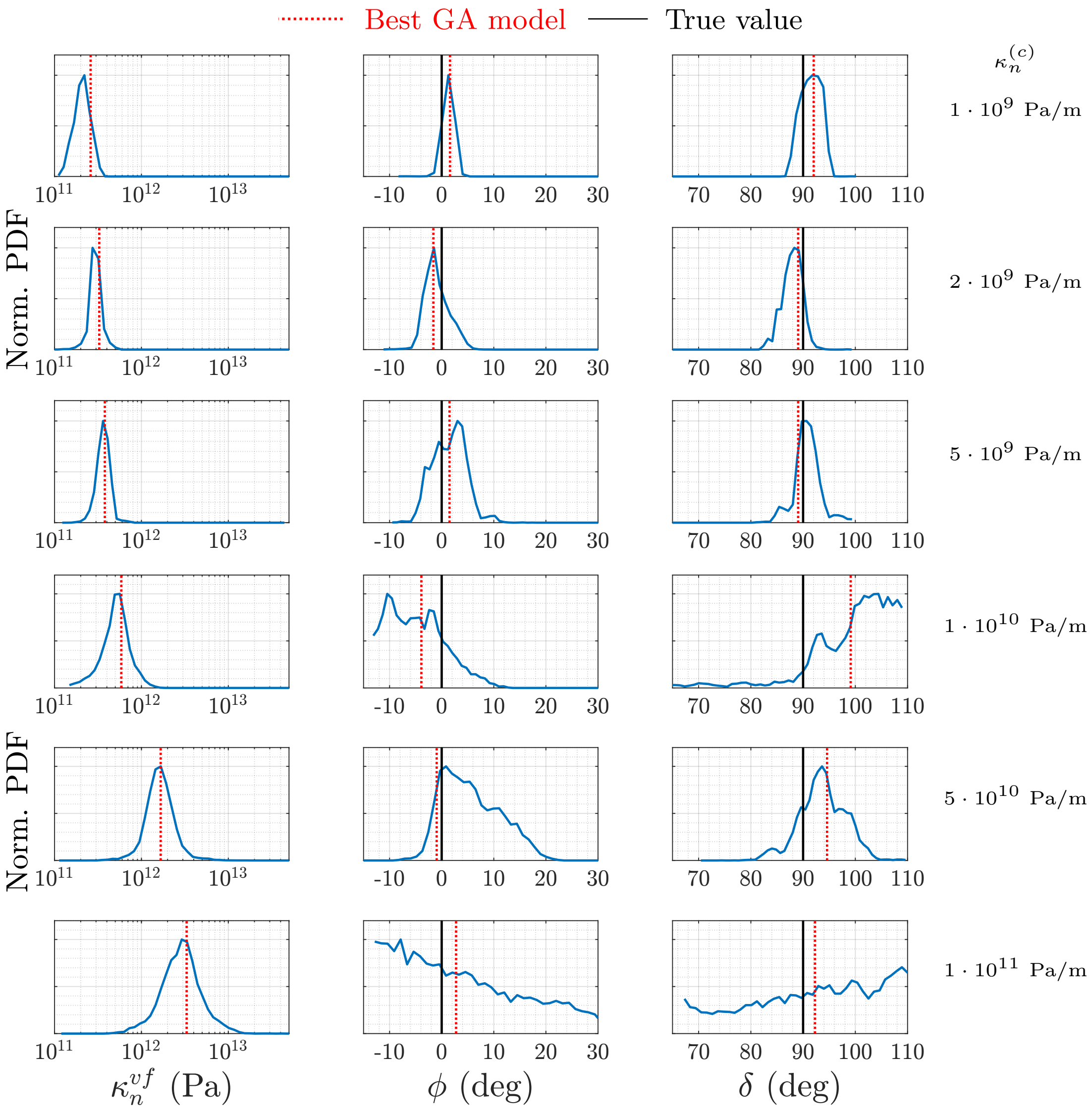

Figure 5.29: The normalised marginal PPD functions for the case $l = 10$ m, and $\epsilon = 0.05$ are represented from top to bottom for the six inverted normal crack stiffness ($\kappa_n^{(c)}$) values. The equivalent medium stiffness κ_n^{vf}, the equivalent fracture strike ϕ, and the equivalent fracture dip δ values are represented in the left, central, and right columns, respectively. The continuous black line represents the the true model parameter, while the dashed red line the elite model predicted by the GA inversion.

Figures 5.30(a), 5.30(c), and 5.30(e) (left column of Figure 5.30) compare the inverted values of effective normal fracture stiffness $\kappa_n^{vf,GA}$ (solid curves) to values predicted from equation (5.16) (shown in Figure (5.17)), for all 54 DFN cases. The color indicates the same crack density (as in Figure (5.17)).

In all cases, $\kappa_n^{vf,GA}$ has a non-linear trend flattening for compliant cracks but approaching the theoretical results for stiff cracks. For crack stiffness for this size crack relative to the background medium, cracks are effectively open for crack stiffnesses lower than $\kappa_n^{(c)} \lesssim 3 \cdot 10^9$ Pa/m, and hence the effective stiffness of the cracked medium is invariant even for lower values of $\kappa_n^{(c)}$. For increasingly stiff cracks however, the numerical results eventually tend towards the linear trend of the relationship predicted by equation (5.15) (Figure 5.30(a), 5.30(c), 5.30(e)).

To better visualise the results obtained through GA inversion and their connection to the corresponding theoretical values, the attribute χ is introduced. It is defined as the ratio between the numerical and the theoretical values of the bulk stiffness, therefore

$$\chi = \frac{\kappa_n^{vf,GA}}{\kappa_n^{vf}}. \tag{5.25}$$

Figure 5.30(b), 5.30(d), and 5.30(f) (rigth-hand column of Figure 5.30) display the χ attribute for the three crack size of this experiment, $l = 3$ m, $l = 4$ m, and $l = 10$ m, respectively. A direct comparison between three curves of the attribute χ shown in Figure 5.30, is displayed in Figure 5.31.

Three clear trends are revealed in Figure 5.31

- chi depends only on crack size and is independent of crack density
- χ tends towards 1 for larger crack sizes
- chi tends towards 1 for increasing crack stiffness

These results also indicate that separating the effect of big or small cracks becomes more and more difficult if cracks are stiffer. Conversely, for case of compliant cracks, χ diverges and it becomes simpler to distinguish crack size.

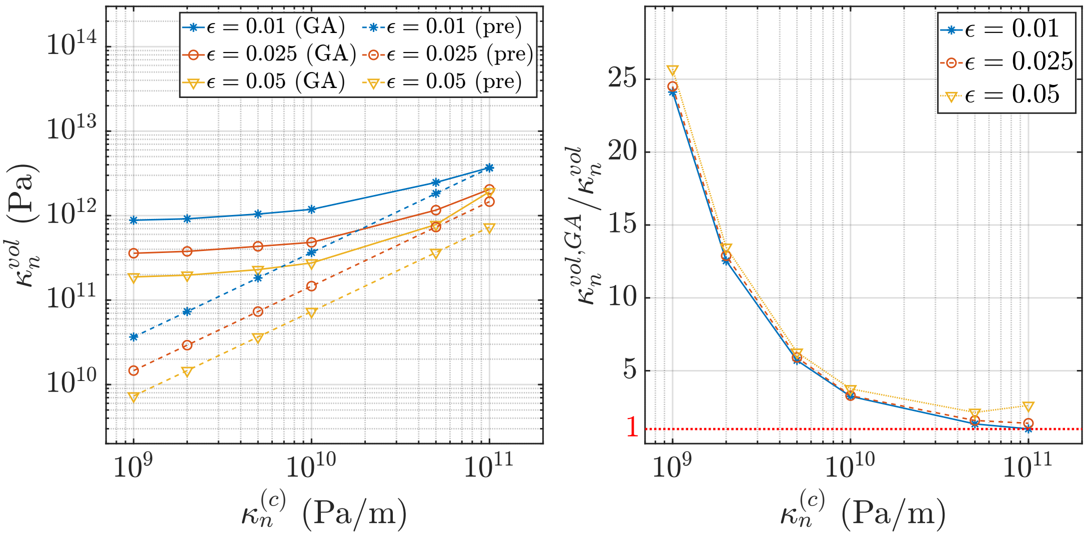

(a) Crack size 3 × 3 m^2.

(b) χ attribute for (a).

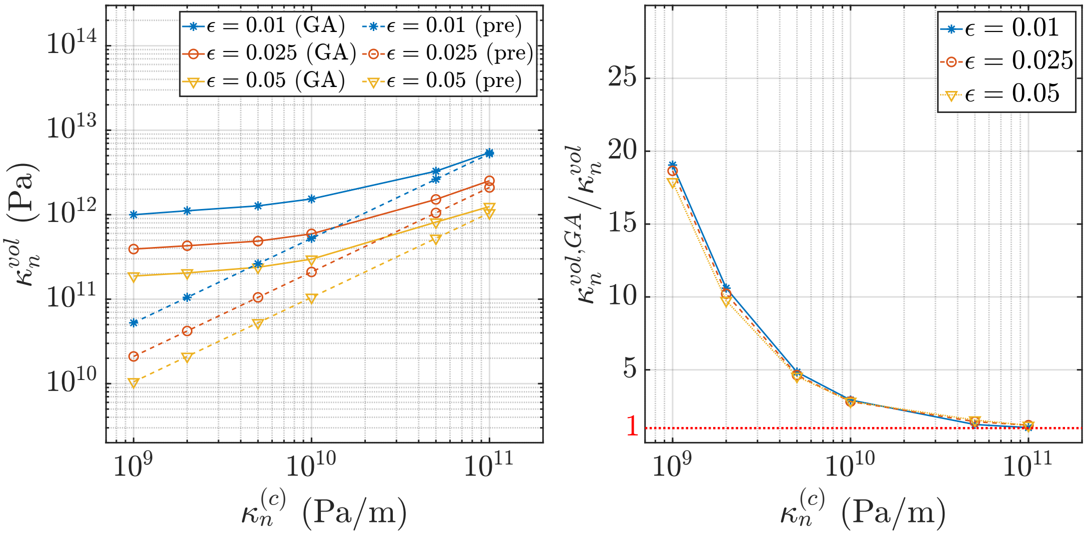

(c) Crack size 4 × 4 m^2.

(d) χ attribute for (c).

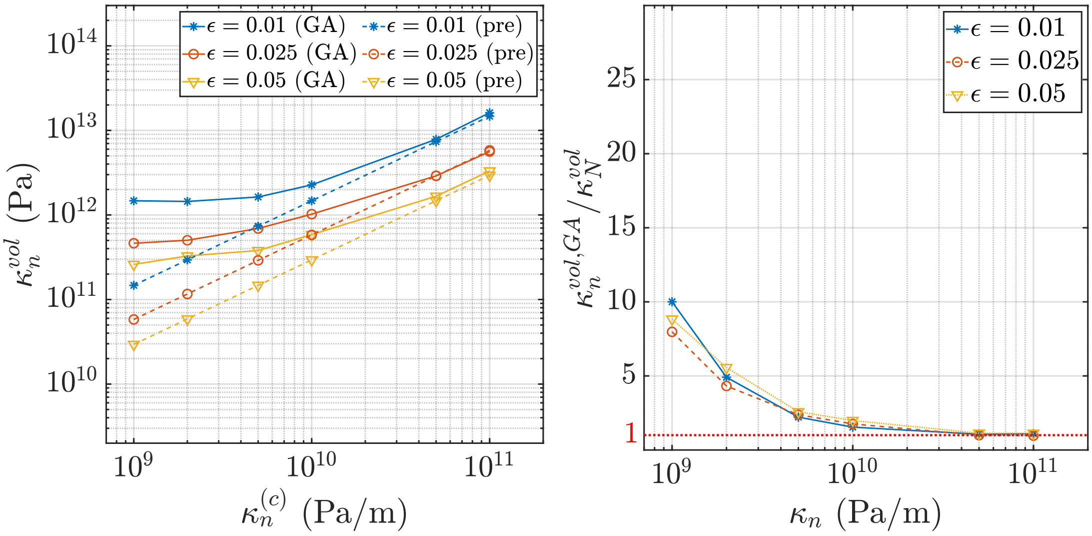

(e) Crack size 10 × 10 m^2

(f) χ attribute for (e).

Figure 5.30: Comparison between the predicted values of κ_n^{vf} (dashed lines) showed in Figure 5.17, and the optimal GA values $\kappa_n^{vf,GA}$ listed in Table 5.6. In (a) the crack length is $l = 3$ m, in (c) $l = 4$ m, in (e) $l = 10$ m. The right column shows the corresponding χ attributes.

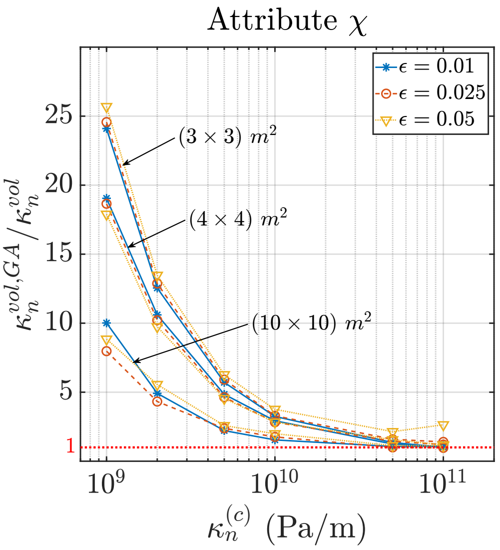

Figure 5.31: Comparison between the attribute χ as function of the specific crack stiffness $\kappa_n^{(c)}$, with respect to the three crack size.

5.5 Discussion

Field measurements of mechanical properties of cracks are very often obtained by employing EM theories, such as inclusion-based theories (e.g. (Hudson, 1980)) or the displacement discontinuity theory (e.g. (Schoenberg and Sayers, 1995)). However, they are valid only when the long wavelength approximation is observed (i.e., the wavelength is much greater than the crack length, and crack spacing). These theories are implemented in a variety of methodologies which deal with the characterisation of seismic anisotropy to estimate, as an inverse process, the physical properties of interest such as crack density, and crack orientation (Worthington, 2007; Hobday and Worthington, 2012; Liu and Martinez, 2012; Verdon and Wüstefeld, 2013; Yousef and Angus, 2016). Nevertheless, the estimation of seismic anisotropy using EM theories needs to be carefully interpreted, since they cannot take into account the spacial distribution of cracks, and because the crack length is not uniquely defined in such theories (Vlastos et al., 2003; Lubbe and Worthington, 2006). In fact, for the long wavelength approximation, EM cannot distinguish small fractures from large ones, since the variation of the overall medium stiffness depends on the effective area of all cracks in the medium, regardless of size (equations (5.9) and (5.15)).

The stochastic waveform inversion method (GA-FWFI) was applied to reveal an improved understanding of the link between the Effective Medium parameters and the explicit crack properties under the long wavelength approximation regime. An uncertainty estimate is obtained through the NA appraisal approach using the GA model ensembles. Section 5.3 estimated the crack orientation for a multi-azimuth acquisition directly from the seismic waveforms was carried out. Section 5.4 then analysed the effect of the transition from open cracks to welded interfaces upon the equivalent medium parameters.

In the multi-azimuth acquisition a good match is attained between the modelled and observed data (Figures 5.10-5.12). This leads to an estimate of the equivalent fracture orientation which is in excellent agreement (Table 5.3) with the crack dip and crack strike (from 0° to 60°) of a medium composed of randomly distributed cracks along parallel planes. The marginal PPDs show that all parameters are well constrained by the inversion (Figure 5.13). The inverted equivalent medium stiffness is consistent with respect to all azimuth angles (approximately $3.2 \cdot 10^{11}$ Pa) with respect to the azimuth angles. Nevertheless, this result is in disagreement with the expected theoretical value (approximately $1.5 \cdot 10^{10}$ Pa) given by the linear relationship between the equivalent medium stiffness and the specific stiffness of the cracks therein contained (equation (5.15)). This mismatch between the optimum value retrieved by GA-FWFI and the expected value theoretical derived by Worthington (2007) and Worthington (2008)) was further explored by systematically analysing the influence of discrete crack parameters on the corresponding equivalent medium ones.

The analysis performed in the second experiment (Section 5.4), has shown that the transition from a medium with open cracks ($\kappa_n^{(c)} \lesssim 2 \cdot 10^9$ Pa/m) to one with welded interfaces ($\kappa_n^{(c)} \gtrsim 5 \cdot 10^{10}$ Pa/m) leads to the equivalent media having the bulk stiffness κ^{vf} non-linearly related to the crack specific stiffness $\kappa^{(c)}$. This holds for media with different crack density and crack size, although with a different degree. The analysis introduces the attribute χ which shows that there is indeed a crack-size dependence upon the equivalent medium stiffness (Figure 5.31). So, in spite of the long wavelength approximation, crack size has an indubitable impact on the variation of the effective parameters. For stiffer cracks, the bulk stiffness estimated through GA-FWFI, tends to the theoretical value for all crack size values analysed. Therefore, for stiffer cracks the attribute χ tends to 1 and the crack size effect, upon the equivalent medium parameters, vanishes. The result that the EM models are more correct for the cases of high crack stiffness is also consistent with results of Yousef and Angus (2016) who observed that the displacement-discontinuity EM theory becomes increasingly inaccurate as the stiffness decreases, as well as Chichinina et al. (2015) who showed analytically that the displacement-discontinuity EM theory is only valid when the anisotropy parameter δ turns to 0, so $\Delta_n = \Delta_s$ or for the case of $\Delta_n = 0$, so $\kappa_n \to \infty$ (see equation (2.15, Chapter 2). On the contrary, for compliant cracks, crack size has a greater impact on the attribute χ, and the distinction between larger cracks and smaller ones is more prominent. Furthermore, the larger the cracks the more χ flattens towards 1, making this consistent with the theoretical assumption such that the fracture set spans the entire volume (from the case in Figure 5.1(b) to the case in Figure 5.1(a)). The properties of χ can therefore be employed to guide the interpretation of a cracked medium by giving a range of likely values for crack size and crack stiffness.

The systematic analysis of the uncertainties for all 54 DFN scenarios through the NA method (Figures 5.21-5.29) has shown that this method produces a good well-constrained estimate of the bulk stiffness, although the PPDs widen for larger and stiffer cracks. The DFN scenario that exhibited the highest variance in the bulk stiffness characterisation was the case with crack length $l = 10$ m and $\epsilon = 0.01$. This is likely caused by the combination of small crack density with relatively large cracks, which produces a non-uniform distribution of fractures within the volume, and leaving portion of the model intact (see the bottom left side of Figure 5.32(a)). During the inversion the equivalent medium volume remains unchanged and the associated bulk stiffness is uniform throughout the volume. Therefore, this always leads to a mismatch in waveform fitting and thus a wider interval of accepted stiffness values, due to the fracture distribution asymmetry and waves travel path. As matter of fact, this was not observed for the smaller cracks as the high number of cracks within the volume resulted in their more even distribution (Figure 5.32(b)). Moreover, a higher degree of uncertainty is caused by high stiffness cracks which behave like closed cracks, making the transmitted wavefield less sensitive to the crack stiffness, and in turn widening the range of possible solutions.

Contrary to the bulk stiffness uncertainty estimation, the PPDs related to the fracture orientation (both fracture strike and fracture dip) suffer of crosstalk between the two angles as well as multimodality especially for low crack density and high stiffness cracks. As previously noted, this behaviour becomes even more evident for the cases of $l = 10$ m cracks (Figure (5.27), and Figure (5.28)) where the PPDs are mostly flat within the intervals considered. This can again be related to the fracture distribution asymmetry for the case $\epsilon = 0.01$, leading to a less constrained inversion due to the loss of sensitivity of the transmitted waves with respect to the stiff cracks.

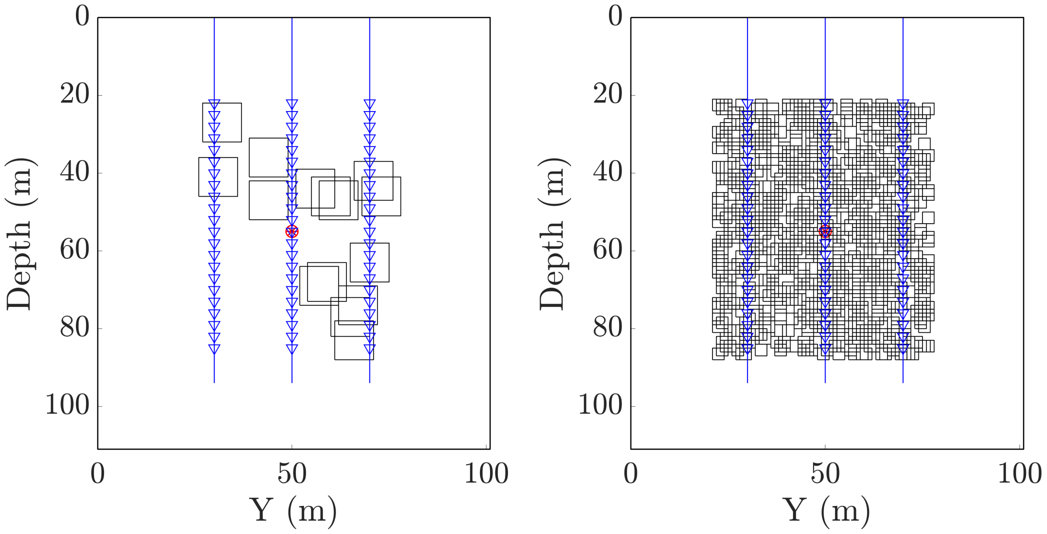

(a)

(b)

Figure 5.32: (a) Lateral 2D projection on $(depth, y)$-plane of Figure 5.14(g) ($l = 10$ m, $\epsilon = 0.01$). (b) Lateral 2D projection on $(depth, y)$-plane of Figure 5.14(a) ($l = 3$ m, $\epsilon = 0.01$).

5.6 Summary and Conclusions

This chapter has attempted to unveil the coupling between the discrete fracture parameters and the equivalent fractured zone properties, by means of a stochastic waveform inversion approach (GA-FWFI). When seismic wavelengths are comparable to crack size and spacing, EM theory fails in retrieving crack properties since it cannot model scattering phenomena by individual discontinuities. On the other hand, for the long wavelength approximation, EM cannot distinguish small fractures from large ones, since the variation of the overall medium stiffness depends on the effective area of all cracks in the medium, regardless of size. Nevertheless, the attribute χ shows that crack size indeed has an impact on the variation of effective fracture parameters. Only for stiff cracks, despite their size and density, do κ_n^{vf} values follow the theoretical trend $\chi \to 1$; hence, it becomes difficult to separate the effect of big or small cracks. On the contrary, for compliant cracks, the attribute χ is able to distinguish the crack size and it approaches unity for larger cracks.

This attribute can be utilised to better determine the crack stiffness in real field scenarios. However, inverting only for the volumetric stiffness both crack size and crack stiffness cannot be uniquely and simultaneously characterised using χ. Hence two independent measures of crack size and crack spacing (e.g. from outcrops or boreholes) are needed – the latter is used to estimate κ^{vol}. In this way the mechanical properties of the cracks in the rock volume, paramount for both mechanical and hydraulic models, are uniquely defined.

Finally, GA-FWFI has shown accuracy and robustness in estimating fracture strike ϕ and fracture dip δ by analysing a narrow azimuth seismic dataset.

Chapter 6

Conclusions and suggestions for future studies

6.1 Summary of key findings

This thesis develops a novel approach for characterising individual fracture properties as well as fractured rock volumes within the framework of full waveform inversion.

The proposed approach, named Genetic Algorithm Full-Waveform Fraction Inversion (GA-FWFI), employs the genetic algorithm as optimisation method to best fit the *observed data* with *forward modelled data* in order to estimate fracture stiffness (both specific and volumetric), fracture location and background material properties. The model ensembles generated through GA are subsequently utilised to estimate the posterior probability distributions using the Neighbourhood Algorithm (NA) technique.

The key achievements and findings of this thesis can be summarised as follows:

1. Successful development of the genetic algorithm method in *Python*. The code has been parallelised using the message-passing interface (MPI) protocol to be distributed over a large multi-core multi-node cluster and to mitigate the computational burden given by solving thousands of forward problems;
2. Implementation of the NA methodology to characterise the uncertainty associated

with the inverted model parameters, and describe qualitatively the whole model space;

3. The degree of accuracy and convergence of the algorithm, and the ability of the NA method to appraise the model ensemble, has been established through diagnostic analytical experiments. A population size around 25 times the space dimension was shown a good compromise between efficiency and computing time;
4. Synthetic ultrasonic experiments for a fractured medium containing 5 parallel fractures were successfully inverted. Here, the specific stiffnesses (normal and shear) of each fracture, their location along the x-axis, and the background velocity were correctly estimated by the inversion. All the inverted parameters were well constrained as shown by the PPDs. They did not exhibit cross-talk;
5. The GA-FWFI method was successfully applied to a laboratory experiment to mechanically characterise a rock joint during shear failure. The GA-FWFI method was applied to characterise the discontinuity in terms of its mechanical properties (both κ_n and κ_s) by best fitting the experimental transmitted and reflected S- and P-waves. To generalise the process for cases where the analytical solution could fail, P- and S-wave velocity, and the joint location along the x-axis were added as free parameters;
6. The inversion of the experiment gave estimates of the joint location and background velocities agreed with the corresponding ground-truth. The inverted fracture specific stiffness values followed with a high degree of accuracy the analytical trend, and the precursors to the shear failure were also correctly characterised;
7. The Bayesian analysis of all inverted parameters for the experiment showed that they were well constrained. Exceptions were shear fracture stiffness for P-wave inversions and normal fracture stiffness for S-wave inversions, which are insensitive due to the wave propagation being normal to the joint;
8. GA-FWFI was applied to synthetic seismic data generated in simulated multi-azimuth cross-hole experiments across a medium containing discrete randomly

distributed parallel cracks. Effective fracture strike ϕ and fracture dip δ, along with the equivalent fracture stiffness were estimated. A good match was obtained between the modelled and observed data. This leads to an estimate of the equivalent fracture orientation which is in excellent agreement with the crack dip and crack strike (from 0° to 60°);

9. GA-FWFI was applied to quantify the extent that discrete crack properties impact the overall elastic properties of an HTI material containing randomly distributed parallel cracks. The data analysis was performed over 54 different discrete fracture networks. It has shown that the transition from a medium with open cracks (low crack stiffness) to one with welded interfaces (high crack stiffness) is described by a non-linear relationship between the crack specific stiffness and the bulk fracture stiffness. This was verified for media with different crack densities and crack sizes;

10. Results showed that even in the long wavelength approximation, crack size has an indubitable impact on the variation of the effective fracture parameters. The attribute χ was introduced to characterise the crack-size dependence of the equivalent medium stiffness in real field scenarios. However, independent measures of crack size and crack spacing are needed. This attribute was shown to be independent of crack density;

11. The attribute χ captures the behaviour of media with stiff cracks which approach the linear trend. This holds for any crack size.

12. The uncertainties associated with the inverted stiffness increase for stiff crack cases, showing flat and multimodal PPDs.

13. The properties of χ can be therefore employed to guide the interpretation of a cracked medium by giving a range of likely values for crack size and crack stiffness;

6.2 Conclusions

The key role of fractures in a variety of physical processes in the subsurface make them a prominent target in a variety of geo-industrial applications, such as hydrocarbon and geothermal exploration, stability of underground openings, carbon capture and storage, and nuclear waste repositories.

Conventional seismic methods, which are used to detect and interpret the presence of fractures in seismic data, deal with the characterisation of the fracture-induced anisotropy making use of equivalent medium theories. These analyses are provided by processing only the change in wave amplitude or traveltime. However, these approaches need to be used with caution when the seismic wavelength decreases and approaches the order of magnitude of the fracture size and fracture spacing. For these cases it is necessary to account for the physics of scattering at each individual discrete fracture by making use of the discrete fracture representation. Experimental investigation of amplitude, or phase, changes as a function of explicit fracture properties have been carried out in controlled laboratory experiments with simple fracture geometries. However, a gap exists in linking different fracture model representations within a more comprehensive seismic method which can employ both the discrete fracture and the effective fracture models.

This thesis bridges this gap by developing and implementing a waveform inversion method (GA-FWFI) to advance and improve seismic processing methods by reducing the need to manually condition the data (e.g. manual picking) and providing a robust means to explore multiple solutions.

GA-FWFI facilitated the estimation of physical properties (fracture specific stiffness, fracture location, and background material properties) with a very high degree of accuracy in both synthetic and measured active ultrasonic waveforms. Moreover, the GA-FWFI approach was applied to unveil the coupling between the discrete fracture parameters with the equivalent fractured zone properties, showing that there is a non-linear relationship between the bulk fracture stiffness and crack specific stiffness and producing good estimates of the equivalent fracture orientation even for narrow azimuth data.

This work demonstrates that mechanical properties of fractures can be retrieved through a data driven methodology such as GA-FWFI. The set of information derived using the proposed methodology is useful to address a broad range of applications. From characterising, for instance, the fractured region closest to a tunnel (the Excavation Damage Zone), to a fundamental question of how to link different fracture media representations (e.g. discrete fractures to equivalent media approaches). The results shown in Chapter 5 demonstrates that the estimates of the mechanical properties of cracks are inaccurate (always underestimates) if the theoretical derivation is used. The mismatch increases as the cracks become more compliant and smaller.

Further work may be needed to explore these findings in a wider variety of settings, but the insights presented here provide a solid foundation on which to build future studies.

6.3 Recommendations for future studies

Future research and further GA-FWFI implementation includes, but is not limited to, the following:

1. **Non uniform fracture stiffness**

   The numerical experiments on explicit fractures carried out in this work have considered a uniform stress state which produces a uniform fracture stiffness along the fracture. Nevertheless, when the stress state is not uniform, fracture stiffness varies along the fracture. It is therefore worth extending this approach to invert for spatially varying fracture stiffness both for interpreting stress and as an alternative to stress dependent stiffness.

2. **Localised Effective Medium (LEM)**

   Further improvement of the inversion algorithm can be obtained by implementing the LEM approach (Parastatidis et al., 2021) to model explicit fractures. The discrete fracture representation in WAVE3D has the main limitation of creating explicit fractures only along the rectangular FD grid, so tilted fractures cannot be modelled. However, the LEM approach condenses the advantages of the explicit representation and those of the equivalent medium approach by readily creating tilted fractures. This leads to a generalised approach for a more complete fracture characterisation.

3. **Medium with two or more fracture sets**

   Characterising a medium with several fracture sets can be more challenging due to a potential cross-talk between stiffness and fracture orientation of the different sets. However, the GA-FWFI method could be used to quantitatively assess the relationship between these parameters.

4. **Algorithmic improvements**

   There exist many variants of GA which aim to improve its accuracy, robustness, convergence, and computing time. One GA scheme that could be adopted to better characterise fractures is an implementation which uses multiple populations within a single generation, where each population evolves in a different model space region. This has shown more robustness against premature convergence and a better sampling of the model space, improving in turn the uncertainty estimation (Aleardi and Mazzotti, 2017).

5. **GPU implementation**

   With the aim to improve the computing cost a GPU (graphics processing unit) implementation, thanks to its highly parallel architecture, would allow for a significant reduction of computing cost. This can significantly enhance the possibility of application to larger data volumes.

References

Aleardi, M. and A. Mazzotti (2017). “1D elastic full-waveform inversion and uncertainty estimation by means of a hybrid genetic algorithm–Gibbs sampler approach”. In: *Geophysical Prospecting* 65.1, pp. 64–85.

Alford, R. (1986). “Shear data in the presence of azimuthal anisotropy: Dilley, Texas”. In: *SEG Technical Program Expanded Abstracts 1986*. Society of Exploration Geophysicists, pp. 476–479.

Aliabadi, M. H. (Feb. 1997). “Boundary Element Formulations in Fracture Mechanics”. In: *Applied Mechanics Reviews* 50.2, pp. 83–96.

Allison, J. (2012). *Simplified Gradient Descent Optimization*. MATLAB File Exchange.

Angus, D. A., J. P. Verdon, Q. J. Fisher, and J.-M. Kendall (2009). “Exploring trends in microcrack properties of sedimentary rocks: An audit of dry-core velocity-stress measurements”. In: *Geophysics* 74.5, E193–E203.

Bakulin, A., V. Grechka, and I. Tsvankin (2000). “Estimation of fracture parameters from reflection seismic data—Part I: HTI model due to a single fracture set”. In: *Geophysics* 65.6, pp. 1788–1802.

Bandis, S., A. Lumsden, and N. Barton (1983). “Fundamentals of rock joint deformation”. In: *International Journal of Rock Mechanics and Mining Sciences & Geomechanics Abstracts*. Vol. 20. 6. Elsevier, pp. 249–268.

Bansal, R. and M. K. Sen (2010). “Ray-Born inversion for fracture parameters”. In: *Geophysical Journal International* 180.3, pp. 1274–1288.

Barbosa, N. D., E. Caspari, J. G. Rubino, A. Greenwood, L. Baron, and K. Holliger (2019). “Estimation of fracture compliance from attenuation and velocity analysis of full-waveform sonic log data". In: *Journal of Geophysical Research: Solid Earth* 124.3, pp. 2738–2761.

Barbosa, N. D., A. Greenwood, E. Caspari, N. Dutler, and K. Holliger (2021). "Estimates of Individual Fracture Compliances Along Boreholes From Full-Waveform Sonic Log Data". In: *Journal of Geophysical Research: Solid Earth* 126.5, e2021JB022015.

Belding, T. C. (1995). "The distributed genetic algorithm revisited". In: *arXiv preprint adap-org/9504007*.

Bourne, V. R., C. D. Cantu Bendeck, M. W. Hildyard, R. A. Clark, and W. Wills (2021). "Fracture-generated frequency-dependent seismic Q measured from a VSP in granite". In: *EGU General Assembly Conference Abstracts*, EGU21–12766.

Brossier, R. (2011). "Two-dimensional frequency-domain visco-elastic full waveform inversion: Parallel algorithms, optimization and performance". In: *Computers & Geosciences* 37.4, pp. 444–455.

Budiansky, B. and R. J. O'Connell (1976). "Elastic moduli of a cracked solid". In: *International journal of Solids and structures* 12.2, pp. 81–97.

Bunks, C., F. M. Saleck, S. Zaleski, and G. Chavent (1995). "Multiscale seismic waveform inversion". In: *Geophysics* 60.5, pp. 1457–1473.

Chavent, G. (1974). "Identification of functional parameters in partial differential equations". In: *Joint Automatic Control Conference*. 12, pp. 155–156.

Chen, G. and Z. Wang (2017). "Robust full-waveform inversion based on particle swarm optimization". In: *2017 SEG International Exposition and Annual Meeting*. OnePetro.

Chen, T., K. Tang, G. Chen, and X. Yao (2012). "A large population size can be unhelpful in evolutionary algorithms". In: *Theoretical Computer Science* 436, pp. 54–70.

Chichinina, T., I. Obolentseva, and G. Dugarov (2015). "Effective-medium anisotropic models of fractured rocks of TI symmetry: Analysis of constraints and limitations in linear slip model". In: *2015 SEG Annual Meeting*. OnePetro.

Chichinina, T., V. Sabinin, and G. Ronquillo-Jarillo (2006). “QVOA analysis: P-wave attenuation anisotropy for fracture characterization”. In: *Geophysics* 71.3, pp. C37–C48.

Choi, M.-K., A. Bobet, and L. J. Pyrak-Nolte (2014). “The effect of surface roughness and mixed-mode loading on the stiffness ratio κ_x/κ_z for fractures”. In: *Geophysics* 79.5, pp. D319–D331.

Claerbout, J. F. (1976). *Fundamentals of geophysical data processing.* Vol. 274. Citeseer.

— (1985). *Imaging the earth’s interior.* Vol. 1. Blackwell scientific publications Oxford.

Clark, R. A., P. M. Benson, A. J. Carter, and C. A. G. Moreno (2009). “Anisotropic P-wave attenuation measured from a multi-azimuth surface seismic reflection survey”. In: *Geophysical Prospecting* 57.5, pp. 835–845.

Coates, R. T. and M. Schoenberg (1995). “Finite-difference modeling of faults and fractures”. In: *Geophysics* 60.5, pp. 1514–1526.

Collino, F. and C. Tsogka (2001). “Application of the perfectly matched absorbing layer model to the linear elastodynamic problem in anisotropic heterogeneous media”. In: *Geophysics* 66.1, pp. 294–307.

Crampin, S. (1981). “A review of wave motion in anisotropic and cracked elastic-media”. In: *Wave motion* 3.4, pp. 343–391.

— (1984). “Effective anisotropic elastic constants for wave propagation through cracked solids”. In: *Geophysical Journal International* 76.1, pp. 135–145.

Crampin, S., R. McGonigle, and D. Bamford (1980). “Estimating crack parameters from observations of P-wave velocity anisotropy”. In: *Geophysics* 45.3, pp. 345–360.

Cundall, P. (1992). “Theoretical basis of the program WAVE”. In: *Unpublished internal report, COMRO (now Miningtek, CSIR, South Africa)*, pp. 1–12.

Datta, D. and M. K. Sen (2016). “Estimating a starting model for full-waveform inversion using a global optimization method”. In: *Geophysics* 81.4, R211–R223.

Debens, H. A. (2015). “Three-dimensional anisotropic full-waveform inversion”. PhD thesis. Imperial College London.

Dershowitz, W. S. and H. H. Herda (1992). “Interpretation of fracture spacing and intensity”. In: *The 33rd US Symposium on Rock Mechanics (USRMS).* OnePetro.

Dershowitz, W. (1998). “FracMan interactive discrete feature data analysis, geometric modeling and exploration simulation”. In: *User documentation*.

Dieterich, J. M. and B. Hartke (2012). “Empirical review of standard benchmark functions using evolutionary global optimization”. In: *arXiv preprint arXiv:1207.4318*.

Fabien-Ouellet, G., E. Gloaguen, and B. Giroux (2017). “Time domain viscoelastic full waveform inversion”. In: *Geophysical Journal International* 209.3, pp. 1718–1734.

Fichtner, A. (2010). *Full seismic waveform modelling and inversion*. Springer Science & Business Media.

Fountain, A. G., R. W. Jacobel, R. Schlichting, and P. Jansson (2005). “Fractures as the main pathways of water flow in temperate glaciers”. In: *Nature* 433.7026, pp. 618–621.

Fuggi, A., M. Hildyard, R. Clark, A. Hooper, and J. Brittan (2021). “Seismic expression of cracks: reconciling discrete fracture network modelling and effective medium approaches”. In: *82nd EAGE Annual Conference & Exhibition*. Vol. 2021. 1. European Association of Geoscientists & Engineers, pp. 1–5.

Fuggi, A., W. Hildyard, A. Hooper, R. Clark, and J. Brittan (2019). “Genetic Full Waveform Inversion to Characterise Fractures”. In: *81st EAGE Conference and Exhibition 2019*. 1. European Association of Geoscientists & Engineers, pp. 1–5.

Fuggi, A., P. de Groot, A. Huck, H. Jaglan, and N. Hemstra (2020). “AVOA modeling for fracture-induced anisotropy based on the elastic impedance formalism”. In: *SEG Technical Program Expanded Abstracts 2020*. Society of Exploration Geophysicists, pp. 315–319.

Gallagher, K., M. Sambridge, and G. Drijkoningen (1991). “Genetic algorithms: An evolution from Monte Carlo Methods for strongly non-linear geophysical optimization problems”. In: *Geophysical Research Letters* 18.12, pp. 2177–2180.

Gao, Z., J. Gao, Z. Pan, and X. Zhang (2014). “Building an initial model for full waveform inversion using a global optimization scheme”. In: *SEG Technical Program Expanded Abstracts 2014*. Society of Exploration Geophysicists, pp. 1136–1141.

Goldberg, D. E. (1989). *Genetic algorithms in search, optimization, and machine learning*. Tech. rep.

Gonçalves, J. F., J. J. de Magalhães Mendes, and M. G. Resende (2005). “A hybrid genetic algorithm for the job shop scheduling problem”. In: *European journal of operational research* 167.1, pp. 77–95.

Goodman, R. E., R. L. Taylor, and T. L. Brekke (1968). “A model for the mechanics of jointed rock”. In: *Journal of the soil mechanics and foundations division* 94.3, pp. 637–659.

Grechka, V. and I. Tsvankin (1998). “Feasibility of nonhyperbolic moveout inversion in transversely isotropic media”. In: *Geophysics* 63.3, pp. 957–969.

Guasch, L., M. Warner, I. Stekl, and A. Umpleby (2010). “3D Elastic wavefield inversion in the time domain”. In: *72nd EAGE Conference and Exhibition incorporating SPE EUROPEC 2010*. European Association of Geoscientists & Engineers, cp–161.

Hedayat, A., L. J. Pyrak-Nolte, and A. Bobet (2014a). “Multi-modal monitoring of slip along frictional discontinuities”. In: *Rock mechanics and rock engineering* 47.5, pp. 1575–1587.

— (2014b). “Precursors to the shear failure of rock discontinuities”. In: *Geophysical Research Letters* 41.15, pp. 5467–5475.

Hedayat, A. (2013). “Mechanical and geophysical characterization of damage in rocks”. PhD thesis. Purdue University West Lafayette, IN.

Herrera, F., M. Lozano, and J. L. Verdegay (1998). “Tackling real-coded genetic algorithms: Operators and tools for behavioural analysis”. In: *Artificial intelligence review* 12.4, pp. 265–319.

Hildyard, M., R. Young, R. Collins, and W. Pettit (2005). “Seismic wave propagation to diagnose the state of fracturing”. In: *Journal of the Southern African Institute of Mining and Metallurgy* 105.6, pp. 437–446.

Hildyard, M. W. (2001). “Wave interaction with underground openings in fractured rock”. PhD thesis. University of Liverpool.

Hildyard, M. (2007). “Manuel Rocha Medal Recipient Wave interaction with underground openings in fractured rock”. In: *Rock Mechanics and Rock Engineering* 40.6, pp. 531–561.

Hildyard, M., A. Daehnke, and P. Cundall (1995). “WAVE: A computer program for investigating elastodynamic issues in mining”. In: *The 35th US Symposium on Rock Mechanics (USRMS).* American Rock Mechanics Association.

Hildyard, M. and R. P. Young (2002). “Modelling seismic waves around underground openings in fractured rock”. In: *The Mechanism of Induced Seismicity.* Springer, pp. 247–276.

Hobday, C. and M. Worthington (2012). “Field measurements of normal and shear fracture compliance”. In: *Geophysical Prospecting* 60.3, pp. 488–499.

Holland, J. H. (1975). “Adaptation in natural and artificial systems. An introductory analysis with application to biology, control, and artificial intelligence”. In: *Ann Arbor, MI: University of Michigan Press*, pp. 439–444.

Hopkins, D. L., N. G. Cook, and L. R. Myer (1987). “Fracture stiffness and aperture as a function of applied stress and contact geometry”. In: *The 28th US Symposium on Rock Mechanics (USRMS).* OnePetro.

Hornby, B., D. Johnson, K. Winkler, and R. Plumb (1989). “Fracture evaluation using reflected Stoneley-wave arrivals”. In: *Geophysics* 54.10, pp. 1274–1288.

Hou, S., H. Dai, and X. Li (2013). “Waveform inversion for fracture-induced anisotropy”. In: *SEG Technical Program Expanded Abstracts 2013.* Society of Exploration Geophysicists, pp. 357–361.

Hsu, C.-J. and M. Schoenberg (1993). “Elastic waves through a simulated fractured medium”. In: *Geophysics* 58.7, pp. 964–977.

Hudson, J. A. (1980). “Overall properties of a cracked solid”. In: *Mathematical Proceedings of the Cambridge Philosophical Society.* Vol. 88. 2. Cambridge University Press, pp. 371–384.

— (1981). “Wave speeds and attenuation of elastic waves in material containing cracks”. In: *Geophysical Journal International* 64.1, pp. 133–150.

Hunziker, J., A. Greenwood, S. Minato, N. D. Barbosa, E. Caspari, and K. Holliger (2020). “Bayesian full-waveform inversion of tube waves to estimate fracture aperture and compliance”. In: *Solid Earth* 11.2, pp. 657–668.

Iding, M. and P. Ringrose (2009). “Evaluating the impact of fractures on the long-term performance of the In Salah CO2 storage site”. In: *Energy Procedia* 1.1, pp. 2021–2028.

Igel, H. (2017). *Computational seismology: a practical introduction.* Oxford University Press.

Janikow, C. Z. and Z. Michalewicz (1991). “An experimental comparison of binary and floating point representations in genetic algorithms.” In: *ICGA*, pp. 31–36.

Jiang, X.-W., L. Wan, X.-S. Wang, S.-H. Liang, and B. X. Hu (2009). “Estimation of fracture normal stiffness using a transmissivity-depth correlation”. In: *International Journal of Rock Mechanics and Mining Sciences* 46.1, pp. 51–58.

Jones, I. F. (2018). *Velocities, Imaging and Waveform Inversion: The Evolution of Characterising the Earth’s Subsurface.* EAGE Publications.

Kennedy, J. and R. Eberhart (1995). “Particle swarm optimization”. In: *Proceedings of ICNN’95-international conference on neural networks.* Vol. 4. IEEE, pp. 1942–1948.

Kirkpatrick, S., C. D. Gelatt, and M. P. Vecchi (1983). “Optimization by simulated annealing”. In: *science* 220.4598, pp. 671–680.

Komatitsch, D. and J. Tromp (2003). “A perfectly matched layer absorbing boundary condition for the second-order seismic wave equation”. In: *Geophysical Journal International* 154.1, pp. 146–153.

Lailly, P. (1983). “The seismic inverse problem as a sequence of before stack migrations”. In: *Conference on inverse scattering: theory and application.* Siam Philadelphia, PA, pp. 206–220.

Levander, A. R. (1988). “Fourth-order finite-difference P-SV seismograms”. In: *Geophysics* 53.11, pp. 1425–1436.

Liu, E., J. A. Hudson, and T. Pointer (2000). “Equivalent medium representation of fractured rock”. In: *Journal of Geophysical Research: Solid Earth* 105.B2, pp. 2981–3000.

Liu, E. and A. Martinez (2012). *Seismic fracture characterization: Concepts and practical applications.* EAGE.

Lou, M. and J. Rial (1995). “Modelling elastic-wave propagation in inhomogeneous anisotropic media by the pseudo-spectral method”. In: *Geophysical Journal International* 120.1, pp. 60–72.

Lu, Y., Y. Tien, and C. Juang (2017). “Uncertainty of 1-D fracture intensity measurements”. In: *Journal of Geophysical Research: Solid Earth* 122.11, pp. 9344–9358.

Lubbe, R., J. Sothcott, M. Worthington, and C. McCann (2008). “Laboratory estimates of normal and shear fracture compliance”. In: *Geophysical Prospecting* 56.2, pp. 239–247.

Lubbe, R. and M. Worthington (2006). “A field investigation of fracture compliance”. In: *Geophysical Prospecting* 54.3, pp. 319–331.

MacQuarrie, K. T. and K. U. Mayer (2005). “Reactive transport modeling in fractured rock: A state-of-the-science review”. In: *Earth-Science Reviews* 72.3-4, pp. 189–227.

Mallick, S. (1995). “Model-based inversion of amplitude-variations-with-offset data using a genetic algorithm”. In: *Geophysics* 60.4, pp. 939–954.

March, R., F. Doster, and S. Geiger (2018). “Assessment of CO2 storage potential in naturally fractured reservoirs with dual-porosity models”. In: *Water Resources Research* 54.3, pp. 1650–1668.

Mavko, G., T. Mukerji, and J. Dvorkin (2020). *The rock physics handbook.* Cambridge university press.

Mazzotti, A., N. Bienati, E. Stucchi, A. Tognarelli, M. Aleardi, and A. Sajeva (2016). “Two-grid genetic algorithm full-waveform inversion”. In: *The Leading Edge* 35.12, pp. 1068–1075.

Menke, W. (2012). *Geophysical data analysis: discrete inverse theory: MATLAB edition.* Vol. 45. Academic press.

Michalewicz, Z., T. Logan, and S. Swaminathan (1994). “Evolutionary operators for continuous convex parameter spaces”. In: *Proceedings of the 3rd Annual conference on Evolutionary Programming.* World Scientific, pp. 84–97.

Mikhailenko, B. G. (2000). “Seismic modeling by the spectral-finite difference method”. In: *Physics of the Earth and Planetary Interiors* 119.1-2, pp. 133–147.

Moffat, L., R. Clark, M. van der Baan, and T. Manning (2010). “Azimuthal Anisotropy Characterization Using 3D Multi-azimuth Towed Streamer Dataset”. In: *72nd EAGE Conference and Exhibition incorporating SPE EUROPEC 2010.* European Association of Geoscientists & Engineers, cp–161.

Mora, P. (1987). “Nonlinear two-dimensional elastic inversion of multioffset seismic data”. In: *Geophysics* 52.9, pp. 1211–1228.

Mosegaard, K. and A. Tarantola (1995). “Monte Carlo sampling of solutions to inverse problems”. In: *Journal of Geophysical Research: Solid Earth* 100.B7, pp. 12431–12447.

Myer, L. R. (2000). “Fractures as collections of cracks”. In: *International Journal of Rock Mechanics and Mining Sciences* 37.1-2, pp. 231–243.

Nakagawa, S., K. Nihei, and L. Myer (2000). “Shear-induced conversion of seismic waves across single fractures”. In: *International Journal of Rock Mechanics and Mining Sciences* 37.1-2, pp. 203–218.

Operating system ARC4 (2021). `https://arcdocs.leeds.ac.uk/systems/arc4.html`. Accessed: 19/11/2021.

Parastatidis, E., M. Hildyard, and G. Stuart (2017). “Modelling P-wave propagation in a medium with multiple parallel fractures and direct comparison with experimental recordings.” In: *51st US Rock Mechanics/Geomechanics Symposium.* OnePetro.

Parastatidis, E., M. W. Hildyard, and A. Nowacki (2021). “Simplified Seismic Modelling of Fractured Rock: How Effective is the Localised Effective Medium Compared to Explicit Representation of Individual Fractures”. In: *Rock Mechanics and Rock Engineering*, pp. 1–17.

Petrovitch, C. L., D. D. Nolte, and L. J. Pyrak-Nolte (2013). “Scaling of fluid flow versus fracture stiffness”. In: *Geophysical Research Letters* 40.10, pp. 2076–2080.

Pierini, S., M. Aleardi, and A. Mazzotti (2019). “A method to attenuate genetic drift in genetic-algorithm optimizations: Applications to analytic objective functions and two seismic optimization problems”. In: *Geophysics* 84.2, R295–R310.

Plessix, R.-E. (2006). “A review of the adjoint-state method for computing the gradient of a functional with geophysical applications”. In: *Geophysical Journal International* 167.2, pp. 495–503.

Pohlheim, H. (2005). “GEATbx Introduction Evolutionary Algorithms: Overview, Methods and Operators”. In: *Documentation for: GEATbx version* 3.

Pratt, R. G. (1999). “Seismic waveform inversion in the frequency domain, Part 1: Theory and verification in a physical scale model”. In: *Geophysics* 64.3, pp. 888–901.

Pratt, R. G., C. Shin, and G. Hick (1998). “Gauss–Newton and full Newton methods in frequency–space seismic waveform inversion”. In: *Geophysical Journal International* 133.2, pp. 341–362.

Pratt, R. G. and R. M. Shipp (1999). “Seismic waveform inversion in the frequency domain, Part 2: Fault delineation in sediments using crosshole data”. In: *Geophysics* 64.3, pp. 902–914.

Provenzano, G., M. E. Vardy, and T. J. Henstock (2018). “Decimetric-resolution stochastic inversion of shallow marine seismic reflection data: dedicated strategy and application to a geohazard case study”. In: *Geophysical Journal International* 214.3, pp. 1683–1700.

Pyrak-Nolte, L. J., L. R. Myer, and N. G. Cook (1990a). “Anisotropy in seismic velocities and amplitudes from multiple parallel fractures”. In: *Journal of Geophysical Research: Solid Earth* 95.B7, pp. 11345–11358.

— (1990b). “Transmission of seismic waves across single natural fractures”. In: *Journal of Geophysical Research: Solid Earth* 95.B6, pp. 8617–8638.

Pyrak-Nolte, L. J. and D. D. Nolte (2016). “Approaching a universal scaling relationship between fracture stiffness and fluid flow”. In: *Nature communications* 7.1, pp. 1–6.

— (1992). “Frequency dependence of fracture stiffness”. In: *Geophysical Research Letters* 19.3, pp. 325–328.

Pyrak-Nolte, L. (1996). “The seismic response of fractures and the interrelations among fracture properties”. In: *International journal of rock mechanics and mining sciences & geomechanics abstracts*. Vol. 33. 8. Elsevier, pp. 787–802.

Rao, Y. and Y. Wang (2009). “Fracture effects in seismic attenuation images reconstructed by waveform tomography”. In: *Geophysics* 74.4, R25–R34.

Rogers, S., D. Elmo, G. Webb, and A. Catalan (2015). “Volumetric fracture intensity measurement for improved rock mass characterisation and fragmentation assessment in block caving operations”. In: *Rock Mechanics and Rock Engineering* 48.2, pp. 633–649.

Rüger, A. (1997). “P-wave reflection coefficients for transversely isotropic models with vertical and horizontal axis of symmetry”. In: *Geophysics* 62.3, pp. 713–722.

— (1998). “Variation of P-wave reflectivity with offset and azimuth in anisotropic media”. In: *Geophysics* 63.3, pp. 935–947.

Rüger, A. and I. Tsvankin (1997). “Using AVO for fracture detection: Analytic basis and practical solutions”. In: *The Leading Edge* 16.10, pp. 1429–1434.

Sajeva, A., M. Aleardi, B. Galuzzi, E. Stucchi, E. Spadavecchia, and A. Mazzotti (2017). “Comparing the performances of four stochastic optimisation methods using analytic objective functions, 1D elastic full-waveform inversion, and residual static computation”. In: *Geophysical Prospecting* 65.S1, pp. 322–346.

Sajeva, A., M. Aleardi, E. Stucchi, N. Bienati, and A. Mazzotti (2016). “Estimation of acoustic macro models using a genetic full-waveform inversion: Applications to the Marmousi model”. In: *Geophysics* 81.4, R173–R184.

Sambridge, M. (n.d.). “Inverse problems in a nutshell”. In: *Center for Advanced Data Inference, Research School of Earth Sciences, Australian National University, ACT* 200 ().

Sambridge, M. (1999a). “Geophysical inversion with a neighbourhood algorithm—I. Searching a parameter space”. In: *Geophysical journal international* 138.2, pp. 479–494.

— (1999b). “Geophysical inversion with a neighbourhood algorithm—II. Appraising the ensemble”. In: *Geophysical Journal International* 138.3, pp. 727–746.

Sambridge, M. and G. Drijkoningen (1992). “Genetic algorithms in seismic waveform inversion”. In: *Geophysical Journal International* 109.2, pp. 323–342.

Sambridge, M. and K. Mosegaard (2002). “Monte Carlo methods in geophysical inverse problems”. In: *Reviews of Geophysics* 40.3, pp. 3–1.

Sayers, C. and M. Kachanov (1991). “A simple technique for finding effective elastic constants of cracked solids for arbitrary crack orientation statistics”. In: *International Journal of Solids and Structures* 27.6, pp. 671–680.

Sayers, C. M. (2007). “Introduction to this special section: Fractures”. In: *The Leading Edge* 26.9, pp. 1102–1105.

Schoenberg, M. (1983). “Reflection of elastic waves from periodically stratified media with interfacial slip”. In: *Geophysical prospecting* 31.2, pp. 265–292.

Schoenberg, M. and J. Douma (1988). “Elastic wave propagation in media with parallel fractures and aligned cracks”. In: *Geophysical prospecting* 36.6, pp. 571–590.

Schoenberg, M. (1980). “Elastic wave behavior across linear slip interfaces”. In: *The Journal of the Acoustical Society of America* 68.5, pp. 1516–1521.

Schoenberg, M. and F. Muir (1989). “A calculus for finely layered anisotropic media”. In: *Geophysics* 54.5, pp. 581–589.

Schoenberg, M. and C. M. Sayers (1995). “Seismic anisotropy of fractured rock”. In: *Geophysics* 60.1, pp. 204–211.

Sears, T. J., S. Singh, and P. Barton (2008). “Elastic full waveform inversion of multicomponent OBC seismic data”. In: *Geophysical Prospecting* 56.6, pp. 843–862.

Sen, M. K. and P. L. Stoffa (1991). “Nonlinear one-dimensional seismic waveform inversion using simulated annealing”. In: *Geophysics* 56.10, pp. 1624–1638.

— (1992). “Rapid sampling of model space using genetic algorithms: examples from seismic waveform inversion”. In: *Geophysical Journal International* 108.1, pp. 281–292.

— (2013). *Global optimization methods in geophysical inversion.* Cambridge University Press.

Shukla, A., H. M. Pandey, and D. Mehrotra (2015). “Comparative review of selection techniques in genetic algorithm”. In: *Futuristic Trends on Computational Analysis and Knowledge Management (ABLAZE), 2015 International Conference on.* IEEE, pp. 515–519.

Snieder, R. (1998). “The role of nonlinearity in inverse problems”. In: *Inverse problems* 14.3, p. 387.

Stoffa, P. L. and M. K. Sen (1991). “Nonlinear multiparameter optimization using genetic algorithms: Inversion of plane-wave seismograms”. In: *Geophysics* 56.11, pp. 1794–1810.

Tarantola, A. (1984a). “Inversion of seismic reflection data in the acoustic approximation”. In: *Geophysics* 49.8, pp. 1259–1266.

— (1984b). “Linearized inversion of seismic reflection data”. In: *Geophysical prospecting* 32.6, pp. 998–1015.

— (2005). *Inverse problem theory and methods for model parameter estimation.* SIAM.

Thomsen, L. (1986). “Weak elastic anisotropy”. In: *Geophysics* 51.10, pp. 1954–1966.

Tognarelli, A., E. Stucchi, and A. Mazzotti (2020). “Velocity model estimation by means of Full Waveform Inversion of transmitted waves: An example from a seismic profile in the geothermal areas of Southern Tuscany, Italy”. In: *Geothermics* 88, p. 101894.

Tognarelli, A., E. Stucchi, N. Bienati, A. Sajeva, M. Aleardi, and A. Mazzotti (2015). “Two-grid stochastic full waveform inversion of 2D marine seismic data”. In: *77th EAGE Conference and Exhibition 2015.* Vol. 2015. 1. European Association of Geoscientists & Engineers, cp–451.

Tran, K. T. and D. R. Hiltunen (2012). “One-dimensional inversion of full waveforms using a genetic algorithm”. In: *Journal of Environmental and Engineering Geophysics* 17.4, pp. 197–213.

Tromp, J., C. Tape, and Q. Liu (2005). “Seismic tomography, adjoint methods, time reversal and banana-doughnut kernels”. In: *Geophysical Journal International* 160.1, pp. 195–216.

Tsang, C.-F., F. Bernier, and C. Davies (2005). “Geohydromechanical processes in the Excavation Damaged Zone in crystalline rock, rock salt, and indurated and plastic clays—in the context of radioactive waste disposal”. In: *International Journal of Rock Mechanics and Mining Sciences* 42.1, pp. 109–125.

Tsang, C.-F., I. Neretnieks, and Y. Tsang (2015). “Hydrologic issues associated with nuclear waste repositories”. In: *Water Resources Research* 51.9, pp. 6923–6972.

Tsvankin, I. (1997). “Reflection moveout and parameter estimation for horizontal transverse isotropy”. In: *Geophysics* 62.2, pp. 614–629.

Tsvankin, I. and L. Thomsen (1994). “Nonhyperbolic reflection moveout in anisotropic media”. In: *Geophysics* 59.8, pp. 1290–1304.

Verdon, J. P. and A. Wüstefeld (2013). “Measurement of the normal/tangential fracture compliance ratio (Z_N/Z_T) during hydraulic fracture stimulation using S-wave splitting data”. In: *Geophysical Prospecting* 61, pp. 461–475.

Verdon, J., J.-M. Kendall, and A. Wüstefeld (2009). “Imaging fractures and sedimentary fabrics using shear wave splitting measurements made on passive seismic data”. In: *Geophysical Journal International* 179.2, pp. 1245–1254.

Virieux, J. (1986). “P-SV wave propagation in heterogeneous media: Velocity-stress finite-difference method”. In: *Geophysics* 51.4, pp. 889–901.

Virieux, J. and S. Operto (2009). “An overview of full-waveform inversion in exploration geophysics”. In: *Geophysics* 74.6, WCC1–WCC26.

Vlastos, S., E. Liu, I. G. Main, and X.-Y. Li (2003). “Numerical simulation of wave propagation in media with discrete distributions of fractures: effects of fracture sizes and spatial distributions”. In: *Geophysical Journal International* 152.3, pp. 649–668.

Wan, W. and J. B. Birch (2013). “An improved hybrid genetic algorithm with a new local search procedure”. In: *Journal of Applied Mathematics* 2013.

Warner, M., A. Ratcliffe, T. Nangoo, J. Morgan, A. Umpleby, N. Shah, V. Vinje, I. Stekl, L. Guasch, C. Win, G. Conroy, and A. Bertrand (2013). “Anisotropic 3D full-waveform inversion”. In: *Geophysics* 78, R59–R80.

Warner, M. and L. Guasch (2016). “Adaptive waveform inversion: Theory”. In: *Geophysics* 81.6, R429–R445.

Washington, I. J. of (2010). *Edge of Pine Island Glacier’s ice shelf is ripping apart, causing key Antarctic glacier to gain speed.* [Online; accessed October 27, 2021].

Weise, T. (2009). *Global optimization algorithms-theory and application.* Self-Published Thomas Weise.

Willis, M. E., D. R. Burns, R. Rao, B. Minsley, M. N. Toksöz, and L. Vetri (2006). "Spatial orientation and distribution of reservoir fractures from scattered seismic energy". In: *Geophysics* 71.5, O43–O51.

Worthington, M. (2008). "Interpreting seismic anisotropy in fractured reservoirs". In: *First Break* 26.7, pp. 57–73.

Worthington, M. (2007). "The compliance of macrofractures". In: *The Leading Edge* 26.9, pp. 1118–1122.

Wuestefeld, A., O. Al-Harrasi, J. P. Verdon, J. Wookey, and J. M. Kendall (2010). "A strategy for automated analysis of passive microseismic data to image seismic anisotropy and fracture characteristics". In: *Geophysical Prospecting* 58.5, pp. 755–773.

Yang, P., R. Brossier, L. Métivier, and J. Virieux (2016). "A review on the systematic formulation of 3-D multiparameter full waveform inversion in viscoelastic medium". In: *Geophysical Journal International* 207.1, pp. 129–149.

Yousef, B. and D. Angus (2016). "When do fractured media become seismically anisotropic? Some implications on quantifying fracture properties". In: *Earth and Planetary Science Letters* 444, pp. 150–159.

Zhang, Z., T. Alkhalifah, J.-W. Oh, and I. Tsvankin (2017). "Estimation of fracture parameters using elastic full-waveform inversion". In: *2017 SEG International Exposition and Annual Meeting*. OnePetro.

Zhe, Y. and G. Hanming (2013). "Non-linear prestack seismic inversion with global optimization using an edge-preserving smoothing filter". In: *Geophysical Prospecting* 61.4, pp. 747–760.

Zimmerman, R. and I. Main (2004). "Hydromechanical behavior of fractured rocks". In: *International Geophysics Series* 89, pp. 363–422.